



**HAL**  
open science

# Conception and realization of an indoor multi-user Light-Fidelity link

Mounir Mohammedi Merah

► **To cite this version:**

Mounir Mohammedi Merah. Conception and realization of an indoor multi-user Light-Fidelity link. Networking and Internet Architecture [cs.NI]. Université Paris-Saclay, 2019. English. NNT : 2019SACLV061 . tel-02409159v1

**HAL Id: tel-02409159**

**<https://theses.hal.science/tel-02409159v1>**

Submitted on 13 Dec 2019 (v1), last revised 19 Dec 2019 (v2)

**HAL** is a multi-disciplinary open access archive for the deposit and dissemination of scientific research documents, whether they are published or not. The documents may come from teaching and research institutions in France or abroad, or from public or private research centers.

L'archive ouverte pluridisciplinaire **HAL**, est destinée au dépôt et à la diffusion de documents scientifiques de niveau recherche, publiés ou non, émanant des établissements d'enseignement et de recherche français ou étrangers, des laboratoires publics ou privés.

# Conception et Réalisation d'un lien Light-Fidelity multi-utilisateurs en intérieur

Thèse de doctorat de l'Université Paris-Saclay  
préparée à Université de Versailles-Saint-Quentin-en-Yvelines

Ecole doctorale n°580 Sciences et technologies de l'information et de la  
communication (STIC)  
Spécialité de doctorat : Réseaux, Information, Communications

Thèse présentée et soutenue à Laboratoire d'Ingénierie des Systèmes de Versailles, le 08 octobre 2019, par

**MOUNIR M. MERAH**

Composition du Jury :

Véronique Vèque Professeure, Centrale Supélec	Présidente
Maite Brandt-Pearce Professeure, Université de Virginie	Rapporteur
Ali Khalighi Professeur, Ecole Centrale Marseille	Rapporteur
Razvan Stanica Professeur, INSA Lyon	Examineur
Luc Chassagne Professeur, Université de Versailles	Directeur de thèse
Hongyu Guan Ingénieur de recherche, Université de Versailles	Co-directeur de thèse



**Titre :** Conception et Réalisation d'un lien Light-Fidelity multi-utilisateur en intérieur

**Mots clés :** Communication par lumière visible, modulation multiband sans porteuse et en amplitude et phase, multi-utilisateur, attocell

**Résumé :** De nos jours, le nombre d'appareils connectés nécessitant un accès aux données mobiles est en augmentation constante. L'arrivée d'encre plus d'objets multimédias connectés et la demande croissante d'informations par appareil ont mis en évidence les limites de la quatrième génération de réseaux cellulaires (4G). Cela a poussé au développement de nouvelles méthodes, dont la 5G. L'objectif est d'être en mesure de prendre en charge la croissance des systèmes portables, des capteurs ou des systèmes associés à l'internet des objets (IoT). La vision derrière la 5G est de permettre une société entièrement mobile et connectée avec une expérience consistente.

Les petites cellules sont la base des normes de communication avancées telles que 4G et maintenant 5G. Ils résultent de l'utilisation de bandes de fréquences plus élevées pour l'accès radiofréquences (RF) afin de supporter de nouvelles normes et exigences croissantes en bande passante. La 5G utilise des ondes millimétriques et nécessite un déploiement dans un environnement urbain intérieur et urbain dense, ce qui peut s'avérer être un défi. C'est là que la 5G devra inclure des solutions de réseau hybrides et pouvoir coexister avec d'autres technologies d'accès sans fil. La communication par lumière visible (VLC) s'inscrit dans ce moule puisque la lumière visible correspond à la bande comprise entre 400 et 800 THz. Le spectre disponible est des milliers de fois plus large que le spectre RF et il n'interfère pas avec celui-ci. Le principe se base sur la combinaison de l'éclairage avec un lien de communication pouvant atteindre des dizaines de gigabits par seconde. Le potentiel est d'offrir un complément à la 5G dans un réseau hybride, offrant une vitesse élevée, aucune interférence et une sécurité accrue au prix d'une couverture limitée et d'une faible maturité technologique.

L'objectif de cette thèse est donc de proposer et d'évaluer une implémentation expérimentale d'un système VLC en intérieur et multi-utilisateurs afin de répondre aux objectifs de la configuration light-fidelity (Li-Fi) dans le contexte d'une petite cellule. La première étape de cette étude est un état de l'art détaillé sur le principe de VLC dans la communication sans fil en intérieur et de l'accès multi-utilisateur. Cela permet de mieux expliquer le concept de notre design et de comparer notre approche aux travaux existants. La deuxième étape consiste en une analyse des principes et des hypothèses pour le système VLC multi-utilisateurs en intérieur portant à la fois sur la technique de modulation et sur les schémas d'accès multi-utilisateurs. Les conclusions tirées des analyses théoriques et numériques servent de base pour la suite du travail. La troisième étape consiste en plusieurs analyses expérimentales sur l'optimisation des performances de diffusion pour un utilisateur unique, puis sur les performances multi-utilisateurs du système à l'aide de divers schémas d'accès. Le débit total avec une LED blanche commerciale atteint 163 Mb/s avec un taux d'erreur réduit d'un facteur de 3,55 grâce au processus d'optimisation des performances. Cette technique a l'avantage d'augmenter la flexibilité pour un scénario avec plusieurs utilisateurs sans augmenter la complexité car seuls les paramètres des filtres de modulation sont altérés. La taille de la cellule obtenue est de 4.56 m<sup>2</sup> à une distance de 2,15 mètres du transmetteur. Le débit peut atteindre jusqu'à 40 utilisateurs, ou 40.62 Mb/s dans un scénario à 4 utilisateurs. Il est donc démontré que le système proposé pourrait fonctionner comme une cellule à une distance réaliste, avec un débit de données élevé et la capacité de répondre aux besoins d'un grand nombre d'utilisateurs tout en limitant les coûts de mise en œuvre.

**Title :** Conception and Realization of an Indoor Multi-User Light-Fidelity Link

**Keywords :** Visible light communication, multiband carrierless amplitude and phase, multi-user, attocell

**Abstract :** Nowadays, the number of connected devices requiring access to mobile data is considerably increasing. The arrival of even more connected multimedia objects and the growing demand for more information per device highlighted the limits of the fourth generation of broadband cellular networks (4G). This pushed for the development of new methods, one of which is 5G. The goal is to be able to support the growth of wearable, sensors, or related internet-of-object (IoT) systems. The vision behind 5G is to enable a fully mobile and connected society with a consistent experience. In consequence, there is a fundamental need to achieve a seamless and consistent user experience across time and space.

Small cells are the basis of advanced communications standards such as 4G and now, 5G. They exist as a result of using higher frequency bands for RF access in order to support new standards and the increasing demands in bandwidth. 5G use millimeter waves and requires a deployment across indoor and dense urban environment which may prove to be a challenge. This is where 5G will need to include hybrid networking solutions and be able to coexist with other wireless access technologies. Visible light communication (VLC) fits into that mold since visible light corresponds to the band between 400 and 800 THz. The available spectrum is multiple thousand times the size of the RF spectrum and it does not interfere with it. The technique combines illumination with communication at possibly tens of gigabits per second. It has the potential to offer a synergistic pairing with 5G in a hybrid network, offering high speed, no interferences, and more security at the cost of limited coverage and

low technological maturity.

The goal of this thesis is thus to propose and evaluate an experimental implementation of an indoor multi-user VLC system in order to answer the objectives of Li-Fi setup in the context of a small cell. The first step of this study is a detailed state-of-the-art on VLC in indoor wireless communication and multi-user access. It allows the design of our work to be better explained and to compare our approach with existing works. The second step is an analysis of the principles and hypothesis supporting the indoor multi-user VLC system in the study both on the modulation technique and the multi-user access schemes. The conclusions drawn from theoretical and numerical analysis are used as a basis for the rest of the work. The third step is the experimental setup investigations on the single-user broadcast performances optimization and then on the multi-user performances of the system using various schemes. The total throughput using an off-the-shelf white LED reaches 163 Mb/s with a bit-error rate decreased by a factor of 3.55 thanks to the performance optimization process. This technique has the advantage of increasing the flexibility for a multi-access scenario while not augmenting the complexity as it only optimizes the modulation filter parameters. The multi-user access is obtained for a cell size of 4.56 m<sup>2</sup> at a distance of 2.15 meter away from the transmitter. The user capacity can reach up to 40 users, or 40.62 Mb/s in a 4-user scenario. It is thus demonstrated that the proposed system could function as a cell at a realistic range, with high data rate and the ability to provide for a large amount of users while limiting the cost of implementation.





## *Remerciements*

Les travaux ici présentés sont le fruit de mes trois années de thèse au Laboratoire d'Ingénierie des Systèmes de Versailles de l'Université de Versailles Saint-Quentin-en-Yvelines. Je remercie donc tout d'abord Luc Chassagne, directeur du laboratoire, de m'avoir donné la chance de réaliser ce doctorat.

Cette thèse a été réalisée sous la direction de Luc Chassagne, que je tiens de nouveau à remercier chaleureusement, pour son suivi constant et bienveillant ainsi que pour ses précieux conseils qui m'ont aiguillé tout au long de mon parcours de doctorant. Elle a par ailleurs été co-encadrée par Hongyu Guan, que je remercie vivement pour toutes ses remarques constructives.

Tous mes remerciements vont également à Mme. Maite Brandt-Pearce et M. Ali Khalighi, pour l'intérêt qu'ils ont porté à mon travail en acceptant d'en être les rapporteurs et à Mme. Véronique Vèque pour avoir présidé le jury de soutenance..



# Contents

<b>List of Figures</b>	<b>ix</b>
<b>List of Tables</b>	<b>xix</b>
<b>List of Abbreviations</b>	<b>xxi</b>
<b>List of Symbols and Notations</b>	<b>xxvii</b>
<b>1 Introduction of the thesis</b>	<b>1</b>
1.1 Introduction about communication systems . . . . .	1
1.2 Objectives and Outline of the Thesis . . . . .	6
1.2.1 Objectives of This Work . . . . .	6
1.2.2 Report Outline . . . . .	7
<b>2 Visible Light Communication for Indoor Applications</b>	<b>11</b>
2.1 What Is Visible Light Communication? . . . . .	11
2.1.1 Brief Historical Overview of VLC . . . . .	12
2.1.2 Basic Principles of VLC . . . . .	13
2.1.2.1 Data Emission End . . . . .	13
2.1.2.2 Free Space Signal Propagation . . . . .	15
2.1.2.3 Data Reception End . . . . .	16
2.1.3 Comparison as a Wireless Communication Technology . . . . .	16
2.1.4 Applications of Visible Light Communication . . . . .	19
2.2 Review on Indoor Visible Light Communication . . . . .	20
2.2.1 Physical Structure of an Indoor VLC System . . . . .	20
2.2.1.1 Optical Wireless Channel . . . . .	20
2.2.1.2 Light Emitting Diodes Types and Structures . . . . .	22
2.2.1.3 Photodiodes Types and Structures . . . . .	26
2.2.2 Multiple Input Multiple Output . . . . .	27
2.2.2.1 Multi-Chip LEDs . . . . .	27
2.2.2.2 Imaging Sensors . . . . .	28
2.2.2.3 MIMO in VLC . . . . .	28
2.2.3 Modulation Schemes . . . . .	30
2.2.3.1 Single Carrier Modulation . . . . .	30
2.2.3.2 Multi-Carrier Modulation . . . . .	32
2.2.3.3 Modulation Schemes Specific to VLC . . . . .	34

2.2.3.4	Comparison When Applied to VLC Systems . . . . .	35
2.2.4	Multi-Access Schemes . . . . .	42
2.2.4.1	Orthogonal Multi-Access Schemes . . . . .	42
2.2.4.2	Non-Orthogonal Multi-Access Schemes . . . . .	43
2.2.4.3	Multi-Users MIMO . . . . .	45
2.2.4.4	Comparison When Applied to VLC Systems . . . . .	45
2.2.5	Performance Enhancement in VLC . . . . .	48
2.2.5.1	Bandwidth Exploitation Efficiency . . . . .	48
2.2.5.2	Channel Estimation and Equalization . . . . .	49
2.2.5.3	Non-linearity Compensations . . . . .	51
2.3	Design Approach . . . . .	51
2.3.1	Communication Broadcast Structure . . . . .	51
2.3.1.1	Transmitter and Receiver Structures . . . . .	51
2.3.1.2	Modulation Scheme . . . . .	52
2.3.2	Multi-Users Access Techniques . . . . .	54
2.3.3	Placing our Approach . . . . .	54

### **3 Principles of an Indoor Multi-Users Visible Light Communication system** **59**

3.1	Introduction to the Multi-Users Multiband CAP VLC System . . . . .	59
3.1.1	Carrierless Amplitude and Phase Modulation . . . . .	60
3.1.2	Multi-Band Carrierless Amplitude and Phase Modulation . . . . .	62
3.1.3	Natural Association with Subcarrier Multiplexing . . . . .	65
3.1.4	Association with Other Schemes . . . . .	69
3.1.4.1	Association with Code Division Multiple Access . . . . .	69
3.1.4.2	Association with Power Domain Non-Orthogonal Multiple Access . . . . .	72
3.1.4.3	Association with Optical Space Division Multiple Access . . . . .	74
3.1.5	Refining Our Approach . . . . .	75
3.2	Broadcast Channel Performances Breakdown . . . . .	77
3.2.1	Block Diagram . . . . .	78
3.2.2	Modulation and Performances . . . . .	80
3.2.2.1	M-QAM Mapping . . . . .	80
3.2.2.2	Filter Parameters . . . . .	82
3.2.3	Performances Enhancements . . . . .	84
3.2.3.1	Channel Estimation . . . . .	84
3.2.3.2	Equalization . . . . .	88
3.2.3.3	Subcarrier Spacing . . . . .	92
3.3	Application with Multi-Access Schemes . . . . .	94
3.3.1	The Definition of an Attocell in VLC . . . . .	95
3.3.2	Characteristics of an Attocell . . . . .	95
3.3.3	User Allocation . . . . .	98

3.3.3.1	In SCM . . . . .	98
3.3.3.2	In MC-CDMA . . . . .	100
3.3.3.3	In PD-NOMA . . . . .	102
3.3.3.4	In SDMA . . . . .	103
3.4	Conclusions . . . . .	104
<b>4</b>	<b>Experimental Investigation of the VLC Indoor System and Proof of Concept</b>	<b>107</b>
4.1	Proof-of-Concept Design . . . . .	107
4.1.1	Transmitter Design . . . . .	108
4.1.1.1	LED Choice and Characterization . . . . .	108
4.1.1.2	LED Driving Circuit . . . . .	109
4.1.1.3	Signal Generation with the Arbitrary Waveform Generator . . . . .	110
4.1.2	Receiver Design . . . . .	110
4.1.2.1	Receiving Circuit . . . . .	110
4.1.2.2	Oscilloscope for Offline Post-Processing . . . . .	112
4.1.2.3	Signal Identification and Reconstruction . . . . .	113
4.1.3	Experimental Setup . . . . .	114
4.2	System Characterization Methods . . . . .	116
4.2.1	Modulation Order in Quadrature Amplitude Modulation . . . . .	117
4.2.1.1	Subcarrier Evaluation . . . . .	117
4.2.1.2	Selection of Constellation Size . . . . .	119
4.2.2	Equalization . . . . .	121
4.2.2.1	Pre-Equalization . . . . .	121
4.2.2.2	Post-Equalization with Channel Estimation . . . . .	122
4.3	Experimental Performance Enhancements . . . . .	124
4.3.1	Initial Performances of Multiband CAP . . . . .	124
4.3.2	Individual Subcarrier Filter Optimization . . . . .	128
4.3.2.1	Roll-Off Factor . . . . .	128
4.3.2.2	Filter length . . . . .	129
4.3.3	Subcarrier Spacing . . . . .	131
4.3.3.1	Subcarrier Spacing Impact on Individual Subcarriers . . . . .	131
4.3.3.2	Uniform and Optimized Subcarrier Spacing . . . . .	134
4.3.4	Flexibility and Performance Optimization . . . . .	136
4.3.5	Single-User Broadcasting Characterization . . . . .	138
<b>5</b>	<b>Experimental Investigation of the Multi-Users Capabilities</b>	<b>141</b>
5.1	Multi-Users Capabilities Evaluation Methods . . . . .	141
5.1.1	Updated Experimental Setup . . . . .	142
5.1.2	Attocell Characterization Process . . . . .	144
5.1.2.1	BER Distribution . . . . .	144
5.1.2.2	Attocell Size . . . . .	144

5.1.3	User Serviceability . . . . .	145
5.1.3.1	With SCM . . . . .	145
5.1.3.2	With MC-CDMA . . . . .	146
5.1.3.3	With PD-NOMA . . . . .	147
5.2	Characterization of the Multi-Users Systems . . . . .	149
5.2.1	Utilization of the Multi-Access Schemes Associated with m-CAP	151
5.2.1.1	SCM . . . . .	151
5.2.1.2	MC-CDMA . . . . .	152
5.2.1.3	PD-NOMA . . . . .	153
5.2.2	Impact of the 3D Distributions . . . . .	154
5.2.3	User Allocations . . . . .	157
5.2.3.1	SCM . . . . .	157
5.2.3.2	MC-CDMA . . . . .	159
5.2.3.3	PD-NOMA Combined with SCM . . . . .	160
5.2.3.4	PD-NOMA Combined with MC-CDMA . . . . .	161
5.2.3.5	Number of Usable Independent Channels at a Defined Tolerated Deviation . . . . .	161
5.2.4	Impact of the Distance Between the Transmitter and the Re- ceivers . . . . .	163
5.2.5	Total System Characterization . . . . .	163
<b>6</b>	<b>Conclusions and Future Works</b>	<b>169</b>
6.1	Contributions . . . . .	169
6.1.1	Low-Cost Performance Optimization for Multiband CAP . . . . .	169
6.1.2	Experimental Comparison of the Performances of Multi-Users Access Schemes Associations with m-CAP in Indoor VLC . . . . .	171
6.2	Future Challenges . . . . .	172
6.2.1	Improving the Single-User Broadcast Performances . . . . .	173
6.2.2	Enhancing the Multi-Users Performances . . . . .	174
6.2.3	Bidirectional link . . . . .	174
6.3	List of Publications from this work . . . . .	174
	<b>Bibliography</b>	<b>177</b>
<b>A</b>	<b>Components Impacts Breakdown</b>	<b>201</b>
A.1	Transmitter Hardware and Optics . . . . .	201
A.2	Receiver Hardware and Optics . . . . .	205
A.3	Channel, Range, Noise, and Incidence angle . . . . .	207
A.4	Simulation of a BER Distribution . . . . .	211
<b>B</b>	<b>Experimental Setup Hardware Components Specifications</b>	<b>215</b>
B.1	Basis of Implementation of CAP for the Numerical Simulations . . . . .	215
B.2	Basis of Implementation of m-CAP for the Numerical Simulations . . . . .	217

<b>C</b>	<b>Experimental Setup Hardware Components Specifications</b>	<b>221</b>
C.1	Specifications for LED Driver Minicircuit ZHL-6A+ and Bias-Tee Minicircuit ZFBT-282 . . . . .	221
C.2	Specifications for Thorlabs Lens LA1027 and Thorlabs PIN Photodiode and Transimpedance Amplifier PDA10A-EC . . . . .	221
<b>D</b>	<b>Résumé Détaillé en Français</b>	<b>225</b>



# List of Figures

1.1	Schematic illustrating the evolution of the mobile communication generations. . . . .	2
1.2	Illustration of a home application scenario for the near future, where new applications are enabled by the use of high-performance wireless communication technologies. . . . .	3
1.3	(a) Mobile video Will generate nearly four-fifths of mobile data traffic by 2022. (b) Cisco forecasts 77 exabytes per month of mobile data traffic by 2022. Both figures are from [4] . . . . .	3
1.4	Illustration of the frequency spectrum for radio-communication and light. . . . .	3
1.5	Image illustrating the mmWave used in 5G as compared to larger wavelength used in 4G systems. . . . .	4
1.6	Image illustrating the fact that the visible light communication bandwidth spectrum is 10 thousand times the size of the radio-frequency bandwidth. . . . .	5
1.7	The prospect of 6G for an all-spectrum network system. . . . .	6
1.8	Schematic illustrating the objective for a small cell using VLC as the base technology. . . . .	8
2.1	Illustration of the principle of a VLC system where an access point based on an LED down-light can communicate with one or more terminals. . . . .	13
2.2	Graph representing the number of VLC related publications as referenced by the IEEE Xplore library every year until 2018. . . . .	14
2.3	Schematic representing a basic block diagram explaining the principle of a VLC system. . . . .	14
2.4	White LED GW.KAGMB5.EM parameters as extracted from its datasheet [16] illustrating the (a) package outline, (b) relative spectral emission and (c) radiation characteristics. . . . .	15
2.5	Osram photodiode BPX 61 parameters as extracted from its datasheet [17] illustrating the (a) relative spectral sensitivity and (b) the directional characteristics. . . . .	17
2.6	Figure illustrating the different transmitter-receiver configurations in both line-of-sight and non-light-of-sight situations in a VLC system, as referenced in [18]. . . . .	17

2.7	Geometry used for the channel gain derivation, with $\theta$ and $\phi$ the polar and azimuth angles of emission, $\psi$ the angle of incidence, $A_r$ the PD area, $A_{eff}$ the effective PD area seen from the transmitter and $d$ the distance from the transmitter to the receiver. . . . .	21
2.8	Graph representing the luminous efficacy of LEDs against incandescent and fluorescent light sources [29]. . . . .	22
2.9	Global commercial lighting revenue forecast [30]. . . . .	23
2.10	Illustration of the principle of a phosphor-based white LED where a part of the blue light emitted by a blue chip is converted to yellow with the phosphor layer. . . . .	23
2.11	Close-up image of a BPW34 PIN photodiode. . . . .	26
2.12	Schematic illustrating the principle of a multi-chip LED with the example of a RGB LED using a red, green and blue chip. . . . .	28
2.13	Figure illustrating the principle of an imaging sensor. The example uses here a red and a green LED to transmit two different data streams. The imaging lens system map both optical signals to distinct pixels of the imaging sensor. . . . .	29
2.14	Figure illustrating the principles of SISO, MISO, SIMO, MIMO systems. . . . .	30
2.15	Schematic illustrating the basis of a single carrier modulation with a representation of the frequency spectrum in the frequency domain. . . . .	30
2.16	Single carrier modulation waveform examples for (a) OOK, (b) M-PPM, and (c) M-PAM. . . . .	32
2.17	Schematic illustrating the basis of a multi carrier modulation with a representation of the frequency spectrum in the frequency domain. . . . .	33
2.18	Schematic illustrating the CIE 1931 color space. It is the basis of the color shift keying modulation scheme. . . . .	34
2.19	Illustration of the base principle in terms of user resource allocation for (a) TDMA, (b) FDMA, (c) CDMA and (d) WDMA. The users are represented by different colors. . . . .	44
2.20	Illustration of the base principle in terms of user allocation resource for PD-NOMA where the users are assigned to a power level and represented by different colors. . . . .	45
2.21	Illustration of the principle of MU-MIMO, where, in this example, each user uses multiple channels thanks to multiple PDs and the transmitter uses multiple LEDs. . . . .	46
2.22	Illustration of the principle of blue filtering in VLC. . . . .	48
2.23	Figure showing the principle of equalization and channel estimation at the receiver for a VLC system. . . . .	50
2.24	Schematic of principle for an adaptive equalization technique. . . . .	50
2.25	Example of an IV characteristic for a referenced LED with a representation of the turn-on voltage and the optical signal saturation with an example of optical power characteristic. . . . .	51

2.26	Structure of the multi-users indoor VLC system analyzed in this work with a table summarizing the objectives set for the experimental setup.	53
2.27	: Illustration of the approach taken by this work in terms of cost of implementation. The graph is an estimation of the level of complexity of the VLC experimental setup versus the spectral efficiency. The blue area is the most explored, where the spectral efficiency is between 2 and 7 b/s/Hz and the estimated complexity is higher than 6. The red area is the objective aimed by our work, with a spectral efficiency around 5 and an estimated complexity around 6. References [122], [119] and [108] are laser based experiments used as a comparison. Reference [131] is a micro-LED-based experimental with a spectral efficiency below 5 b/s/Hz.	56
2.28	Illustration of the approach taken by this work in terms of system range. The graph is the range of the VLC experimental setup versus the spectral efficiency. The blue area is the most explored, where the spectral efficiency is between 3 and 7 b/s/Hz and the range is around 1 m. The red area is the objective aimed by our work, with a spectral efficiency around 5 b/s/Hz and a range above 2 m.	57
2.29	Illustration of the approach taken by this work in terms of maximum number of users and range. The graph is the range of the multi-users VLC experimental setup versus the maximum number of users. The blue area is the most explored, where the maximum number of users ranges from 2 to 8 users and the range is below 1.5 m. The red area is the objective aimed by our work, with a maximum number of users greater than 10 and a range above 2 m.	58
3.1	(a) Illustration of the square root raised cosine pulse shaping for the in-phase component and quadrature component. (b) Example of a time-domain CAP modulated signal. (c) Spectrum example of a CAP modulated signal.	63
3.2	(a) Example of a time-domain $m$ -CAP modulated signal. Spectrum example of an $m$ -CAP modulated signal for (b) $m = 4$ , (c) $m = 10$ and (d) $m = 20$ .	66
3.3	(a) Diagram representing the principle of an SCM-based multiple access control layer (b) Illustration of a spectrum with an SCM-based repartition of 2 users.	68
3.4	Example of frequency spectrums for a 4-users SCM allocation in a multiband CAP modulated signal.	68
3.5	(a) Schematic representing the principle of a transmitter using SCM-based multi-users Multi-band CAP (MU- $m$ -CAP) (b) Schematic representing the principle of a receiver using SCM-MU- $m$ -CAP.	69

3.6	Diagram describing the principle of a Code Division Multiple Access scheme in the case of (a) Direct Spreading CDMA and (b) Multi-Carrier CDMA. . . . .	70
3.7	Spectrum example for an MC-CDMA 4-users allocation in a $m$ -CAP modulated signal. . . . .	71
3.8	Diagram describing the principle of an MC-CDMA and $m$ -CAP association for the (a) transmitter and the (b) receiver. . . . .	72
3.9	Diagram describing the principle of a Power Domain Non-Orthogonal Multiple Access scheme. . . . .	73
3.10	Spectrum example for a PD-NOMA 4-users allocation in an $m$ -CAP modulated signal. . . . .	74
3.11	Diagram describing the principle of a PD-NOMA and $m$ -CAP association for the (a) transmitter and the (b) receiver for the close user and (c) receiver for the far user. . . . .	75
3.12	(a) Illustration of a Space Division Multiple Access scheme in Visible Light Communication using a 4-elements transmitter. (b) Diagram representing the principle of a SDMA scheme. . . . .	76
3.13	Simplified diagram of the association of $m$ -CAP (a) with SCM, (b) with MC-CDMA, and (c) with PD-NOMA (d) with SDMA. . . . .	78
3.14	Block diagram representing the system model in conventional CAP used throughout the numerical simulations. The hardware elements are replaced by models as described by the following subsections. . . . .	79
3.15	Illustration representing a Gray mapped constellation. . . . .	80
3.16	Simulated received constellation for $M = 16$ at an SNR value equal to (a) 3 dB, (b) 6 dB, (c) 12 dB and (d) 18 dB. . . . .	81
3.17	(a) Illustration of the filter impulse response for different roll-off factor values and (b) different filter length. . . . .	83
3.18	(a) Simulated impact of the roll-off factor on the BER for different filter spans. (b) Simulated impact of the signal bandwidth for different oversampling factors. (c) Simulated impact of the SNR on the BER for different oversampling factors. . . . .	85
3.19	Simulated impact on the simulated BER against the SNR by the use of no channel estimation, an LS-based method and MMSE-based technique. . . . .	88
3.20	Simplified illustration of the principle for a Decision Feedback Equalizer (DFE). . . . .	90
3.21	Simulated impact on the BER against the SNR of the use of pre- and post- equalization for a signal bandwidth of (a) 20 MHz, (b) 50 MHz and (c) 80 MHz. . . . .	91
3.22	Multiband CAP filters responses illustration and the impact of sub-carrier spacing with factor $p$ . $\Delta_f$ is the frequency increment between each subband without spacing. $\Delta_{f_{spacing}}$ is the frequency increment between each subband with spacing. . . . .	93

3.23	(a) Simulated spectrum emitted for an $m$ -CAP signal using subcarrier spacings values of 0% (top left), 10 % (top right), 20% (bottom left) and 30% (bottom right). (b) Simulated impact on the BER using different subcarrier spacing values and for each of the 10 subcarriers of the 10-CAP simulated signal. . . . .	94
3.24	Illustration representing an attocell in VLC. . . . .	95
3.25	Simulated 3D SNR distribution for a distance between the transmitting and receiving planes of (a) 1.5 m and (b) 2.15 m. . . . .	96
3.26	Algorithm implementation for the fiber-optics-based algorithm. . . . .	99
3.27	Algorithm implementation for the proposed algorithm 1. The changes with the fiber-optics-based algorithm are highlighted in color. . . . .	99
3.28	Algorithm implementation for the proposed algorithm 2. The changes with the fiber-optics-based algorithm are highlighted in color. . . . .	100
3.29	Simulated deviation from a random target for different number of sub-carrier in (a) a 4-users scenario and (b) an 8-users scenario. . . . .	101
3.30	Simulated deviation from a random target for different number of sub-carrier in a 4-users scenario. . . . .	102
3.31	Simulated deviations from target for different number of subcarrier in a 4-users scenario in the case of an association of (a) PD-NOMA and SCM and (b) PD-NOMA and MC-CDMA. . . . .	103
4.1	Photo of the phosphor-based white LED down-light used in the experimental setup. . . . .	108
4.2	Experimental setup characteristics. (a) Measured white LED current response versus voltage. (b) Measured white LED illumination response versus voltage. (c) LED relative spectrum response versus wavelength characteristic. (d) Measured experimental system modulation frequency response. . . . .	109
4.3	Schematic for the circuit that drives the LED in the experimental setup.	110
4.4	Illustration of the principle for the process of transfer and generation of the modulated signal with an AWG. . . . .	111
4.5	Example of a 100,000 points $m$ -CAP modulated signal before transmission to the AWG. . . . .	111
4.6	Schematic of the receiving circuit for the experimental setup. . . . .	112
4.7	(a) Illustration of the principle of the signal identification and reconstruction process. (b) Total transmitted example waveform with a low spectrum impact pulse (A) and a series of known symbols (B) added to the CAP modulated data frame (DATA). . . . .	113
4.8	Simplified process schematic for the principle of identification of the first frame. . . . .	114
4.9	Simplified process schematic for the principle of amplitude and phase correction. . . . .	115

4.10	Schematic representing the experimental setup for the transmitted based on an AWG, an office down-light, and a receiver based on a photodiode and an offline post-process with MATLAB. . . . .	116
4.11	Schematic representing 16-QAM constellations at the transmitter and the receiver of a multiband CAP system for one of the subcarriers. The $m$ -CAP principle diagram is simplified and $m$ represents the number of subcarriers. TX block regroups the parts necessary for transmission of a VLC signal, including the LED. RX block regroups the parts needed for the reception, including a photodiode. In the constellation on the right, phase, gain and IQ distortions have been corrected in the CAP demodulation block. . . . .	118
4.12	Constellation diagram with a representation of the EVM. $P_{error}$ is the RMS amplitude of the error vector. $P_{ref}$ is the amplitude of the highest power point in the reference signal constellation [251]. . . . .	120
4.13	Schematic diagram of the bridged-T amplitude equalizer [252]. . . . .	121
4.14	Measured spectral efficiency versus signal bandwidth for different pre-equalization implementations. . . . .	122
4.15	Measured spectral efficiency versus signal bandwidth for different post process methods. . . . .	123
4.16	Measured electrical spectrum at the receiver of a (a) 4-CAP and (b) 10-CAP signal showing the constellations associated with some subcarriers. Different modulation orders are set for each subcarrier as a representation of the bit-loading method. . . . .	126
4.17	(a) Measured impact of the number of subcarriers on the BER for a modulation order of $M = 16$ and $M = 64$ . (b) Measured impact of the number of subcarriers on the obtained data rate. . . . .	127
4.18	Measured impact of the roll-off factor on the BER of each subcarrier on a 20-CAP signal, for subcarriers (a) 1 to 5, (b) 6 to 10 (c) 11 to 15 and (d) 16 to 20 of a multiband CAP modulated waveform. (e) Measured roll-off factor associated to the lowest BER for each subcarrier. . . . .	130
4.19	Measured impact of the filter length on the BER of each subcarrier on a 20-CAP signal, for subcarriers (a) 1 to 5, (b) 6 to 10 (c) 11 to 15 and (d) 16 to 20 of a multiband CAP modulated waveform. . . . .	131
4.20	Measured impact of subcarrier spacing on the BER of each subcarrier on a 20-CAP signal, for subcarriers (a) 1 to 5, (b) 6 to 10 (c) 11 to 15 and (d) 16 to 20 of a multiband CAP modulated waveform. (e) Measured subcarrier spacing factor associated to the lowest BER for each subcarrier. . . . .	133
4.21	Measured performance variation for different values of subcarrier spacing for the whole signal at various sampling rates. . . . .	134

4.22	Measured impact of subcarrier spacing on the maximum attainable data rate (a). Obtained while maximizing the data rate against the number of subcarriers. The measurements are performed without spacing, with the same spacing value and with a spacing value optimized between each subband. Measured spectrum in a 4 subcarriers signal with no spacing (b), 5% spacing (c), 10% spacing (d), and 20% spacing (e). . . . .	135
4.23	Optimization process pseudo-code for obtaining the optimized filter parameters in both the uniform optimization and the full optimization process. . . . .	137
4.24	Measured change in data rate performances compared to no filter parameter optimization in the experimental setup. The process is applied on subcarrier spacing, the roll-off factor or both. . . . .	137
5.1	Schematic representing the experiment setup in a multi-users scenario for the transmitter based on an AWG, an office downlight, and a receiver for a user k based on a photodiode and an offline post-process with MATLAB. . . . .	143
5.2	Simplified experimental setup diagram in the case of the multiband CAP association with SCM. . . . .	145
5.3	Illustration of an SCM association with a measured frequency spectrum of the signal received. User 1 is in black, user 2 in blue, user 3 in green and user 4 in red. . . . .	146
5.4	Simplified experimental setup diagram in the case of the multiband CAP association with MC-CDMA. . . . .	147
5.5	Illustration of an MC-CDMA association with a measured frequency spectrum of the signal received on a 4-code scenario. User 1 is in black, user 2 in blue, user 3 in green and user 4 in red. . . . .	147
5.6	Simplified experimental setup in the case of the multiband CAP association with (a) PD-NOMA combined with SCM and (b) PD-NOMA combined with MC-CDMA. . . . .	148
5.7	Illustration of a PD-NOMA association with (a) SCM and (b) MC-CDMA on a measured frequency spectrum of the signal at the receiver. User 1 is in black, user 2 in blue, user 3 in green and user 4 in red. . .	150
5.8	Graph representing the measured impact of the association with SCM on the single-user data rate against the total number of users. . . . .	152
5.9	Graph representing the measured impact of the association with MC-CDMA on the single-user data rate against the total number of users. . . . .	152
5.10	Graph representing the measured impact of the association of PD-NOMA with SCM and MC-CDMA on the single-user data rate against the total number of users. . . . .	153

5.11	Measured transformation from (a) a BER 3D Distribution, to a 3D representation of the maximum number of users in the case of the multiband CAP association with (b) SCM. . . . .	155
5.12	Measured transformation from a BER 3D Distribution, to a 3D representation of the maximum number of users in the case of the multiband CAP association with MC-CDMA. . . . .	156
5.13	(a) Measured deviation from user target data rate in function of the number of users, (b) Measured deviation from user target in function of the number of subcarriers. The multiband CAP modulation is associated with SCM. . . . .	158
5.14	(a) Measured deviation from user target data rate in function of the number of codes, (b) Measured deviation from user target in function of the number of subcarriers. The multiband CAP modulation is associated with MC-CDMA. . . . .	159
5.15	(a) Measured deviation from user target data rate in function of the number of users, (b) Measured deviation from user target in function of the number of subcarriers. The multiband CAP modulation is associated with PD-NOMA+SCM. . . . .	160
5.16	(a) Measured deviation from user target data rate in function of the number of codes, (b) Measured deviation from user target in function of the number of subcarriers. The multiband CAP modulation is associated with PD-NOMA+MC-CDMA. . . . .	162
5.17	Measured number of usable independent channels for a set allowed deviation when using every association of multiband CAP with SCM, MC-CDMA and PD-NOMA. . . . .	163
5.18	(a) Measured data rate versus range of the system with or without applying the optimization process. (b) Measured attocell size versus range of the system with or without applying the optimization process. . . . .	164
5.19	Graph representing the measured 3D BER surface on a plane a) without and b) with applying the broadcast performances optimization process. . . . .	165
5.20	Measured 3D BER in a 5x5x3 m <sup>3</sup> indoor room for the experimental setup. . . . .	167
6.1	: Illustration of the approach taken by this work in terms of cost of implementation as per figure 2.27. The results obtained by this work are added as a comparison. . . . .	171
6.2	Illustration of the approach taken by this work in terms of system range as per figure 2.28. The results obtained by this work are added as a comparison. . . . .	171

6.3	Illustration of the approach taken by this work in terms of maximum number of users and range as per figure 2.29. The results obtained by this work are added as a comparison. . . . .	173
A.1	(a) Simulated bode diagram for a white and blue LED model, (b) Simulated optical power received for different transmitter configuration. (c) Simulated luminous flux emitted in three-dimension in a 5x5x3 m <sup>3</sup> room for a transmitter with a 20-degree semi-angle at half power (left) and 60-degree semi-angle (right). . . . .	203
A.2	(a) Simulated optical power received for a receiver comprised of a lens and a photodiode and a (b) receiver composed of a photodiode without the optical concentrator. . . . .	207
A.3	(a) Simulated BER in 1-CAP for different signal bandwidth values at a range of 1 meter and direct line of sight, for a fixed SNR of 12 dB and multiple constellation sizes. (b) Simulated BER in 1-CAP for different values of SNR, a fixed signal bandwidth of 1 MHz, the same 1-meter range and multiple constellation sizes. . . . .	211
A.4	Simulated 3D bit error rate distribution in a 5x5x3 m indoor room. Characteristics of the simulation are included in Table A.5. . . . .	212
A.5	Simulated 3D bit error rate distribution on plane using a color map. The simulation is the same as described figure A.4. . . . .	214
B.1	Schematic describing the basis of implementation for the raised cosine filter generation in a conventional CAP modulation process. . . . .	216
B.2	Schematic presenting the principle of implementation for the CAP modulation process. . . . .	216
B.3	Schematic presenting the principle of implementation for the CAP demodulation process. . . . .	217
B.4	Schematic describing the basis of implementation for the raised cosine filter generation in a multiband CAP modulation process. . . . .	218
B.5	Schematic presenting the principle of implementation for the CAP modulation process. . . . .	218
B.6	Schematic presenting the principle of implementation for the CAP demodulation process. . . . .	219
C.1	Graph of the gain versus frequency the electrical amplifier ZHL-6A+ from Minicircuit. . . . .	221
C.2	Graph of the noise figure versus frequency the electrical amplifier ZHL-6A+ from Minicircuit. . . . .	222
C.3	Summary of the characteristics for the electrical amplifier ZHL-6A+ from Minicircuit. . . . .	222
C.4	Graph of the insertion loss versus frequency for the bias-tee ZFBT-282 from Minicircuit. . . . .	222

C.5	Graph of the isolation versus frequency for the bias-tee ZFBT-282 from Minicircuit. . . . .	223
C.6	Summary of the characteristics for the bias-tee ZFBT-282 from Minicircuit. . . . .	223
C.7	Characteristics of the Thorlabs LA1027 lens. . . . .	223
C.8	Characteristics of the silicon photodiode and transimpedance amplifier. Both the PD and TIA are contained in Thorlabs PDA10A-EC in this experimental setup. . . . .	224

# List of Tables

1.1	Comparison of wireless communication protocols typically used for indoor systems. . . . .	5
2.1	Comparison of VLC, IR and RF communication technologies, reproduced from [7]. . . . .	19
2.2	Comparison of the main characteristics of the different type of LEDs. . . . .	26
2.3	Comparison of qualities for each modulation scheme when applied to VLC. . . . .	35
2.4	State of the art on the performances obtained by experimental demonstrations in indoor VLC. . . . .	36
2.5	Qualitative comparison of the multi-users access schemes in VLC. . . . .	46
2.6	Summary of state-of-the-art on multi-users access experimental setups in VLC. . . . .	47
2.7	Definition of the estimated level of complexity for a VLC experimental setup. . . . .	55
3.1	Simulation parameters used to obtained the $M$ -QAM constellations on figure 3.16. . . . .	81
3.2	Theoretically required SNR in order for the BER at reception to be above the 7% FEC limit for each $M$ constellation size in a CAP signal. . . . .	82
3.3	Simulation parameters used to obtain the CAP filter responses on figure 3.17. . . . .	83
3.4	Simulation parameters used to obtain the impact of channel estimation on the BER in figure 3.19. . . . .	88
3.5	Simulation parameters used to obtain the impact of equalization on the BER in figure 3.21. . . . .	92
3.6	Simulation parameters used to obtain the 3D SNR distributions in figure 3.25. . . . .	97
4.1	Theoretically required SNR for the usable modulation order at each subcarrier in a multiband CAP signal. . . . .	120
4.2	Experimental parameters used for the measurements on the impact of the number of subcarriers on $m$ -CAP in figures 4.16 and 4.17. . . . .	125
4.3	Baseline characteristic for a 20-CAP signal in a single-user broadcast setup corresponding to Table 4.2. . . . .	128

4.4	Optimized characteristics for a 20-CAP signal in a single-user broadcast setup corresponding to Table 4.2. . . . .	139
5.1	Optimized characteristics for a 20-CAP signal in a single-user broadcast setup. Summary of chapter 4 results. . . . .	151
5.2	Summary of the total indoor multi-users VLC experimental system. . . . .	166
A.1	Simulation parameters for figure A.1 (a). The values were obtained with measures on a commercially available white LED. . . . .	203
A.2	Simulation parameters for figure A.1 (b) and (c). . . . .	204
A.3	Simulation parameter used to obtain the received optical power in figure A.2. . . . .	206
A.4	Simulation parameters used to obtain the BER in different conditions in figure A.3. . . . .	212
A.5	Simulation parameters used to obtain the 3D BER distribution in figure A.4. . . . .	213

# List of Abbreviations

<b>2D</b>	Two-Dimensional
<b>3D</b>	Three-Dimensional
<b>ACO-OFDM</b>	Asymmetrically clipped Optical Orthogonal Frequency Division Multiplexing
<b>ADC</b>	Analog-to-Digital Converter
<b>ADO-OFDM</b>	Asymmetrically clipped Direct current biased Optical Orthogonal Frequency Division
<b>AP</b>	Access Point
<b>APD</b>	Avalanche Photodiode
<b>AlGaN</b>	Aluminum Gallium Nitride
<b>ANN</b>	Artificial Neural Network
<b>AWG</b>	Arbitrary Waveform Generator
<b>AWGN</b>	Additive White Gaussian Noise
<b>BER</b>	Bit Error Rate
<b>BJT</b>	Bipolar Junction Transistor
<b>BT</b>	Bias-Tee
<b>BW</b>	Bandwidth
<b>CAP</b>	Carrierless Amplitude and Phase
<b>CCT</b>	Corrected Color Temperature
<b>CD-NOMA</b>	Code Division Non-Orthogonal Multiple Access
<b>CDMA</b>	Code Division Multiple Access
<b>CIM</b>	Color Intensity Modulation
<b>CMMA</b>	Cascaded Multi-Modus-Algorithm
<b>CMOS</b>	Complementary Metal Oxyde Semiconductor
<b>CSK</b>	Color Shift Keying
<b>DAC</b>	Digital-to-Analog Converter
<b>DC</b>	Direct Current
<b>DCO-FBMC</b>	Direct Current-biased Optical Filter Bank Multi-Carrier
<b>DCO-OFDM</b>	Direct Current biased Optical Orthogonal Frequency Division Multiplexing
<b>DD</b>	Direct Detection
<b>DFE</b>	Decision Feedback Equalizer
<b>DFT-S-OFDM</b>	Discrete Fourier Transform Spread Orthogonal Frequency Division Multiplexing
<b>DS-CDMA</b>	Direct Spread Code Division Multiple Access
<b>DSSS</b>	Direct Sequence Spread Spectrum
<b>EA</b>	Electrical Amplifier
<b>EDGE</b>	Enhanced Data rates for GSM Evolution
<b>EU</b>	European Union

<b>EMI</b>	Electromagnetic Interference
<b>eU-OFDM</b>	Enhanced Uni-polar Orthogonal Frequency Division Multiplexing
<b>EVM</b>	Error Vector Magnitude
<b>FCC</b>	Federal Communications Commission
<b>FDMA</b>	Frequency Division Multiple Access
<b>FEC</b>	Forward Error Correction
<b>FET</b>	Field-Effect Transistor
<b>FFT</b>	Fast Fourier Transform
<b>FHSS</b>	Frequency Hoping Spread Spectrum
<b>FIR</b>	Finite Impulse Response
<b>FOV</b>	Field-of-View
<b>FPGA</b>	Field-Programmable Gate Array
<b>FSK</b>	Frequency-Shift Keying
<b>FSO</b>	Free Space Optical
<b>GaN</b>	Gallium Nitride
<b>GBWP</b>	Gain-Bandwidth Product
<b>GPIO</b>	General Purpose Input/Output
<b>GRPS</b>	General Packet Radio Service
<b>GSSK</b>	Generalized Space Shift Keying
<b>HSPA</b>	High Speed Packet Access
<b>ICI</b>	Inter-Channel Interference
<b>ICSA</b>	Infrared Communication Systems Association
<b>ICT</b>	Information and Communication Technology
<b>IEEE</b>	Institute of Electrical and Electronics Engineers
<b>IM</b>	Intensity Modulation
<b>InGaN</b>	Indium Gallium Nitride
<b>IoT</b>	Internet-of-Objects
<b>IR</b>	Infrared
<b>IrDA</b>	Infrared Data Association
<b>ISI</b>	Inter-Symbol Interference
<b>ITS</b>	Intelligent Transportation Systems
<b>ITU</b>	International Telecommunication Union
<b>IV</b>	Intensity-Voltage
<b>JEITA</b>	Japan Electronics and Information Technology Industries Association
<b>Laser</b>	light Amplification by Stimulated Emission of Radiation
<b>LD</b>	Laser Diode
<b>LDS</b>	Low-Density Signature
<b>LED</b>	Light-Emitting Diode
<b>LiFi</b>	Light Fidelity
<b>LMS</b>	Least Mean Squares
<b>LOS</b>	Line-of-Sight
<b>LPMA</b>	Lattice Partition Multiple Access

<b>LS</b>	Least Squares
<b>LTE</b>	Long-Term Evolution
<b>LTI</b>	Linear Time-Invariant
<b><i>m</i>-CAP</b>	Multiband Carrierless Amplitude and Phase
<b>MAC</b>	Medium Access Control
<b>MAI</b>	Multiple Access Interferences
<b>MC-CDMA</b>	Multi-Carrier Code Division Multiple Access
<b>MCM</b>	Multi-Carrier Modulation
<b>MIMO</b>	Multiple Input Multiple Output
<b>MISO</b>	Multiple Input Single Output
<b>MLP</b>	Multi Layer Perceptron
<b>MM</b>	Metametric Modulation
<b>MMSE</b>	Minimum Mean-Square-Error
<b>MOSFET</b>	Metal Oxide Semiconductor Field-Effect Transistor
<b>MRC</b>	Maximum Ratio Combining
<b>MSE</b>	Mean Square Error
<b>MU-MIMO</b>	Multi-User Multiple Input Multiple Output
<b>MUA</b>	Multi-Access Scheme
<b>MUD</b>	Multi-Users Detector
<b>NA</b>	Non-Applicable
<b>ND</b>	Non-Defined
<b>NFC</b>	Near Field Communication
<b>NIR</b>	Near-Infrared
<b>NLOS</b>	Non-Line-of-Sight
<b>NOMA</b>	Non-Orthogonal Multiple Access
<b>NUV</b>	Near Ultra-Violet
<b>OCC</b>	Optical Camera Communication
<b>OFDM</b>	Orthogonal Frequency Division Multiplexing
<b>OFDMA</b>	Orthogonal Frequency Division Multiple Access
<b>OLED</b>	Organic Light Emitting Diode
<b>OMA</b>	Orthogonal Multiple Access
<b>OMEGA</b>	Home Gigabit Access
<b>OOK</b>	On-Off-Keying
<b>OWC</b>	Optical Wireless Communication
<b>PAM</b>	Pulse Amplitude Modulation
<b>PAM-DMT</b>	Pulse Amplitude Modulated Discrete Multi-Tone Modulation
<b>PAPR</b>	Peak-to-Average Power Ratio
<b>PD</b>	Photodiode
<b>PDMA</b>	Pattern Division Multiple Access
<b>Ph-LED</b>	Phosphor-based Light Emitting Diode
<b>PHY</b>	Physical Layer
<b>PIN</b>	Positive Intrinsic Negative

<b>PLL</b>	Phase-Locked Loop
<b>PPM</b>	Pulse Position Modulation
<b>PRBS</b>	Pseudo Random Binary Sequence
<b>PWM</b>	Pulse Width Modulation
<b>QAM</b>	Quadrature Amplitude Modulation
<b>QoS</b>	Quality-of-Service
<b>QPSK</b>	Quadrature Phase-Shift Keying
<b>Radar</b>	Radio Detection and Ranging
<b>Rc-LED</b>	Resonant Cavity Light Emitting Diode
<b>RF</b>	Radio Frequency
<b>RGB</b>	Red Green Blue
<b>RGBY</b>	Red Green Blue Yellow
<b>RLS</b>	Recursive Least Squares
<b>RMS</b>	Root Mean Square
<b>RPO-OFDM</b>	Reverse Polarity Optical Orthogonal Frequency Division Multiplexing
<b>SC</b>	Superposition Coding
<b>SCM</b>	Subcarrier Multiplexing
<b>SCMA</b>	Sparse Code Multiple Access
<b>SDMA</b>	Space Division Multiple Access
<b>SIC</b>	Successive Interference Cancellation
<b>SIMO</b>	Single Input Multiple Output
<b>SISO</b>	Single Input Single Output
<b>SNR</b>	Signal-to-Noise Ratio
<b>SRRC</b>	Square Root Raised Cosine
<b>TDMA</b>	Time Division Multiple Access
<b>TG</b>	Task Group
<b>TIA</b>	Trans-Impedance Amplifier
<b>TOF</b>	Time-Of-Flight
<b>U-OFDM</b>	Uni-polar Orthogonal Frequency Division Multiplexing
<b>UFMC</b>	Universal Filtered Multi-Carrier
<b>UMTS</b>	Universal Mobile Telecommunications System
<b>USRP</b>	Universal Software Radio Peripheral
<b>UV</b>	Ultra-Violet
<b>UWB</b>	Ultra-Wide Band
<b><math>\mu</math>-LED</b>	Micro Light Emitting Diode
<b>VCSEL</b>	Vertical-Cavity Surface-Emitting Laser
<b>VLC</b>	Visible Light Communication
<b>VLCA</b>	Visible Light Communication Association
<b>VLCC</b>	Visible Light Communication Consortium
<b>VPPM</b>	Variable Pulse Position Modulation
<b>WDM</b>	Wavelength Division Multiplexing
<b>WDMA</b>	Wavelength Division Multiple Access

<b>WLAN</b>	Wireless Local Area Network
<b>WiFi</b>	Wireless Fidelity
<b>WiMAX</b>	Worldwide Interoperability for Microwave Access
<b>XOR</b>	Exclusive Or
<b>YAG</b>	Yttrium Aluminum Garnet
<b>ZF</b>	Zero-Forcing



# List of Symbols and Notations

$a_{k,j}$	Subcarrier number $j$ associated to user number $k$	no units
$A_c$	Surface area of the attocell	$\text{m}^2$
$A_{eff}$	Photodiode effective area seen from the transmitter	$\text{m}^2$
$A_r$	Photodiode sensitive area	$\text{m}^2$
$B$	Receiver bandwidth	Hz
$B_n$	Noise bandwidth	Hz
$B_a$	Amplifier bandwidth	Hz
$b_n$	Feed-back filter tap coefficients	no units
$c$	Speed of light ( $= 2.99792458 \times 10^8$ )	$\text{m}\cdot\text{s}^{-1}$
$c_k$	Group of subcarriers allocated to user number $k$	no units
$c_n$	Feed-forward filter tap coefficients	no units
$d$	Transmitter-to-receiver absolute distance	m
$d_k$	Transmitter-to-receiver for user $k$	m
$D_{tar}$	Target data rate	b/s
$\hat{d}_{m-n}$	Previously estimated symbol at the DFE	no units
$E_v$	Illuminance	lux
$f_I$	In-phase pulse shaping filter	no units
$f_Q$	Quadrature pulse shaping filter	no units
$F_s$	Sampling rate	sample/s
$F_{s_{AWG}}$	Sampling rate at the AWG	Hz
$G_b$	Equivalent gain of the blue light component	no units
$G_y$	Equivalent gain of the yellow light component	no units
$\hat{H}_{LS}$	Normalized value of a LS channel estimation	no units
$\hat{H}_{MMSE}$	Normalized value of a MMSE channel estimation	no units
$I_2$	Noise-bandwidth factor	no units
$I_3$	Noise-bandwidth factor	no units
$\bar{j}_k$	Total number of subcarriers allocated to one user	no units
$\bar{k}$	Total number of users	no units
$k$	Number of bits per modulation symbols	b/symbol
$k_{tar}$	Target bits per symbols	b/symbol
$L$	Maximum number of available codes	no units
$L_f$	Number of filter taps	no units
$L_{SPAN}$	Total length of filter	no units
$L_{signal}$	Number of samples in the signal	samples

$m$	Number of subcarriers in the modulation scheme	no units
$M$	Quadrature amplitude modulation constellation order	no units
$N_m$	Number of subcarriers allocated to user $m$	no units
$p$	Subcarrier spacing factor	no units
$P_{error}$	Root mean-square amplitude of the error vector	no units
$p_i$	Power allocated to user number $i$	no units
$p_{cu}$	Power allocated to users in the far group	no units
$p_{fu}$	Power allocated to users in the close group	no units
$P_n$	Noise power of the ambient light	W
$P_t$	Optical power transmitted	W
$P_r$	Average optical power received	W
$P_{ref}$	Amplitude of the highest point in the reference constellation	no units
$P_\omega$	Power calculated from the emission spectrum	W
$q$	Electronic charge ( $= 1.6 \times 10^{-19}$ )	C
$r_a$	Radius of the attocell	m
$R_s$	System baud rate	symbols/s
$R_{b/y}$	PD responsivity to the blue or yellow component	$A \cdot W^{-1}$
$R_H$	Covariance matrix of channel coefficient	no units
$R_w$	Covariance matrix of noise	no units
$S_M$	Set of available users	no units
$S_N$	Set of available subcarriers	no units
$T_f$	Fall time of the LED	s
$T_r$	Rise time of the LED	s
$T_s$	Symbol period	s
$X_I$	In-phase data stream	no units
$X_Q$	Quadrature data stream	no units
$y_{m-n}$	Detected symbol at the DFE	no units
$\alpha$	Roll-off factor	no units
$\alpha^R$	Radiation incident angle	rad
$\alpha^T$	Angle of irradiance	rad
$\Delta_f$	Frequency increment between each subcarrier	Hz
$\Delta_{fspacing}$	Frequency increment between each subcarrier after spacing	Hz
$\eta_{diff}$	Diffuse channel loss	no units
$\theta$	Polar angle of emission	rad
$\lambda$	Wavelength of the light signal	m
$\sigma_{amplifier}^2$	Amplifier noise variance	$V^2/Hz$
$\sigma_{shot}^2$	Shot noise variance	$V^2/Hz$
$\sigma_{thermal}^2$	Thermal noise variance	$V^2/Hz$
$\sigma_{total}^2$	Total noise variance	$V^2/Hz$
$\phi$	Azimuth angle of emission, or irradiance angle	rad
$\rho_i$	Reflectivity of the surface $i$	no units
$\varepsilon(.)$	Sum of squared errors	no units

$\Phi_{1/2}$	Semi-angle at half power	rad
$\psi$	Incidence angle	rad
$\Psi_{FOV}$	Photodiode field-of-view	rad
$\Psi_c$	Photodiode field-of-view	rad
$\tau_b$	Time constant of the blue light component	s
$\tau_y$	Time constant of the yellow light component	s



## Chapter 1

# Introduction of the thesis

### Contents

---

<b>1.1</b>	<b>Introduction about communication systems . . . . .</b>	<b>1</b>
<b>1.2</b>	<b>Objectives and Outline of the Thesis . . . . .</b>	<b>6</b>
1.2.1	Objectives of This Work . . . . .	6
1.2.2	Report Outline . . . . .	7

---

### 1.1 Introduction about communication systems

Historically, voice service has been the main focus of mobile telecommunications for years. Not until Enhanced Data Rates for GSM Evolution (EDGE) did the technique allowed for sufficient data transmission rates for more than voice exchange [1]. With improved data rates, new applications could finally be considered. With this new perspective, the 3rd Generation Partnership Project (3GPP), a standardization organization for radio access, was created [2]. Pre-3G and 3G, short for third generation, were standardized for General Packet Radio Service (GPRS) in 1998, EDGE in 1999 and 3G Universal Mobile Telecommunications System (UMTS) in 2000. It started a profound evolution in mobile telecommunications. Data rates could theoretically attain 42 Mb/s when evolved High Speed Packet Access (HSPA) or 3G++ was used [3]. The possibility for video calling and mobile access to the internet was enabled. This shift in paradigm took another step with 4G Long Term Evolution (LTE) and LTE-Advanced. 4G networks support considerably more advanced services than before with video streaming or gaming, which require higher speeds and lower latency.

Multimedia and internet-based services now occupy a growing part of the traffic share [4]. Projections also tend to predict that the number of connected devices will increase. It will be driven by wearable, sensors, or related Internet-of-Object (IoT) systems. High quality content streaming and production, payment, cloud gaming, mobile TV, virtual and augmented reality are all expected services to be available with this paradigm change. This means that the needs for bandwidth, or data rate, for home applications will grow in the near future. Indeed, services like 4K video

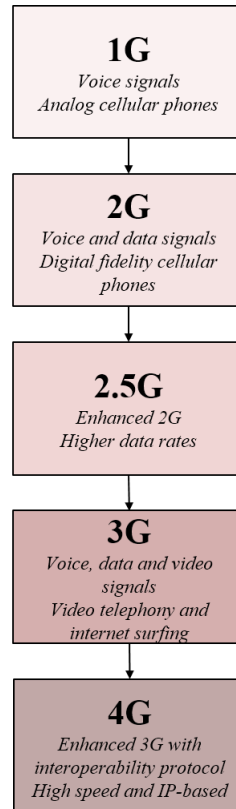


FIGURE 1.1: Schematic illustrating the evolution of the mobile communication generations.

streaming or augmented reality will cap the capabilities of current technologies, because of their very large requirements for throughput in a small area. IoT systems for smart homes also need large amounts of communication channels in a similarly small area. Metrics that can be used are the data rate per unit of area and the total number of users in a network cell. As an example, a 4K ultra high definition stream requires at least 25 Mb/s in a 1 m<sup>2</sup> area. It can also require a large number of connected devices in a small area, such as kitchen appliances. An illustration of such a scenario in a house is represented figure 1.2.

These types of throughput requirements are expected to increase, as shown in figure 1.3. In consequence, the data rate per unit area requirements are thus expected to increase in such scenarios, demanding new communication solutions. The same requirements are found in the supported amount of users with the increasing number of connected devices. For each cell illustrated in figure 1.2, there is a need for more data rate, capacity and lower latency. These new bandwidth-hungry applications need a technology that can provide a high data rate per unit area and high capacity in a network cell. However, the saturation in radio-frequency bandwidth is a challenge for current wireless communication system. This is where 5G and hybrid networks are now considered.

5G will operate in highly heterogeneous environment. It is characterized by the

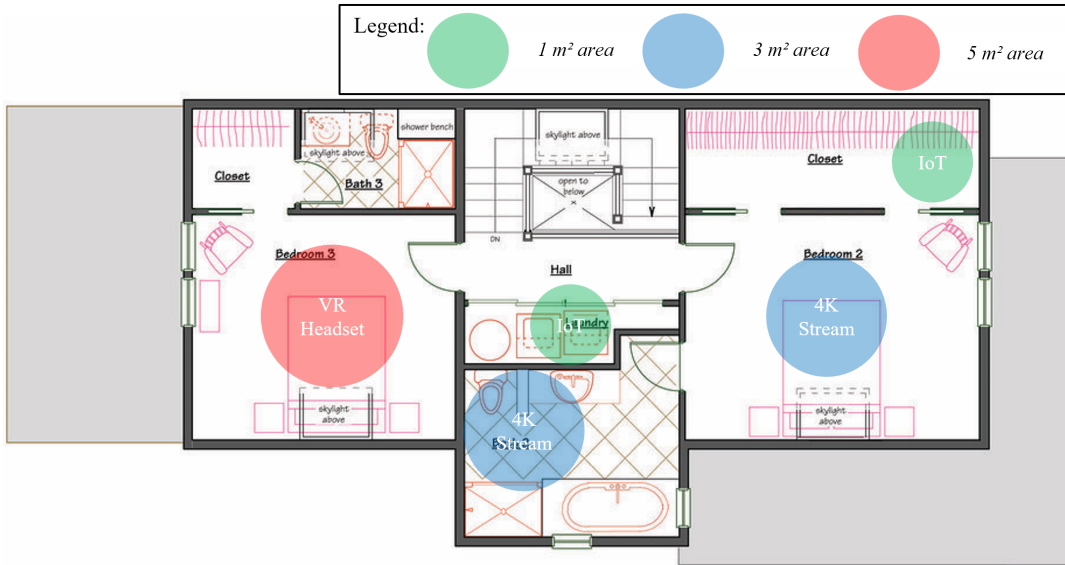


FIGURE 1.2: Illustration of a home application scenario for the near future, where new applications are enabled by the use of high-performance wireless communication technologies.

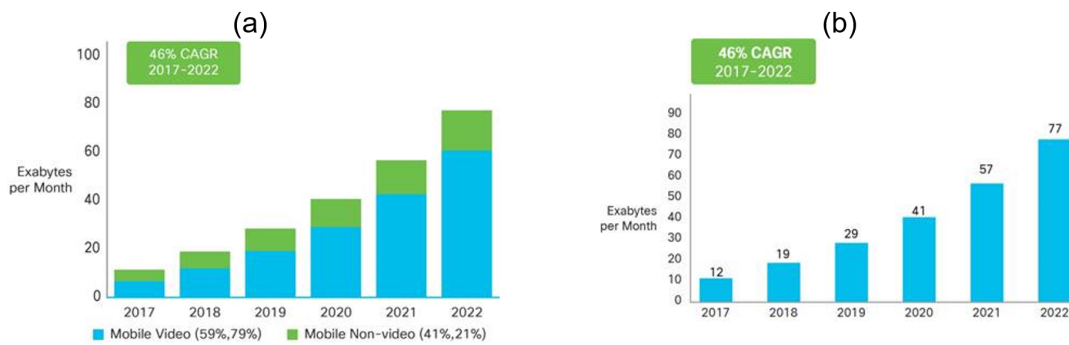


FIGURE 1.3: (a) Mobile video Will generate nearly four-fifths of mobile data traffic by 2022. (b) Cisco forecasts 77 exabytes per month of mobile data traffic by 2022. Both figures are from [4]

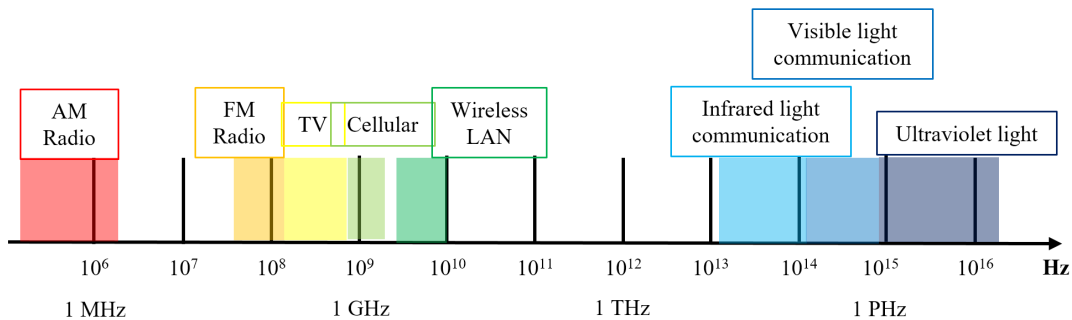


FIGURE 1.4: Illustration of the frequency spectrum for radio-communication and light.

co-existence of multiple access technologies, multi-layer networks, multiple types of devices, multiple types of user interactions, etc. As illustrated by figure 1.4, the frequency spectrum for radio- and light- communication contains a number applications. In such an environment, there is a fundamental need for 5G to achieve seamless and

consistent user experience across time and space. Along with the increased demands in network capacity, this necessity for 5G has forced researchers to investigate the viability of unused frequency bands such as the millimeter wave band (mmWave). These mmWaves correspond to the frequency spectrum between 30 and 300 GHz. They were limited to use in indoor applications and microwave transmissions because of their high path loss. However, they allow for larger bandwidth in order to answer the increasing need in data.

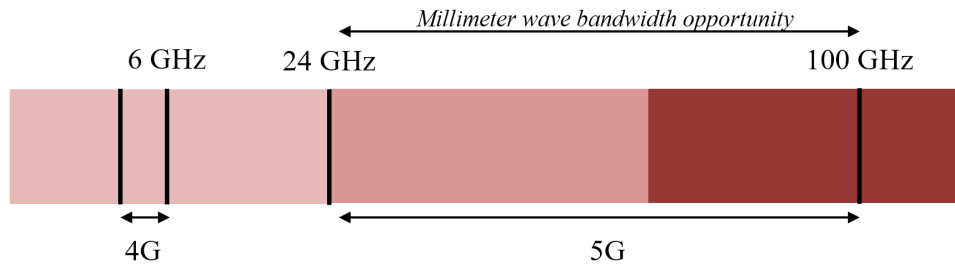


FIGURE 1.5: Image illustrating the mmWave used in 5G as compared to larger wavelength used in 4G systems.

One key problematic is that the deployment of 5G networks across dense indoor urban environment with mmWaves may prove to be a challenge because of the low effectiveness of higher frequencies in penetrating structures. However, it is estimated that 80% of all wireless traffic is consumed indoor. This is where 5G will need to include hybrid networking solutions and be able to coexist with other wireless access technologies. Especially in indoor environments, with smaller coverage area based techniques such as Wi-Fi or the recently explored visible light communication (VLC). Indeed, Wi-Fi can easily penetrate most indoor walls. And, while the light emitting diodes (LEDs) used in VLC can't, they are present everywhere to offer smaller coverage area.

Small cells exist as a result of using higher and higher frequency bands for RF access. Indeed, as new communication standards emerged, new and higher frequencies were used. In part because of the increasing demands in data which can require more and more bandwidth. Visible light communication fits into that mold. Using even higher frequency bands: visible light which corresponds to the band between 400 and 800 THz. The available spectrum is multiple thousand times the size of the radio-frequency spectrum, as illustrated by figure 1.6. It combines lighting with communication, bringing advantages with the benefits of very small cells.

Smaller cells bring many benefits. A first one is the fact that the implementation cost is lower when compared to larger conventional towers. They are not only cheaper but also quicker to install, allowing them to be deployed in constrained environments. Small cells thus offer increased quality of service as well as flexibility at lower cost. Additional advantages include lower latency, better indoor coverage and better coverage at the edge of other cells. In 5G, the biggest disadvantage includes the considerable challenge with implementing the backhaul of small cell base stations without such a

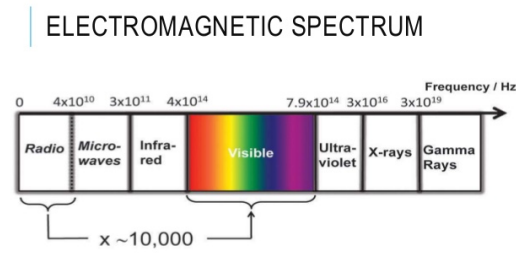


FIGURE 1.6: Image illustrating the fact that the visible light communication bandwidth spectrum is 10 thousand times the size of the radio-frequency bandwidth.

high cost. The fact that fiber need to be laid at new spots to support these 5G small cells is costly. They thus require coexistence with already existing and upcoming wireless indoor communication such as Wi-Fi, Bluetooth and VLC. Although visible light communication requires a new infrastructure, it has some complementarity with the RF-based systems, as summarized in table 1.1.

TABLE 1.1: Comparison of wireless communication protocols typically used for indoor systems.

	VLC/Li-Fi	Wi-Fi	mmWave	Bluetooth	ZigBee	NFC
<b>Standard</b>	802.11bb	802.11 b/g/n/ac	5G	Bluetooth v5	802.15.4	NFCIP-1
<b>Carrier frequency</b>	400-800 THz	2.4 GHz, 5 GHz	30-300 GHz	2.4 GHz	900 MHz, 2.14 GHz	13.56 MHz
<b>Range (m)</b>	<10	<100	<500	<350	<10	<0.1
<b>Data rate (Mb/s)</b>	10-10000	11/ 54/ 450/ 1300	<10000	1-3	0.02-0.25	0.42
<b>Power consumption</b>	With illumination	>100 mW	>100 mW	<100 mW	<10 mW	<10 mW

Table 1.1 is a summary of some of the characteristics of the main wireless communication protocols used in indoor scenarios. Wi-Fi and mmWaves are the radio technologies that are the most commonly used right now for indoor applications. They are the most comparable to Li-Fi. While Bluetooth, ZigBee and NFC are also wireless communication techniques they are used for different types of applications. Indeed, Bluetooth and ZigBee are very low power and low data rate protocols mainly used for low energy devices communication. On the other hand, NFC is a very short range protocol for data exchange between a device and a reader.

Li-Fi, Wi-Fi and the mmWaves-based are the only wireless communication technologies that can allow bandwidth-hungry indoor applications such as in-home wireless augmented reality. Li-Fi has the potential to offer a synergistic pairing in a hybrid network. Indeed, similarly to an RF solution like Wi-Fi, the data rates can largely

surpass the Gb/s in the case of 802.11.ax (or Wi-Fi 6) [5] and VLC. But, VLC offer some key distinctions.

The benefits of VLC over mmWaves and Wi-Fi include, at first, the fact that RF systems in the 30-300 GHz range require complicated and expensive antenna beam-forming techniques in order to achieve the same data rates as VLC. A second benefit is the fact that VLC do not interfere with other radio-frequency systems and the reuse efficiency is thus higher. Thirdly, the data is more secure as it is confined within a single area and does not penetrate walls. Also, the power consumption is also contained with the needs of the LED illumination. A fifth advantage is the possibility to use Li-Fi systems in environments where radio-waves are forbidden like hospitals and planes. Finally, the Li-Fi networks can be implemented by reusing the existing lighting system which makes it less complex and costly.

Disadvantages include the preference for line-of-sight communication, the limited coverage area because of non-structure-penetrating signals, and the necessity of a new back-haul and the low maturity of the VLC systems as compared to Wi-Fi. Despite these disadvantages, the place of Li-Fi as a complementary solution for indoor communication along with 5G, Wi-Fi or even with the prospect of 6G [6] is very clear. Especially because of the ubiquity of LEDs. An example for such an all-spectrum network system is shown figure 1.7.

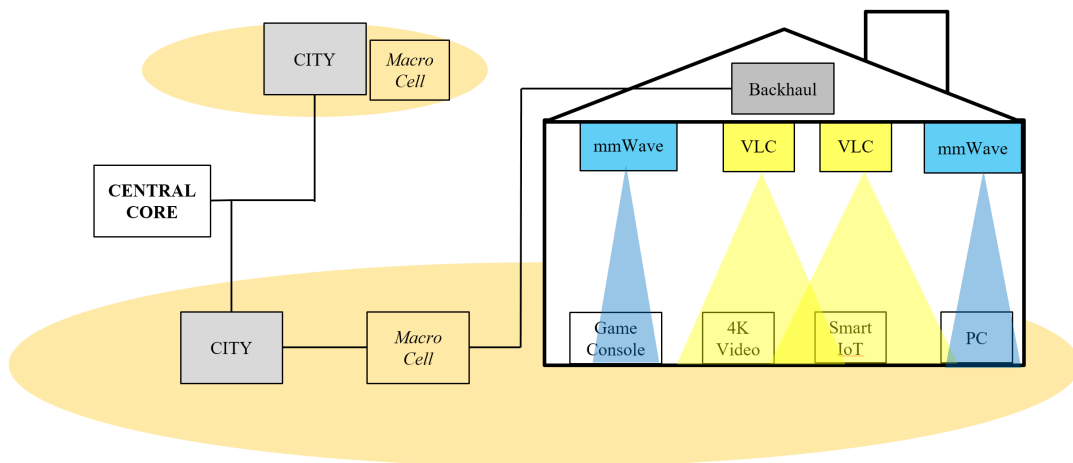


FIGURE 1.7: The prospect of 6G for an all-spectrum network system.

## 1.2 Objectives and Outline of the Thesis

### 1.2.1 Objectives of This Work

VLC, or Li-Fi, has the potential to be a complementary solution for the problematic of spectrum saturation in RF. With 5G, Li-Fi would be included in hybrid networks using small indoor cells. Associating illumination with data access can bring power savings, more data security and lower impact on health as compared to radio-frequency.

In this work, an indoor multi-users VLC system is experimentally demonstrated in order to answer the objectives of a Li-Fi setup in the context of a small cell contained in a larger hybrid network. The following goals are thus defined:

- **Range:** The average distance between a ceiling, where a VLC emitter would be placed, and an office desk, where a VLC receiver would be placed, is 2.15 meters. Thus, the range should be around that value for realism of the experimental setup.
- **High data rate:** In France, high data rate is defined as above 100 Mb/s. It is chosen as a value that enables home applications such as 4K video streaming or cloud computing.
- **Multi-users access:** The small cell should be able to independently serve multiple receivers. Indeed, a VLC system would be used in indoor situations with high bandwidth requirements because of a large number of IoT or multiple users demanding high data speeds. As such, the cell should be able to divide its throughput to multiple receivers. At the same time, for a multi-users access to make sense, the coverage area needs to be large enough to contain at least 4 users.
- **Ease of implementation:** The fact that VLC systems can use the already existing infrastructure of LED illumination is an advantage. Thus, the complexity of the system need to be limited in order to conserve that edge.

The objectives for the system conceived in this work are illustrated in figure 1.8

### 1.2.2 Report Outline

The report is separated in 6 chapters.

Chapter 1 introduces the place of visible light communication in the context of wireless communication systems. Firstly, the fifth generation of broadband mobile systems is presented in the context of its history and with its principle and role in indoor communications. Then, Li-Fi, or VLC, is introduced as a complementary solution in potential hybrid networks. Finally, the goals of this work are presented as a guideline for the rest of the report.

Chapter 2 is a state-of-the-art and overview of visible light communication. The goal is to present a more complete overview of the objectives of this work. The basics of VLC are first explained in order to provide an initial understanding of the technology. Then, a review of the VLC techniques is offered as a mean to expose the state of the domain in the literature. These observations allow the design of our work and to compare our approach with existing works. With this complete presentation of the ambitions of our experimental setup, the technical details can be addressed.

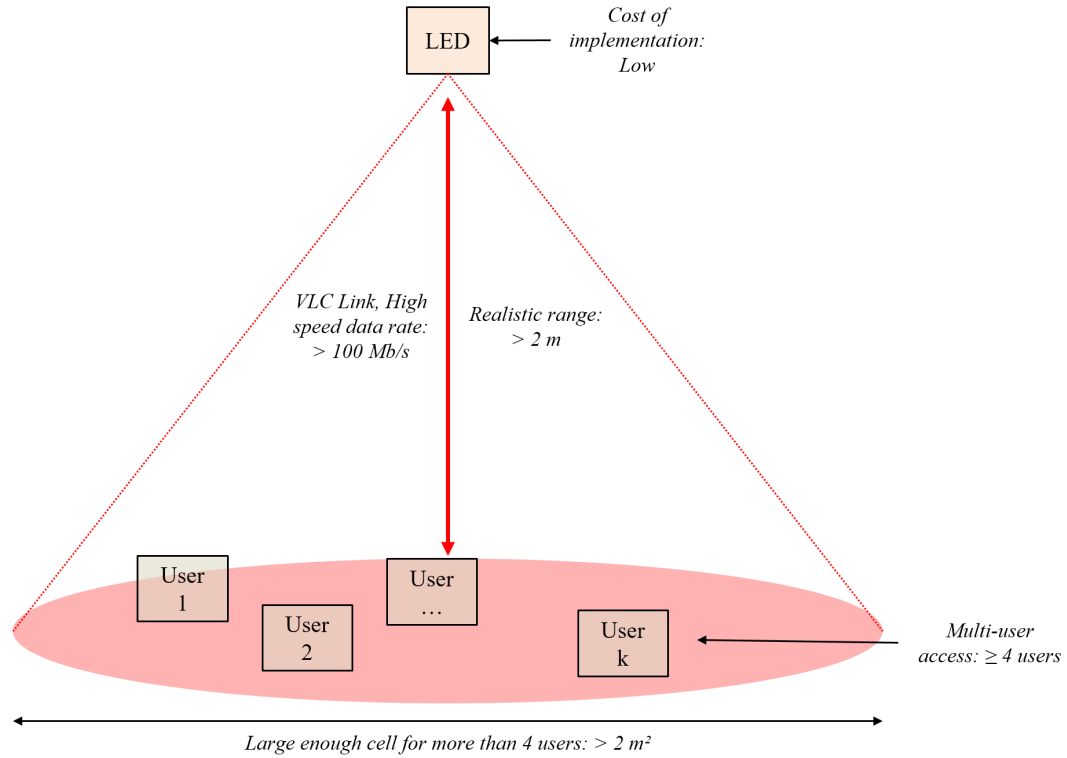


FIGURE 1.8: Schematic illustrating the objective for a small cell using VLC as the base technology.

Chapter 3 offers an analysis of the principles and hypothesis supporting our indoor multi-users VLC system. The basis behind the modulation and multi-users access schemes is first investigated in order to understand the possible associations between the different techniques used for this system. A numerical simulation analysis is then performed in order to list the parameters of both the modulation and multi-users access schemes and examine their impact on the performances. Conclusions are drawn from this numerical simulation investigation and serve as a basis for the experimental investigations.

Chapter 4 is the first part of the experimental investigations, on the single-user broadcast performances of the system. The experimental setup is completely presented, from the characteristics of the hardware elements to the full schematic. Then, the methods of broadcast performance characterization are introduced with definition of the measured parameters and measurement process. The optimization of the spectral efficiency is the guideline of the experimental process. The initial performances of the modulation are investigated. Then, the different solutions for data rate optimization are analyzed. The objective is to define an optimization process for the broadcast performances, which is compared with the initial results as a conclusion.

Chapter 5 is the second part of the experimental investigations, on the multi-users performances of the system with the various multi-access schemes used in association with the modulation. At first, the performance metrics that are used in the

---

experimental setup characterization are defined. Then, the system is evaluated experimentally. At first, the impact of the multi-users access schemes on the broadcast performances is evaluated. Secondly, the cell coverage area is measured and compared between all associations. Thirdly, the performances in user allocation are also compared. All the results from the setup characterization are compiled for the conclusion.

Chapter 6 is the conclusion of the report. It compiles the results obtained throughout the experimental analysis performed in chapters 4 and 5. They are then compared to the initial objectives defined in chapter 1 as well as compared to the approach precisely defined in chapter 2. Following the conclusions of the report, a perspective on future works is offered.



## Chapter 2

# Visible Light Communication for Indoor Applications

### Contents

---

<b>2.1</b>	<b>What Is Visible Light Communication?</b>	<b>11</b>
2.1.1	Brief Historical Overview of VLC	12
2.1.2	Basic Principles of VLC	13
2.1.3	Comparison as a Wireless Communication Technology	16
2.1.4	Applications of Visible Light Communication	19
<b>2.2</b>	<b>Review on Indoor Visible Light Communication</b>	<b>20</b>
2.2.1	Physical Structure of an Indoor VLC System	20
2.2.2	Multiple Input Multiple Output	27
2.2.3	Modulation Schemes	30
2.2.4	Multi-Access Schemes	42
2.2.5	Performance Enhancement in VLC	48
<b>2.3</b>	<b>Design Approach</b>	<b>51</b>
2.3.1	Communication Broadcast Structure	51
2.3.2	Multi-Users Access Techniques	54
2.3.3	Placing our Approach	54

---

## 2.1 What Is Visible Light Communication?

VLC is an optical wireless communication (OWC) technique where the light produced by a light-emitting diode (LED) in the visible spectrum is used as a data carrier through the use of intensity modulation (IM). VLC is actually a branch of OWC technologies. Its origin is explained in section 2.1.1. Section 2.1.2 details the basic principles. Then section 2.1.3 places the technology in a comparison with other wireless communication methods in order to list advantages and drawbacks. Finally, the potential of VLC is specified by detailing its applications in section 2.1.4.

### 2.1.1 Brief Historical Overview of VLC

Communication with light has been used for the longest time in history. Beacon fires or smoke signals are the most ancient examples. As times progressed, new techniques were developed. At the end of the 18th century, semaphore telegraphs were developed by Claude Chappe and used in various countries such as France, Sweden or the United Kingdom. The principle is to transmit information with visual signals using towers and pivoting shutters. This method and other early optical wireless communication (OWC) used specific codes like the Morse. At the end of the 19th century, in 1880, Alexander Graham Bell developed the photo-phone where the voice signal was modulated and transmitted over hundreds of meters by using a vibrating mirror and a parabolic receiver [7]. A follow-up to this technology happened in the 1960s with the invention of light amplification by stimulated emission of radiation (laser) systems. Lasers are able to emit concentrated and narrow light beams. At first, point-to-point communication systems were developed for outdoor long-range transmission based on infrared (IR) or near-infrared (NIR) light. Hundreds of km of range were possible for a modulated signal using these lasers as transmitters. Free space optical (FSO) communication experienced an increasing interest in various applications and the development of new opto-electronic devices allowed for commercialization of reliable systems. For example, Japan uses 30000 IR beacons all over their road network in order to provide road traffic information directly to the car navigation screen [8]. OWC also met interest for indoor scenarios. As an example, Gfeller and Bapst demonstrated a diffuse radiation IR system broadcasting at 1 Mb/s in an office room in 1979 [9]. The technology, present in remote control devices, obtained a defined set of protocols and standards by the Infrared Data Association (IrDA) in 1993.

In the 1990s, Shuji Nakamura, Isamu Akasaki and Hiroshi Amano work led to the development of high-intensity blue LEDs. Following this key invention, white LEDs were able to be developed using a simple yellow phosphor layer. The advantage for illumination over more ancient light sources is the energy-saving as well as the much longer lifespan. They also have faster response times than incandescent and gas-discharge lamps. As a result, the OWC techniques which were previously only considered for IR communications were also studied for visible light. The first research teams in the 1990s quickly published works on Visible Light Communication (VLC) in both indoor and outdoor scenarios. The principle is illustrated in figure 2.2 for an indoor scenario.

In 2003, pioneers in research on VLC, among which Shinichiro Haruyama and Masao Nakagawa from the Keio University, founded in Japan the Visible Light Communication Consortium (VLCC) [10] and the Nakagawa Laboratories Inc. [11]. The latter developed and sold VLC kits for indoor or underwater applications while filing more than ten patents [12]. The VLCC, replaced by the Visible Light Communication Association (VLCA) [13] in 2014, was dedicated to the VLC promotion by exploring its potential and involving companies in its development. The works carried out by

the VLCC led in 2007 to the publication of two standards by the Japan Electronics and Information Technology Industries Association (JEITA), the JEITA CP-1221 and JEITA CP-1222. In 2008, the EU launched the Home Gigabit Access (OMEGA) project which aimed at conceiving a 1 Gb/s home network access using VLC. In 2009, the VLCC associated with the IrDA and the Infrared Communication Systems Association (ICSA) issued standards extending the IR physical (PHY) layer to VLC and characterizing VLC local networks. The same year, the IEEE started a Task Group (TG), the TG7 [14], to establish a new standard on VLC. This standard, the IEEE 802.15.7 [15], was published in 2011 and has then possibly played a crucial role in the exponential growth of the number of works on VLC outlined by Figure 2.2. This growth seems to stale as of very recently because of the transition of the technology to market. A first revision of the IEEE 802.15.7 led by the TG7r1 since 2014 is released in 2017. One of the major goals of this revision was to provide a framework for VLC using cameras as receivers, a technique called optical camera communication (OCC). In July of 2018, the IEEE has launched the creation of 802.11bb, the new Li-Fi standard. It is expected to release in 2021 and focuses on interoperability among light sources, up-link and down-link operation with visible and IR light, and a PHY layer with a single-link operation of at least 10 Mb/s and another of at least 5 Gb/s.

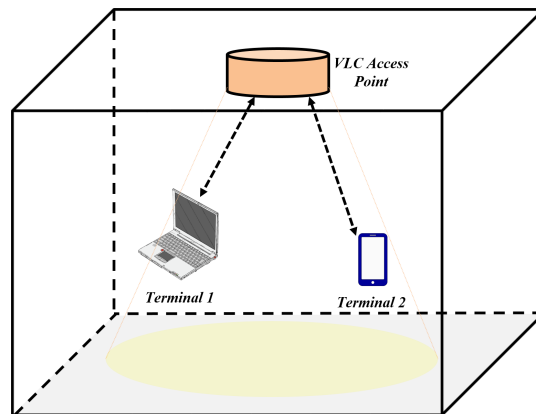


FIGURE 2.1: Illustration of the principle of a VLC system where an access point based on an LED down-light can communicate with one or more terminals.

## 2.1.2 Basic Principles of VLC

As already mentioned, VLC is an OWC technology using the visible light produced by LED as both data carrier and illumination. The general architecture of a VLC system, given on Figure 2.3, is composed of an emission block separated from a reception block by a FSO channel.

### 2.1.2.1 Data Emission End

Data emission, as the name suggests, gather the data to be transmitted. Then, it is encoded and modulated. Finally, the modulated signal is passed through a LED

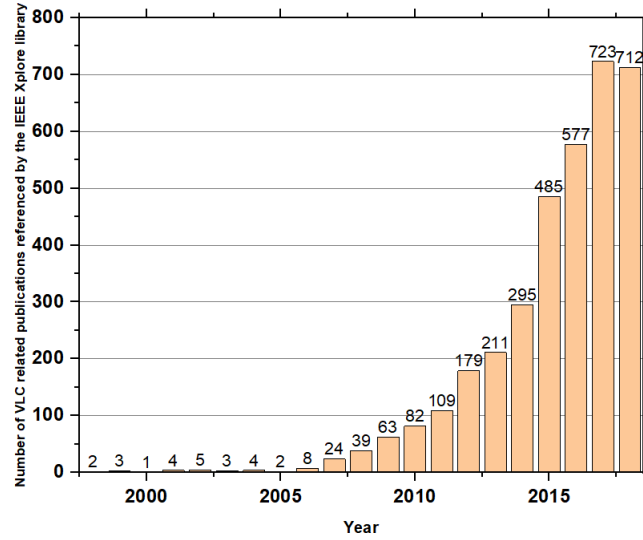


FIGURE 2.2: Graph representing the number of VLC related publications as referenced by the IEEE Xplore library every year until 2018.

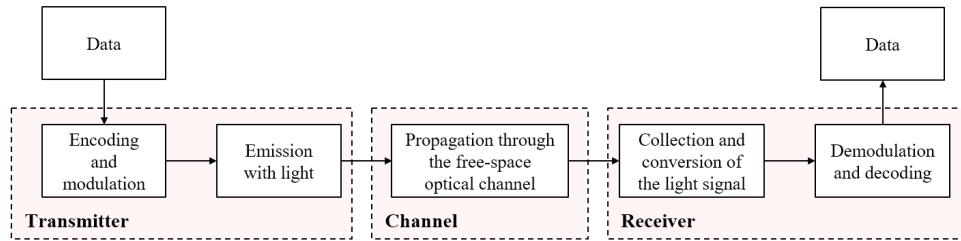


FIGURE 2.3: Schematic representing a basic block diagram explaining the principle of a VLC system.

driver in order to convert it into an optical signal. The LED emits that signal towards the receiver with its intensity depending on the modulation technique, seen in section 2.2.3. This is called intensity modulation (IM).

The semiconductor is generally inserted on a package, as represented on Figure 2.4 (a), which protects the chip and shapes the light beam. Figure 2.4 (b) illustrates the relative spectrum emission of a typical, off-the-shelf, white LED. As shown, 2 peaks at the blue wavelength and around the yellow wavelength are produced. It corresponds to the blue chip light and some of its photons converted to yellow by the phosphor layer. Figure 2.4 (c) represents the beam pattern of the LED represented on Figure 2.4 (a) and shows that the light signal transmitted intensity depends on the direction of emission. It reaches its maximum intensity in the reference axis and then decreases with the angle of emission. This spatial distribution is usually characterized by the semi-angle at half power  $\Phi_{1/2}$  which is the semi-angle at which the power is half of its maximum value. It will have a direct impact on the VLC link configuration.

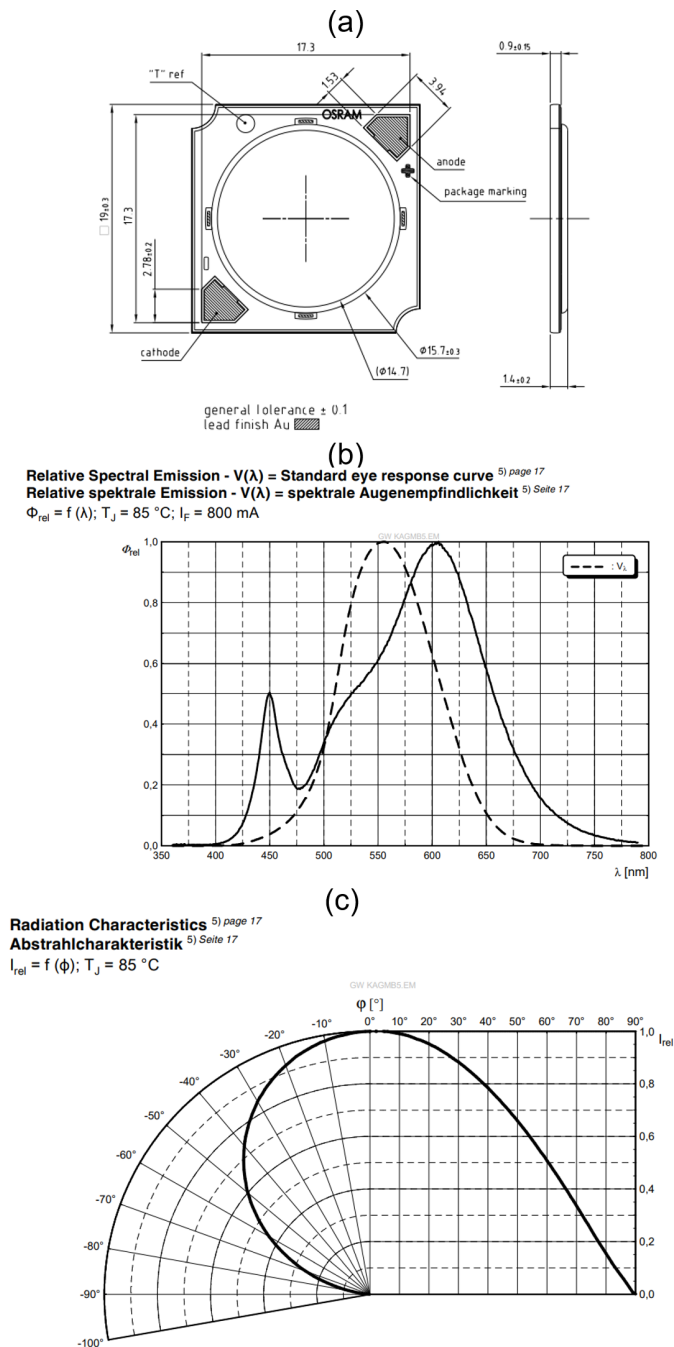


FIGURE 2.4: White LED GW.KAGMB5.EM parameters as extracted from its datasheet [16] illustrating the (a) package outline, (b) relative spectral emission and (c) radiation characteristics.

### 2.1.2.2 Free Space Signal Propagation

Free space propagation corresponds to the step where the optical signal propagates through the free space optical channel before attaining the receiver. This will be detailed in appendix A.1. The channel is modeled with the distortions that the optical signal experiences. The distortions include distance-induced attenuation, distortions-induced weather, or noise induced by the electrical components.

### 2.1.2.3 Data Reception End

The receiver of a VLC system must first convert the light received from the transmitter into an electrical signal for data recovery. This reception process is named direct detection (DD) in VLC systems since the optical signal, containing data, is transformed into a proportional electric signal. Photodiodes (PD) and image sensors are the most commonly used components for this role and more is said about them in sections 2.2.1 and 2.2.2.

Figure 2.5 (a) shows the relative spectrum sensitivity of an off-the-shelf photodiode (PD), where it is shown to be more sensitive to certain wavelengths than others. Figure 2.5 (b) then illustrates its directional characteristics, where the direction from which the light is coming change the sensitivity of the PD, analog to an LED's FOV. Figure 2.6 shows the different link types according the different possible alignments of the PD and LED FOV. The main arrangement is the line-of-sight (LOS) and non-line-of-sight (NLOS) configurations. The link has LOS when the light signal can be directly collected by the receiver or, in other words, when a part of the emitter beam pattern falls into the FOV of the receiver. When this condition is not fulfilled, then the link has NLOS communication.

### 2.1.3 Comparison as a Wireless Communication Technology

VLC has several advantages which makes it an interesting technology to complement radio-based systems:

- The visible light spectrum corresponds to a huge bandwidth of around 300 THz that is free and not regulated.
- A LED can be modulated at very high speed which means data rates of hundreds of Mbps can be achieved with high spectral efficiency modulations.
- The corresponding frequencies do not interfere with radio waves and cannot pass through obstacles, which means VLC system can be used along with RF systems while providing an increased privacy.
- A LED has a low power consumption and its price keeps decreasing. For these reasons, LED are progressively replacing traditional light sources. Consequently, there is already a network of potential VLC emitters installed everywhere.

All these characteristics can be confronted with the drawbacks of RF-based technologies:

- First, the RF spectrum covers only 300 GHz, mainly regulated by the International Telecommunication Union (ITU) and already overcrowded. This shortage will obviously get worse over the next years given the growth of the mobile and

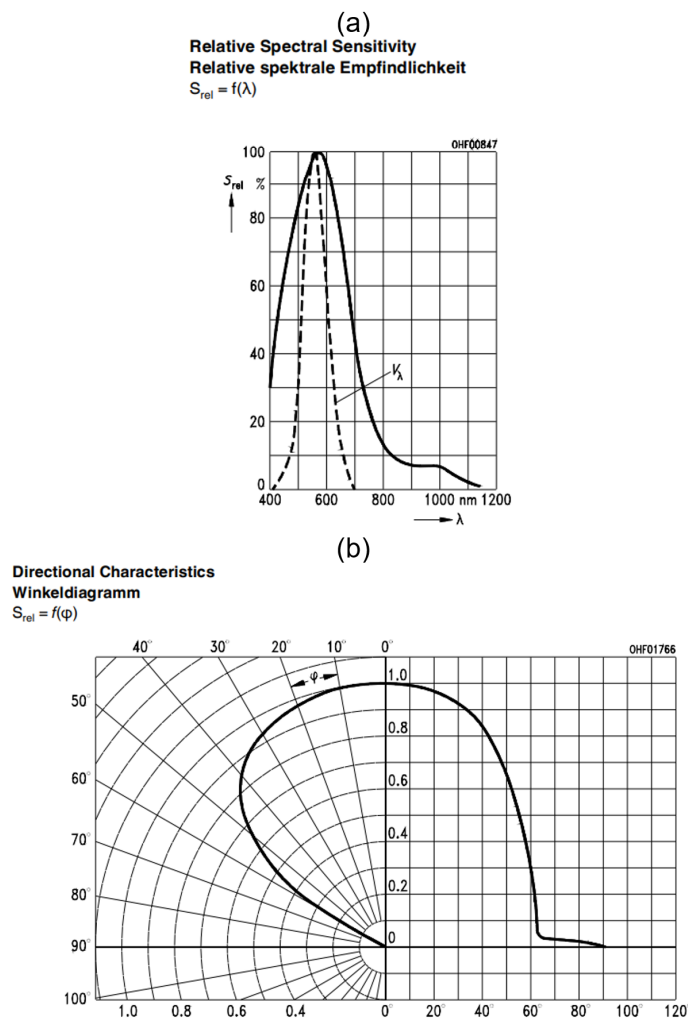


FIGURE 2.5: Osram photodiode BPX 61 parameters as extracted from its datasheet [17] illustrating the (a) relative spectral sensitivity and (b) the directional characteristics.

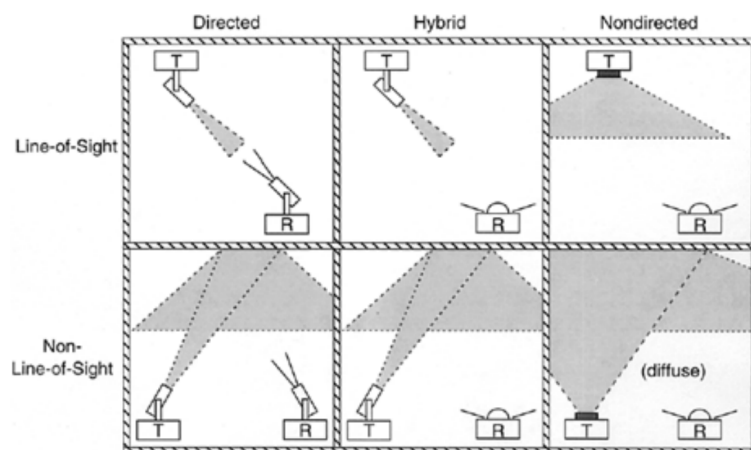


FIGURE 2.6: Figure illustrating the different transmitter-receiver configurations in both line-of-sight and non-light-of-sight situations in a VLC system, as referenced in [18].

connected devices market and the changes in the type of data exchanged that are now mainly video streams [19].

- In addition, RF systems are sensitive to electromagnetic interference and are not fully protected from jamming or intrusions. Because they can interact with other devices, but also because their use is not safe or inefficient in certain conditions, RF systems are banned from certain areas like hospitals, mines or oil platforms.
- Furthermore, they are based on a grid of base stations that are expensive to maintain and consume a lot of power. According to the IPCC, the information and communication technologies (ICT) actually accounts for 2% of the global greenhouse gas emissions, a share that keeps rising [20]. The power efficiency of RF systems can be increased, but it is necessarily at the cost of the spectral efficiency which, in a context of spectrum shortage, is a tricky tradeoff. Finally, there are still doubts concerning the effects of RF on health.

This quick confrontation shows that VLC can complement RF technologies by discharging the RF bandwidth and providing greener communication systems while enabling data transmission in non-covered areas. However, we cannot expect VLC to replace RF systems because it also has numerous drawbacks:

- Since VLC uses light sources primarily dedicated to lighting or signaling, what happens if the user chooses to turn them off, or at least to reduce their intensity? This functionality, usually referred as dimming, must be taken into account in any VLC system design.
- Similarly, the flicker problem, which corresponds to variations in the light intensity that are slow enough to be noticed by the human brain, must be carefully managed since it may cause epileptic seizures in certain cases [21]. However, flicker can be easily prevented by ensuring its frequency is always over 200 Hz using line coding like Manchester coding.
- If the inability of light to pass through obstacles is an advantage for privacy, it is a real challenge when trying to maintain a reliable communication link. In indoor, NLOS paths of a diffuse link, as represented on Figure 2.6, can be used to overcome this issue [22]. In outdoor, however, such reflections on the ground or on buildings are much more difficult to exploit, which means a LOS link is usually vital. This requirement necessarily limits the possibilities in terms of relative mobility between the emitter and the receiver, except if the receiver is able to track the light beam of interest.
- Another common problem in outdoor applications is the impact of the ambient light, and especially of the sunlight. It is the major source of interferences in

VLC and is really challenging to fully manage. However, it is a lower problem in indoor applications in most cases. The indoor FSO channel introduces attenuation that limits the optical power collected by the light sensor.

All characteristics of comparison are summed up in Table 2.1, which compares VLC, RF and IR communications.

TABLE 2.1: Comparison of VLC, IR and RF communication technologies, reproduced from [7].

Property	VLC	IR	RF
<b>Bandwidth of the carrier</b>	400-700 nm (very large and unregulated)	800-1600 nm (very large and unregulated)	300 GHz (saturated and regulated)
<b>Electromagnetic interferences and hazard</b>	No	No	Yes
<b>Range</b>	Short to Medium	Short to Medium (outdoor)	Short to long (outdoor)
<b>Security</b>	Good	Good	Poor
<b>Service</b>	Illumination and communication	Communication	Communication
<b>Noise sources</b>	Sunlight and other ambient lights	Sunlight and other ambient lights	All electrical and electronic appliances
<b>Power consumption</b>	Relatively low	Relatively low	Medium
<b>Mobility</b>	Limited	Limited	Good
<b>Coverage</b>	Narrow	Narrow	Mostly wide

#### 2.1.4 Applications of Visible Light Communication

Given all the advantages and drawbacks listed above, VLC has naturally been considered for applications in both indoor and outdoor environments:

- **Indoor positioning:** Numerous light sources are used to triangulate the position of a receiver with centimeter accuracy.
- **Data access where coverage is limited:** VLC can be used where RF systems are forbidden, such as in hospitals. It can also be deployed as a data access solution in places where RF is not functional such as under water.
- **Home network:** Like Wi-Fi, the objective is to provide wireless communication access. The LED light sources of the infrastructure are thus turned into access points.
- **Transport communication:** The VLC technology can support the emerging applications in the vehicle domain, such as platooning and self-driving cars. It has also started to be studied for deployment in plane cabins and cockpits [23][24].

## 2.2 Review on Indoor Visible Light Communication

A review of the technologies behind VLC are summarized in this part, from the physical components to the modulations and multi-users access process. Section 2.2.1 is an overview of the physical structure of indoor VLC systems with a description of the optical free space propagation channel as well as LEDs and photodiodes technology analysis. Then, section 2.2.2 describes the principle of multi-input multi-output (MIMO) systems. Section 2.2.3 is a state-of-the-art on the modulation schemes used in VLC followed by section 2.2.4 which focuses on multi-users access schemes. Finally, section 2.2.5 concludes on the various techniques used to improve the performances of VLC systems.

### 2.2.1 Physical Structure of an Indoor VLC System

The study of a system needs a first approach on its model for a simulation investigation. In the VLC case, the transmission channel can be modeled and represents the path between the LED and the photodiode. The physical elements of the system themselves need also to be modeled to form the complete interaction between the channel path and the physical devices. The model is further described in appendix A and explained through simulations.

#### 2.2.1.1 Optical Wireless Channel

In a VLC system, the optical power of a light source is modulated, and the resulting light signal is, after free space propagation, collected by a photodiode (PD) and converted into a photo-current. The perturbations experienced by the signal from its initial light form to its final photo-current form are taken into account by the free-space optical (FSO) channel model. This channel is a complex entity that gathers the degradation induced by the atmospheric conditions, the natural and artificial surrounding light sources or the electronics used for light collection and conversion. However, these degradations are generally divided into two main categories: the signal attenuation and the receiver noise. The FSO channel can thus be modeled as a baseband time-invariant (LTI) system of input  $X(t)$ , output  $Y(t)$ , channel impulse response  $h(t)$  and additive channel noise  $n(t)$  [18]:

$$Y(t) = X(t) \otimes h(t) + n(t) \quad (2.1)$$

The output  $Y(t)$  of this LTI system is actually the photo-current produced by the PD. The input  $X(t)$  is the equivalent photocurrent theoretically transmitted by the light source.

The first source of distortion introduced by the FSO channel is the attenuation due to the channel impulse response  $h(t)$ , or equivalently to the channel frequency response

$H(f)$ . Since the frequency response of FSO channels is relatively flat at low frequencies [7],  $H(f)$  can be approximated by its DC gain  $H(0)$ , which links the average transmitted and received power  $P_t$  and  $P_r$  by:

$$H(0) = \frac{P_r}{P_t} \quad (2.2)$$

The expression of  $H(0)$ , as seen in appendix A, considers a configuration where a LED emits a signal with the polar and azimuth angles  $\theta$  and  $\phi$  according to its reference axis. This signal is then received by the PD, of sensitive area  $A_r$ , with an incidence angle  $\psi$  that limits the effective area seen from the transmitter to  $A_{eff}$ .

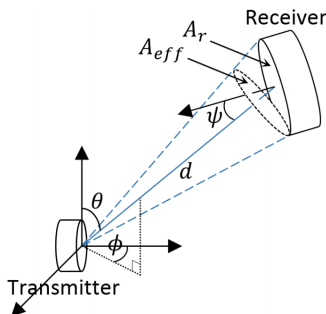


FIGURE 2.7: Geometry used for the channel gain derivation, with  $\theta$  and  $\phi$  the polar and azimuth angles of emission,  $\psi$  the angle of incidence,  $A_r$  the PD area,  $A_{eff}$  the effective PD area seen from the transmitter and  $d$  the distance from the transmitter to the receiver.

The optical power received decreases with  $d^2$  and is affected by the orientation of the receiver. It also depends on the transmission beam which is not necessarily uniform but may have a complex form depending on geometrical parameters. This is the case of the Lambertian beam pattern which is the most commonly used. Most LED can be considered as having a generalized Lambertian radiant intensity emission model [25], especially in an indoor situation. In an indoor VLC configuration, the transmitters are located at the ceiling and point downward to the floor. The receiver is also pointed to the ceiling. A part of the light produced by the down-light may also be collected after reflections on the walls. In order to determine the share of these NLOS rays in the total optical power collected, a similar analysis can be carried out and the corresponding channel DC gain can be derived [26]. However, it was shown that the NLOS contribution is negligible compared to the LED one [27]. Consequently, only the latter will be considered in the simulations presented in chapter 3.

The second source of distortion in FSO channels is the additive noise  $n(t)$ , which is produced by the PD and has two main forms: shot noise and thermal noise. The shot noise is linked with the number of photons collected and thus increases with the incident luminous flux. This noise source is only dominant in outdoor conditions, where the light source of interest is necessarily surrounded by various ambient light sources that are either natural or artificial. The shot noise is modeled as an additive

white Gaussian noise (AWGN) of variance  $\sigma_{shot}^2$ . The thermal noise, on the other side, reflects the movement of the charge carriers when they are at a certain temperature and depends strongly on the kind of pre-amplifier used. With a field-effect transistor (FET) based TIA, the thermal noise is also modeled as a signal independent Gaussian noise of variance  $\sigma_{thermal}^2$ . Note that here, the  $1/f$  noise is neglected since the signal transmitted is modulated at high-frequency. The gate leakage current is also neglected, which means that the total noise variance  $N$  will simply be the quadratic sum of the shot noise and thermal noise variances.

### 2.2.1.2 Light Emitting Diodes Types and Structures

Light emitting diodes, or LEDs, are opto-electronic devices capable of emitting light when an electric current runs through it. These devices, when used for illumination, provides a considerable advantage in electrical consumption and lifetime in all domains over traditional fluorescent-based and incandescent-based lighting systems. Considering their advantageous characteristics, the global LED market is expected to reach \$42.7 billion by 2020, with an annual growth of 13.5 percent from 2014. This corresponds to an estimated 20 percent share of the global lighting market by 2020 [28]. The LED current can be modulated at speeds ranging from around a MHz to more than multiple hundreds of MHz depending on the type and structure of the LED. Their ubiquity and their high modulation bandwidth make them ideal transmitters for VLC, with the possibility of offering a small data access point on top of power efficient illumination.

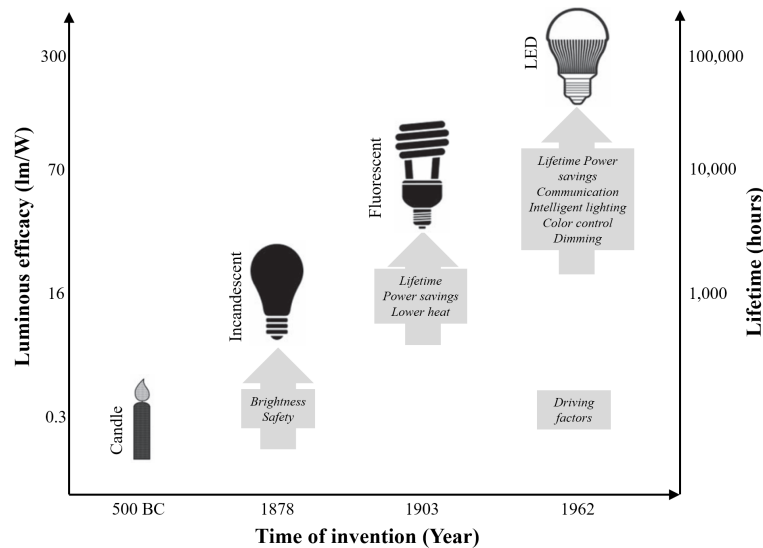


FIGURE 2.8: Graph representing the luminous efficacy of LEDs against incandescent and fluorescent light sources [29].

As LEDs are not recent, multiple different categories of LEDs with various features exist. Each type is different enough from the others to be considered for numerous distinct application with specific requirements:

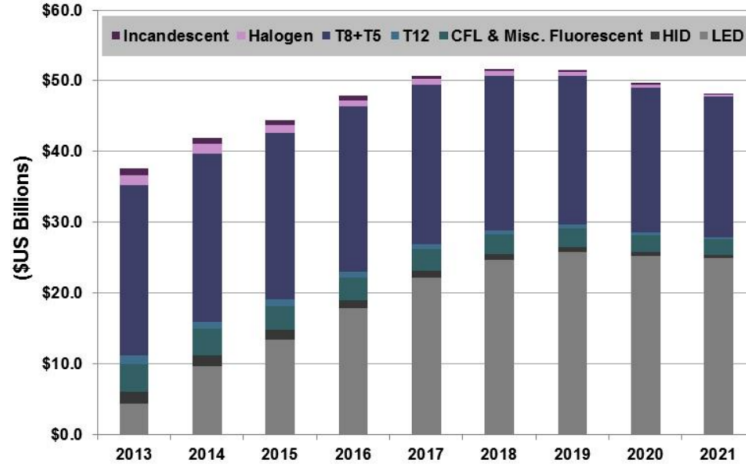


FIGURE 2.9: Global commercial lighting revenue forecast [30].

**2.2.1.2.1 Phosphor-based white LEDs (ph-LED):** The first method to produce white light is to use phosphor in a single LED by combining a short wavelength LED such as blue or UV with a yellow phosphor coating. The blue or UV photons have a chance to either be altered by the yellow photons in the layer or to be emitted without change. The result is a simultaneous emission of both blue and yellow light which produces a white color [31]. During the manufacturing process, a phosphor layer is deposited on a LED chip, typically a single blue Indium Gallium Nitride (In-GaN) die. The white color temperature is decided by both the phosphor composition, typically an Yttrium Aluminum Garnet (YAG) coating, and the wavelength of the blue LED. White LEDs produced by this manufacturing process can be categorized as cool-white, neutral-white or warm-white by Correlated Color Temperature (CCT).

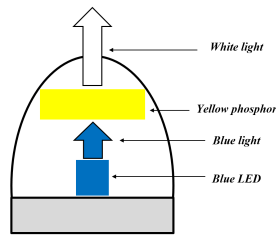


FIGURE 2.10: Illustration of the principle of a phosphor-based white LED where a part of the blue light emitted by a blue chip is converted to yellow with the phosphor layer.

In the context of VLC, the modulation bandwidth of an LED is one of the most important characteristic. Indeed, the higher it is, the higher the attainable data rate will be if the device is used as a Li-Fi access point. However, since the structure of ph-LED uses a yellow layer, the slow relaxation time of the phosphor limits the intrinsic modulation bandwidth to only several MHz. Despite the advantage in lower complexity to produce white light, this limitation hinders the potential of ph-LEDs in the context of high data rates for a VLC system. This is related in the results obtained when experimentally demonstrating white ph-based LED in indoor VLC

systems. The highest measured data rate for a VLC system using a single phosphor-based white LED is 2.32 Gb/s, as reported by Y. Zhou *et al.* in [32]. The spectral efficiency is measured at 5.155 b/s/Hz when maximizing the data rate. The metric is defined as the division between the total data rate and the total signal bandwidth at the LED. On top of using orthogonal frequency division multiplexing (OFDM), a two-stage equalizer and a maximum ratio combining (MRC) algorithm on two receivers are used. The limited bandwidth is mainly circumvented by the use of heavily complex techniques such as multi-stages equalization and the use of high spectral efficiency modulation formats.

White light can also be produced by properly mixing red, green and blue light. This method utilizes 3 or more LED chips emitting different colors and provides higher modulation bandwidth than ph-LEDs because of the removal of a slow phosphor layer. However, the cost of implementation and complexity is increased. The increase in available modulation bandwidth and the ability to transmit three parallel independent information streams, such as in [33], allow for much higher attained data rates experimentally.

**2.2.1.2.2 Organic LEDs (OLED):** Organic LEDs, or OLEDs, are mainly used in flat panel displays and can generate light. It uses an organic layer between positive and negative carriers to produce light. The frequency response is far lower than inorganic LEDs, at approximately 100 kHz [34]. However, equalization has been used to successfully extend the modulation bandwidth. For example, an increase of up to six times, as reported by P. A. Haigh *et al.* in [35]. The highest measured data rate for a VLC system using a single monochromatic organic LED is 51.6 Mb/s, as reported by H. Chen *et al.* in [36]. The measured 3 dB bandwidth of the OLED is 460 kHz and both a LMMSE and DFE equalizers are used to expand the frequency response. Thus, using OFDM, a data rate of 51.6 Mb/s is attained at a distance of 12.5 cm. Alternatively, multi-color OLEDs were used by P. A. Haigh *et al.* in [37] in order to attain a transmission speed of 54.9 Mb/s, divided into 27.9 Mb/s, 18.6 Mb/s and 8.4 Mb/s for the blue, red and green OLEDs respectively. Their 3 dB modulation bandwidths were measured at 600 kHz, 350 kHz and 110 kHz respectively. A distance of 5 cm was used and the equalizer is an artificial neural network (ANN) based multi-layer perceptron (MLP). The low luminescence of OLEDs limited the distances used in the experimental setups in VLC and their low 3 dB bandwidth forced the use of very complex equalizers.

**2.2.1.2.3 Micro-LED ( $\mu$ LED)::** Micro-light emitting diodes, or  $\mu$ LEDs, come in arrays and typically emit light in the 370-520 nm wavelength range (blue). This originates from the AlGaIn micro-LEDs developed for optical fiber communication [38]. They offer a 3 dB bandwidth in excess of 450 MHz allowing much higher throughput per LED than a traditional inorganic LED. The size of  $\mu$ LEDs allows for a very low capacitance which is the reason behind the higher bandwidth. The highest

measured data rate for a VLC system using an array of violet micro-LEDs is 11.95 Gb/s, as reported by M. S. Islim *et al.* in [39]. Two sets of inner and outer pixels were used in the array with an OFDM-based VLC system using adaptive bit and power loading and equalization. The distance was set at 16 cm due to the low luminescence of the micro LED array. The 6 dB electrical to optical bandwidth of a single micro LED is measured at 655 MHz thanks to the smaller active area.

**2.2.1.2.4 Resonant cavity LED (rc-LED):** The extraction efficiency of conventional LEDs is poor in majority because of the large difference in refractive index between the narrow gap semiconductor and the surrounding medium, which is typically air. Resonant cavity enhancement improves the light extraction near the infrared wavelength range [40]. Thus, rc-LEDs typically emit light at 650 nm with a narrow line width and be modulated in excess of 100 MHz [41]. The highest measured data rate for a VLC system using a single rc-LED is reported at 4 Gb/s, by H. Chun *et al.* in [42]. The commercial red rc-LED is used in combination with both a green and blue  $\mu$ LED. The distance used is 1.5 m and the signal bandwidth for the red channel is at 1000 MHz and uses an OFDM signal. The 3 dB bandwidth is also measured at around 100 MHz and is extended with both pre- and post- adaptive equalization. The green and blue channels, on the other side offer a 2558 Mb/s and 4724 Mb/s data rate respectively.

**2.2.1.2.5 Laser Diode (LD):** Laser diodes (LD) exhibit a much larger modulation bandwidth [43] (>GHz) than LEDs or  $\mu$ LEDs as well as a higher pumping efficiency [44]. Extremely high data rates are thus possible when used for wireless communication when using LDs and vertical-cavity surface-emitting lasers (VCSEL) but it requires high-speed optical and electrical devices which lead to a sizable increase in cost. The highest measured data rate for a VLC system using laser diodes is reported at 105.41 Gb/s, by D. Tsonev *et al.* in [45]. However, the results were extrapolated from the use of a RGB LD triplet where the red LD achieved a data rate of 3.156 Gb/s, the green LD 3.049 Gb/s and the blue one 2.579 Gb/s, or an aggregate throughput of 8.784 Gb/s. Since the laser diodes occupy a narrow wavelength of around 4 nm, it was then assumed that 12 RGB LDs triplet would occupy the full visible light spectrum and thus attain 105.41 Gb/s of total data rate on 36 parallel stream channels, at a distance of 1 m. On the other hand, an actually measured data rate of 40 Gb/s was reported for a VLC system by L.-Y. Wei *et al.* in [46]. The distance was set at 2 m and polarized multiplexed RGB LDs are used. Using OFDM and 6 channels through the p- and s- polarization on the red, green and blue streams, a data rate of 40.665 Gb/s is thus attained.

Laser diodes are not considered in this work because of their very high implementation cost and the focus on more off-the-shelf solutions in order to conceive a realistic indoor VLC system, as will be further discussed in part 2.3 of this chapter.

**2.2.1.2.6 Comparison:** The main characteristics of the LED types described in subsection 2.2.1.2 are compared in table 2.2.

TABLE 2.2: Comparison of the main characteristics of the different type of LEDs.

	ph-LED	RGB LED	$\mu$ LED	OLED	RC-LED
<b>Bandwidth</b>	3 to 5 MHz	10 to 20 MHz	>300 MHz	<1 MHz	>100 MHz
<b>Luminous efficacy</b>	130 lm/W	65 lm/W	N/A	45 lm/W	>130 lm/W
<b>Cost</b>	Low	High	High	Very low	High
<b>Complexity</b>	Low	Moderate	Very high	High	High

### 2.2.1.3 Photodiodes Types and Structures

Intensity modulation (IM) is used at the transmitter to change the instantaneous emitted power of the LED in order to modulate the signal to be transmitted into optical power. At the receiver, the incident optical signal needs to be converted into a proportional electrical current using direct detection (DD) as the only feasible down conversion method. An optical filter can be used to potentially improve system performances, as discussed in subsection 2.2.5. An optical concentrator is also often used in order to focus the optical signal into the effective area of the converting receiver. As photo-resistance and photo-transistors are slower than photodiodes (PD), the latter are almost always used in the study of VLC systems [47].

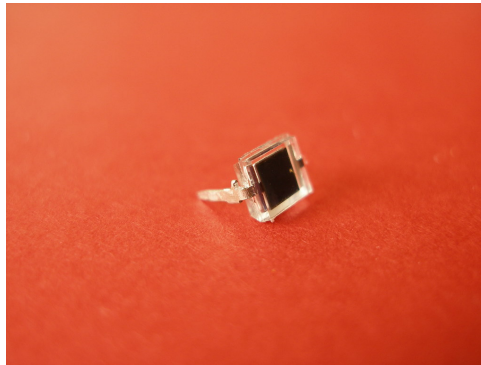


FIGURE 2.11: Close-up image of a BPW34 PIN photodiode.

Two types of PDs can be used in VLC: the PIN PD and the avalanche PD (APD). The ‘PIN’ comes from the wide intrinsic (‘i’) semiconductor region sandwiched between ‘p’ type and ‘n’ type semiconductor regions. The first one has the advantage of being available at lower costs and also have a higher temperature tolerance. It also has better performances under important ambient light [48]. Thus, PIN PD have been more present in the works relating to optical communication. APDs, on the hand, offer higher gains but more shot noise [48]. As demonstrated early on by J. Vucic *et al.* in [49], APDs offer better performances in weak incident light intensity scenarios as compared to PIN PDs.

The receivers can be utilized with a single element or with multiple ones. The first scenario is the use of a single element receiver and have been the most used solution

throughout VLC studies because of the low implementation cost. The second scenario is the use of multiple PDs through a selective combining receiver. An example is presented by J. Armstrong *et al.* in [50] where three receiver designs for VLC systems using OFDM are compared. The diversity combining receiver is shown to have a slightly greater capacity by selection combining a receiver optimized for the entire visible light spectrum and a receiver optimized for blue light. The second receiver uses a blue filter to be optimized for the reception of blue light. The selective combiner principle is to choose the sub-carrier OFDM channel with the higher SNR out of the two receivers. While the performances are slightly increased, the overall system complexity is doubled on that end of the transceivers. The third scenario is the use of image diversity receivers, using a number of photodiodes with lenses. Their role is to set apart the optical signals coming from a number of sources towards a specific PD. This scenario is discussed further in subsection 2.2.2.

The optical receiver front end then consists of a pre-amplifier to amplify the weak current induced by the PD to an exploitable level. High impedance amplifier can be used since it reduces the thermal noise, improves the sensitivity but has low bandwidth. Low impedance on the end is never used because of the important thermal noise. The class of amplifier that has been used in most VLC systems is the trans-impedance amplifier (TIA) because of its high bandwidth and sensitivity to transform the photodiode current into an exploitable voltage.

## 2.2.2 Multiple Input Multiple Output

### 2.2.2.1 Multi-Chip LEDs

Multi-chip LEDs typically combine 3 or more chips using different colors. The most commonly used combination is red, green and blue LEDs (RGB) to produce white light. An advantage is also the ability to control the color emitted by the RGB LED through the variation of light intensities on each chip. A yellow chip can also be added (RGBY LED) with the ability to increase the number of color attainable and increase the energy efficiency for brighter light intensity levels. While multi-chip LEDs are costlier and complex than singular ph-LEDs, they do not have the bandwidth limitation from the slow phosphor layer. Additionally, each of the color component can be a different type of chip from the traditional one. An example was given earlier in [42] where the red channel was an RC-LED and the green and blue channels were micro-LEDs.

When applied to VLC, multi-chip LEDs can be used in different ways:

- The first one is to modulate all the chips at the same time using the same signal. This translates to the same usage as a ph-LED except that the modulation bandwidth is increased without using a blue light filter which would reduce the optical power.

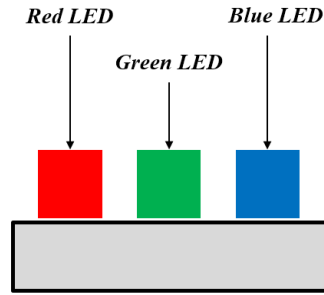


FIGURE 2.12: Schematic illustrating the principle of a multi-chip LED with the example of a RGB LED using a red, green and blue chip.

- The second method is to independently modulate each chip on a single communication channel. This is used in the color shift keying (CSK) modulation where each color represents a specific point in the CIE 1931 color coordinates, simulating a constellation [51]. This will be further discussed in subsection 2.2.3.3.
- The third method is to independently modulate each chip for parallel communication channels on each color. Provided white color is balanced, the receivers use multiple optical filters to extract the signal contained in each color channel [52]. This is used throughout VLC studies in order to provide wavelength division multiplexing (WDM), as demonstrated early on by J. Vucic *et al.* in [53] where an RGB LED was used for an 804 Mb/s WDM link.

### 2.2.2.2 Imaging Sensors

Imaging sensors are a matrix of many PD, with lenses to separate the signals coming from different sources, on an integrated circuit. It provides what is called 'image diversity' and is utilized a lot in MIMO for VLC [54]. Angle diversity receivers, the other name for imaging sensors, also exists with the objective of widening the field-of-view (FoV) [55]. The principle was demonstrated early on by A. H. Azhar *et al.* in [56] where an OFDM-based system using a 2x1 array of white LED transmitted data to a 9 channel imaging receiver using a 3x3 PD array. A data rate of 220 Mb/s over 1 m was attained and the receiver used individual pixel sizes of 2.7 mm with 0.1 mm separations along with an imaging lens.

### 2.2.2.3 MIMO in VLC

Multi-chip MIMO in VLC exploits the fact than with visible light, multiple independent channels with no correlation can be used through the use of multi-chip LEDs and PDs. Each channel uses a transmitted signal that can be isolated from the others using the appropriate optical filter. With no crosstalk between the channels, the parallel transmission configuration allows MIMO VLC systems to attain a performance gain proportionally linear to the number of channels. Subsections 2.2.2.1 and 2.2.2.1 described and illustrated the multi-element emitters and receivers that can be

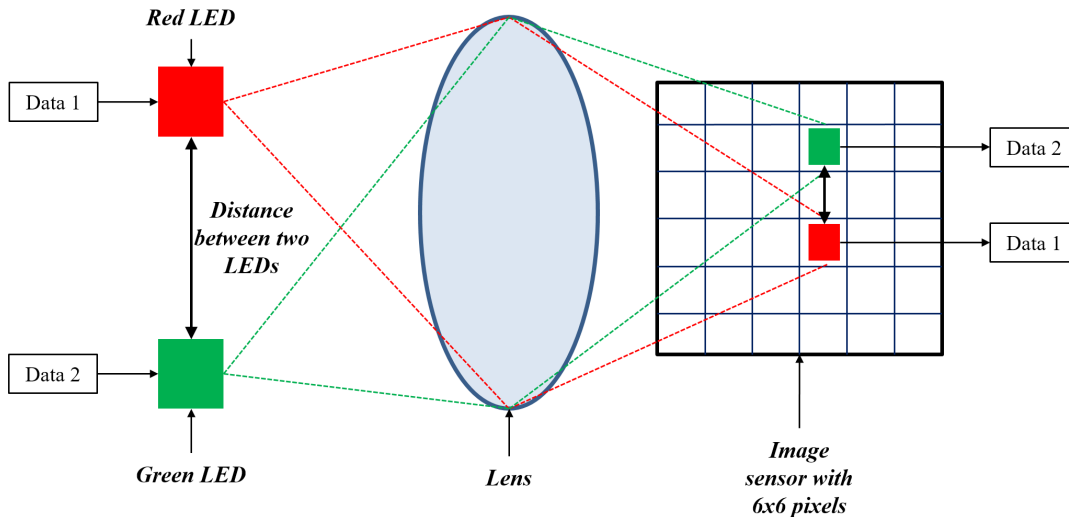


FIGURE 2.13: Figure illustrating the principle of an imaging sensor. The example uses here a red and a green LED to transmit two different data streams. The imaging lens system map both optical signals to distinct pixels of the imaging sensor.

used to achieve parallel communication channels. MIMO can be differentiated from single-input single-output (SISO) systems. While SISO systems use single-element transmitter, receivers and channels, MIMO is the opposite. In consequence, the BER can be lower when compared, as demonstrated by S. Moghe *et al.* in [57] and the data rate can be aggregated to achieve higher throughputs.

The optical cross-talk is necessarily higher, which requires the use of much more complex transmitters and receivers. In non-imaging MIMO systems, optical filters are used in order to avoid optical signal overlapping in-between the receivers, as shown in [58] for example. There, a RGB LED is used at the transmitter to achieve 3 parallel communication channels and the receiver uses 3 different optical filters to identify each of them. In imaging sensor based MIMO systems, the optical cross-talk can happen but is generally minimized by increasing the number of receivers. The example given in [56] in the previous subsection represent such a scenario with only 2 emitting LEDs but 9 receivers in a 3x3 array. L. Zeng *et al.* discussed this problematic in [59] with numerical simulation analysis on imaging based MIMO systems. In their work, it is noted that each pixel on the receiver array is a receiving channel and that the  $H$  matrix described the optical connection between each pixel and each transmitter LED array. The matrix thus need to be full-rank and in order to attain this, more receivers than transmitters must be used. Using MIMO in indoor VLC without lasers, the highest data rate attained was 15.73 Gb/s, as reported by R. Bian *et al.* in [60]. OFDM is chosen as the modulation scheme of choice with the use of WDM on an RGBY LED composed of off-the-shelf red, green, blue and yellow LEDs. The distance between the transmitter and receiver planes is placed at 1.6 m and dichroic mirrors as well as aspheric condenser lenses are used to isolate and concentrate the signal to the photo-detectors. As a result, 4 transmission channels are created for each color. Each

channel uses a 1 GHz signal and offers a data rate of 4.904 Gb/s to 2.925 Gb/s per color. the aggregate 16.92 Gb/s uses a 7% forward error correction coding overhead, resulting in the mentioned 15.73 Gb/s

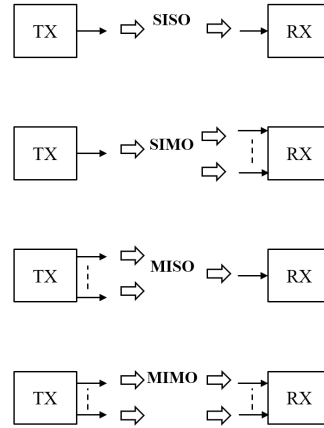


FIGURE 2.14: Figure illustrating the principles of SISO, MISO, SIMO, MIMO systems.

### 2.2.3 Modulation Schemes

In general, modulation for VLC systems are separated into three types. The first one is single carrier modulations, or carrier-less modulation schemes. The second one is multi-carrier modulations. A third type is the schemes that are specific to the use of visible light for communication because the modulation resource is the light or the color of the light. Most techniques were adapted from radio-frequency (RF) communications in order to be used in VLC because of the necessity for the optical signal to be real and positive.

#### 2.2.3.1 Single Carrier Modulation

This first type of modulation scheme includes carrier-less and single carrier techniques. In this case, the source data is directly mapped to symbols without the use of multiple carriers [61].

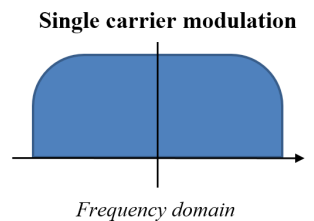


FIGURE 2.15: Schematic illustrating the basis of a single carrier modulation with a representation of the frequency spectrum in the frequency domain.

- **On-Off Keying (OOK):** This modulation scheme switches on the LED transmitter for bit 1 and off for bit 0 [62]. Because of its nature, OOK can naturally provide dimming support by refining the ON/OFF levels or applying

symbol compensation [63][64]. The first method maintains the same data rate but under-perform at low dimming levels. The second method is achieved by inserting additional symbols to attain the desired dimming level. To avoid possible flickering caused by long strings of 0 or 1, run-length limited (RLL) codes may be used [65].

- **Pulse Position Modulation (PPM):** In PPM, a pulse corresponding to a certain bit is transmitted in one of the time slots within a symbol period [62]. PPM is more power-efficient than OOK but is less bandwidth efficient [66]. A variant of PPM, named variable-PPM (VPPM) provide dimming support by changing the duration of a pulse in the same symbol period [67]. VPPM is sometimes viewed as a combination of PPM and pulse-width modulation (PWM). Overlapping PPM (OPPM) is a generalization of PPM as it allows more than one overlapping pulse to be transmitted during the same symbol period [68]. Multi-pulse PPM (MPPM) uses the same principle but the pulses do not have to be continuous during a symbol duration [69]. These last two can also be combined into overlapping MPPM (OMPPM), increasing the spectral efficiency even more [70]. In differential PPM (DPPM), the OFF symbols after the pulse in a PPM symbol are deleted and the next symbol starts right after the pulse of the previous symbol, effectively reducing the average power [71]. Expurgated PPM (EPPM) is another variation of MPPM where the symbols are expurgated to maximize the inter-symbol distance [72]. Finally, multi-level EPPM (MEPPM) extends that last design with the support of multiple amplitude levels, increasing the spectral efficiency.
- **Pulse Amplitude Modulation (PAM):** PAM is another basic modulation scheme where the data is modulated into the amplitude level of the signal [62]. This technique is subject to non-linearity in LEDs luminous efficacy and shifts in color temperature due to the variation in the drive current.
- **Generalized Space Shift Keying (GSSK):** GSSK is a generalization of spatial modulation (SM) [73]. In SM, the spatial dimension is used with constellation diagrams to allow the transmission of additional bits where one transmitter sends data while the others are off at any point of time. In GSSK, instead of one transmitter being active at a time, multiple ones can be active at the same time. A limitation is the necessity to have different channel gain values to reduce errors, making the technique suitable for low mobility receivers [74].
- 
- **Carrierless Amplitude and Phase Modulation (CAP):** CAP is a variant of quadrature amplitude modulation (QAM). It uses two orthogonal signals as opposed to the in-phase and quadrature signals in QAM schemes but does not need overhead and carriers. A data stream is encoded into two independent symbol streams. Each one is passed through in-phase and quadrature filters,

whose impulse responses form an orthogonal pulse shaping filter pair. Square root raised cosine is used as the pulse shaping waveform.

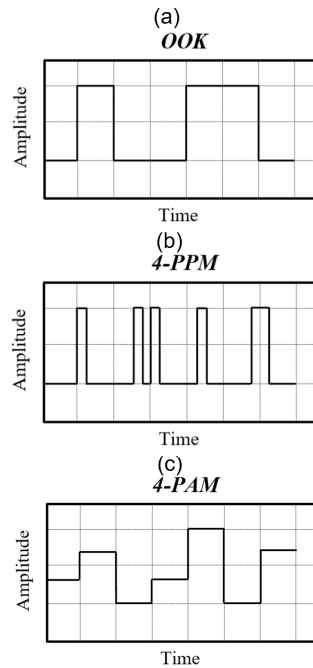


FIGURE 2.16: Single carrier modulation waveform examples for (a) OOK, (b) M-PPM, and (c) M-PAM.

### 2.2.3.2 Multi-Carrier Modulation

Multi-carrier modulation schemes separate the data to be transmitted into multiple channels in frequency. Each individual carrier can have a narrower bandwidth and this brings advantages for higher speed modulation systems. Indeed, when trying to increase the spectral efficiency, the single-carrier modulation schemes such as OOK, PPM and PAM suffer from non-linear signal distortion at the LED and inter-symbol interferences due to non-linear frequency response of visible light communication channels [75]. Therefore, one solution to attain high speed optical wireless communications (OWC) is to use multi-carrier modulations. They are less energy-efficient but much more bandwidth efficient. In RF communication, orthogonal frequency division multiplexing (OFDM) has been vastly adopted due to its effectiveness in combating the inter-symbol interferences and multi-path fading [76]. In this modulation, the data is separated and modulated into multiple orthogonal subcarriers sent in parallel sub-streams. OFDM for VLC can attain much higher spectral efficiency than OOF, PPM or PAM by reducing the inter-symbol interference. However, it needs to be adapted since the IM/DD system requires real-valued unipolar signals and OFDM generates complex-valued bipolar signals. Knowing the channel response helps using bit and power loading to further enhance the performance of each subcarrier [77][78].

The numerous techniques to transform the bipolar signal into a uni-polar one separate

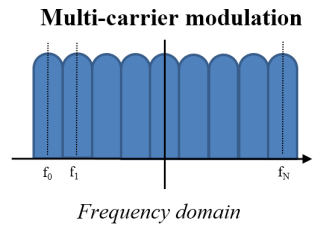


FIGURE 2.17: Schematic illustrating the basis of a multi carrier modulation with a representation of the frequency spectrum in the frequency domain.

OFDM into multiple variants. Additionally, CAP can be generalized into a multi-carrier modulation scheme:

- **Direct Current (DC) biased Optical OFDM (DCO-OFDM):** Hermitian symmetry can achieve real valued output and combined with a positive DC offset to make the signal uni-polar, forms the DCO-OFDM technique [79]. The spectral efficiency is the same as a classical OFDM signal but the consumed power is higher [80].
- **Asymmetrically clipped Optical OFDM (ACO-OFDM):** ACO-OFDM is another technique which is more power efficient than DCO-OFDM [80]. It uses a Hermitian symmetry as well but only the odd subcarriers are used for transmitting data while the even ones are set to zero [79]. Therefore, only a small DC bias is required but the spectral efficiency is half compared to DCO-OFDM.
- **Asymmetrically clipped DC biased Optical OFDM (ADO-OFDM):** ADO-OFDM is a combination of DCO-OFDM and ACO-OFDM. Each technique is used on a different type of subcarrier. ACO-OFDM is used on the odd subcarriers and DCO-OFDM on the even ones [81]. This modulation scheme can outperform the two previous in power efficiency [80].
- **Reverse Polarity optical OFDM (RPO-OFDM):** RPO-OFDM is a combination of OFDM and PWM. The scheme offers dimming support with the PWM signal duty cycle [82].
- **flip-OFDM or uni-polar OFDM (U-OFDM):** flip-, or uni-polar-OFDM is an alternative to ACO-OFDM with better optical and power efficiency [83]. In flip-OFDM, also known as U-OFDM, the original real bipolar OFDM signal has its positive and negative sections transmitted in two distinct OFDM symbols, with the negative part being flipped [84].
- **Enhanced uni-polar OFDM (eU-OFDM):** eU-OFDM is a modulation scheme allowing uni-polar signal generation without the spectral efficiency loss [85]. The scheme uses the same structure as U-OFDM where the positive and

negative parts of an OFDM signal are separated but superimposes multiple U-OFDM streams in order to not reduce the spectral efficiency.

- **Multi-band Carrier amplitude and phase (*m*-CAP):** Multiband CAP changes conventional CAP into a multi-carrier format. The frequency spectrum is separated into multiple subcarriers, each using a CAP modulation process with a Hilbert pulse shaping filter pair at the center frequency corresponding to that subband [86]. It reduces the sensitivity from non-flat channel response in conventional CAP and increases the flexibility of the scheme with the ability to use bit and power loading techniques like in OFDM [87].
- **Pulse Amplitude Modulated Discrete Multi-Tone Modulation (PAM-DMT):** In PAM-DMT, the information is transmitted using all subcarriers, however, only the imaginary parts of the signal are modulated on each sub-carrier [88]. Signal distortion caused by asymmetric clipping falls on the real component, and is orthogonal to the information-carrying signal, causing no penalty.

### 2.2.3.3 Modulation Schemes Specific to VLC

VLC is a domain of wireless communication where the transmitters use visible light to transmit data. Thus, a new resource for the signals other than its amplitude and phase can be used: the color of the light. As such, some VLC modulation techniques are designed specifically for multi-colored LEDs such as RGB LEDs or RGBY LEDs. These modulation schemes use the CIE 1931 color space defined by the international commission on illumination.

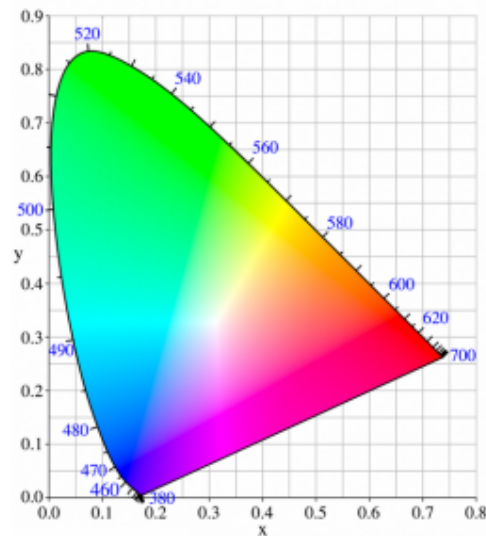


FIGURE 2.18: Schematic illustrating the CIE 1931 color space. It is the basis of the color shift keying modulation scheme.

- **Color Shift Keying (CSK)**: This modulation scheme is part of IEEE 802.15.7 for VLC. The standard defines 7 colors to support for multicolored LED communication. For a given transmitted stream, each bit or group of bits is represented by a specific color in the CIE 1931 color space coordinates [51]. An RGB source can pick three of the seven possible wavelength bands to form a triangle inside which the constellation points of the CSK symbols lie. The color coordinates for each symbol are generated by modulating the intensity of each RGB chip.
- **Color Intensity Modulation (CIM)**: CIM encodes the data into the intensities of a LED luminary while maintaining a static perceived color [89]. CIM maximizes the capacity, as opposed to CSK, by first choosing a specific region in signal space called the target subspace then mapping from a region in color space. The minimal inter-symbol distance is maximized by adding a new degree of freedom.
- **Metameric Modulation (MM)**: Based on CSK, MM achieve higher energy efficiency with more control over the color quality by the implementation of additional and independent LEDs [90].

#### 2.2.3.4 Comparison When Applied to VLC Systems

A qualitative comparison of the modulation schemes is shown in Table 2.3. The first metric is the spectral efficiency, which indicates what data rate is attainable in function of the usable signal bandwidth for any given modulation scheme. The power efficiency is the second metric important for VLC system, as the modulated signal will drive the LED transmitter. Complexity is another essential metric indicating the cost of implementation for any of the modulation technique. Finally, the presence of a method offering dimming support inherent to the modulation scheme is added as a fourth metric.

TABLE 2.3: Comparison of qualities for each modulation scheme when applied to VLC.

	Spectral efficiency	Power efficiency	Complexity	Dimming Support
<b>OOK</b>	Low	Low	Low	Yes
<b>PPM</b>	Low	High	Moderate	Yes
<b>PAM</b>	Moderate	Low	Low	No
<b>CAP</b>	High	High	Moderate	No
<b>GSSK</b>	High	Low	Low	No
<b>OFDM</b>	High	Moderate	High	Yes
<b><i>m</i>-CAP</b>	High	High	Moderate	No
<b>CSK</b>	Moderate	Low	High	Yes
<b>CIM</b>	Moderate	Low	High	Yes
<b>MM</b>	Moderate	Moderate	High	Yes

It was concluded that high spectral efficiency was a key characteristic for a modulation scheme adapted to high speed VLC. In that regards, it can be seen that CAP and *m*-CAP are an option for large power and spectral efficiency. OFDM comes at the

cost of a slightly higher complexity because of the Fast Fourier Transform and GSSK comes at the cost of much lower power efficiency.

Table 2.4 is a resume of the most relevant experimental demonstrations for a VLC single point communication system. The highest data rates are obtained with VCSEL because of their large 3 dB bandwidth but in scenarios not suited for illumination. The MIMO approach is another way to obtain very high data rates. High spectral efficiency modulation schemes such as OFDM or CAP are almost always used to attain higher speed communication links ( $> 1$  Gb/s). Another remark is that even the simplest equalization techniques (1-tap, zero forcing) extends the LED modulation bandwidth considerably.

TABLE 2.4: State of the art on the performances obtained by experimental demonstrations in indoor VLC.

Year	Data Rate, Bandwidth	Range (m)	MIMO	Emitter	Modulation	Note	Ref.
2019	1.25 Gb/s, /	1	No	Blue LD	OOK	/	[91]
2019	400 Mb/s, /	0.8	No	Red LED	PAM	K-means equalization	[92]
2019	2 Gb/s, 500 MHz	1.2	No	Ph-LED	CAP	Hardware pre-equalization and linear and non-linear post-equalization	[93]
2019	1.6 Gb/s, /	1	2x2	Blue LDs	OFDM	/	[94]
2019	200 Mb/s, 60 MHz	15	No	Red LED	CAP	Hybrid digital equalization	[95]
2019	15.73 Gb/s, 4 x 1 GHz	1.6	No	RGBY LEDs	DCO-OFDM	/	[60]
2019	40.665 Gb/s, /	2	No	RGB LDs, s- and p-polarization	OFDM	Pre- and post-equalization	[46]
2018	20.231 Gb/s, /	1	No	RGB LDs	OFDM	/	[96]
2018	3.2 Gb/s, /	0.01	No	Blue LD	OFDM	/	[97]

2018	1.26 Gb/s, 2 x 310 MHz	1	2x2	Red LED	<i>m</i> -CAP	Hardware pre-equalizer and LMS-Volterra based joint MIMO equalizer	[98]
2018	343 Mb/s, 75MHz	0.8	No	Blue LED	OFDM	Bit-interleaved polar-coded modulation (BIPCM) based on an orthogonal circulant matrix transform (OCT)	[99]
2018	262 Mb/s, /	5	No	Ph-LED	OOK	FPGA-based pre-distortion waveform shaping	[100]
2018	249 Mb/s, 4 x 20MHz	1	4x4	Ph-LED	<i>m</i> -CAP	Hardware pre-equalizer based on RC components	[101]
2018	1.5 Gb/s, 250MHz	0.2	No	Red LD	DCO-FBMC	Pre- and Post-equalization	[102]
2018	1.75 Gb/s, 3 x 250MHz	1	No	RGB LED	CAP	2-stage hardware pre-equalizer and post-equalization	[103]
2018	1.57 Gb/s, 300 MHz	2	No	RGB LED	DCO-OFDM	/	[104]
2018	51.6 Mb/s, /	0.0125	No	OLED	OFDM-OQAM	2-stage equalizer with a decision feedback equalizer (DFE)	[36]
2018	800 Mb/s, /	0.35	No	$\mu$ -LED	GSSK, 16 $\mu$ LEDs, 4 APD	/	[105]
2017	1.5 Gb/s, /	1	2x2	Green LDs	DCO-OFDM	Pre- and post-equalization	[106]
2017	172 Mb/s, 95 MHz	4	No	Red LED	DCO-OFDM	Hardware pre- and post-equalization	[107]

2017	5.95 Gb/s, 1.042 GHz	5	No	Blue LD	DCO-OFDM	Pre- and Post-equalization	[108]
2017	17.6 Gb/s, 4 GHz	16	No	Blue LD	UFMC additive, OFDM	/	[109]
2017	10.18 Gb/s, /	2	No	RGBY LDs	OOK	/	[110]
2017	1.25 Gb/s, 1 GHz	0.015	No	NUV-LD	OOK	/	[111]
2017	7.48 Gb/s, 9 x 50 MHz	0.5	9x9	$\mu$ -LED	PAM	Pre-equalizer and post-equalization based on decision feedback equalizer (DFE)	[112]
2017	6.36 Gb/s, 2 x 3 x 200 MHz	1	2x2	RGB LED	DCO-OFDM	/	[113]
2017	600 Mb/s, /	6	2x2	Red LED	OOK	Pre- and Post-equalization	[114]
2017	7.36 Gb/s, 1.81 GHz	0.016	No	$\mu$ -LED	DCO-OFDM	1-tap equalizer	[39]
2016	3.5 Gb/s, 800 MHz	0.05	No	$\mu$ -LED	PAM	Pre- and Post-equalization	[115]
2016	5.37 Gb/s, 800 MHz	0.05	No	$\mu$ -LED	DCO-OFDM	Pre- and Post-equalization	[115]
2016	2 Gb/s, / MHz	0.6	No	$\mu$ -LED	PAM	3-tap feed-forward pre-equalization	[116]
2016	2.08 Gb/s, 500 MHz	1	No	Ph-LED	DCO-OFDM	Power exponential pre-equalization and post-equalization	[117]
2016	150 Mb/s, 130 MHz	1	No	RC-LED	OOK	/	[118]

2016	11.1 Gb/s, 1.875 GHz	1.2	No	VCSEL	DCO-OFDM	1-tap post-equalization	[119]
2016	1 Gb/s, 2 x 125 MHz	0.6	2x2	Ph-LED	DCO-OFDM	Pre- and Post-equalization	[120]
2016	1.4 Gb/s, 3 x MHz	2.5	2x2	RGB LED	DCO-OFDM	Pre- and Post-equalization	[121]
2016	11.2 Gb/s, Red 1000 MHz, Green 625 MHz, Blue 1000MHz	1.5	No	Red RC-LED and blue and green $\mu$ -LEDs	DCO-OFDM	/	[42]
2016	2.32 Gb/s, 450 MHz	1	No	Ph-LED	DCO-OFDM	2-staged software equalizer	[32]
2015	9 Gb/s, 1.5 GHz	5	No	Blue LD	DCO-OFDM	/	[122]
2015	5.6 Gb/s, 4 x 500 MHz	1.5	No	RGBY LED	DCO-OFDM	/	[123]
2015	2 Gb/s, 600 MHz	1.5	No	Ph-LED	DCO-OFDM	Hardware pre-emphasis and post-equalization	[124]
2015	6.52 Gb/s, 1.43 MHz	0.35	No	Blue LD	DCO-OFDM	Pre- and Post-equalization	[125]
2015	8 Gb/s, 4 x 32 MHz	1	No	RGBY LED	CAP	Hybrid post-equalizer	[126]
2015	750 Mb/s, 150MHz	2	No	Red LED	DCO-OFDM	Hardware pre-emphasis and post-equalization	[127]
2015	4.5 Gb/s, 3 x 250 MHz	1.5	No	RGB LED	CAP	RLS adaptive equalization	[128]
2015	682 Mb/s, 143 MHz	1	No	Ph-LED	DCO-OFDM	Analog equalizers	[129]

2015	1 Gb/s, 4 x 125 MHz	1	4x9	$\mu$ -LED	PAM	/	[130]
2015	14 Gb/s, 3 x 1 GHz	0.3	No	RGB LEDs	DCO- OFDM	/	[45]
2015	4 Gb/s, 2.6 GHz	0.15	No	Blue LD	OOK	/	[43]
2015	54.9 Mb/s, /	0.05	No	RGB OLED	OOK	Hardware post- emphasis circuit and ANN based MLP	[37]
2015	31.53 Mb/s, 6.5 MHz	1	No	GaN- LED	<i>m</i> - CAP	/	[131]
2014	550 Mb/s, 233 MHz	0.6	No	Ph-LED	OOK	Pre-emphasis circuit and active hardware post- equalization	[132]
2014	340 Mb/s, 151 MHz	0.43	No	Ph-LED	OOK	Hardware post- equalization using RC components	[133]
2014	1.35 Gb/s, 3 x 87.5 MHz	0.3	No	RGB LED	<i>m</i> - CAP	Pre- and Post- equalization	[134]
2014	500 Mb/s, 2 x 125MHz	0.3	2x2	Blue LED	4- QAM	Zero-forcing (ZF), post- equalization	[135]
2014	10 Gb/s, 4 x 2.5 GHz	15	4x4	VCSEL	OFDM	/	[136]
2014	3 Gb/s, 625 MHz	0.05	No	$\mu$ -LED	DCO- OFDM	Pre- and Post- equalization	[137]
2014	/	1	No	RGB- LED	CSK	/	[51]
2013	575 Mb/s, 2 x 56.25 MHz	0.66	No	RGB- LED	OFDM	Pre- and Post- equalization	[138]
2013	500 Mb/s, 180 MHz	2	No	Ph-LED	DCO- OFDM	/	[139]
2013	3.22 Gb/s, /	0.25	No	RGB- LED	CAP	Decision feedback equalizer (DFE)	[58]

2013	1.5 Gb/s, 4 x 150 MHz	/	4x4	$\mu$ -LED	OOK	/	[140]
2013	1.1 Gb/s, 4 x 65MHz	1	4x9	Ph-LED	DCO- OFDM	Pre- and Post- equalization	[141]
2012	3.4 Gb/s, 750 MHz	0.3	No	RGB- LED	DMT	Zero-forcing (ZF)	[33]
2012	1.1 Gb/s, 280 MHz	0.23	No	Ph-LED	CAP	Decision feedback equalizer (DFE)	[142]
2012	1 Gb/s, 180 MHz	0.5	No	Ph-LED	DMT	Zero-forcing (ZF)	[143]
2012	750 kb/s, 170 kHz	0.03	No	OLED	/	ANN in con- junction with pre-distorted zero-forcing	[35]
2012	200 kb/s, 2 MHz	2.5	No	RGB- LED	VPPM	/	[67]
2012	10 Mb/s,	1	No	Ph-LED	PAM	/	[144]

A number of observations can be made from these numerous cited works:

- The first observation is that the most used modulation scheme is OFDM; used by around 45% of the systems. The main reason is that in 80% of the cases, a data rate of more than 1 Gb/s was attained. Recently, the trend is to use OFDM directly, without justification. Comparatively, CAP and *m*-CAP can attain similar spectral efficiency as OFDM [145] but are 6 to 7 times less likely to be considered.
- Another observation is the predominance of lasers for very high speeds, with 37% of the works attaining more than a Gb/s using them because of their large available modulation bandwidth. Otherwise, multi-colored LEDs are used in 33% of the cases because of their ability to produce multiple channels of communications.
- Only a 20% of the works have a system range greater than 1 meter. While the objectives of these papers is focused other results, it still shows an overall lack of realism in the experimental setups provided. As a matter of fact, when not using a laser, only 9% of systems have a range superior to 2 m.
- The majority of the works used pre- and/or post- equalization schemes in order to increase the performances. Various implementations can be found, from

the simple RC-based hardware equalizer to the ANN-based multi-stages post-equalization schemes. The highest spectral efficiencies are almost always tied with the use of a complex post-process block.

These observations will be used in part 2.3 of this chapter in order to explain our design approach.

## 2.2.4 Multi-Access Schemes

### 2.2.4.1 Orthogonal Multi-Access Schemes

Orthogonal multiple access (OMA) schemes refer to the conventional multi-users allocation techniques where a resource is divided between users. Typically, these resources are frequency, time and space. OMA is an older area that is used in 4G or earlier networks to provide a multi-users capability to a modulation. 2G cellular systems supported techniques such as time division multiple access (TDMA) or frequency division multiple access (FDMA) [146]. Then, 3G systems adopted techniques such as code division multiple access (CDMA) [146]. In 4G systems, orthogonal division multiple access (OFDMA) is more typically used [146]. The schemes often used in VLC systems are described below:

- **Time Division Multiple Access (TDMA):** TDMA is a widely used access scheme due to its simplicity of implementation. Users are assigned a time slot at any given time and information is transmitted on these slots [147]. The orthogonal assignation of the slots ensures that the interferences are removed in case of an overlapping coverage area. However, the efficiency of the allocation is limited since only one user is served at any given time, and synchronization is difficult in VLC systems [148].
- **Frequency Division Multiple Access (FDMA):** FDMA is, similarly to TDMA, a widely used technique because of its low cost of implementation. The signal bandwidth is cut into parts that are dynamically attributed to each user [147]. Every receiver will be served by one or more frequency band. It can sometimes be called subcarrier multiplexing (SCM).
- **Code Division Multiple Access (CDMA):** CDMA in the optical realm relies on orthogonal codes to provide access to the same channel for multiple users [147]. The principle was the basis of a lot of schemes used in fiber optics [149]. Each user is assigned orthogonal spreading codes which are basically binary sequences. Typically, in VLC, they are one dimensional codes such as Gold sequences, optical orthogonal codes (OOC), and prime codes but can also be two-dimensional codes with a spreading in both time and wavelength [150][151]. Data rates at high number of users are generally limited because of the difficulty in maintaining orthogonality in VLC channels.

- **Orthogonal Frequency Division Multiple Access (OFDMA):** OFDMA is based on OFDM and is a multi-carrier multiple access scheme [152]. Each user is assigned a different set of subcarriers for communication [153], similarly to FDMA or SCM. It is a natural extension to utilizing OFDM for modulation in the physical layer. Data rate per receiver are obviously limited with the number of users.
- **Space Division Multiple Access (SDMA):** In general, in SDMA, multiple narrow beams are generated by an array of transmitters according to the positions of the active users [154]. When adapted to VLC, directional light beams are generated with narrow FoV LEDs. Optical SDMA thus consists in an angle diversity transmitter which generates directional beams of light towards narrow FoV receivers to reduce path loss and inter-user interferences [155][156]. In VLC, it makes SDMA a scheme that is very difficult to implement [157].
- **Wavelength Division Multiple Access (WDMA):** In WDMA, users are transmitted data using a specific wavelength [42]. In VLC, it means that multi-chip LEDs using multi-colors are used to transmit data to the receivers. While WDMA shares the problem of high complexity with SDMA, it is also difficult to find LEDs for VLC that can allow for more than 3 or 4 available wavelengths [157].

#### 2.2.4.2 Non-Orthogonal Multi-Access Schemes

Non-orthogonal multiple access (NOMA) was proposed as a promising candidate scheme in RF for 5G and beyond wireless communications [158]. Different from the conventional orthogonal multiple access technologies discussed in the previous subsection, NOMA allow the allocation of users via non-orthogonal resource allocation. It means that multiple users can be served in the same time, frequency and space dimensions. Advantages over OMA schemes include an improved spectral efficiency, better user fairness, higher capacity and lower latency while the disadvantages include an increase in implementation cost and inter-user interferences [159]. There are various multiplexing schemes for NOMA, separated under three groups: power domain NOMA (PD-NOMA), code domain NOMA (CD-NOMA) and multiple domain NOMA. The schemes are presented in the following list:

- **Power Domain NOMA (PD-NOMA):** PD-NOMA is the more widely adopted one and is the scheme where data from different users is multiplexed in the power domain. Successive interference cancellation (SIC) is used at the receiver to cancel inter-user interferences [160]. The channel gain difference in-between receiver is also exploited to successfully separate the multiplexed user signals. Indeed, in a 2-user scenario, a user further away from the access point will be allocated more power than a second user closer to it. At the far user, the signal from the close user, which has been allocated less power, is considered as noise

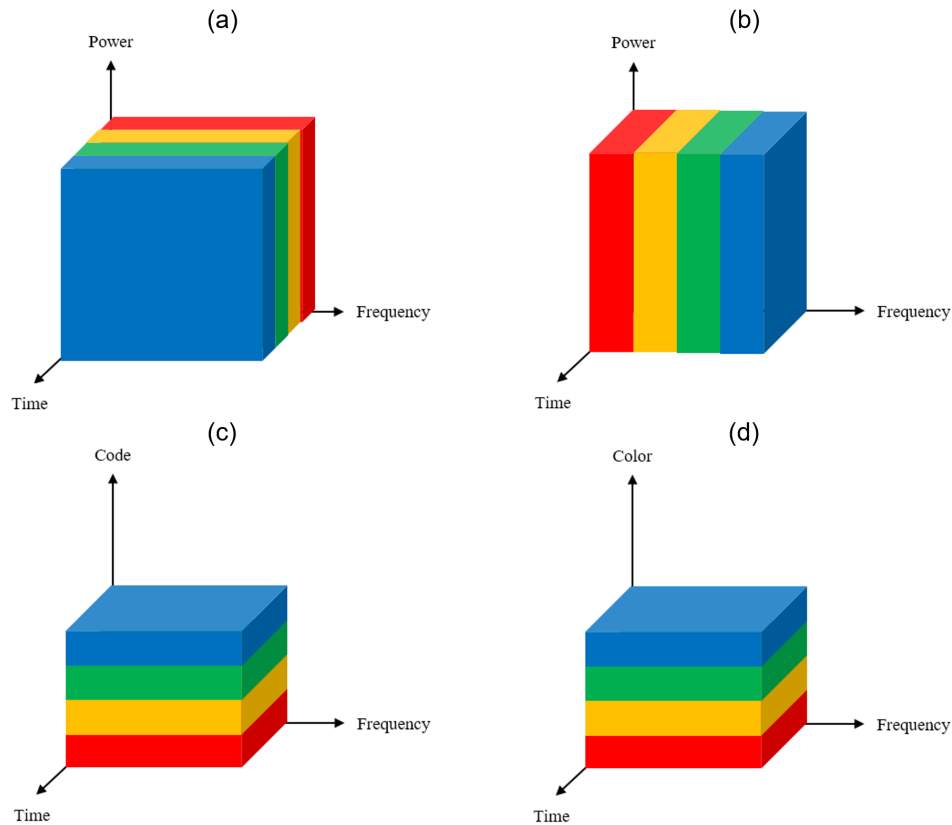


FIGURE 2.19: Illustration of the base principle in terms of user resource allocation for (a) TDMA, (b) FDMA, (c) CDMA and (d) WDMA. The users are represented by different colors.

and the receiving waveform is directly decoded, without SIC [161]. At the close user, the signal from the far user, which has been allocated more power, benefit from a high SNR and the receiver will thus have an easier time decoding and removing it from the received signal before decoding its own. Additionally, user-grouping can be used in order to have a close user group and a far user group for lower implementation cost [162] by reducing the need for the costly SIC method. This user-clustering technique can be used in a NOMA schemes to reduce the disadvantage of increased complexity over OMA techniques.

- **Code Domain NOMA (CD-NOMA):** CD-NOMA includes multiple solutions where each user is assigned to a different code with the objective of sharing multiple transmission channels within the same frequency and time resource [163]. Low-density signature for synchronous CDMA (LDS-CDMA), low-density signature for OFDM (LDS-OFDM), sparse code multiple access (SCMA), multi-users shared access (MUSA), and successive interference cancellation amenable multiple access (SAMA) have all been proposed respectively by [164][165][166][167] and [168].
- **Multiple domain multiplexing NOMA:** This area of NOMA is proposed when multiple different NOMA domains are shared at the same time, namely

power domain with code domain and/or space domain. Pattern division multiple access (PDMA), (BOMA), and lattice partition multiple access (LPMA) have been proposed respectively by [169][170] and [171].

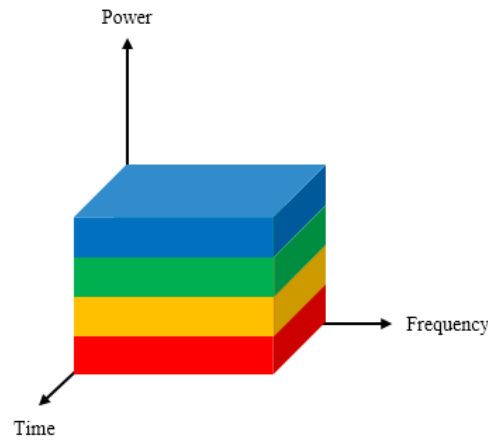


FIGURE 2.20: Illustration of the base principle in terms of user allocation resource for PD-NOMA where the users are assigned to a power level and represented by different colors.

### 2.2.4.3 Multi-Users MIMO

Multi-users MIMO (MU-MIMO) is an advanced MIMO technique that have gained interest over the last ten years. MU-MIMO allows the sharing of the total throughput of a MIMO system and the emission of data to 2 or more users. MU-MIMO is already used in the LTE-Advanced standard, or 4G [172]. As an example, in RF, 4 antennas could be used at the transmitter and 2 antennas per user at the receivers. The multiplexing is performed in the spatial domain and grants an increase in cellular spectral efficiency without the need of a large number of antennas in each receiver. In VLC, the multiple LEDs at the transmitter can be coordinated to transmit data to different users. The inter-user interferences are mitigated with zero-forcing (ZF) precoding [173]. Precoding can thus reduce the receiver computational complexity and power consumption as these are two of the more important drawbacks for MU-MIMO systems [174][175] compared to the schemes described in the two previous subsections.

### 2.2.4.4 Comparison When Applied to VLC Systems

A qualitative comparison of the multi-users access schemes is shown in table 2.5. The first metric used is the spectral efficiency per user, which indicates which throughput a user can attain in function of the signal bandwidth for any given multi-users access scheme. The second important metric for a multi-receiver VLC system is the flexibility which corresponds to the ability of a scheme to compensate for a varying channel state. This is especially key in wireless optical communications since receivers experience large swings in channel attenuation depending on their position and incident angle in regard to the access point. Complexity is a third essential metric indicating

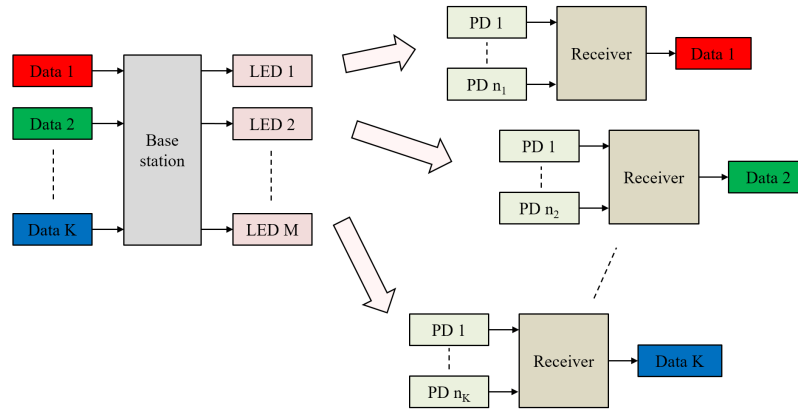


FIGURE 2.21: Illustration of the principle of MU-MIMO, where, in this example, each user uses multiple channels thanks to multiple PDs and the transmitter uses multiple LEDs.

the cost of implementation for any of the multi-users access technique. Finally, the maximum number of users is compared as the fourth metric. The most widely used schemes in VLC have been compared, leaving out TDMA, CD-NOMA and multiple domain multiplexing NOMA. Since OFDMA is comparable to FDMA/SCM it also has been omitted.

TABLE 2.5: Qualitative comparison of the multi-users access schemes in VLC.

	Spectral efficiency	Flexibility	Complexity	Maximum number of users
FDMA/SCM	Low	Moderate	Low	High
CDMA	Moderate	Moderate	Moderate	Moderate
SDMA	High	High	High	Moderate
WDMA	High	Moderate	High	Low
PD-NOMA	High	High	High	Low
MU-MIMO	High	High	High	High

Table 2.6 is a resume of the most relevant experimental demonstrations for a multi-users indoor VLC system. The first observation is the fact that all displayed results used multi-carriers, high spectral efficiency modulations such as multiband CAP or OFDM. A varied range of number of users and throughput per user is attained, as well as a number of multi-access scheme explored. The range does not exceed 1.5 meters.

The first observation is that the number of such experiments in the literature is very small. The focus of most research on multi-users access schemes is indeed to decrease the amount of inter-user and inter-cell interferences using numerical simulations. The two types of works are complementary as one details the performances of individual access points while the others show the architecture of a VLC network. This complementarity is limited because of the lack of practical multi-access VLC cells demonstration.

Other trends in the works summarized are difficult to identify because of the low amount of references. The number of user's independent channels is generally limited

TABLE 2.6: Summary of state-of-the-art on multi-users access experimental setups in VLC.

Year	Data rate per user	Max. number of users	Range (m)	Emitter	Modulation	MUA scheme	Ref
2019	5 Mbaud	2	0.7	Ph-LED	OFDM	PD-NOMA	[176]
2019	250 Mbaud	32	1.5	Red LED	/	CDMA	[177]
2019	1.7 Mbaud	2	0.75	Ph-LED	OFDM	Optical PD-NOMA	[178]
2018	22.5 Mb/s	2	1	Ph-LED	OFDM	PD-NOMA	[179]
2018	19.41 Mb/s	6	0.1	Ph-LED	OFDM	Polarity Division Sparse Code NOMA	[180]
2018	1.6 Gb/s	2	1	Blue LDs	OFDM	MU-MIMO + PD-NOMA	[181]
2017	1.7 Mbaud	2	0.3	Ph-LED	OFDM	PD-NOMA	[182]
2017	64 Mb/s	5	/	Red LED	<i>m</i> -CAP	SCM	[183]
2016	3.73 Gb/s	3	1.5	Red RC LED and Green and Blue $\mu$ LED	OFDM	WDMA	[42]
2015	15 Mb/s	/	0.05	Ph-LED	OFDM	OFDMA	[184]
2015	47 Mb/s	16	1.5	Red LED	OFDM	MC-CDMA	[185]
2014	150 Mb/s	9	0.3	RGB LED	<i>m</i> -CAP	SCM + WDMA	[134]
2013	143.75 Mb/s	4	0.66	RGB LED	OFDM	SCM + WDMA	[138]

to 2 and very rarely surpass 10 except when CDMA is used. This is mainly because the single experimental receiver is considered for all users in both [185] and [177]. This removes the fact that the orthogonality between each code is reduced when the distance from the receiver increases in CDMA. Both experiments are unrealistic in the sense that all user cannot be at the same place at the same time. Then, range is also limited to below 1.5 meters in most cases, making most systems far from realistic. OFDM is often the modulation of choice and various types of emitters and MUA schemes are used. A final trend to note is that MU-MIMO and SDMA are not yet used experimentally and limited to numerical simulations such as in [186], [187], or [188]. Indeed, the VLC transmitters for these MUA schemes are complicated to implement. These observations will be used in part 2.3 of this chapter in order to explain our design approach.

## 2.2.5 Performance Enhancement in VLC

Visible light communications have numerous advantages over other methods that can lead to an interesting complementary technique for 5G and beyond. However, numerous challenges have to be addressed in order to realize its potential.

### 2.2.5.1 Bandwidth Exploitation Efficiency

The major limitation on the performances of VLC systems is on the limited bandwidth of most types of LEDs, as seen in subsection 2.2.1.2. Ph-LED only have 3 dB modulation bandwidth of a few MHz while single color LED only around 10 to 20 MHz [189]. While  $\mu$ -LED, rc-LED or laser diodes provide much higher bandwidth, they come at the added cost of complexity and difficulty to obtain them. Ph-LED have the lowest cost and are the easiest to obtain, explaining their prevalence in the experimental demonstration summarized previously. In order to overcome the bandwidth limitation of LEDs in general, numerous methods can be used:

**2.2.5.1.1 Blue filtering:** Ph-LED use a slow phosphor coating with a faster blue chip in order to produce white light. It is why its modulation bandwidth is around a few MHz instead of more than 10s of MHz [190]. At higher modulation frequencies, the phosphorous part is too slow to react to the signal driving the LED, generating a constant light that the PD convert into noise. Using a blue optical filter at the receiver, the modulation bandwidth of the LED to PD link is not limited by the slow yellow light but by the faster blue one [191]. As an example in VLC, in [143], a blue optical filter is used to extend the usable modulation bandwidth of a ph-LED and enable a 1 Gb/s transmission using discrete multi-tone modulation.

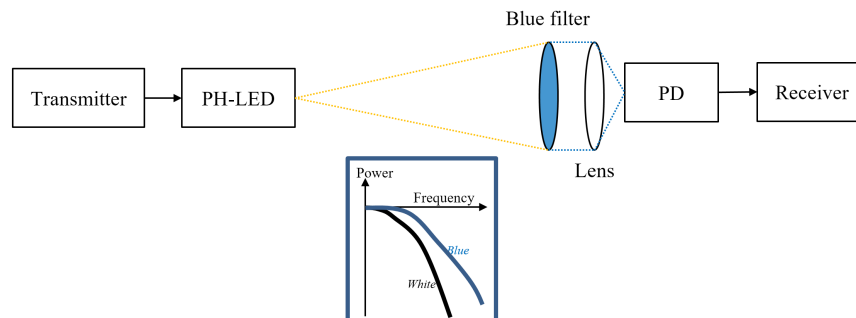


FIGURE 2.22: Illustration of the principle of blue filtering in VLC.

**2.2.5.1.2 Modulation beyond the 3dB bandwidth:** Modulation of the transmitter beyond its 3 dB bandwidth corresponds to a simple version of the techniques linked to equalization at the transmitter, presented in the following subsection. In essence, the aim is to enhance the responsiveness of the LED in order to improve the modulation bandwidth beyond the -3 dB mark. The method used is to shape the current driving the emitter. This technique comes from fiber optics communication where the rise and fall times of LED are reduced with pulse shaping. As an example

in VLC, in [100], current shaping is used to enable a real-time 262 Mb/s VLC system, reducing the rise and fall times from 28 ns to 12 ns on a ph-LED.

**2.2.5.1.3 Bit and power loading, or subcarrier equalization:** Multi-carrier modulations use multiple subcarriers in order to transmit data. Each subband can use a different modulation order and power level. For example, in a conventional OFDM scheme in VLC, a first aspect is that each subcarrier is associated to an  $M$ -QAM constellation with  $M$  calculated with the number of bits per symbols. A second aspect, as will be seen in the following subsection, equalization at the transmitter, or pre-equalization, aims at shaping the signal before transmission in order to adapt it to the channel state. With subcarriers, each one can be adapted using the same principle. These two aspects are known as bit and power loading respectively. As an example in VLC, in [192] as well as most OFDM-based VLC setups described in table 2.4, bit and power loading was used in order to maximize the transmission rate and enable a 1.25 Gb/s VLC system.

## 2.2.5.2 Channel Estimation and Equalization

Another aspect of bandwidth enhancement is channel estimation and equalization. Equalizers aim at reversing the distortions induced by the channel by focusing on flattening the frequency response. Channel estimation is used in VLC systems as a support for synchronization and equalization [193].

**2.2.5.2.1 Channel estimation:** Channel estimation, as the name suggests, intends on estimating the channel state in either the frequency or time domains. This is used for both synchronization and equalization. Three types of techniques exist. The first one is channel estimation based on a training sequence, or pilots, added at the transmitter to the signal and known at the receiver in order to estimate the channel. The second type of technique is a blind estimation where the statistical and structural aspects of the signals. The third type of technique is a hybrid of the two first types where both the properties of the signal and pilots are used to estimate the channel. As an example in VLC, in [194], an adaptive statistical Bayesian minimum mean square error channel estimation (AS-BMMSE-CE) method was presented specifically for indoor VLC systems, using previous channel state information to optimize the performances. This technique would correspond to the first type of channel estimation type.

**2.2.5.2.2 Pre-equalization:** Pre-equalization, or sometimes called transmitter equalization, aims at increasing the usable modulation bandwidth of the emitter. The main principle is to increase the magnitude at higher frequencies while reducing the lower frequencies, which counteract the low-pass effect of the optical wireless channel with LEDs. The implementation of the filters used for pre-equalization can be in hardware or in software. As an example in VLC, in [195], a hardware pre-equalizer

is used and the red LED, which have a -3dB bandwidth of 20 MHz, can then allow a transmission of 1.42 Gb/s instead of 1.13 Gb/s without it.

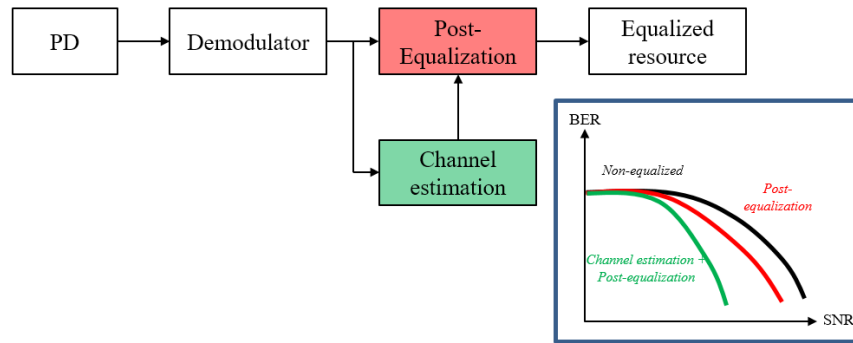


FIGURE 2.23: Figure showing the principle of equalization and channel estimation at the receiver for a VLC system.

**2.2.5.2.3 Post-equalization:** Post-equalization, or sometimes called receiver equalization, aims at minimizing the errors for a better BER. Numerous types of implementations can be found in the literature, attaining that goal in different ways. Linear equalizers use a filter on the received signal either minimizing the error signal with MMSE equalizers or approximating the inverse of the channel with zero-forcing equalizers. Another type is decision feedback equalizer (DFE) that includes a linear equalizer but adds the previous filtered symbol to the process. Adaptive equalizers typically combine one of the numerous linear equalizer type with a DFE, updating the parameters with a feedback loop. Numerous other types of post-equalization process can be found such as Viterbi-based equalizers or even ANN-based equalizers. As a side note, post-equalization can be combined with pre-equalization for better results. As an example in VLC, in [134], a post-equalizer based on a modified cascaded multi-modulus-algorithm (CMMA) is used along with the multiband CAP modulation in order to reduce the inter-symbol interferences due to timing offsets. A RGB LED is used to attain 1.35 Gb/s over 30 cm. The BER performances of the modified CMMA are shown to improve as compared to conventional CMMA. Many other types of post-equalizers have been used to attain very large gains in data rates and can be found in the state-of-the-art presented in table 2.4.

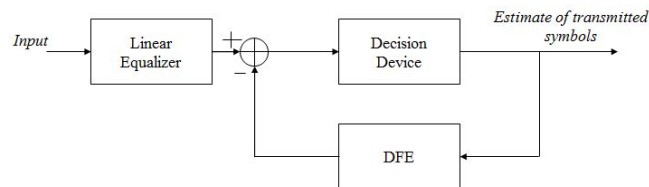


FIGURE 2.24: Schematic of principle for an adaptive equalization technique.

### 2.2.5.3 Non-linearity Compensations

Every LED has different intensity to voltage (IV) characteristics that need to be taken into account. The driving modulated signal is usually set to use as much of the linear range of the IV curve. The larger the magnitude of the driving voltage, the larger the optical power and hence the higher the performances. With both the optimal operating point and maximized LED dynamic range [196], the VLC system performances can be enhanced. In consequence, non-linearity need to be taken into considerations at the turn on voltage and at the saturation current [197]. As a result, many methods are used to counteract the adverse effects of non-linearity using signal clipping [198], power reduction [199], pre-distortion or post-distortion [200][201].

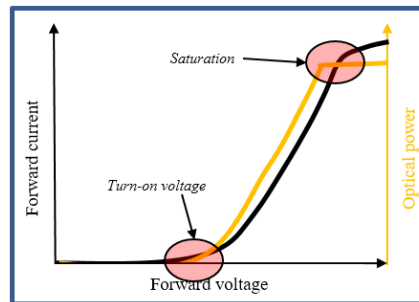


FIGURE 2.25: Example of an IV characteristic for a referenced LED with a representation of the turn-on voltage and the optical signal saturation with an example of optical power characteristic.

## 2.3 Design Approach

This part is an overview of the design approach of this work. The choices made are explained and justified. The approach is also compared to existing works. Section 2.3.1 begins with the structure of the indoor VLC system in a single-user broadcast way. The transceiver structure design is presented and justified and the modulation scheme choice is analyzed. Then, section 2.3.2 explains the approach taken for the study of the multi-users access schemes when applied to the indoor VLC system. Finally, the approach is compared with existing work in the literature.

### 2.3.1 Communication Broadcast Structure

#### 2.3.1.1 Transmitter and Receiver Structures

The transmitter structure is composed of a digital signal processing block to generate the modulated signal, a LED driver and the LED itself. Real-time implementation is not studied in this work then the choice of LED has the most impact on the performances.

The main focus of the design is chosen to be the realism of the experiment and is tied with the final objective which is to conceive an experimental indoor multi-users VLC system. As seen in the state-of-the-art summarized in table 2.6, all works fall

behind 1.5 m range in an indoor scenario while the average distance of ceiling to desk is 2.15 m in real life. The second limitation comes in the very heavy and restrictive post-equalizations and performances enhancement methods used throughout all high spectral efficiency results in tables 2.4 and 2.6. In a multi-users scenario, the condition throughout a VLC cell change drastically. An important element is thus the flexibility of the scheme. Indeed, the more flexible the technique is, the easier it will be to respond to a sudden change in conditions. In consequence, this work aims to be both lower complexity by not using heavy post-processing and higher flexibility by offering enhancement techniques with flexibility and low implementation cost.

An off-the-shelf ph-LED is used as the transmitter. It is typically found in museums, hospitals or offices and is a white down-light able to provide sufficient illumination throughout an indoor room from the ceiling. It adds to the realism and low friction aspect of the design illustrated figure 2.26. However, one main limitation that have been discussed is the lower usable bandwidth. In order to attain high speed data rates ( $>100\text{Mb/s}$ ) with this type of slower LEDs, two paths are simultaneously explored. The first is the extension of the 3 dB bandwidth with equalization. The second is the optimization of the bandwidth usage with the exploration of a high spectral efficiency modulation scheme. Ultimately, the raw throughput will not be comparable to some of the work presented in table 2.4 but the spectral efficiency will be. The use of an emitter with a larger modulation bandwidth such as an RC-LED would potentially provide throughout in the gigabit range.

The receiver structure is composed of a photodiode-based receiver and a digital signal processing block to decode the received signal. As real-time implementation is not studied in this work, the latter part is processed off-line with a PC. The choice in the receiver structure comes to the photodiode. APDs offer a greater level of sensitivity over PIN PDs because of the avalanche effect. On the other hand, it produces a higher level of noise because of that same effect being non-linear. While they are other differences, they do not impact the performances as much as this characteristic. Ultimately, we ended up using a PIN PD as it is not an essential element in the investigations performed throughout this work.

### 2.3.1.2 Modulation Scheme

The main limitation to attain high speed data rates ( $>100\text{ Mb/s}$ ) with a VLC system is the LED limited usable bandwidth. Pre- and post- equalization can be applied to extend it. But, as observed in Table 2.4, high spectral efficiency modulations are the main responsible for the majority of high speed throughput results in the literature thanks to their ability to optimize the bandwidth use.

Table 2.2 summarized a qualitative comparison of most of the modulation schemes used in VLC experimental setups. When narrowing down the choice to high spectral efficiency techniques, CAP,  $m$ -CAP, GSSK and OFDM and its variants are the

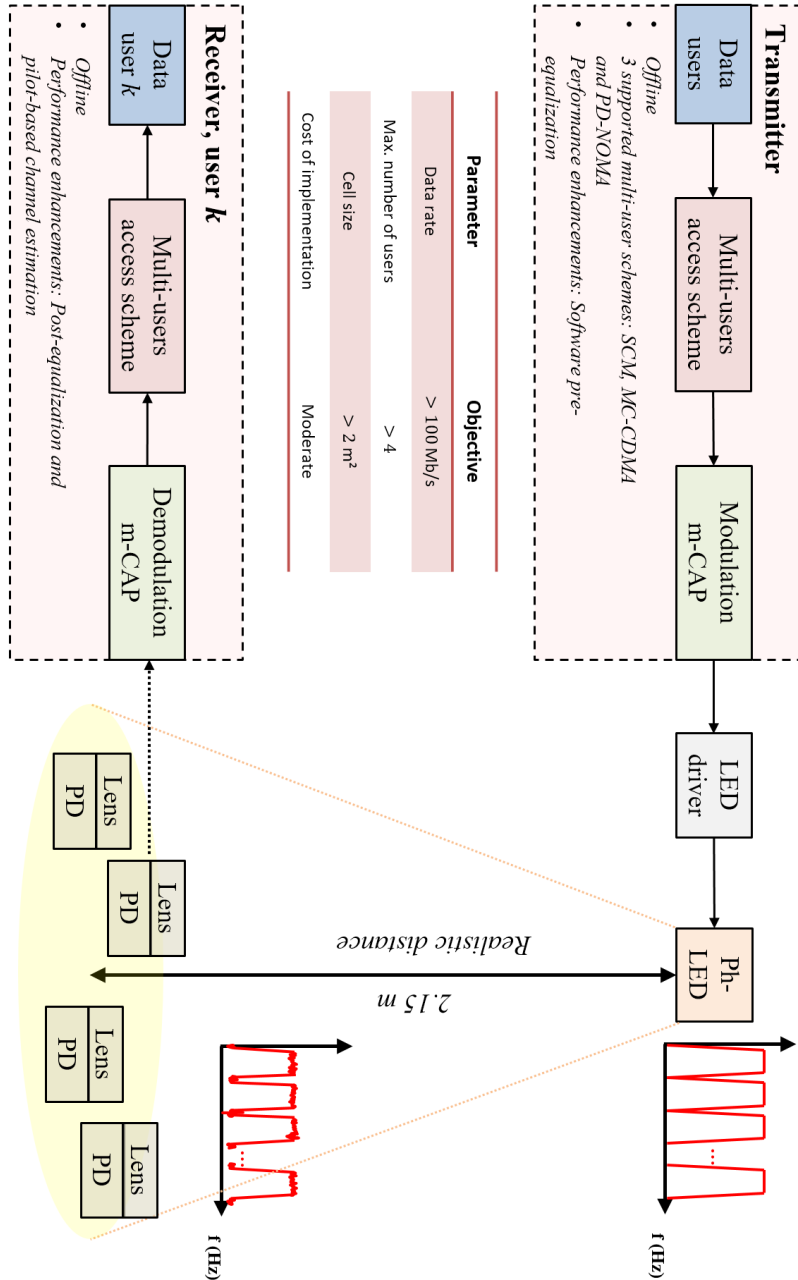


FIGURE 2.26: Structure of the multi-users indoor VLC system analyzed in this work with a table summarizing the objectives set for the experimental setup.

remaining ones. Multiband CAP and CAP can be counted as one scheme as conventional CAP is just 1-CAP. As flexibility is a main focus in the multi-users scenario, the fact that OFDM and  $m$ -CAP are multi-carrier modulation schemes favors them. Both remaining choices are based on quadrature and amplitude modulation (QAM) with OFDM using Fast Fourier Transforms (FFT) in the modulation process and  $m$ -CAP/CAP using pairs of orthogonal pulse shaping filters instead. Spectral efficiency on both schemes can attain the same range [145] and CAP has been shown to provide better peak-to-average power ratio (PAPR), even when combined with other schemes [202]. Alternatives for OFDM exist in order to reduce this characteristic [203] but

CAP directly provides better power efficiency. The fact that the orientation of our work is on easier installation and lower implementation cost favors  $m$ -CAP because it does not use FFT. In consequence, this work focuses on the exploration of multi-band CAP for the indoor multi-users VLC system. Additionally, one motivation for this choice is the fact that OFDM has already been explored profoundly when applied to VLC and  $m$ -CAP is relatively new in comparison with very few works.

### 2.3.2 Multi-Users Access Techniques

Adding a multi-users access scheme to the experimental indoor VLC system involves a choice between the available techniques that were compared qualitatively in table 2.5. Using a single ph-LED rules out WDMA since no multi-color LED is used. Both MU-MIMO and SDMA are also unusable since only one transmitter is used. The choice of multi-users access techniques in this work is then narrowed down to FDMA, CDMA, and PD-NOMA.

FDMA/SCM is the multi-users access scheme with the lowest implementation cost and a high possible amount of user channels but its spectral efficiency is limited since the bandwidth is physically shared. CDMA offers average characteristics across the board and does not stand out in any metric. PD-NOMA is one of the promising technology for 5G and beyond and its application in VLC has advantages in spectral efficiency, flexibility and maximum amount of users over the other options. However, as seen in table 2.6, the amount of experimental implementations for multi-users VLC systems is limited and the amount of conclusions that can be taken is limited. As a result, we believe that a comparison of the impact of each of the three schemes in the experimentation demonstration is a valuable contribution and would help in identifying the advantages using the same modulation scheme.

### 2.3.3 Placing our Approach

In this work, the  $m$ -CAP modulation is associated with multiple multi-access schemes for experimental demonstrations of indoor multi-users VLC systems with the objective of improving the flexibility of the design for better attocell performances. The demonstration uses a realistic indoor scenario with low complexity post processing for multiple users. The approach taken by this work can be illustrated with multiple graphs shown in the following figures.

Figure 2.27 shows the objective in spectral efficiency against the complexity level this work aims at in a comparison with available state of the art. The complexity of an experimental VLC system is defined as the sum of the level of complexity on each part of the transmission chain. Table 2.7 details the level of complexity for each part of a typical system. The references that were retained contain a VLC indoor experimental demonstration using an LED. Laser-based systems were included when relevant for the comparison. The redundant references were removed when the same setup is reused through multiple papers from the same authors, keeping the most relevant

results. This figure is subjective and its interpretation remains at the discretion of every reader. However, it depicts a distinct vision of our approach relating the cost of implementation of the scheme.

TABLE 2.7: Definition of the estimated level of complexity for a VLC experimental setup.

Transceiver block	Technology	Estimation of the level of complexity
<b>Modulation and Demodulation</b>	OOK, PAM or similar	+0
	CAP, GSSK	+2
	Multiband CAP, OFDM, FBMC	+3
	DFT-S OFDM	+4
<b>Pre-equalization</b>	None	+0
	Present	+2
<b>Post-equalization</b>	None	+0
	1-stage	+2
	Multi-stage, machine-learning	+3
<b>Emitter technology</b>	Single LED	+0
	LED Matrix	+2
	MIMO	+3

The figure 2.27 depicts a clear vision of the first part of our approach with this work. Indeed, the system uses an off-the-shelf ph-LED as well as low-complexity performance enhancements techniques, which will be described in chapters 3 and 4. Works with similar characteristics all used lasers as the emitters, such as in [108], [119] or [122]. The spectral efficiency improvements are attained using a technique similar to bit and power loading but on the filter parameters of the multiband CAP modulation scheme. The main contribution along with this previous one is the use of subcarrier spacing to answer the need for spectral efficiency and flexibility in multi-users scenarios. This work thus presents, to the best of our knowledge, one of the highest spectral efficiencies for a phosphorous white LED.

Figure 2.28 shows the objective in system range against the spectral efficiency this work aims at in a comparison with the available state of the art. The goal is to demonstrate that the conditions of the experimental setup was chosen to be as realistic as possible. Indeed, as a multi-users VLC system, the range needs to be at least around the average distance from ceiling to desk. Additionally, this translates into a serviceable area at the receiver plane that is much larger than the shorter range systems.

This figure adds to the vision of the first part of our approach, on the single-user broadcast performances of the indoor VLC system. As show, most works use ranges under a meter. The main reason is the fact that they often focus on demonstrating something other than range and thus do not focus on this parameter. Nonetheless, in the context of the realism of our experimental setup, our approach aims at a range of

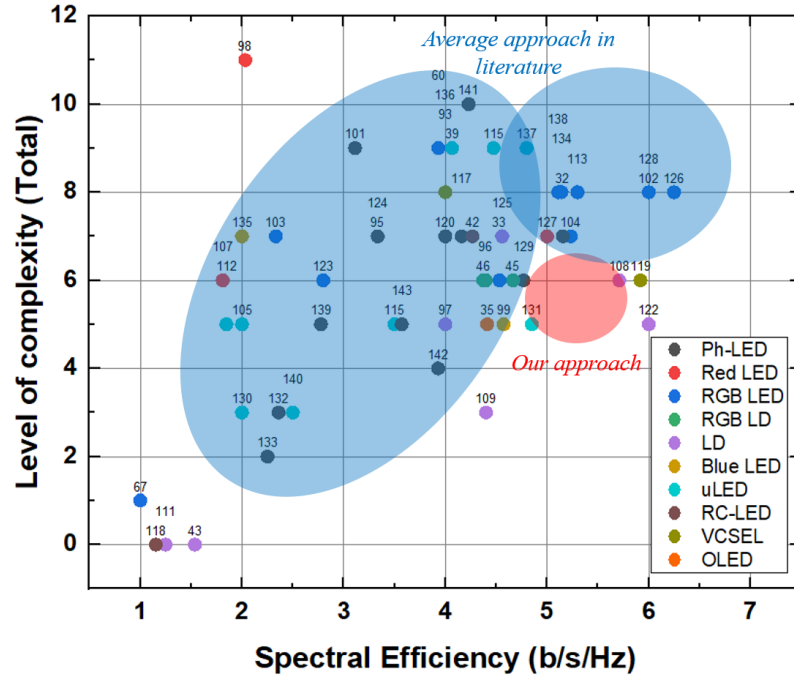


FIGURE 2.27: : Illustration of the approach taken by this work in terms of cost of implementation. The graph is an estimation of the level of complexity of the VLC experimental setup versus the spectral efficiency. The blue area is the most explored, where the spectral efficiency is between 2 and 7 b/s/Hz and the estimated complexity is higher than 6. The red area is the objective aimed by our work, with a spectral efficiency around 5 and an estimated complexity around 6. References [122], [119] and [108] are laser based experiments used as a comparison. Reference [131] is a micro-LED-based experimental with a spectral efficiency below 5 b/s/Hz.

more than 2 m along with the high spectral efficiency of around 5 b/s/Hz. This needs to be contrasted with the fact that our LED will be more powerful than what most works use below 2 m of range, as we will see in chapter 4. In the same way as with the previous figure, laser-based systems often exceed this goal. In terms of contribution, this appends the fact that this is the ph-LED-based setup with the highest range, to the best of our knowledge, to the previous contribution.

Figure 2.29 shows the objective on the maximum number of users against the range in a comparison with the available state of the art. This maximum number of users is shown as a metric that can give an idea of the flexibility of the system. For example, if a system can only serve a maximum of 4 users in a 4-users scenario, chances are it is less flexible than one that can allocate a larger number of receivers. Indeed, it will have more available independent channels per users.

The first observation that can be made with this figure is the very low amount of work implementing an indoor multi-users VLC system. In this condition, the amount of accuracy to presenting our approach in a comparison is very limited. Here, in this figure, the aim of our approach is shown to offer a high number of independent

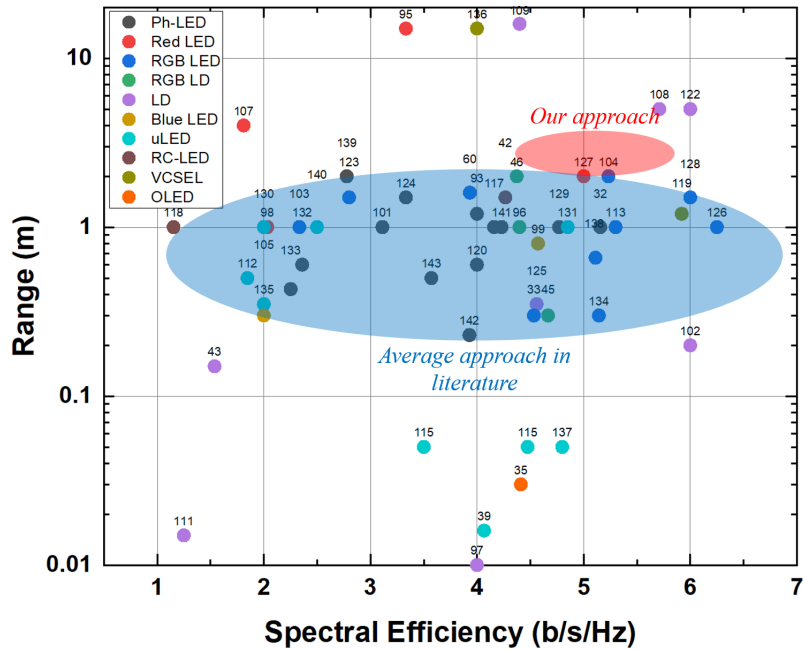


FIGURE 2.28: Illustration of the approach taken by this work in terms of system range. The graph is the range of the VLC experimental setup versus the spectral efficiency. The blue area is the most explored, where the spectral efficiency is between 3 and 7 b/s/Hz and the range is around 1 m. The red area is the objective aimed by our work, with a spectral efficiency around 5 b/s/Hz and a range above 2 m.

channels at a range beyond 2 m. The first part is synonymous with the increased system flexibility that we want to attain with our work. The second part is to add to the realism of the experiment, as explain with the previous figure. The contribution in this regard is the fact that this is, to the best of our knowledge, the multi-users indoor VLC system with the most range and one of the highest maximum number of users. However, this does not give a more complete overview of our approach because of the limited comparison. In consequence, the contribution also contains a first-time comparison of the performances of SCM, MC-CDMA and PD-NOMA as multi-users access schemes in VLC. In addition, attocell characteristics such as the experimentally measured attocell size as well as the deviation from a user data rate target are analyzed for the first time in a VLC system, to the best of our knowledge.

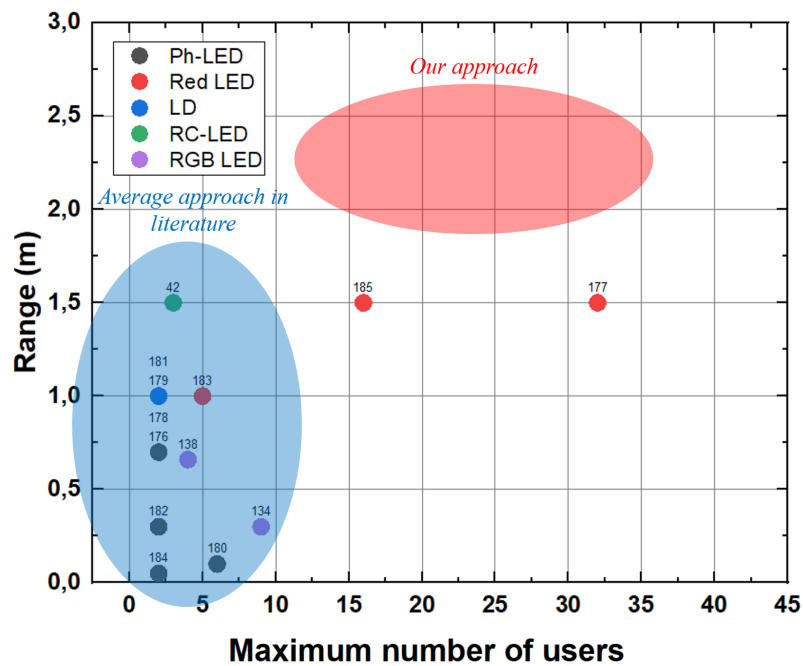


FIGURE 2.29: Illustration of the approach taken by this work in terms of maximum number of users and range. The graph is the range of the multi-users VLC experimental setup versus the maximum number of users. The blue area is the most explored, where the maximum number of users ranges from 2 to 8 users and the range is below 1.5 m. The red area is the objective aimed by our work, with a maximum number of users greater than 10 and a range above 2 m.

## Chapter 3

# Principles of an Indoor Multi-Users Visible Light Communication system

### Contents

---

<b>3.1 Introduction to the Multi-Users Multiband CAP VLC System . . . . .</b>	<b>59</b>
3.1.1 Carrierless Amplitude and Phase Modulation . . . . .	60
3.1.2 Multi-Band Carrierless Amplitude and Phase Modulation . . . . .	62
3.1.3 Natural Association with Subcarrier Multiplexing . . . . .	65
3.1.4 Association with Other Schemes . . . . .	69
3.1.5 Refining Our Approach . . . . .	75
<b>3.2 Broadcast Channel Performances Breakdown . . . . .</b>	<b>77</b>
3.2.1 Block Diagram . . . . .	78
3.2.2 Modulation and Performances . . . . .	80
3.2.3 Performances Enhancements . . . . .	84
<b>3.3 Application with Multi-Access Schemes . . . . .</b>	<b>94</b>
3.3.1 The Definition of an Attocell in VLC . . . . .	95
3.3.2 Characteristics of an Attocell . . . . .	95
3.3.3 User Allocation . . . . .	98
<b>3.4 Conclusions . . . . .</b>	<b>104</b>

---

## 3.1 Introduction to the Multi-Users Multiband CAP VLC System

A multi-users multiband CAP VLC indoor system is an association between a modulation scheme,  $m$ -CAP in this case, and a multi-users access scheme. Section 3.1.1 is a description of the principle behind the conventional CAP modulation while section

3.1.2 expands on the multiband version of the technique. In section 3.1.3 the association with subcarrier multiplexing is explained through its principle. On the other hand, section 3.1.4 details the other possible associations with the multi-users access schemes that are considered in this work. Section 3.1.5 concludes the review on the principle of the associations between multiband CAP and multi-access techniques.

### 3.1.1 Carrierless Amplitude and Phase Modulation

Carrierless Amplitude and Phase modulation is essentially a different implementation of traditional Quadrature Amplitude Modulation (QAM) with similar performances [204]. With QAM, two carrier waves are modulated in amplitude while in CAP, a QAM signal is generated by combining two pulse-amplitude modulation (PAM) signals that are filtered with filters forming a Hilbert Pair. When the impulse responses of these filters are chosen as sine and cosine, the only mathematical difference between a QAM generated signal and a CAP one is that the carrier's phase is reset at the beginning of each symbol [205]. At similar sampling rates, this results in CAP being less costly in implementation while offering the same performances because the modulation of the baseband signal with the quadrature carriers is performed by the pulse shaping filters [206]. In VLC, CAP is highlighted as an advanced modulation format that can help avoid complexity in optical components and cost with its high spectral efficiency while also having the potential for a lower implementation cost.

At the transmitter, the final objective is to transmit a bit sequence as a data stream using the modulation scheme. The sequence is encoded and then mapped using an  $M$ -QAM mapping scheme. Essentially, the bits are converted into symbols to be mapped in a QAM constellation. With  $M = 2^k$  where  $k$  is the number of bits per symbol. If 16-QAM is used, the bit sequence is transformed into a 16-points QAM constellation represented by symbols 0 to 15 ( $M - 1$ ) with  $k = 4$  bits per symbols.

The mapped symbols are represented by their real and imaginary, or in-phase and quadrature, coordinates in the associated  $M$ -QAM constellation. They are then split into  $X_I$  and  $X_Q$  which represent these real and imaginary components. Next, they are up-sampled to match the sample rate of the shaping filters, which is in accordance to the number of samples per symbol, given by the ratio between the sampling frequency and the symbol rate.

The two data streams  $X_I$  and  $X_Q$  must be shaped to achieve a Hilbert Pair, which means that they must occupy the same frequency band but must be orthogonal [207]. The typically used pulse shaping filter is the square-root raised cosine (SRRC) to achieve shaping in the same frequency range [208]. Additionally, a cosine and sine waveform are multiplied to form orthogonality and thus, a Hilbert Pair. The SRRC temporal form is given by:

$$g_{SRRC}(t) = \frac{2\alpha[\cos(\frac{(1+\alpha)\pi t}{T_S}) + (\frac{4\alpha t}{T_S})^{-1} \sin(\frac{(1-\alpha)\pi t}{T_S})]}{\pi\sqrt{T_S}[1 - (\frac{4\alpha t}{T_S})^2]} \quad (3.1)$$

Where,  $\alpha$  is the filter roll-off factor,  $T_S = 1/R_S$  is the symbol period,  $R_S$  is the system baud rate, and  $t$  is the instantaneous time sample. An example of these filters is given in figure 3.1 (a), with in-phase filter in black and quadrature one in blue, for a filter length  $L_f$  of 120 taps. The resulting complete pulse shaping filters,  $f_I$  and  $f_Q$ , are as follows for their temporal forms:

$$f_I(t) = g(t) \cos(\pi \frac{t}{T_S}(1 + \alpha)) \quad (3.2)$$

$$f_Q(t) = g(t) \sin(\pi \frac{t}{T_S}(1 + \alpha)) \quad (3.3)$$

Where  $g(t)$  is equal to  $g_{SRRC}(t)$ . Both  $f_I(t)$  and  $f_Q(t)$  have a finite filter length, defined as  $L_f$ . As shown by P. Chvojka et al in [209],  $L_f$  have an impact on the performances in terms of Bit Error Rate (BER). After the Hilbert pair, the data streams  $X_I$  and  $X_Q$  are shaped as follows:

$$s_I = X_I \otimes f_I \quad (3.4)$$

$$s_Q = X_Q \otimes f_Q \quad (3.5)$$

Where  $\otimes$  denotes convolution. These two signals are thus orthogonal and are summed before transmission and conversion into the analog domain in order to be exploitable by a LED, in the case of VLC. The total output signal can be represented as:

$$S(t) = \sum_{k=-\text{inf}}^{\text{inf}} [X_I \otimes f_I(t - kT_S)] - [X_Q \otimes f_Q(t - kT_S)] \quad (3.6)$$

An example of this output signal is represented both in time-domain in figure 3.1 (b) and in the frequency domain in figure 3.1 (c). This output signal is transmitted by the emitter part and after detection by the receiver part, we consider the received signal  $R(t)$  as:

$$R(t) = S(t) \otimes H(t) \quad (3.7)$$

With  $H(t)$  being the optical channel response. The received signal is digitized by an analog to digital converter (ADC) in order to apply the CAP demodulation. This waveform is separated into  $r_1$  and  $r_2$ , which are equal to the received signal, and

filtered by two matched filters  $f'I_I$  and  $f'I_Q$ . They are the time-reversed matched filters for the in-phase component and quadrature component respectively for the associated orthogonal filters at the transmitter. The output waveforms for both filters can be written as:

$$r_i = r_1 \otimes f'I_I \quad (3.8)$$

$$r_q = r_2 \otimes f'I_Q \quad (3.9)$$

Where  $f'I_I(t) = f_I(-t)$  and  $f'I_Q(t) = f_Q(-t)$ . These recovered symbols  $r_i$  and  $r_q$  are down-sampled to form  $X'I_I$  and  $X'I_Q$ . An associated  $M$ -QAM de-mapper is finally utilized to de-map and recover the original bit sequence. In between the down-sampling and the de-mapping, a linear equalizer is usually operating to guarantee synchronization in the process because of the potential for inter-symbol interferences (ISI) [210] caused by filtering with timing errors [211][212].

The basics of the implementation of the principle behind CAP for the numerical simulations of this chapter are summarized in part B.1 of appendix B.

### 3.1.2 Multi-Band Carrierless Amplitude and Phase Modulation

The principle of multi-band CAP ( $m$ -CAP) is to divide a conventional CAP signal into  $m$  independent subbands occupying different frequency bands. In consequence, an  $m$ -CAP signal can be described as the sum of multiple CAP signals with each one using a different carrier frequency, defined by 3.13. This ability allows the scheme to use a different modulation order and optical power for each of the CAP signal, or subcarriers. Conventional CAP, or 1-CAP, is a scheme that is very sensitive to non-flat channel frequency response and VLC channels do not exhibit flat-band responses. This drawback can be mitigated by dividing the signal into multiple subcarriers since it will reduce the frequency length of each subband for the same total signal bandwidth. The channel response for each band will thus appear 'more flat' than the entire response. This results in  $m$ -CAP being less prone to attenuation induced distortion than conventional CAP. This characteristic is associated with the flexibility inherent to a multi-subcarrier modulation scheme. Each subband can be tailored to the channel response with a specific modulation order through  $M$ -QAM mapping and a specific optical power.

Still, CAP modulation has been preferred mainly because of its lower implementation cost. In consequence, a question is how does  $m$ -CAP compares to this key characteristic. Indeed, when increasing  $m$ , the number of transmission filters increases by  $2m$ . Since the square root raised cosine pulse shaping based filters have a finite impulse responses (FIR), the implementation cost would logically increase. However, the orthogonal pulse shaping pair filters become simpler to implement because each

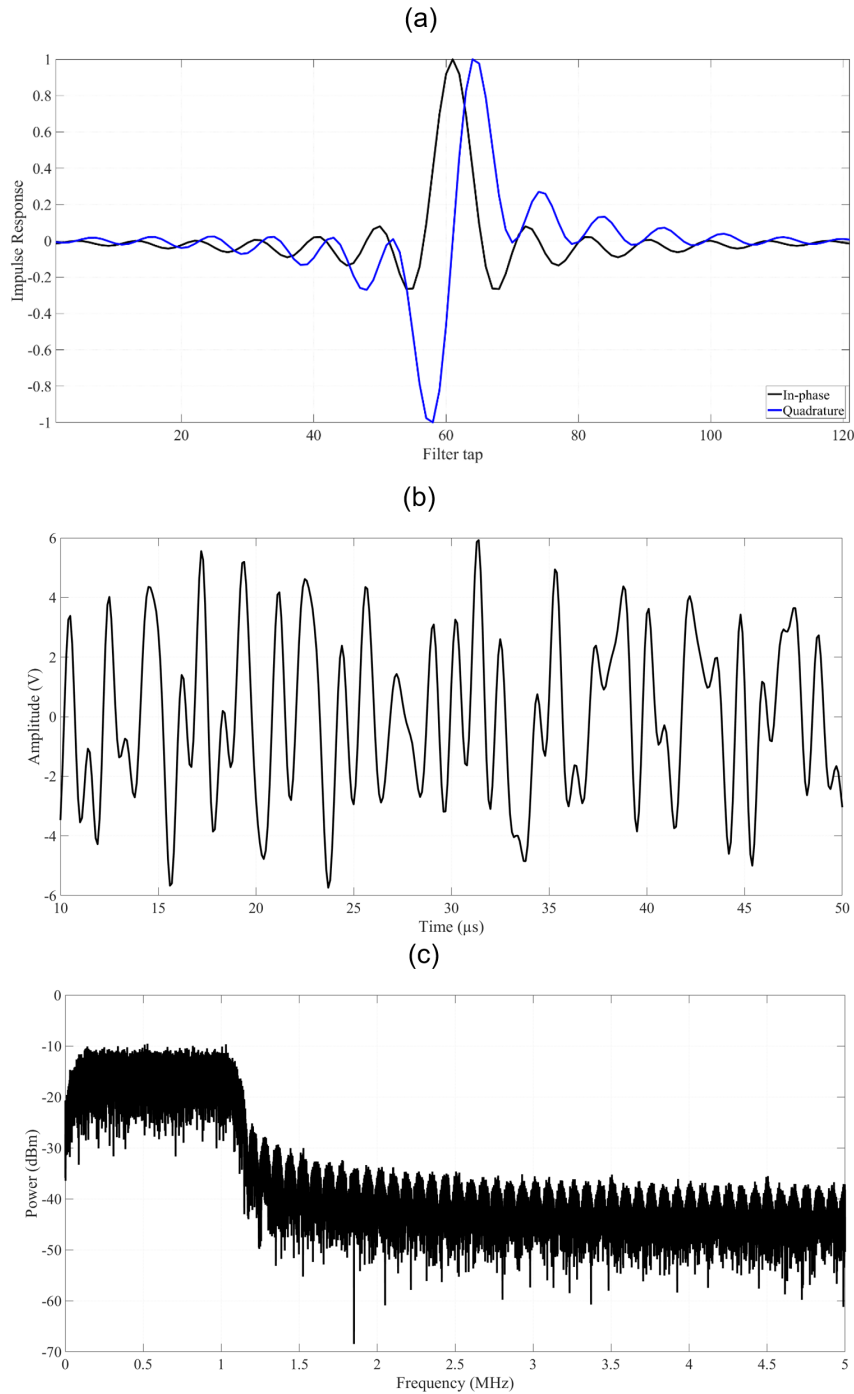


FIGURE 3.1: (a) Illustration of the square root raised cosine pulse shaping for the in-phase component and quadrature component. (b) Example of a time-domain CAP modulated signal. (c) Spectrum example of a CAP modulated signal.

pair covers a smaller frequency band. A sampling rate closer to the Nyquist rate can then be used, which decreases the digital signal processing clock speed because of the up-sampling needs being limited. Multiband CAP thus retains the conventional CAP key characteristic of lower implementation cost but only if the number of subcarriers is not too high, as the sampling rate will not decrease below the Nyquist rate.

At the transmitter,  $m$ -CAP operates the same as multiple CAP process for different carrier frequencies. A bit sequence is used as a data stream, encoded and separated into as many stream as the number of subcarriers, defined by  $m$ . Each stream is encoded and mapped by an  $M$ -QAM mapping scheme. With  $n \in [1 : m]$  representing the  $n^{\text{th}}$  subcarrier, we thus have, after up-sampling and splitting,  $X_I^n$  and  $X_Q^n$  corresponding to the up-sampled in-phase and quadrature  $M^n$ -QAM mapped symbols on the  $n^{\text{th}}$  subcarrier. These data streams must be pulse shaped to achieve a Hilbert Pair. With a pair per subcarrier, the SRRC and the complete pulse shaping filters temporal forms are given by:

$$g_{SRRC}(t) = \frac{2\alpha[\cos(\frac{(1+\alpha)\pi t}{T_S}) + (\frac{4\alpha t}{T_S})^{-1} \sin(\frac{(1-\alpha)\pi t}{T_S})]}{\pi\sqrt{T_S}[1 - (\frac{4\alpha t}{T_S})^2]} \quad (3.10)$$

$$f_I^n = g(t) \cos(\pi \frac{t}{T_S} (2n-1)(1+\alpha)) \quad (3.11)$$

$$f_Q^n = g(t) \sin(\pi \frac{t}{T_S} (2n-1)(1+\alpha)) \quad (3.12)$$

Where  $T_S$  is, again, the symbol duration,  $\alpha$  is the filter roll-off factor,  $t$  is the instantaneous time sample, and  $n$  corresponds to the  $n^{\text{th}}$  subcarrier. The frequencies of carriers generated by the pulse shaping transmit filters  $f_I^n$  and  $f_Q^n$  can be given by:

$$\frac{1}{2T_S}(2n-1)(1+\alpha) \quad (3.13)$$

After each Hilbert pair, the data streams  $X_I^n$  and  $X_Q^n$  are shaped as follows:

$$s_I^n = X_I^n \otimes f_I^n \quad (3.14)$$

$$s_Q^n = X_Q^n \otimes f_Q^n \quad (3.15)$$

Where  $\otimes$  denotes convolution. These signals are summed for each subcarrier before transmission into a total output signal which can be represented as:

$$S(t) = \sum_{n=1}^m [s_I^n - s_Q^n] \quad (3.16)$$

An example of a time-domain  $m$ -CAP signal is represented in figure 3.2 (a), as well as frequency domain example for  $m = 4$ ,  $m = 10$  and  $m = 20$  in figure 3.2 (b), (c), and (d), respectively. This output signal is transmitted by the emitter part and after detection by the receiver part, a received signal  $R(t)$  is considered and defined the

same way as in equation 3.7. This signal is sampled by an ADC before applying to  $m$ -CAP demodulation process. The waveform is separated into  $2m$  equal signals  $r_1^n$  and  $r_2^n$  and each is filtered by its associated matched filter  $f_I^n$  and  $f_Q^n$ . These time-reversed matched filters are defined in same way they were in section 3.1.1. The output waveform for each subcarrier are:

$$r_I^n = r_1^n \otimes f_I^n \quad (3.17)$$

$$r_Q^n = r_2^n \otimes f_Q^n \quad (3.18)$$

After down-sampling,  $X_I^n$  and  $X_Q^n$  are the recovered data streams. They are de-mapped and reassembled to recover the original bit sequence.

The basics of the implementation of the principle behind multiband CAP for the numerical simulations of this chapter are summarized in part B.2 of appendix B.

### 3.1.3 Natural Association with Subcarrier Multiplexing

Subcarrier multiplexing (SCM) or Subcarrier Multiple Access (SCMA) is used to combine different communication signals similarly to wavelength division multiplexing (WDM). Each signal occupies a different portion of the optical spectrum surrounding the center frequency of the whole optical signal. The signals are thus multiplexed in the frequency domain and transmitted by a single wavelength. SCM is used in fiber optics and has the advantage of a lower cost compared to WDM because it does not use an optical multiplexer but is limited in maximum subcarrier frequencies and data rates by the bandwidth of the optical and electrical components. Both SCM and WDM are often used in conjunction for better efficiency, even if the use of SCM alone is sufficient to offer multi-users capabilities for lower-cost systems [213][214].

Figure 3.3 (a) represents the principle of an SCM-based multiple access scheme. The modulated data streams  $d_1$  to  $d_n$  are transmitted at carrier frequencies  $f_1$  to  $f_n$ . At the receiver, the demodulation is operated at each of these carrier frequencies in order to recover the data streams originally transmitted. The scheme is thus a very simple, low-cost path to a multi-users system. As shown in figure 3.3 (b), each user can be assigned to one or more data streams, thus adding flexibility in a potentially dynamic multi-users system. This ability is called carrier aggregation [215].

SCM represents a natural association with multiband CAP in VLC. Indeed, the modulation scheme separates its data into multiple subcarriers around a center frequency with a signal transmitted by an optical component at a specific wavelength. The two schemes share the fact that their lower implementation cost is their main criteria. In practice, with the association of  $m$ -CAP with SCM in multi-users (MU- $m$ -CAP), the multiple subcarriers data streams correspond with multiple users. Each user data is

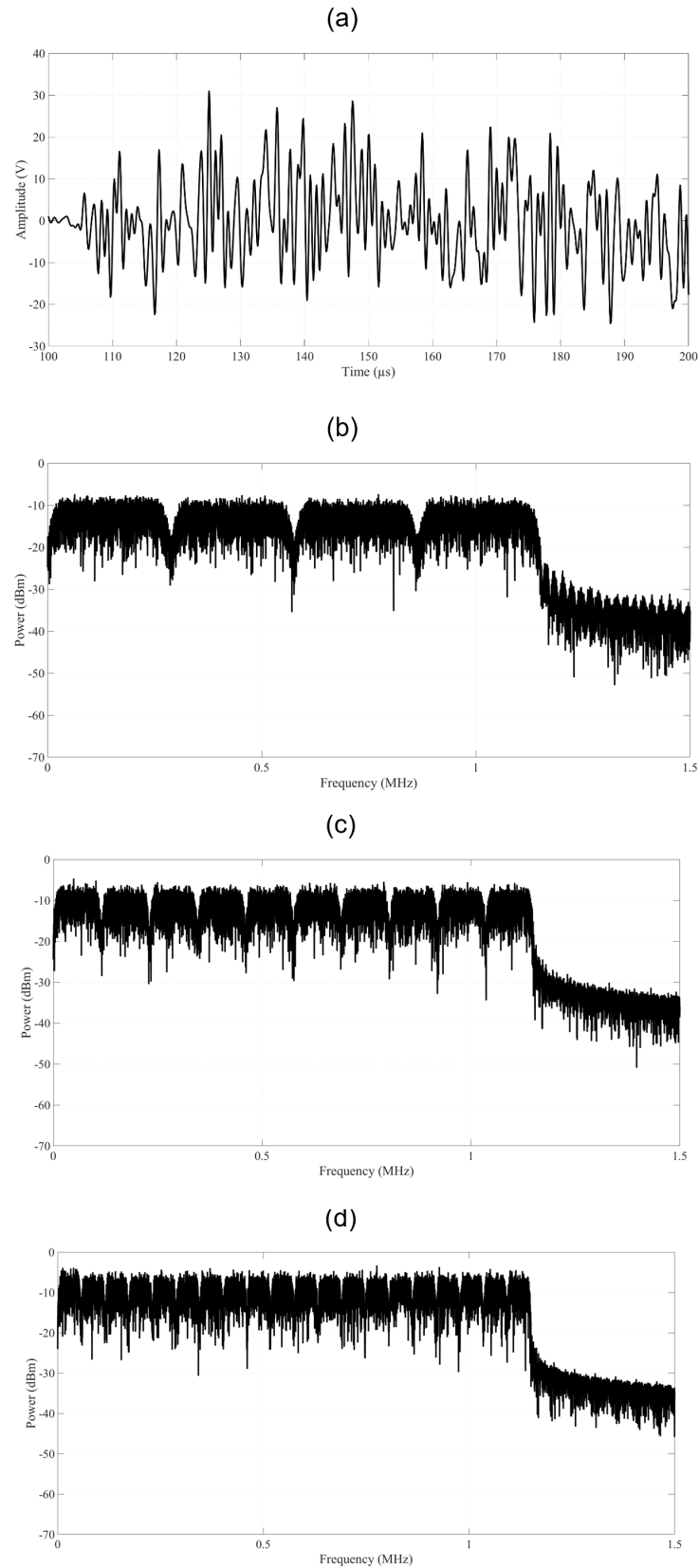


FIGURE 3.2: (a) Example of a time-domain  $m$ -CAP modulated signal. Spectrum example of an  $m$ -CAP modulated signal for (b)  $m = 4$ , (c)  $m = 10$  and (d)  $m = 20$ .

contained in one or more subbands as illustrated on Figure 3.4. For example, if two users are allocated using 4-CAP, two subcarriers per user or three to user 1 and one to user 2 could be allocated. This ability to allocate various number of subbands to each user depends on the needs and channel state, offering MU- $m$ -CAP multiple degree of freedom for increased flexibility in the multi-access scheme. This advantage is offered by carrier aggregation. A user can also be dynamically allocated more subcarriers than the others if it needs a data rate increase or if the quality of its signal decreases, with minimal computing power. Additionally, if  $m$  increases, this flexibility escalates as more subcarriers are available for each user.

In principle, each user  $k$  is allocated to a group of subcarriers which we define as follow:

$$c_k = [a_{k,j}] \quad (3.19)$$

Each  $a_{k,j}$  corresponds to the  $j^{\text{th}}$  subcarrier that is allocated to the user  $k$ . With  $k \in [1 : m]$  and  $j \in [1 : m]$ , there can be up to  $m$  users and one user can have one to  $m$  subcarriers assigned. The total number of users is represented by  $\bar{k}$ . The total number of subcarriers assigned to one user is represented by  $\bar{j}_k$  and thus, the sum of  $\bar{j}_k$  can only be inferior or equal to  $m$ . Each subcarrier can be allocated to one user. At the transmission, each of the  $\bar{k}$  data streams corresponding to each user  $k$  is divided into  $\bar{j}_k$  data streams, essentially for each subcarrier allocated to that specific user. The total  $m$  streams are mapped on their corresponding  $M_{a_{k,j}}$ -QAM mapper, with  $M_{a_{k,j}}$  designating the modulation order at the  $j^{\text{th}}$  subcarrier. The mapped symbols are then up-sampled and split into their in-phase, or real, and quadrature, or imaginary, components. The  $m$  pairs of in-phase and quadrature components (I/Q) are then filtered with square root raised cosine filters forming a Hilbert Pair at different frequencies depending on the subcarrier number.  $M_I^{a_{k,j}}$  and  $M_Q^{a_{k,j}}$  are defined as the up-sampled in-phase and quadrature  $M_{a_{k,j}}$ -QAM mapped symbols on the  $j^{\text{th}}$  subcarrier. The overall sketch of this principle is illustrated in a diagram figure 3.5 (a). Each pair of filter for the  $j^{\text{th}}$  subcarrier is defined in the same way as in equations 3.10, 3.11 and 3.12 except that  $n$  is replaced by  $a_{k,j}$ . Thus the transmitted signal for each user is defined as:

$$s^k(t) = \sum_j [X_I^{a_{k,j}} \otimes f_I^{a_{k,j}} - X_Q^{a_{k,j}} \otimes f_Q^{a_{k,j}}] \quad (3.20)$$

With  $\otimes$  being a time-domain convolution and the final transmitted signal being the sum of each user signal:

$$S(t) = \sum_k s^k(t) \quad (3.21)$$

Each component of the sum represents a subband that can be assigned to a user with SCM. At a typical receiver for user  $k$ , the up-sampled in-phase and quadrature mapped symbols for each of the user's assigned subcarriers ( $c_k$ ) are recovered using the matched transmission pulse shaping filters, as illustrated in figure 3.5 (b). The recovered data stream is obtained after combining the  $\bar{j}_k$  de-mapped symbols streams. The demodulation process is thus essentially the same as described in section 3.1.2 except that the subcarriers concerned by the process are defined by  $c_k$  for the receiver corresponding to user  $k$ .

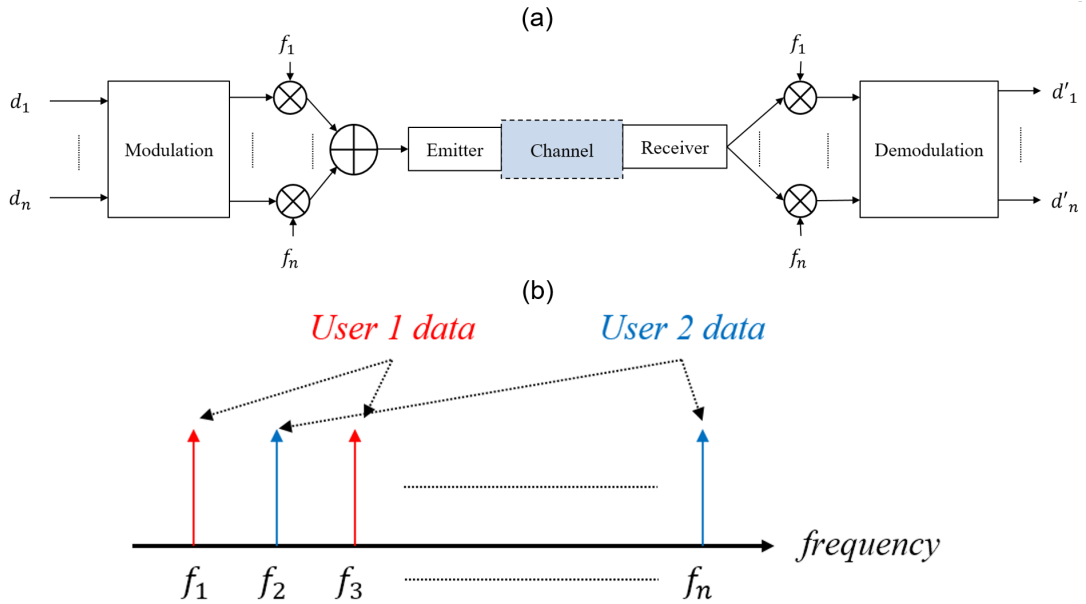


FIGURE 3.3: (a) Diagram representing the principle of an SCM-based multiple access control layer (b) Illustration of a spectrum with an SCM-based repartition of 2 users.

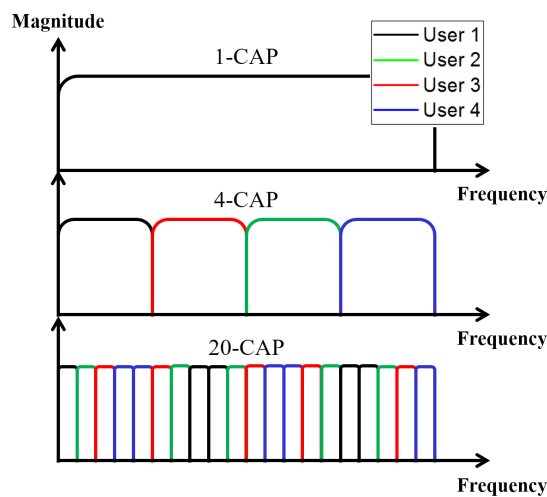


FIGURE 3.4: Example of frequency spectrums for a 4-users SCM allocation in a multiband CAP modulated signal.

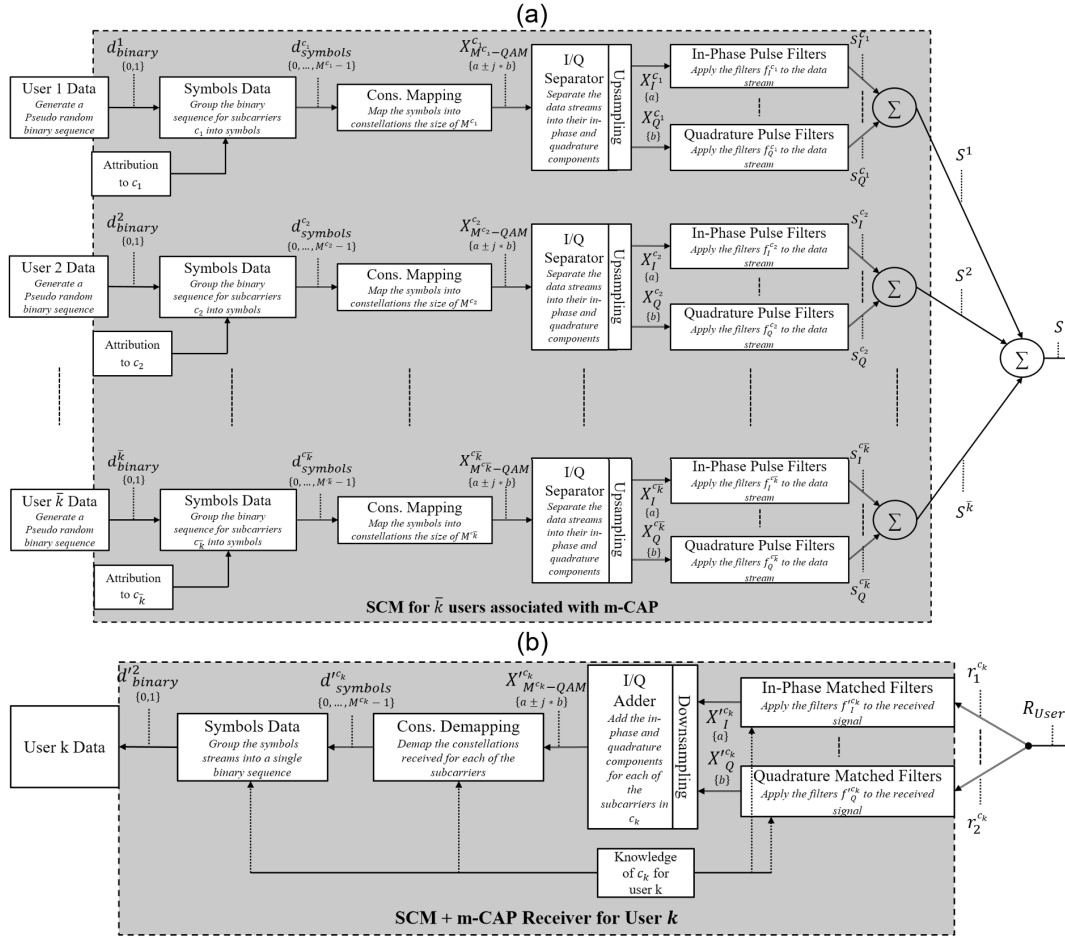


FIGURE 3.5: (a) Schematic representing the principle of a transmitter using SCM-based multi-users Multi-band CAP (MU- $m$ -CAP) (b) Schematic representing the principle of a receiver using SCM-MU- $m$ -CAP.

### 3.1.4 Association with Other Schemes

#### 3.1.4.1 Association with Code Division Multiple Access

Code division multiple access (CDMA) is a multiple access channel method. Multiple users can send information over a single communication channel, thus allowing the sharing of a same signal bandwidth. The principle is to use a spread spectrum technology and a special coding scheme to realize the communication without inter-user interferences. Each user is assigned a code at the transmission. The receiver uses the same code in order to extract the original data transmitted. The code does not contain information. The spreading and despreading of the data can be computationally heavy [216].

The spread spectrum technology comes in three forms. The first one is direct-sequence (DS) spread spectrum for DS-CDMA. As described by figure 3.6 (a), each information bit is replaced by a small series of bits, called a code, extracted from a pseudo random sequence. The second form of spread spectrum technology is frequency hopping

spread spectrum (FHSS) for FH-CDMA [217].  $N$  frequencies are used for a communication and the transmission is operated alternatively on multiple channels following a pseudo random sequence. This is not a method used for signal resistance to interferences and not for high throughput systems and thus will not be described here. The third spread spectrum technology is a variant of direct-sequence spread spectrum for multi-carrier modulation format and called Multi-Carrier CDMA (MC-CDMA). It is used in OFDM to support multiple users over the same frequency band. As described by figure 3.6 (b), each user symbol is carried over multiple parallel subcarriers but is phase-shifted according to the code value. The receiver separates the signals of different users because they have orthogonal code values.

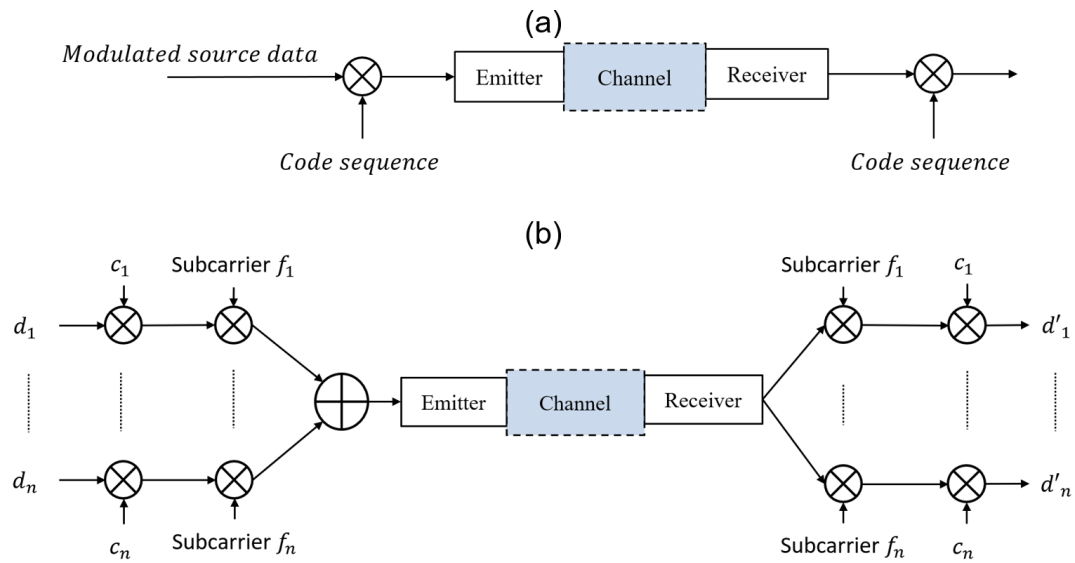


FIGURE 3.6: Diagram describing the principle of a Code Division Multiple Access scheme in the case of (a) Direct Spreading CDMA and (b) Multi-Carrier CDMA.

Like OFDM,  $m$ -CAP also uses a number of parallel subcarriers and can thus be associated with MC-CDMA. As shown as an example in figure 3.7, when associating the modulation scheme with this multiple access method, every user shares the same bandwidth at the same time by using different orthogonal spreading codes. The multi-access part is done in the code domain which removes the limit of receivers per cell in SCM/FDMA or TDMA schemes. The technique offers some flexibility as well since the spreading code length can be modified independently from the number of subbands.

The figure 3.8 (a) describes the principle of an association between MC-CDMA and  $m$ -CAP. Each user is represented by its number  $j$ . The total number of users is  $K$ . Each one follows a modulation process similar to the multiband CAP process described in section 3.1.2. The  $n$  data streams for each user  $j$  are mapped with the associated  $M_n^j$ -QAM mapper. The spreading sequencing comes at this point and the code adopted is a Walsh-Hadamard code. These orthogonal codes are simple to generate using the Hadamard matrix shown in the following equation:

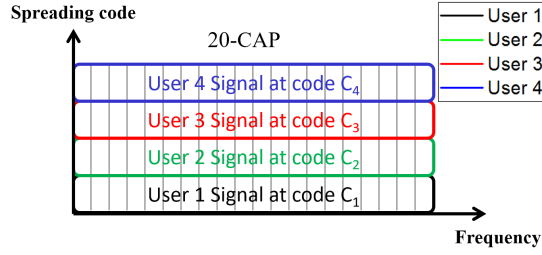


FIGURE 3.7: Spectrum example for an MC-CDMA 4-users allocation in a  $m$ -CAP modulated signal.

$$C_L = \begin{pmatrix} C_{L/2} & C_{L/2} \\ C_{L/2} & -C_{L/2} \end{pmatrix}, \forall L = 2^v, v \geq 1, C_1 = 1 \quad (3.22)$$

Where  $L$  is the maximum number of available codes which corresponds to the maximum number of users. The resulting spread symbol streams are up-sampled and split into their respective in-phase and quadrature data streams, called  $X_I^{j,n}$  and  $X_Q^{j,n}$  for the  $j^{\text{th}}$  user and the  $n^{\text{th}}$  subcarrier. The pulse shaping filters defined by equations 3.11 and 3.12 are applied to the waveforms as follows:

$$s_I^{j,n} = X_I^{j,n} \otimes f_I^n \quad (3.23)$$

$$s_Q^{j,n} = X_Q^{j,n} \otimes f_Q^n \quad (3.24)$$

The resulting output signal for the modulation process of each user is thus:

$$s_j(t) = \sum_n [s_I^{j,n} - s_Q^{j,n}] \quad (3.25)$$

Each of these waveforms are orthogonal because of the spreading using the orthogonal Walsh-Hadamard codes. And, the total output signal after combining the signals is:

$$s(t) = \sum_j [s_j(t)] \quad (3.26)$$

The receiving process follows the same principle as the demodulation process described section 3.1.2 and is illustrated by figure 3.8 (b). The receiver for user  $j$  detects the signal from the transmitter and the signal received  $R(t)$  can be defined as the same way as in equation 3.7. This signal is sampled by an ADC before applying the  $m$ -CAP demodulation process. The waveform is separated into  $2m$  signals  $r_1^{j,n}$  and  $r_2^{j,n}$  and each is filtered by its associated matched filter  $f_I^n$  and  $f_Q^n$ . The output waveforms for each subcarrier can be written as:

$$r_I^{j,n} = r_1^{j,n} \otimes f_I^n \quad (3.27)$$

$$r_Q^{j,n} = r_2^{j,n} \otimes f_Q^n \quad (3.28)$$

After down-sampling and using the despreading sequence corresponding to user  $j$ ,  $X_I^{j,n}$  and  $X_Q^{j,n}$  are the recovered data streams which are de-mapped and reassembled to recover the original bit sequence for that user.

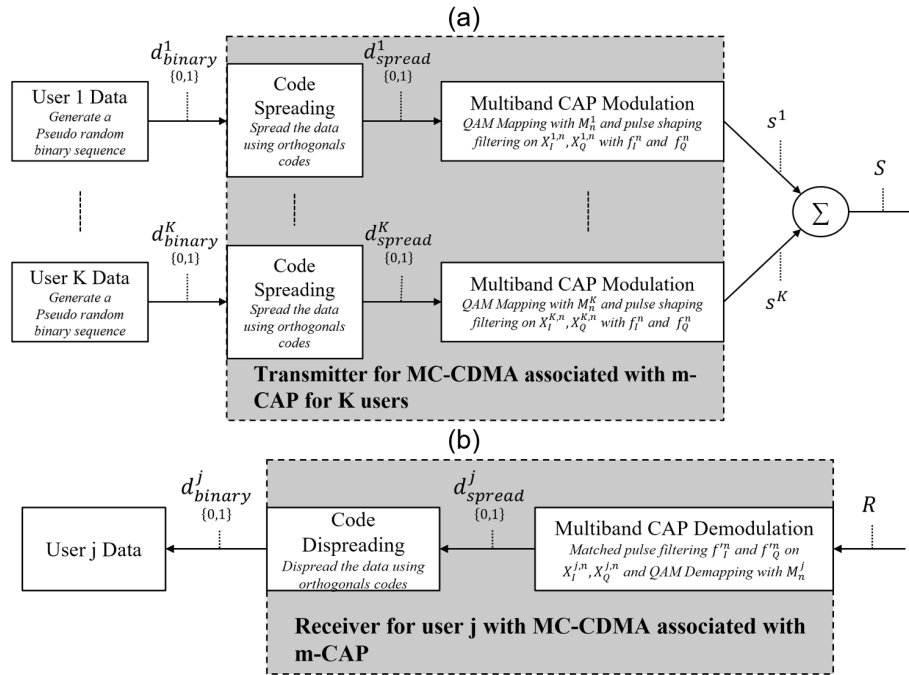


FIGURE 3.8: Diagram describing the principle of an MC-CDMA and  $m$ -CAP association for the (a) transmitter and the (b) receiver.

### 3.1.4.2 Association with Power Domain Non-Orthogonal Multiple Access

The basic concept of behind NOMA is to serve more than one user in the same resource block, e.g., a time slot, code, space, or subcarrier. It promises massive connectivity, reduced latency and improved user fairness and spectral efficiency compared to orthogonal multiple access techniques (OMA) [218]. Multiple types of Non-Orthogonal Multiple Access (NOMA) schemes exist. Code-domain (CD-NOMA) and Power-domain (PD-NOMA) are the two major categories. CD-NOMA multiplexes in code domain. In contrast to CDMA, this category utilizes user-specific spreading sequences that are sparse sequences of non-orthogonal cross-correlation sequences of low correlation coefficient. The focus here is, however, on PD-NOMA which multiplexes data on the power domain. The principle, as described by figure 3.9, is to superimpose multiple users in different power levels and exploit the channel gain difference between multiplexed users. At the transmitter, a superposition encoder is

used to superimpose signals from various users. At the receiver, multi-users detection (MUD) algorithms, such as successive interference cancellation (SIC), are utilized to detect the desired signals.

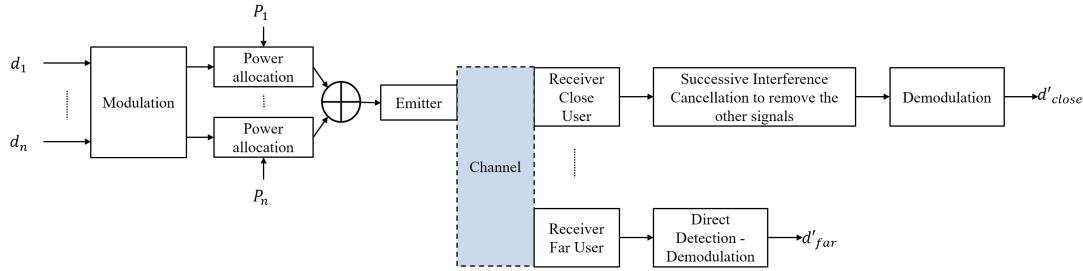


FIGURE 3.9: Diagram describing the principle of a Power Domain Non-Orthogonal Multiple Access scheme.

The superposition coding (SC) is a technique of simultaneous communication from multiple users at a single transmitter. SC is a scheme that attains its capacity on a scalar Gaussian broadcast channel [219]. The source data for each user is encoded into  $x_i$  with  $i \in [1 : N]$  and  $N$  being the number of users. All signals are combined after modulation with a total transmitted power of  $P$ . The resulting time-domain signal can be written as:

$$s(t) = \sum_{i=1}^N \sqrt{p_i} x_i \quad (3.29)$$

Where  $p_i$  is the allocated power for user  $i$  and  $x_i$  is the transmitted time-domain modulated signal for user  $i$ . At the receiver, successive interference cancellation (SIC) is performed. SIC is conceivable by exploiting the differences in signal strength among the signals of interest. Each user signal is successively decoded by each receiver. Once a user signal is decoded, it is subtracted from the signal preceding the decoding. In consequence it is necessary that prior to SIC, users are ordered according to their signal strengths, so that the receiver can decode the stronger signal first, subtract it from the combined signal, and isolate the weaker one from the residue.

The process can be mathematically expressed, in a two-user scenario, as follows:

1. At user 1, considered the far user and having been allocated to a larger power level, a single-user decoder decodes the message  $x_1$  by treating  $x_2$  as noise.
2. At user 2, considered the close user and having been allocated to a lower power level, the following steps are used to decode its message from the received signal  $r_2$ :

- Decode user 1 message  $x_1$  by using the single-user decoder,
- Subtract  $\sqrt{p_1} x_1$  from the received signal  $r_2$ , where  $h_2$  is the complex channel gain at user 2:

$$r'_2 = r_2 - \sqrt{p_1} x_1 \otimes h_2 \quad (3.30)$$

- Decode user 2 message  $x_2$  by applying another single-user decoder.

By nature, NOMA can be combined with multiple different modulation schemes or different multiple access schemes. Indeed, as described in equation 3.29 for superposition coding, the  $x_i$  can be any time-domain signal. In order to exploit PD-NOMA's advantage in increased connectivity without the need for extensive SIC decoding, a 2-power level signal is combined with 2 SCM-based  $m$ -CAP signal. The association thus virtually offers two different multi-users  $m$ -CAP waveforms instead of one under the same bandwidth slot. In principle, the transmitter, illustrated figure 3.11 (a) outputs a signal defined as follows:

$$s = \sqrt{p_1}x_1 + \sqrt{p_2}x_2 \quad (3.31)$$

With  $x_1$  and  $x_2$  being SCM-based  $m$ -CAP signals defined the same way as in equation 3.21. An illustration of an example spectrum for a 4 level allocation is given in figure 3.10. At the receiver for the close user, illustrated figure 3.11 (b), the SIC technique is applied to remove the signal destined to the far user and decode the correct signal. At the receiver for the far user, illustrated figure 3.11 (c), direct decoding is applied.

Since each power level signal uses an SCM-based allocation, the close user can be represented by the users closest to the emitter. In VLC these users would be in the center of the cell. Respectively, the far user can be represented by the users furthest from the emitter. In VLC, these users would be in the edge of the cell.

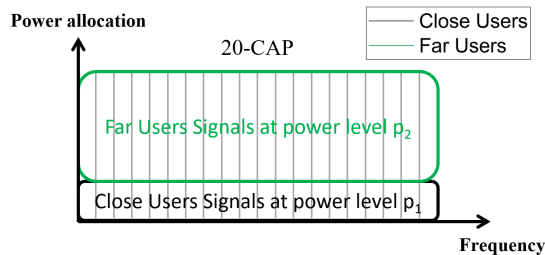


FIGURE 3.10: Spectrum example for a PD-NOMA 4-users allocation in an  $m$ -CAP modulated signal.

### 3.1.4.3 Association with Optical Space Division Multiple Access

Optical Space-division multiple access (SDMA) is a channel access method based on the creation of multiple spatial pipes through the use of an angle diversity transmitter. In VLC, LEDs are used as transmitters and have a limited FOV which can be used to generate directional light beams. Thus the angle diversity transmitter is simply composed of multiple narrow FOV LEDs, called elements. SDMA supports multiple parallel transmissions of signals with the same characteristics, except for the useful data, at the same time provided that the users are spatially separated [220]. Figure 3.12 (a) describes the principle of such a scheme in VLC.

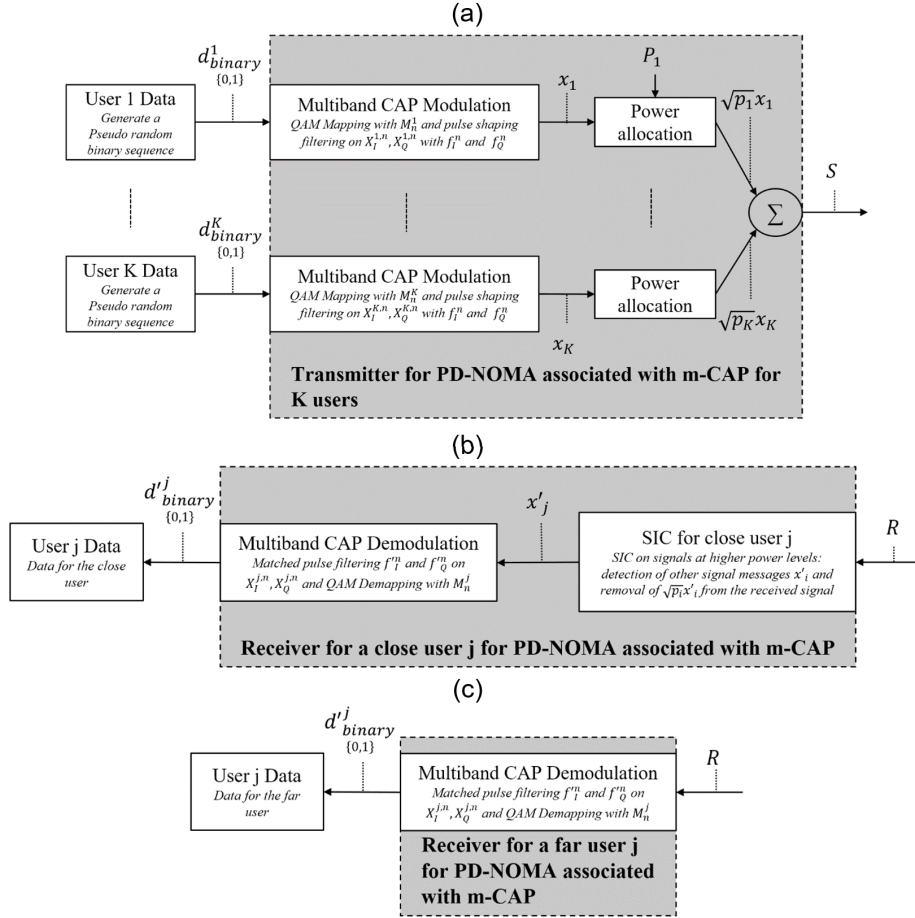


FIGURE 3.11: Diagram describing the principle of a PD-NOMA and m-CAP association for the (a) transmitter and the (b) receiver for the close user and (c) receiver for the far user.

Figure 3.12 (b) explains the principle behind the optical SDMA scheme. Each element transmit a time- or frequency-domain modulated signal  $x_i$  with  $i \in [1 : N]$  and  $N$  being the total number of elements. The element emits a narrow beam towards a spatial division of the cell where one or more users receives the waveform  $x_i$ . In consequence, the association of SCM-based m-CAP signals with SDMA is a process that does not change from the one described in subsection 3.1.3 with each transmitter element transmitting a signal described by equation 3.21.

### 3.1.5 Refining Our Approach

The approach chosen for our indoor multi-users VLC system is to combine a highly spectrally efficient modulation scheme with a multi-access technique in order to offer a low-complexity way to attain high data rates with high multi-users capacity.

Multiband CAP represents the modulation scheme that fit the approach the most. Indeed, the choice of the CAP modulation over OFDM relies on the fact that it does not use FFT or inverse FFT and uses instead simple finite impulse responses filters. Also, the power efficiency is higher while the spectral efficiency remains similar [221].

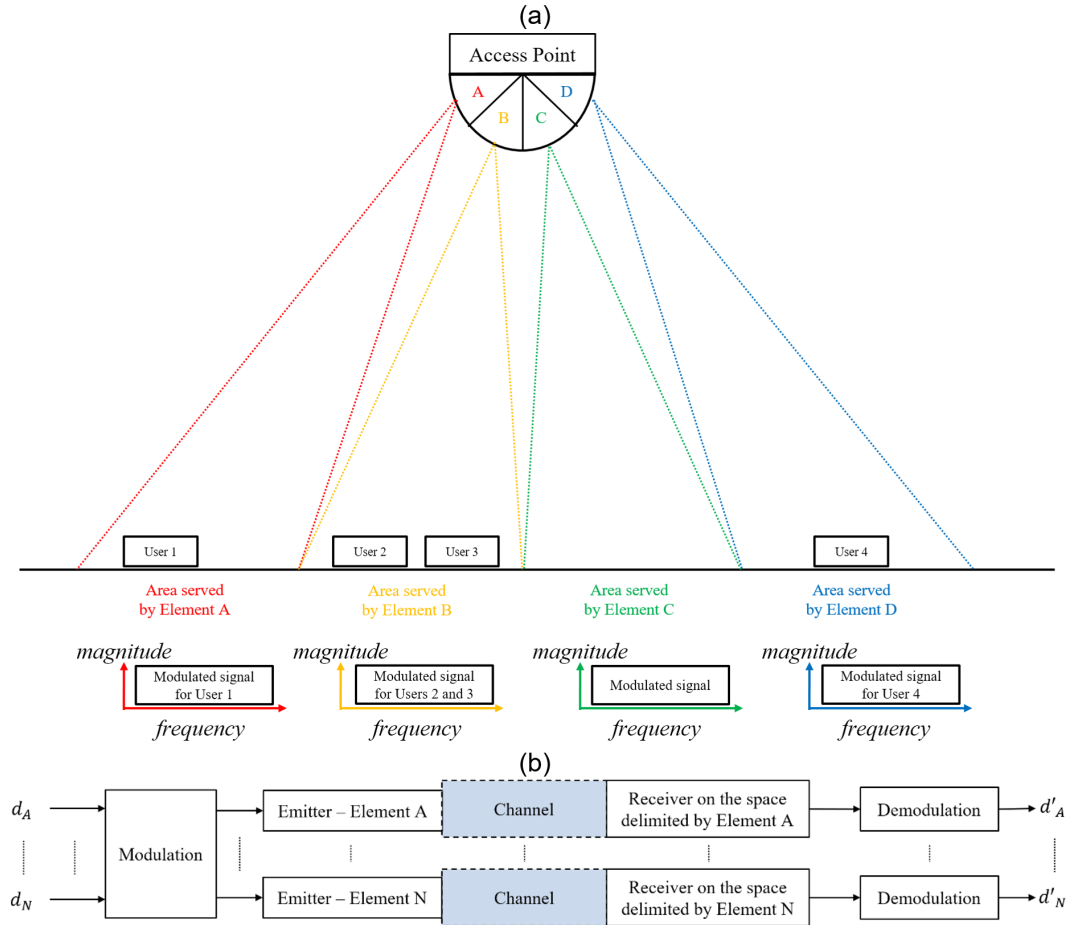


FIGURE 3.12: (a) Illustration of a Space Division Multiple Access scheme in Visible Light Communication using a 4-elements transmitter. (b) Diagram representing the principle of a SDMA scheme.

Multiband CAP uses a multi-subcarriers principle to reduce the sensitivity to non-flat channel response. And, in addition, an increase of the flexibility comes with the ability to select a modulation order for each subband in the same way as bit loading for OFDM. Its potential is too lightly explored in VLC and  $m$ -CAP is thus an ideal modulation scheme for our approach.

One of the most important metrics in a modulation raw performance is the throughput as it shows the ability to attain a high spectral efficiency. Indeed, the LED main limitation is their bandwidth. As such, the capability to maximize throughput for a limited bandwidth is a key characteristic to optimize. In multiband CAP, the main degree of freedom comes in the filter parameters, shown in equations 3.10, 3.11 and 3.12. The filter roll-off factor and the filter span  $L_{SPAN}$  are parameters that can be changed to optimize performances. To further enhance the results, it is also possible in equations 3.11 and 3.12 to add a constant factor to tweak the central frequency of each subcarrier and thus obtain another parameter: subcarrier spacing. Along with post-processing techniques such as channel estimation and equalization, optimizing the filter factors and subcarrier spacing allows  $m$ -CAP to maximize its

spectral efficiency in a variety of ways.

As multiband CAP has yet to be fully explored for indoor VLC, its combination with multi-access schemes is one of the domains that needs more prospecting. Subcarrier multiplexing represents the most natural way to add a multi-users component to the modulation scheme, as shown in section 3.1.3. A considerable number of schemes have also been investigated with the OFDM modulation but not with multiband CAP. The most used is Multi-carrier CDMA and while originally created for OFDM, can be adapted to  $m$ -CAP, as shown in subsection 3.1.4.1. While, TDMA or CSMA could be options, we decided to focus on the most promising modulation schemes for 5G with PD-NOMA and SDMA. Both can be combined with  $m$ -CAP, as shown in subsections 3.1.4.2 and 3.1.4.3. The associations of  $m$ -CAP with SCM, MC-CDMA, PD-NOMA and SDMA, as shown figure 3.13, are yet to be fully explored. As such it is necessary to know how to compare them. The attocell parameters in an indoor VLC situation and the user allocation aspect are the main ways in which we can distinguish the multi-access schemes performances. The attocell, defined later in section 3.3.1 has multiple characteristics such as its size, its capacity, or its ability to interconnect in a cell network that allow the scheme to be better defined. User allocation can be defined as how a user connects to the cell and what performance variations he can expect.

The receiver for a user needs to know the user-subcarriers allocation. A bidirectional link would add the ability to configure the distribution of subbands. But, VLC requires an amount of power to generate light that cannot be attained by mobile devices and therefore, are not the preferred method of choice to add an up-link. Also, interferences are created by the reflected light between the two channels. As a first alternative, radio-frequency (RF) is easy to use but requires the transceivers to work in two domains and cannot be used when electromagnetic interferences (EMI) need to be minimized, such as in hospitals or planes. As a second alternative, retro-reflective transceivers reflect light to transmit data, but the modulation speed is low [222]. However, efforts have been made to overcome this limitation [223] and the technology is promising for VLC. Finally, as suggested in [224], a near ultraviolet (UV) or near infrared (IR) up-link seems to be the most viable solution currently. Indeed, as shown by [225], range for an up-link option is approximately the same between the visible, near UV, and IR bands. This is not the subject of this work and thus will not be studied here.

## 3.2 Broadcast Channel Performances Breakdown

The broadcast single-user performances represents the ability for a VLC system to serve a singular receiver. As such, this part aims at presenting the tools to evaluate the transmission characteristics of CAP, or  $m$ -CAP, in such a scenario. Section 3.2.1 describes and illustrates the model for an indoor VLC system that will be analyzed.

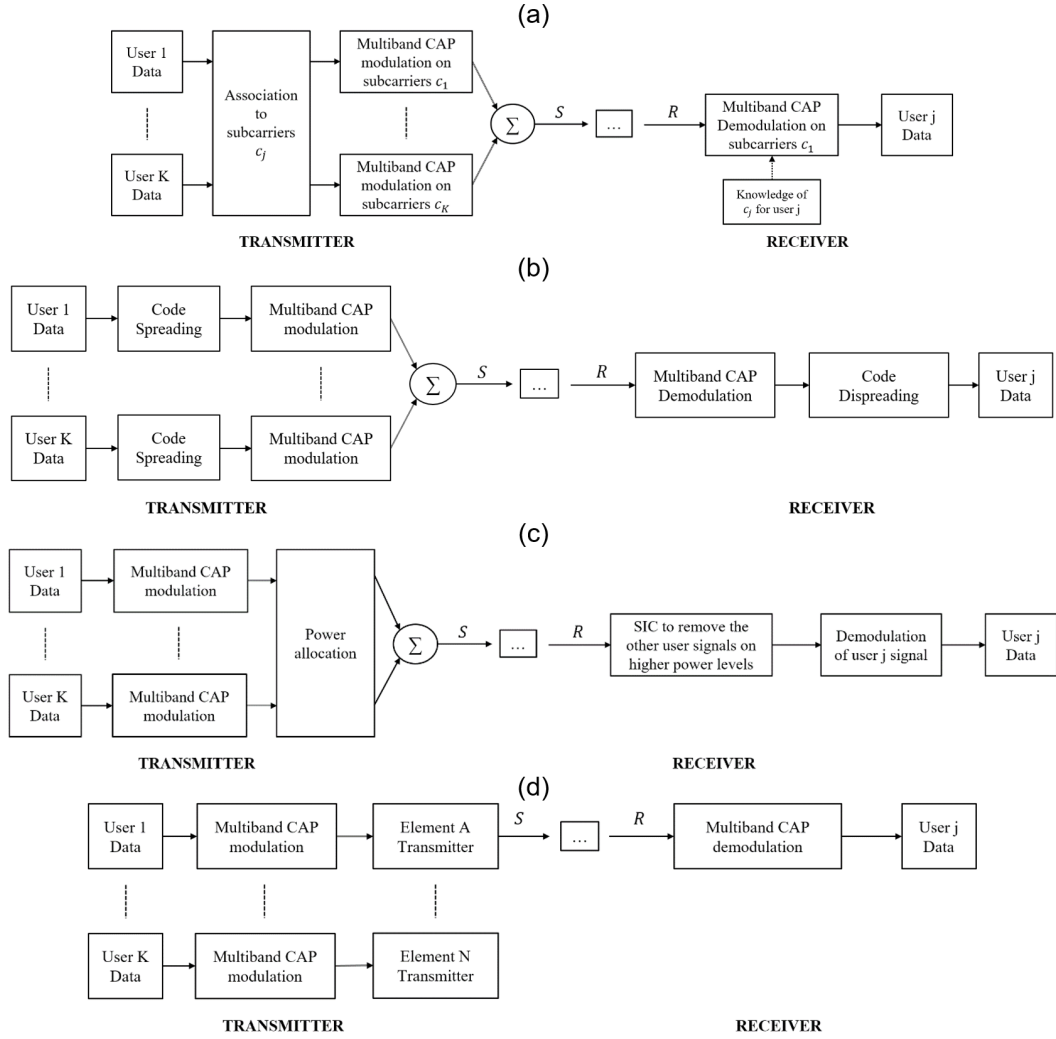


FIGURE 3.13: Simplified diagram of the association of  $m$ -CAP (a) with SCM, (b) with MC-CDMA, and (c) with PD-NOMA (d) with SDMA.

Section 3.2.2 focuses on describing the impact of the CAP, or  $m$ -CAP, modulation process on the transmission characteristics. Finally, section 3.2.3 is an overview of the possibly applicable performance enhancement techniques and their potential impact on the VLC system.

### 3.2.1 Block Diagram

Figure 3.14 is a representation of the indoor VLC system model that will be studied in numerical simulations in order to estimate the impact of each block on the single-user broadcast performances.

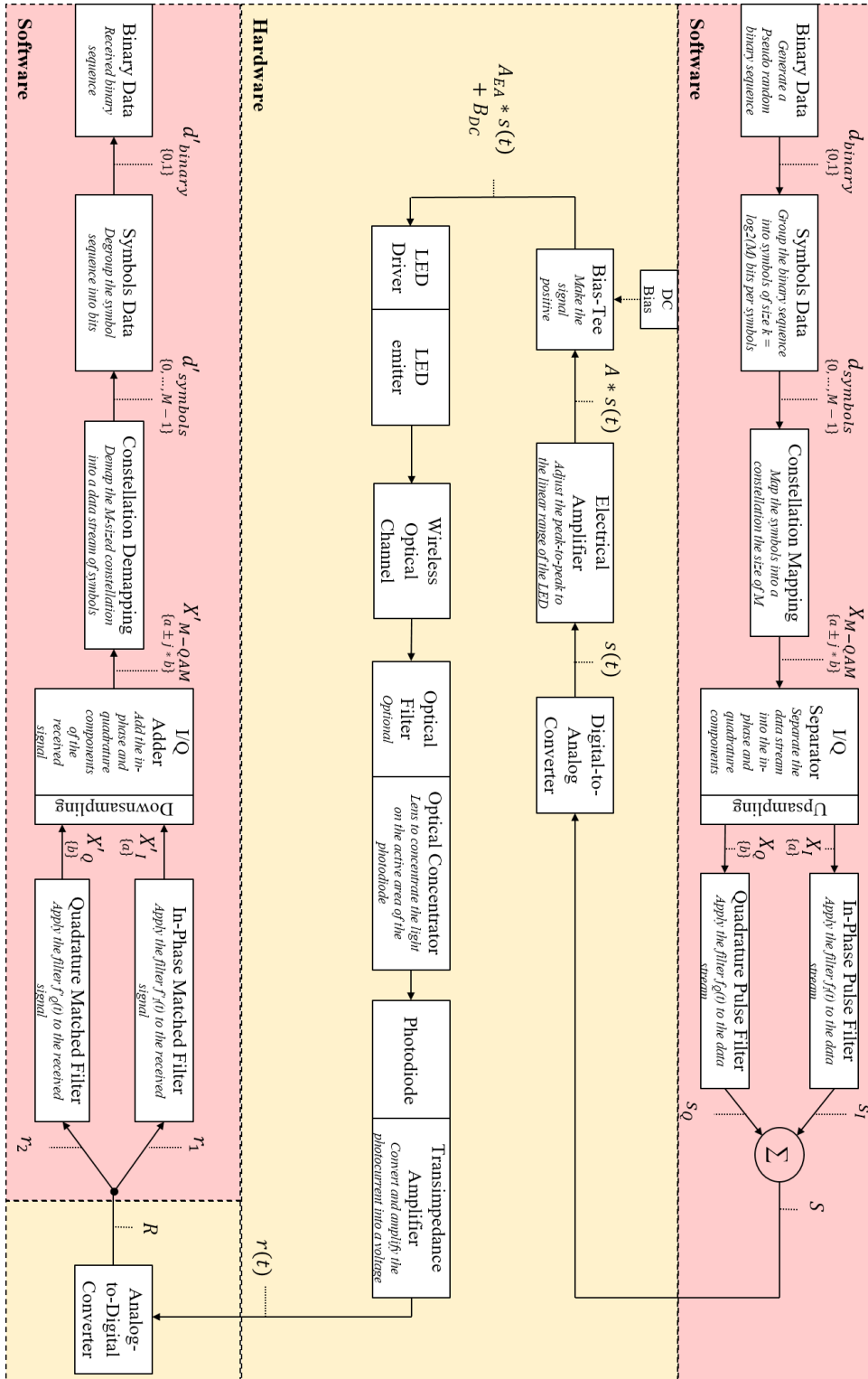


FIGURE 3.14: Block diagram representing the system model in conventional CAP used throughout the numerical simulations. The hardware elements are replaced by models as described by the following subsections.

### 3.2.2 Modulation and Performances

#### 3.2.2.1 M-QAM Mapping

The mapping process is an association between the points of a constellation and the different binary symbols. The size of a constellation designates the number of points and the transmission rate. The binary symbols of certain length are transformed into  $M$  coordinates in the constellation. In general, rectangular constellations are preferred due to their ease of implementation, despite the other shapes being more efficient in certain scenarios [226]. The mapped symbols are represented by their in-phase, or real, and quadrature, or imaginary, components. They correspond to their positions on the constellation map.  $M$  is also called the modulation order. If  $M = 16$ , 4 bits per symbols are transmitted while for  $M = 64$ , 6 bits per symbols are transmitted. For the same energy, the higher  $M$  is, the smaller the distance between each point of the constellation. In consequence, increasing  $M$  boosts the spectral efficiency but also heightens the BER. A constellation of  $M$  coordinates is associated with a set of binary symbols of length  $k = \ln_2(M)$ . Every group of  $k$  bits is transformed into its associated symbol during the mapping process. Different types of mapping exist and some of them limit the BER at the receiver. The Gray mapping is one that restricts the bit error rate [227]. The demodulation associates the received point to the nearest constellation point using the Euclidean distance. Numbers from 0 to 7 can, for example, be coded in binary with: 000, 001, 010, 011, 100, 101, 110, 111 or with the Gray coding: 000, 001, 011, 010, 110, 111, 101, 100. This coding technique ensures the smallest number of operations going from one element to the next. This is called a Hamming distance of 1.

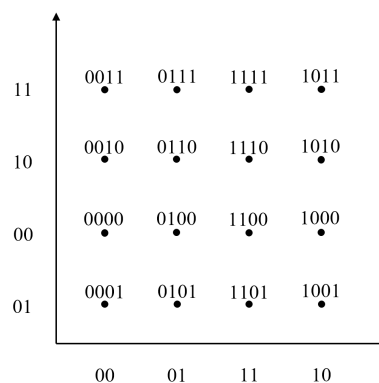


FIGURE 3.15: Illustration representing a Gray mapped constellation.

The spectral efficiency of the CAP signal increases with the number of bits per symbol coded by the  $M$ -QAM mapper, and thus scales with  $M$ . However, as explained previously the distance between each point is reduced and thus the impact of the SNR is more important as  $M$  increases. Figure 3.15 gives an example of a QAM-mapped CAP signal with a modulation order of 16. Figure 3.16 (a), (b), (c) and (d) use an SNR of 3 dB, 6 dB, 12 dB and 18 dB respectively. The simulation parameters are listed in Table 3.1. The lower the SNR is, the more spread out the constellation

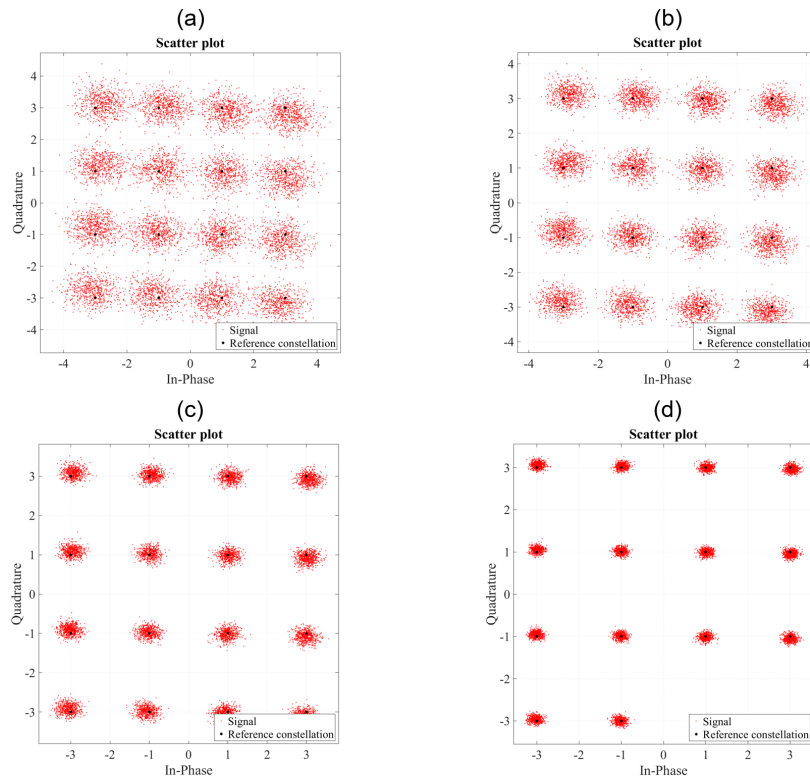


FIGURE 3.16: Simulated received constellation for  $M = 16$  at an SNR value equal to (a) 3 dB, (b) 6 dB, (c) 12 dB and (d) 18 dB.

of the received signal is. If the forward error correction (FEC) at 7% is used, a BER limit of  $3.8 \times 10^{-3}$  can be defined [228], under which a signal can be perfectly decoded given an addition of 7% for the FEC. Essentially, theoretical thresholds for the SNR can be found in order to obtain a modulation order  $M$ , shown in table 3.2.

TABLE 3.1: Simulation parameters used to obtained the  $M$ -QAM constellations on figure 3.16.

Parameter	Value
LED cutoff frequency	5 MHz
LED semi-angle at half power	$70^\circ$
Transmitted power	72 W
Distance between the transmitter and the receiver plane	50 cm
Photodiode active area	$1 \text{ cm}^2$
Receiver half-angle FOV	$60^\circ$
Reflective index of lens at the receiver	1.5
Transmission coefficient of the optical filter	1
Up-sampling factor	10
Roll-off factor	0.15
Filter span	12

TABLE 3.2: Theoretically required SNR in order for the BER at reception to be above the 7% FEC limit for each M constellation size in a CAP signal.

M	Required SNR (dB)
4	6.7
8	9.5
16	10.5
32	13.5
64	14.7
128	18

If the measured SNR on a subcarrier is superior to a SNR threshold value, the associated modulation order can be used for that subcarrier. Theoretically, the BER should end up below the FEC limit. The following subsection is an overview on the SRRC filter attributes and their impact on the modulation process. Indeed, they are the main characteristics that can be changed in the CAP and  $m$ -CAP modulation process to potentially decrease the BER.

### 3.2.2.2 Filter Parameters

The FIR filters are placed at the transmitter and receivers of each CAP or  $m$ -CAP based system and have a considerable impact on the performances of the scheme. The equations for the filter pairs are equations 3.10, 3.11 and 3.12. The two parameters that can be changed are the roll-off factor and the filter span.

The first is a parameter in the range of  $0 \leq \alpha \leq 1$  and defines the excess of bandwidth. The larger  $\alpha$  is, the larger the bandwidth of the signal. The center frequency of each subband has a multiplication factor of  $(1 + \alpha)$ . As illustrated in figure 3.17, increasing  $\alpha$  also decreases the non-linearity of the filter impulse response. With a higher value, the associated subcarrier will experience less clipping. As such, a lower value optimizes spectrum usage while a higher value reduces the impact of clipping noise.

The second parameter, filter span  $L_{SPAN}$  or the number of filter taps, noted  $L_f$ , impacts the performances of the CAP or  $m$ -CAP modulation process since the filters have a finite impulse response. The longer the filters, the more precise the filtering process is and the better the performances. However, it also increases the filter implementation complexity.

In consequence, the association of the number of subcarriers  $m$ , which defines the number of filters, with the roll-off factor  $\alpha$ , which defines the excess bandwidth, and the filter taps  $L_f$ , which defines the accuracy of the filtering process brings a trade-off between performances and implementation cost.

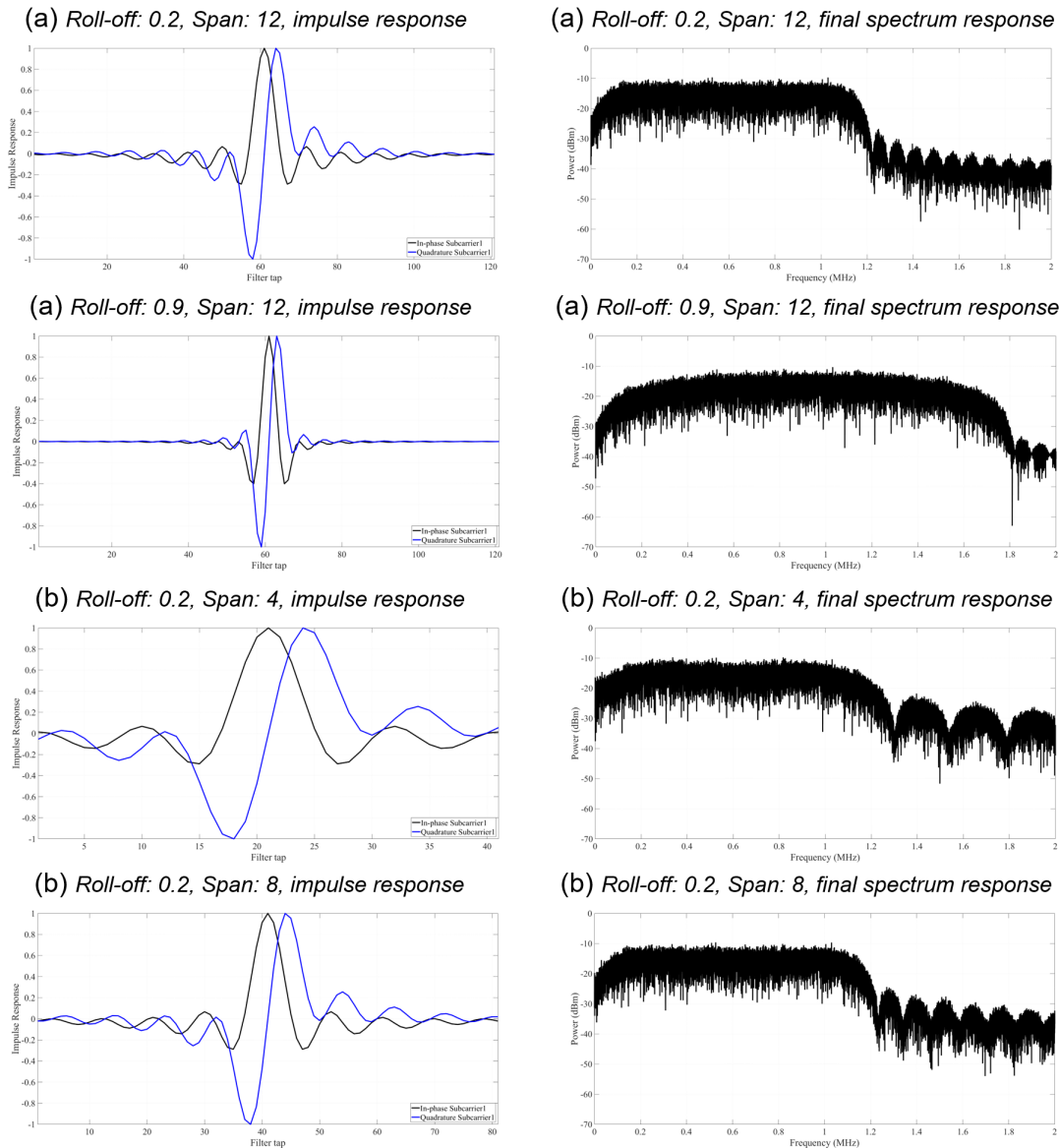


FIGURE 3.17: (a) Illustration of the filter impulse response for different roll-off factor values and (b) different filter length.

Figure 3.17 (a) illustrates the impact of the roll-off factor on the impulse response of the filter and the final spectrum of a CAP modulated signal for a filter span of 12 and roll-off values of 0.2 and 0.9. Figure 3.17 (b) illustrates the impact of the filter span on the impulse response of the filter and the final spectrum of a CAP modulated signal for a roll-off factor of 0.2 and filter span values of 4 and 8. The simulation parameters used here are as follow:

TABLE 3.3: Simulation parameters used to obtain the CAP filter responses on figure 3.17.

Parameter	Value
Number of symbols	10000
Signal bandwidth	1 MHz
Upsampling factor	10

The lower the roll-off factor is, the lower the excess bandwidth is, as shown by the spectrum responses of figure 3.17 (a). Indeed, with a base signal bandwidth of 1 MHz and a roll-off factor of 0.2, the final bandwidth attains 1.2 MHz. The advantage of increasing the roll-off factor can be shown by the impulse responses though, where the higher  $\alpha$  is, the smaller the secondary lobes of the responses are. The impact of the filter span is more straightforward, the lower the value is, the smaller the filter length is, and the more place the main lobe takes over the secondary ones in the impulse response. The impact of the filter parameters can be evaluated more deeply by examining the BER impact of each one.

Figure 3.18 (a) shows the simulated impact of the roll-off factor on the BER, depending on what filter length is used. The simulation parameters for the channel are as described in table 3.1, except the LED cut-off frequency which is set at 2.7 MHz. For figure 3.18 (a), the modulation parameters are the same as table 3.3. The results show that the higher the roll-off factor is, the better the performances until a point where the increase yields no reduction in BER. That point is, however, attained faster with a larger filter. It means that if a larger filter span is used, the optimal roll-off factor value will be lower which translates in less excess in bandwidth. This can, in turn, reduce the impact of the low-pass channel effect in case a signal bandwidth larger than the cutoff frequency is used. The SNR is low here which explains the high error floor.

Figures 3.18 (b) and (c) show an additional filter parameter analysis with the investigation of the impact of the up-sampling factor on the BER. As shown, the larger this value is, the more the signal becomes resilient to the SNR or the low-pass effect due to an increase in signal bandwidth. However, the larger the up-sampling factor is, the larger the filter length and the computational cost is. In consequence, its impact can be compared to the filter span parameter. The LED cutoff frequency is low here which explains the high error floor in this case.

### 3.2.3 Performances Enhancements

#### 3.2.3.1 Channel Estimation

Channel estimation is used at the receiver to compensate for the potential changes in the free-space optical channel with the objective of reducing the BER [229]. In VLC, the channel estimation can be part of the synchronization and equalization process. The multiple existing techniques are classified into three categories [230]. The first one is based on a training sequence called a pilot, which is used to estimate the channel. The second one uses the statistical properties of the signals such as the cyclic prefix or the frequency correlation and is called blind estimation. The third one is a hybrid of both methods using a training sequence and the properties of the signal. In [230] and [231], the authors favored the Least Squares (LS) algorithm and the minimum mean square error (MMSE) algorithm to perform estimation for a VLC-like optical

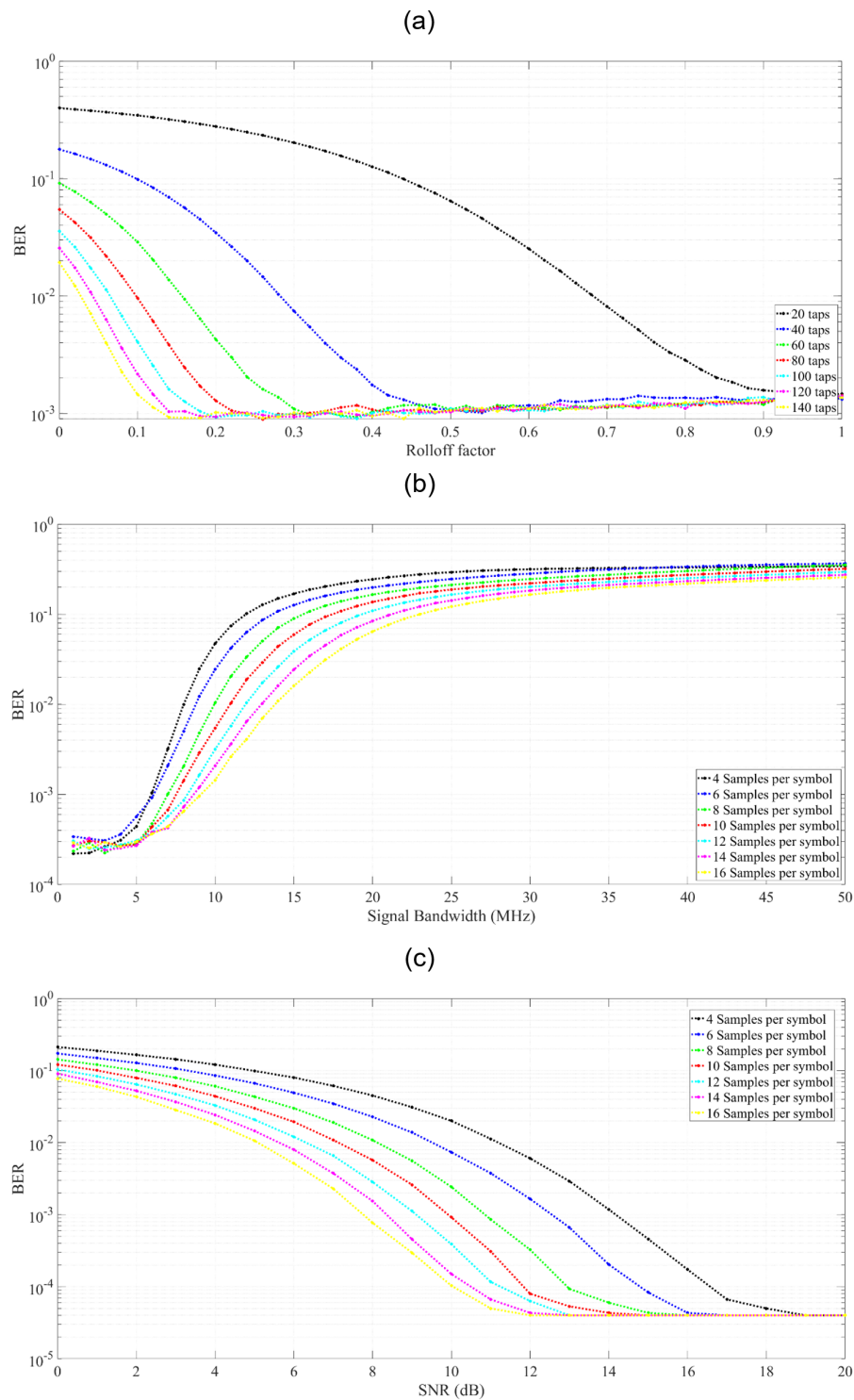


FIGURE 3.18: (a) Simulated impact of the roll-off factor on the BER for different filter spans. (b) Simulated impact of the signal bandwidth for different oversampling factors. (c) Simulated impact of the SNR on the BER for different oversampling factors.

channel. Using a block-type pilot scheme, a group of symbol is defined as pilots and are already known by the receiver in order to be able to estimate the channel using both the algorithms.

**Least Squares:**

A reverse methodology is used at the receiver. A PD receives the modulated and attenuated optical signal which can be expressed in the frequency domain as:

$$Y = \bar{X}H + W \quad (3.32)$$

With  $Y$  the received signal samples in the frequency domain is represented as a vector of size  $N$ , for the number of samples, and noted  $Y = [Y_0, \dots, Y_{N-1}]^T$ .  $\bar{X}$  is a matrix equal to  $diag(X_n)$  with  $X_n$  being the symbol for  $n^{th}$  subcarrier.  $H$  is the impulse channel response in the frequency domain and  $W$  is the additive white Gaussian noise (AWGN). The criteria for the LS estimation method is to minimize the least square errors. Thus, to find the channel estimation, the sum of squared errors  $\varepsilon(.)$  is defined in the frequency domain as:

$$\varepsilon(H) = \|Y - \bar{X}H\|^2 = (Y - \bar{X}H)^H(Y - \bar{X}H) \quad (3.33)$$

Where  $\|\cdot\|$  is the non-negative norm of a vector and  $(\cdot)^H$  is the Hermitian transposition. Thus, the normalized value of the estimation can be given by:

$$\hat{H}_{LS} = \arg \min \varepsilon(H) \quad (3.34)$$

When using the differential derivative, with the channel coefficient appropriately set to zero, the following equation is given:

$$\frac{\partial}{\partial H}(Y - \bar{X}H)^H(Y - \bar{X}H) = 0 \quad (3.35)$$

In the frequency domain, with the LS algorithm applied, the channel estimation is given as below:

$$\hat{H}_{LS} = \frac{Y}{\bar{X}} \quad (3.36)$$

If we substitute equation 3.32 into equation 3.36, we obtain:

$$\hat{H}_{LS} = H + \frac{W}{\bar{X}} \quad (3.37)$$

Where  $W/\bar{X}$  is the estimated error and  $\widehat{H}_{LS}$  is the objective of the channel estimation.

**Minimum Mean Square Error Estimation:**

In order to find the missing parameters that define the channel, MMSE consists in minimizing the mean square error (MSE). To define the method, the linear estimator operator  $L$  needs to be defined as:

$$\hat{H}_{MMSE} = LY \quad (3.38)$$

Thus, the MSE for the channel estimation in a VLC system can be given by:

$$\partial(L) = E[||H - \hat{H}_{MMSE}||^2] \quad (3.39)$$

Where  $E[.]$  denotes the expectations operator. The first step is to determine  $L$  in order to obtain the MMSE channel estimation.  $L$  must be satisfied as defined as follows:

$$\hat{L} = \arg \min \partial(L) \quad (3.40)$$

This looks like the equation 3.34 for LS, and using the differentiating derivative and setting the result to zero appropriately for the coefficient of  $L$ , we find:

$$\frac{\partial}{\partial L} E[(H - LY)(H - LY)^H] \quad (3.41)$$

Solving this equation,  $L$  can be found with:

$$\hat{L} = \frac{R_H \bar{X}^H}{\bar{X} R_H \bar{X}^H + R_w} \quad (3.42)$$

Where  $R_w = E[WW^H]$  is the covariance matrix of noise and  $R_H = E[HH^H]$  is the covariance matrix of the channel coefficient, both in frequency domain. We define the noise variance as  $\sigma^2$ . Thus the MMSE channel estimation method can be formulated as:

$$\hat{H}_{MMSE} = \hat{L}Y = \frac{\partial}{\partial L} E[(H - LY)(H - LY)^H]Y = R_H \left[ \frac{1}{R_H + \sigma^2 \frac{1}{\bar{X}\bar{X}^H}} \right] \hat{H}_{LS} \quad (3.43)$$

This channel estimation method mitigates the noise effects in a better manner than the LS technique, as shown by equation 3.43, but requires more prior knowledge on the covariance matrix and has a higher implementation cost.

Figure 3.19 illustrates the impact of the LS and MMSE channel estimation algorithms on the BER for different SNR values. The simulation parameters were the same as described in Table 3.4 except that the signal bandwidth was set at 10 MHz and  $M$

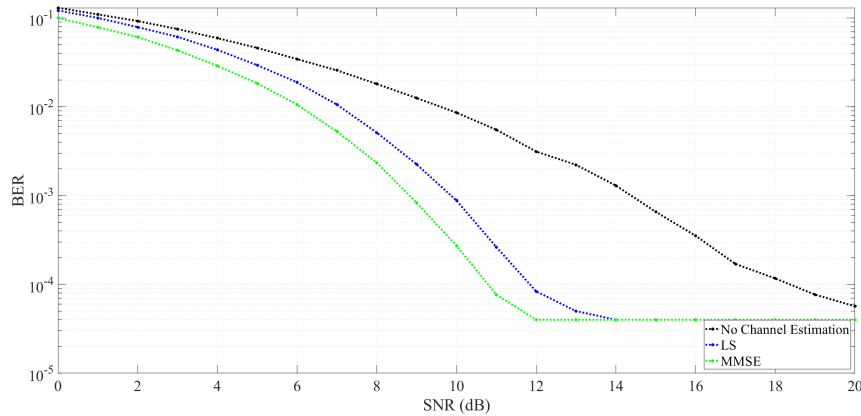


FIGURE 3.19: Simulated impact on the simulated BER against the SNR by the use of no channel estimation, an LS-based method and MMSE-based technique.

was set at 16. The low-pass effect of the channel, due to the bandwidth being higher than the cutoff frequency is compensated. Due to this benefit, the BER is significantly decreased except in situations with a low SNR because the noise dominates the signal. It can potentially be used in association with the performance enhancement technique described in the following subsection, equalization.

TABLE 3.4: Simulation parameters used to obtain the impact of channel estimation on the BER in figure 3.19.

Parameter	Value
LED Cut-off frequency	2.7 MHz or 14 MHz
LED semi-angle at half-power	70°
Transmitted power	72 W
Distance between the transmitter and the received plane	50 cm
Photodiode active area	1 cm <sup>2</sup>
Receiver half-angle FOV	60°
Reflective index of the lens at the receiver	1.5
Transmission coefficient of the optical filter at the receiver	1
Up-sampling factor	10
Roll-off factor	0.3
Filter span	6
Number of symbols	75000

### 3.2.3.2 Equalization

While channel estimation estimates the channel state at the receiver for better performances, equalization is used in at the emitter and receiver in order to correct

the transmission errors by compensating at the pre-equalizer and reducing the inter-symbol interferences at the receiver:

### Pre-equalizer:

When trying to achieve high speed communication with VLC using high power commercial LEDs, numerous problems arise, as discussed so far. The main bottleneck is the commercial LEDs modulation bandwidth which is limited to the upwards of tens of MHz. However, these values are not enough to attain a multi-gigabits wireless optical communication with LEDs, which is one of the main objective of indoor VLC, as seen in chapter 1. One of the main approaches is to extend that -3dB modulation bandwidth with what is called pre-equalization. The principle of the technique is to fit the signal to the transmission channel. It is achieved by increasing the relative power of high frequency component and attenuating the lower frequencies. While it does also bring the noise up, it extends the modulation bandwidth for much higher throughput.

When driven by a short current pulse, LED response can be modeled by a first order RC filter.  $T_r$  is the rise time of the LED response and  $T_f$  is the fall time of the LED response. Fall time in the case of a ph-LED is much longer because of the slow response of the phosphorus LED part.

$$h_{LED} = e^{-\omega_c t} \quad (3.44)$$

With  $\omega_c = \nu / (T_r + T_f)$  and  $\nu$  being a tuning parameter that depends on the LED. This continuous LED temporal response can be transformed with a Laplace transform into the  $S$  domain and is given by:

$$H_{LED}(S) = \frac{1}{S + \omega_c} \quad (3.45)$$

A first order pre-equalizer would thus be designated as:

$$H_{equ}(S) = \frac{1}{H_{LED}(S)} = S + \omega_c \quad (3.46)$$

Such an equalizer would increase the high frequency response along with the noise.

### Post-equalizer:

Post-equalizers are used to reduce inter-symbol interference to allow the recovery of the transmitted symbols. A linear equalizer placed in series with the channel will produce an estimate of the channel inverse transfer function. It consists in a real FIR filter if the transmitted symbols are real as well or a complex FIR filter if they are complex, such as in a QAM based system. Typically, their coefficients

are updated with the least mean square (LMS) algorithm. The performance of a linear equalizer is, however, not optimal for channels with severe amplitude distortion, such as an indoor VLC channel. In fact, since the equalizer reproduces the channel inverse transfer function, in order to compensate for the strong attenuation in certain frequency bands it will be compelled to generate strong gains in the same frequency bands. This means that not only the signal is amplified in those frequency bands, but also any noise will be as well. Decision feedback equalizers (DFE) are used to solve that problem. It is a filter that uses feedback of detected symbols to produce an estimate of the channel output. The DFE is fed with detected symbols and produces an output which is typically subtracted from the output of a linear equalizer. Since the DFE can only estimate the post cursors, it needs to be used in combination with a linear equalizer. During the steady-state operation, the DFE contains an estimation of the impulse response of the channel or the convolution of the channel with the linear equalizer. Since the DFE copies the channel output and this output is subtracted from the incoming signal, it can compensate for severe amplitude distortion without increasing the noise in the highly distorted frequency bands, making it ideal for a VLC indoor channel.

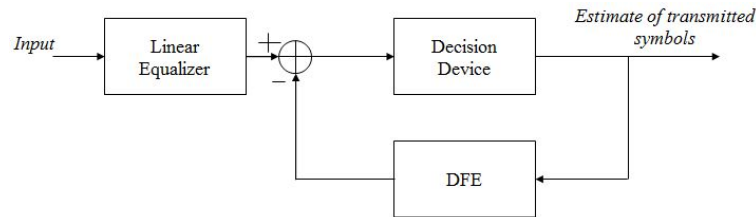


FIGURE 3.20: Simplified illustration of the principle for a Decision Feedback Equalizer (DFE).

DFE can thus be used to mitigate the effect of the ISI. The feedback filter can remove the ISI introduced by the previously detected symbols on the presently estimated symbols. Using [232], the DFE output is given by:

$$q_m = \sum_{i=0}^{N_1} c_n y_{m-n} - \sum_{i=0}^{N_2} b_n \hat{d}_{m-n} \quad (3.47)$$

Where  $c_n$  and  $b_n$  are the filter tap coefficients of the feed-forward and feedback filters, respectively. The detected symbol is given by  $y_{m-n}$  and  $\hat{d}_{m-n}$  is the previously estimated symbol.  $N_1$  and  $N_2$  correspond to the length of the feed-forward and feedback filters.

Figure 3.21 shows the impact of pre-equalization and post-equalization with DFE on the BER for a variation of SNR and a signal bandwidth of 20 MHz (a), 50 MHz (b) and 80 MHz (c). The simulation parameters for the channel were the same as in Table 3.4, with the cut-off frequency of 2.7 MHz and the rest of the parameters were as follow:

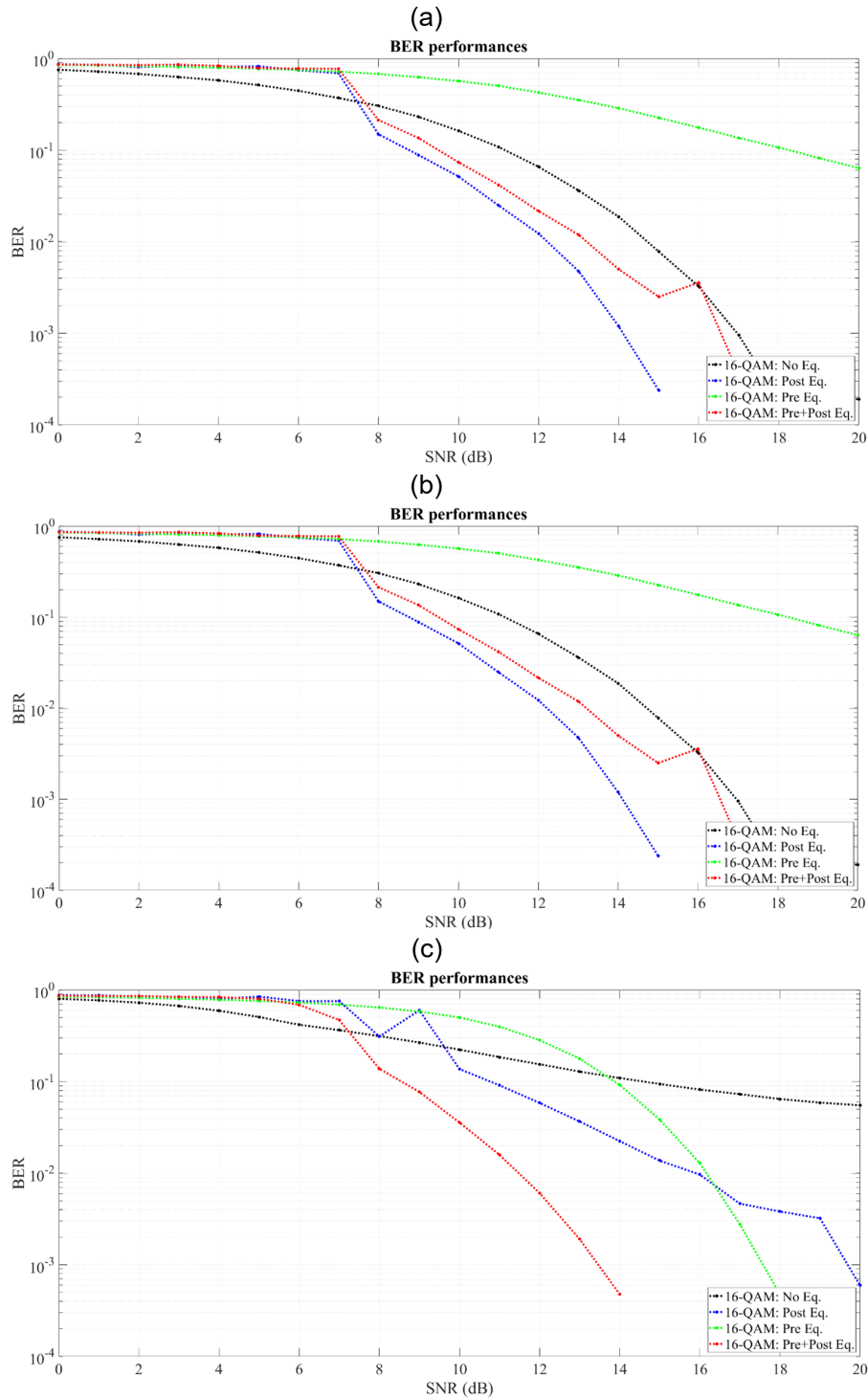


FIGURE 3.21: Simulated impact on the BER against the SNR of the use of pre- and post-equalization for a signal bandwidth of (a) 20 MHz, (b) 50 MHz and (c) 80 MHz.

As shown by figures 3.21 (a), (b) and (c), the effect of the pre-equalization alone is more pronounced the higher the signal bandwidth is. Indeed, since this method fit the signal to the channel it has a more profound impact on signals that are impacted by a signal attenuation due to low-pass channel. However, its performances are only better

TABLE 3.5: Simulation parameters used to obtain the impact of equalization on the BER in figure 3.21.

Parameter	Value
Number of symbols	10000
Modulation order M	16
Up-sampling factor	10
Roll-off factor	0.35
Filter span	12
Linear equalizer type	Recursive Least-Squares (RLS)
Training length	100 symbols
RLS parameter (forget factor)	0.99
Number of feed-forward weights	15
Number of feedback weights	10

than a non-equalized signal when the signal bandwidth is at 50 MHz or 80 MHz and the SNR is larger than 17.2 dB and 13.5 dB respectively. Indeed, while the response at higher frequencies is better for the signal with pre-equalization, the noise has been brought up. The negative effect of pre-equalization at the lower signal bandwidth is also due to the pre-emphasis method being set for the higher frequencies. For the post-equalization scheme, the results are better than a non-equalized signal except when the SNR is too low because this prevents the DFE from removing the ISI. As expected, the combination of the two methods yields the better results as long as the signal bandwidth is not too small. Indeed, at 20 MHz, the result of the combination is worse than the use of only the post-equalization scheme. On the other hand, at 50 MHz and 80 MHz signal bandwidth, while the results for pre-equalization are only better than the non-equalized signal at 17.2 dB of SNR and 13.5 dB, the combination of pre- and post-equalization is better than the non-equalized signal at SNR values of 7.3 dB for figures (b) and (c). In consequence, equalization seems like a justified method to attain larger throughput with a VLC system, at least in simulation.

### 3.2.3.3 Subcarrier Spacing

Multiband CAP uses pulse shaping filters that do not have a perfect rectangular frequency response and is therefore subject to inter-channel interferences (ICI). They reduce the quality of the received signal by adding noise on each adjacent subcarrier. Spacing the subcarriers would mitigate these interferences. The cost is an increase in signal bandwidth but for a reduction in ICI. While the extension of the bandwidth will reduce the SNR because of the low-pass effect of the VLC channel, the BER could potentially still decrease with the diminution of the ICI.

For the definition of the multiband CAP Hilbert pair filters for each subcarrier, we can add a factor to their definition as follow:

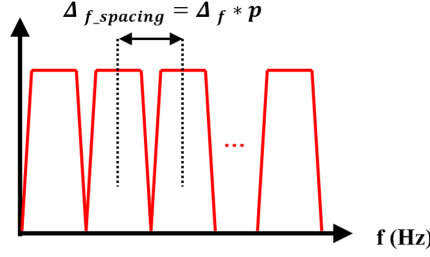


FIGURE 3.22: Multiband CAP filters responses illustration and the impact of subcarrier spacing with factor  $p$ .  $\Delta_f$  is the frequency increment between each subband without spacing.  $\Delta_{f\_spacing}$  is the frequency increment between each subband with spacing.

$$g_{SRRC}(t) = \frac{2\alpha[\cos(\frac{(1+\alpha)\pi t}{T_S}) + (\frac{4\alpha t}{T_S})^{-1} \sin(\frac{(1-\alpha)\pi t}{T_S})]}{\pi\sqrt{T_S}[1 - (\frac{4\alpha t}{T_S})^2]} \quad (3.48)$$

$$f_I^n = g(t) \cos(\pi \frac{t}{T_S} (2n-1)(1+\alpha)p) \quad (3.49)$$

$$f_Q^n = g(t) \sin(\pi \frac{t}{T_S} (2n-1)(1+\alpha)p) \quad (3.50)$$

With  $p$  the subcarrier spacing configuration factor. It is used to configure the spacing between subbands. The value of the center frequency for each subcarrier is changed when  $p$  is adjusted. Initial value is 1, which corresponds to no subcarrier spacing, with  $p \in ]0 : +\infty[$ . When  $p$  increases, the signal bandwidth is extended as well by a factor of  $(p-1) * 100$  percent.

Figure 3.23 (a) shows different spectrum of  $m$ -CAP modulated signals with subcarrier spacing values of 0%, 10%, 20% and 30%. These simulated results were obtained using the same channel parameters as table 3.4, the same equalization parameter as table 3.5 and the same modulation parameter as table 3.5 except that  $m$ -CAP with 20 subcarriers was used and the roll-off factor was set at 0.15. The spacing between each subband increases with the subcarrier spacing factor and as such, the total signal bandwidth increases as well by the same factor. The impact on the BER is illustrated in figure 3.23 (b), for an  $m$ -CAP signal with 10 subcarriers this time for more clarity in the graph. The SNR is low and the signal bandwidth much higher than the LED cutoff frequency in this case, which explains the high BER at the later subcarrier. This scenario simulates our use of a ph-LED with a focus on maximized data rate. The total BER increases with the increase of subcarrier spacing since the signal bandwidth expands by the same factor as well. However, when looking at the BER of each subcarrier individually, the result is different. Essentially, for the subcarriers at the lower frequencies, an increase in subcarrier spacing can reduce the BER of that specific subband. This is the case for subcarrier 1, for subcarrier 2, for subcarrier 3 until a spacing value of 50%, for subcarrier 4 until a spacing value of

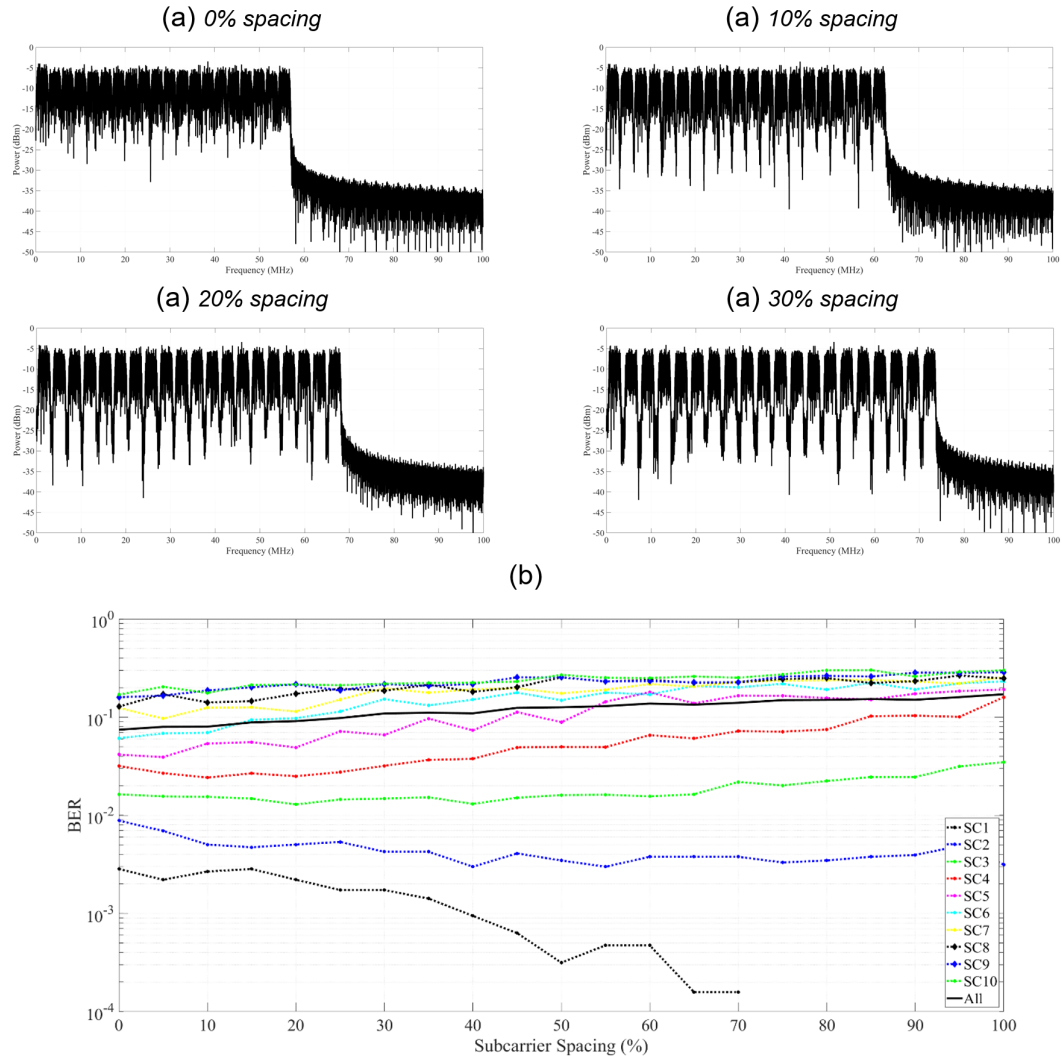


FIGURE 3.23: (a) Simulated spectrum emitted for an  $m$ -CAP signal using subcarrier spacings values of 0% (top left), 10% (top right), 20% (bottom left) and 30% (bottom right). (b) Simulated impact on the BER using different subcarrier spacing values and for each of the 10 subcarriers of the 10-CAP simulated signal.

30% and for subcarrier 5 until a spacing value of 5%. This means that for a given  $m$ -CAP signal characteristic, there exist a value of subcarrier spacing that can optimize the performances of each subband. This attribute will be investigated and expanded upon during the experimental measures in chapter 4.

### 3.3 Application with Multi-Access Schemes

The multi-access schemes allow a modulation like multiband CAP to have the ability to serve multiple users in an indoor VLC system. Each existing scheme use a different principle and offers different performances at the physical layer. Section 3.3.1 describes what an attocell in VLC is in order to set up a basis for comparison between different multi-access schemes. Section 3.3.2 expands on the characteristics of

an attocell and uses simulation results as examples to illustrate them. Finally, section 3.3.3 takes a look at a key problematic with the user allocation issue in VLC.

### 3.3.1 The Definition of an Attocell in VLC

Wireless communications have, in the past, aimed to decrease their cell size in order to improve the network efficiency. Nowadays, cell networks incorporate new cell of various smaller sizes, called microcells, picocells or femtocells in what is now named heterogeneous networks [233][234]. The closest to a VLC cell would be the femtocells [235]. There are cells with a short range, low transmission power, low-cost base stations that are deployed in indoor environment in order to optimally cover an area. The femtocells use the same bandwidth as the larger mobile communications networks and thus increase the data rate per unit area with improved frequency reuse. The main disadvantage is that when they are deployed in an uncoordinated and random manner, the cells will cause inter- and intra-cell interferences, offsetting their potential gains. Optical access points are referred to as attocells [236]. With VLC, they help reduce the interferences due to the light that does not interfere with RF. Wireless network access becomes available anywhere as the users can switch seamlessly between the Li-Fi and RF cells, conserving both mobility and high throughput in any space.

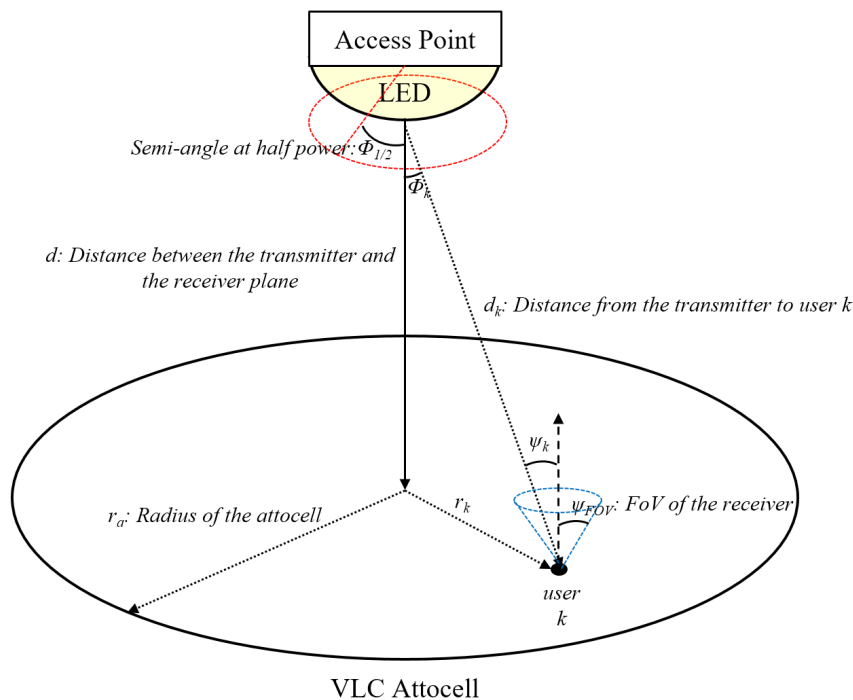


FIGURE 3.24: Illustration representing an attocell in VLC.

### 3.3.2 Characteristics of an Attocell

Figure 3.24 illustrates a VLC access point and the attocell associated with it. The non-line-of-sight paths are not considered in this work as the receiver is directly under

the light source, and the reflections from the floors and walls via the diffuse channel are ignored.

The characteristics of a single VLC attocell are as follow:

- **The cell size:** As shown in the figure, the single attocell is associated to a circle with the covered area equal to  $A_c = \pi.r^2$  with  $r$  the radius of the attocell. All user within that serviceable area should be able to communicate under the same conditions.
- **The range:** It is the distance between the VLC AP plane and a receiver plane served by this access point.
- **The maximum number of users:** It corresponds to the maximum number of independent channels that can be allocated to users by the VLC access point.
- **The throughput:** the maximum data rate available for a single user. The coverage area and the maximum throughput can be tied together with the data rate per unit of area.

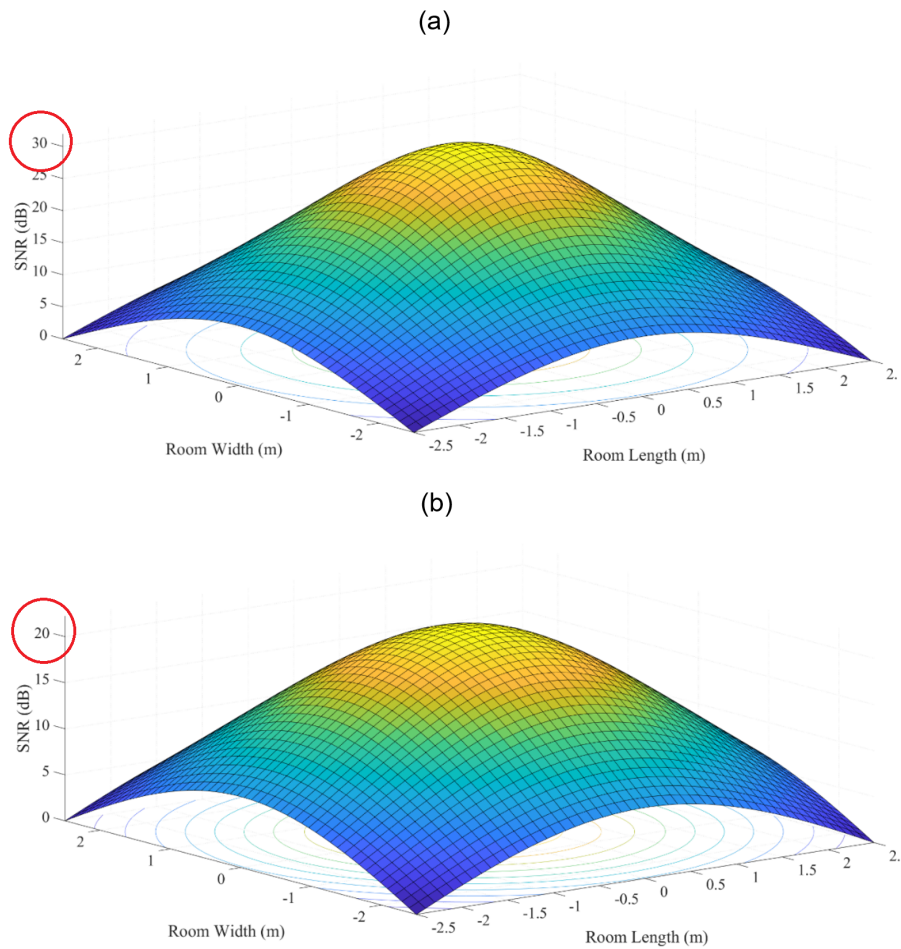


FIGURE 3.25: Simulated 3D SNR distribution for a distance between the transmitting and receiving planes of (a) 1.5 m and (b) 2.15 m.

In order to evaluate these characteristics, an attocell is simulated for an indoor VLC system. As indicated by the numerous measures in appendix A on the broadcast channel performance breakdown, the SNR is a measurable that can represent the performances of a VLC system. Indeed, depending on the SNR value for a receiver at a given point of space, the performances of the system can be estimated. For this reason, figure 3.25 shows the distribution of SNR in a room for a transmitter to receiver plane distance of 1.5 m (a) and 2.15 m (b). The simulation parameters used to obtain these figures were as follow:

TABLE 3.6: Simulation parameters used to obtain the 3D SNR distributions in figure 3.25.

Parameter	Value
Room size	5x5x3 m <sup>3</sup>
Reflection coefficient	0.8
LED Location	(2.5, 2.5, 3)
LED semi-angle at half-power	30°
Transmitted power	72 W
Distance between the transmitter and the receiver plane	1.5 m or 2.15 m
Photodiode active area	1 cm <sup>2</sup>
Receiver half-angle FOV	70°
Refractive index of the lens at the receiver	1.5
Transmission coefficient of the optical filter	1
Photodiode responsivity	0.4 A/W
Amplifier bandwidth	150 MHz
Data rate	1 Mb/s
Dark current	2 uA
Open-loop voltage gain	5000 V/A
Absolute temperature	298 K
Fixed capacitance of the photodiode per unit area	112 pF
FET trans-conductance	0.03 S
Noise-bandwidth factor $I_2$	0.562
Noise-bandwidth factor $I_3$	0.0868

The amplifier characteristics come from the Thorlabs PDA10A-EC [237]. In figure 3.25 (a), we can see the SNR distribution in the room for a distance between the transmitter and the receiver plane of 1.5 m. In that scenario, the SNR is above 30 dB in a circle of 1 m of diameter directly under the transmitter. If we take as a condition a SNR above 18 dB, for a modulation order  $M = 128$  or 7 bits per symbols, a circle of 3.36 m of diameter is obtained, or an area of 8.867 m<sup>2</sup>. This translates to an attocell size of 8.867 m<sup>2</sup>, with a QAM modulation order of at least 7 bits per symbols per subcarrier, under the bandwidth of the amplifier. If the association of SCM with  $m$ -CAP is used, the maximum number of users would be equal to the number of subcarriers used by the modulation. If the distance between the transmitter and the

receiver plane is 2.15 m on the other hand, the results differ, as shown in figure 3.25 (b). Indeed, with the same SNR condition, a circle of 2.26 m of diameter is obtained directly below the transmitter. This translates to an attocell size of only 4.01 m<sup>2</sup>, where a QAM modulation order of at least 7 bits per symbols per subcarrier can be used. The characteristics of the attocell are very sensitive to the distribution of SNR throughout the room.

### 3.3.3 User Allocation

User allocation is a key problematic associated with the capacity of a single attocell both in terms of the number of users and the throughput per user. Every association of  $m$ -CAP with a multi-users access scheme involves a resource that will be shared by the users. In the case of SCM it is a subcarrier, with MC-CDMA it is a code, with PD-NOMA it is a power level and with SDMA it is an element of the transmitter. A user allocation algorithm needs to associate each user to a resource in an optimal way. Additionally, in VLC, higher variations in signal-to-noise ratio are present [238][239] and as such, user allocation algorithms need to be adapted to these conditions. To evaluate a user allocation algorithm in a practical way in VLC, we define a target data rate for every user in a given scenario. Depending on the allocation, the data rate attained by each user might be deviated from this target. This measurable allows for an easy way to evaluate the efficiency of a user allocation algorithm.

#### 3.3.3.1 In SCM

In an association between subcarrier multiplexing and multiband CAP, each user is associated to one or more subcarriers. Each subband will potentially have a different modulation order, represented by  $M$ .  $k$  is defined as the number of bits that each constellation symbol corresponds to. Each user has a target data rate, defined as  $D_{tar}$  and the aim of the algorithms is to get as close as possible to that objective, knowing that the number of subcarriers allocated is limited. The associated  $k$  is called  $k_{tar}$ . Four algorithms are investigated. Performances are estimated with the attained deviation from the target data rate. This parameter is equal to 0 % when the target is attained or exceeded. When the target is not attained, the deviation from it is represented as a positive percentage. The sum of the target throughput for each user is equal to the total available data rate.

The first algorithm is a direct static allocation where the average center frequency of all the allocated subcarriers to a specific user is close to the center of the total signal bandwidth. It is not represented with figures 3.26, 3.27, and 3.28 because it is a straight non-dynamic allocation. The aim is to ensure equal quality of service (QoS) for each user in terms of SNR. This scheme also has low implementation cost. In the measures presented in figures 3.29 and 3.31 it is called 'static allocation'. The second algorithm is an SCM allocation scheme first found for OFDM in fiber-optic communication [240]. It is recalculated when the system changes the modulation

order of a subcarrier, thus being a dynamic scheme. In the measures presented in figures 3.29 and 3.31 it is called 'fiber allocation'. The third algorithm is based on the second one and is adapted to the conditions of large swings in SNR in a VLC channel. This algorithm is named 'proposed method 1'. In the measures presented in figures 3.29 and 3.31 it is called 'dynamic allocation 1'. The fourth algorithm, named 'proposed method 2' is the same as the previous one except that QoS for each user is considered in the same way as in the first algorithm. In the measures presented in figures 3.29 and 3.31 it is called 'dynamic allocation 2'.

Figures 3.26, 3.27, and 3.28 represents the algorithms for the fiber optic user allocation method and the two proposed algorithms. For these figures, we define  $N$  as the number of subcarriers with  $n$  representing the  $n^{\text{th}}$  subcarrier and  $\in [0, N - 1]$ .  $M$  is the number of users with  $m \in [1, M]$ .  $S_N$  is the set of available subcarriers and  $S_M$  is the set of available users with less than  $k = N/M$  subcarriers allocated to it.  $N_m$  is the number of subcarriers allocated to user  $m$ .  $c(n)$  is the index of the user being assigned to subcarrier  $n$ .  $S_N \setminus n$  denotes the removal of the  $n^{\text{th}}$  subcarrier from the set  $S_N$ .  $D_m$  is the current data rate for the  $m^{\text{th}}$  user and  $D_{tar,m}$  is the target data rate for user  $m$ .

Algorithm 2: Otani Algorithm 1

```

1: Initialize
2:    $c(n) = 0, \forall n \in \{1, \dots, N\}$ 
3:    $N_m = k, \forall m \in \{1, \dots, M\}$ 
4:    $S_N = \{1, 2, \dots, N\}$ 
5:    $S_M = \{1, 2, \dots, M\}$ 
6:   While  $||S_N|| > 0$  do
7:      $m, n = \arg \max_{m \in S_M, n \in S_N} |H_{m,n}|$ 
8:      $c(n) = m$ 
9:      $S_N = S_N \setminus \{n\}$ 
10:     $N_m = N_m - 1$ 
11:    If  $N_m = 0$  then
12:       $S_M = S_M \setminus \{m\}$ 
13:    End If
14:  End While
15: End

```

FIGURE 3.26: Algorithm implementation for the fiber-optics-based algorithm.

Algorithm 3: Proposed Algorithm 1

```

1: Initialize
2:    $c(n) = 0, \forall n \in \{1, \dots, N\}$ 
3:    $N_m = k, \forall m \in \{1, \dots, M\}$ 
4:    $S_N = \{1, 2, \dots, N\}$ 
5:    $S_M = \{1, 2, \dots, M\}$ 
6:   While  $||S_N|| > 0$  do
7:      $m, n = \arg \max_{m \in S_M, n \in S_N} |H_{m,n}|$ 
8:      $m, n = \arg \min_{m \in S_M, n \in S_N} |D_{tar,m} - D(n)|$ 
9:      $c(n) = m$ 
10:     $S_N = S_N \setminus \{n\}$ 
11:    If  $D_m \approx D_{tar,m}$  then
12:       $S_M = S_M \setminus \{m\}$ 
13:    End If
14:  End While
15: End

```

FIGURE 3.27: Algorithm implementation for the proposed algorithm 1. The changes with the fiber-optics-based algorithm are highlighted in color.

Algorithm 4: Proposed Algorithm 2

```

1: Initialize
2:    $c(n) = 0, \forall n \in \{1, \dots, N\}$ 
3:    $S_N = \{1, 2, \dots, N\}$ 
4:    $S_M = \{1, 2, \dots, M\}$ 
5: While  $\|S_N\| > 0$  do
6:   For  $m = 1$  to  $M$  then
7:      $n = \arg \max_{n \in S_N} |H_{m,n}|$ 
8:      $n = \arg \min_{n \in S_N} |D_{tar,m} - D(n)|$ 
9:      $c(n) = m$ 
10:     $S_N = S_N \setminus \{n\}$ 
11:    If  $D_m \approx D_{tar,m}$  then
12:       $S_M = S_M \setminus \{m\}$ 
13:    End If
14:  End For
15: If  $\|S_N\| \leq 0$  then
16:   break
17: End If
18: For  $m = M$  to  $1$  then
19:    $n = \arg \max_{n \in S_N} |H_{m,n}|$ 
20:    $n = \arg \min_{n \in S_N} |D_{tar,m} - D(n)|$ 
21:    $c(n) = m$ 
22:    $S_N = S_N \setminus \{n\}$ 
23:   If  $D_m \approx D_{tar,m}$  then
24:      $S_M = S_M \setminus \{m\}$ 
25:   End If
26: End For
27: End While
28: End

```

FIGURE 3.28: Algorithm implementation for the proposed algorithm 2. The changes with the fiber-optics-based algorithm are highlighted in color.

Figure 3.29 represents the deviation from the target obtained after allocation for each of the algorithm and averaged for every user in a 4-users scenario (a) and an 8-users scenario (b). The simulation parameters for the allocation algorithms were the same as in table 3.5 except that the number of subcarrier was varying from 4 to 100. Also, the modulation order of each subcarrier was randomized around the optimal values already attained in simulation. This was to simulate the varying conditions of a VLC attocell. The static algorithm offers the worse performances since it does not directly aim at reducing the deviation and only allocate in a fixed manner without adapting to the changes in modulation order. The fiber and dynamic allocations performed similarly except that the latter are more adapted to the large SNR changes in the simulated VLC environment. However, the more subcarriers there is available and the lesser the difference is between the algorithms. It should also be noted that a periodicity corresponding with when the number of users and the number of subcarriers are divisible is observable. Indeed, a lower deviation is then attained because all users are allocated to the same number of subcarriers and have relatively equal quality of signal. Finally, when doubling the number of users to 8, the behavior already observed do not change but the value of the deviation increases considerably.

### 3.3.3.2 In MC-CDMA

In an association between multi-carrier CDMA and multiband CAP, each user is associated to a different code. The work presented here will be the evaluation of

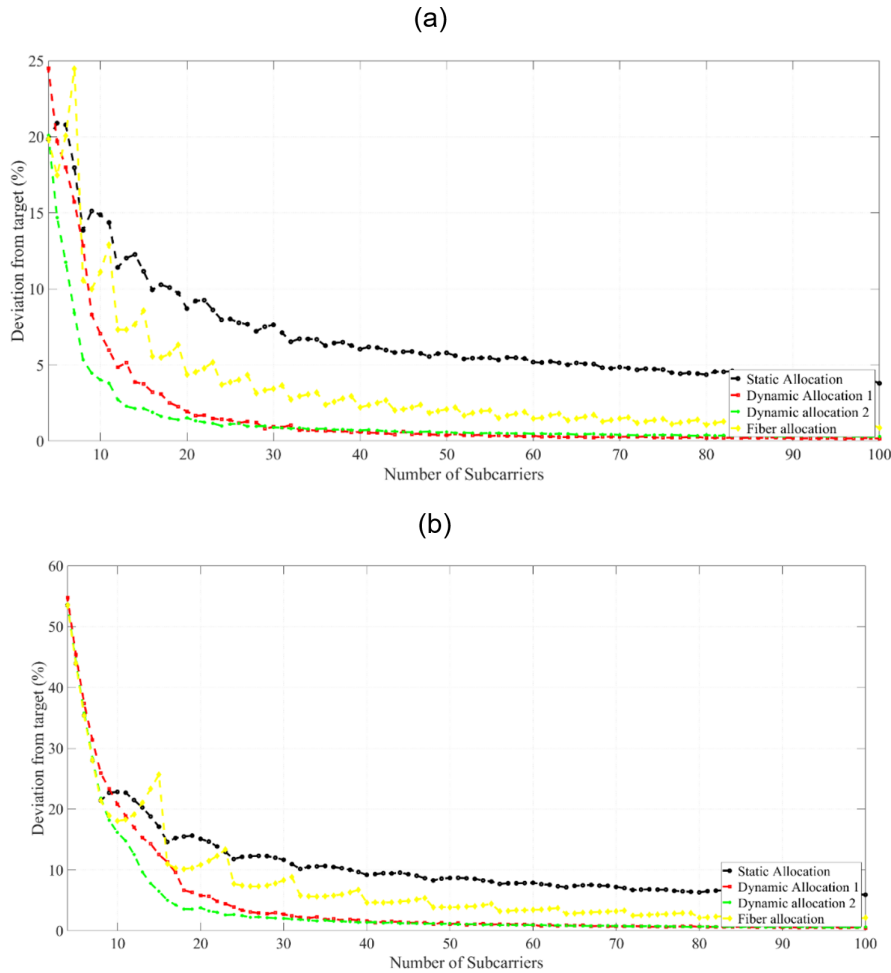


FIGURE 3.29: Simulated deviation from a random target for different number of subcarrier in (a) a 4-users scenario and (b) an 8-users scenario.

the user allocation algorithms in a numerical simulation. In the case of M-CDMA, every orthogonally coded  $m$ -CAP signal contains the same number of subcarrier to be allocated and they are not divided between users. The key problematic that needs to be highlighted is the fact that signal attenuation, which is very high in a VLC system, will decrease the SNR. With a lower value, orthogonality between codes becomes partially impaired by the noise. Hence, for a given target, variations in the modulation order of certain subcarriers will need to happen in order to maintain a sufficient SNR to preserve orthogonality. Another issue that needs to be highlighted is the fact that adding users and thus the number of spreading codes will reduce the QoS.

The user allocation in the case of MC-CDMA associated with  $m$ -CAP only consists in associating each user to a different orthogonal spreading code. The same number of subcarriers is used and the number of total code sequences is increased from 1 to 20. Figure 3.30 is the simulated deviation from target in these conditions. The overall deviation obtained is lower than in the case of the SCM association. A maximum

of 10% deviation from target is attained here while the previous subsection showed a maximum of 23% when 10 subcarriers were used in a 4 users scenario. As noted previously, the modulation orders for the subbands in the  $m$ -CAP signals need to be adapted because of the variations in the state of the channel. As a result, the target data rate defined at first can sometimes not be attained.

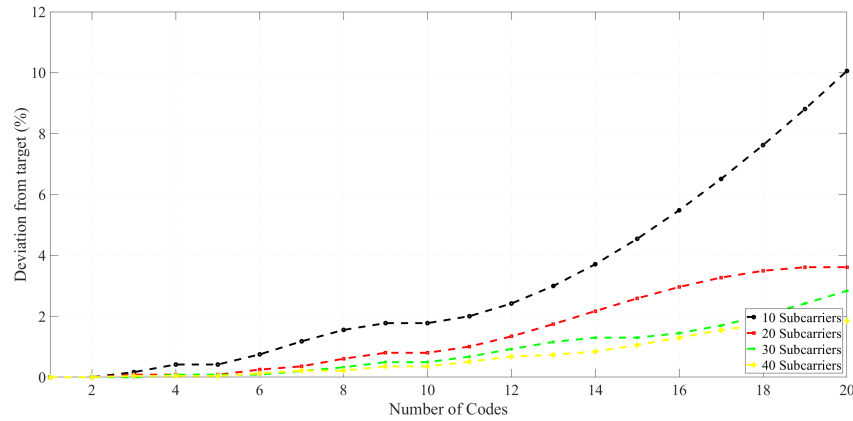


FIGURE 3.30: Simulated deviation from a random target for different number of subcarrier in a 4-users scenario.

### 3.3.3.3 In PD-NOMA

In an association between power-domain NOMA and multiband CAP, each user is theoretically associated to a different power level. However, the larger the number of power level, the more complex the SIC detection algorithm will be to implement. The study here will thus focus on the evaluation of the user allocations algorithms when associating PD-NOMA with SCM or MC-CDMA. Essentially, two power levels will be used, one for far users and one for close users. Each group will use either a SCM user allocation or a MC-CDMA user allocation. In the case of SCM, each algorithm described in subsection 3.3.3.1 will be reused. In the case of the PD-NOMA-MC-CDMA association, the process for each group is similar to subsection 3.3.3.2. PD-NOMA has the benefit of greatly increasing the total user capacity for a same resource. The following simulations performed with PD-NOMA used two power levels only, virtually doubling the capacity. Each group is served by either SCM or MC-CDMA at a higher power level if they are ‘far’ and at the lower power level if they are ‘close’. This is better exploited by the ability of PD-NOMA of reaching better performances the greater the difference between the channel gains [241]. The cost is the presence of multiple access interferences (MAI) and the reduced signal power because of the superposition in power.

Figure 3.31 (a) shows the deviation from the target obtained in the case of an association between PD-NOMA and SCM. The simulation parameters used here are the same as in subsection 3.3.3.1. Since this method virtually reduces the number of users per “group” of subcarriers, the deviation attained in this scenario is divided by two.

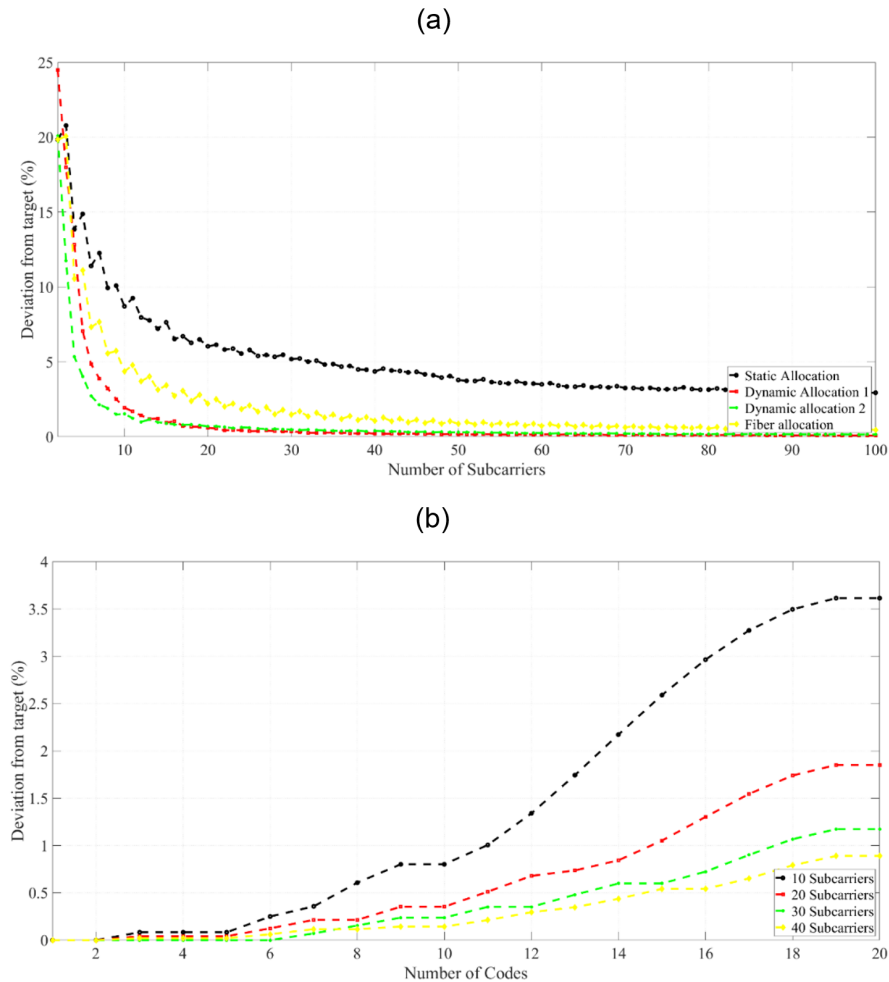


FIGURE 3.31: Simulated deviations from target for different number of subcarrier in a 4-users scenario in the case of an association of (a) PD-NOMA and SCM and (b) PD-NOMA and MC-CDMA.

This characteristic of NOMA-like scheme is compelling for the conception of a high capacity communication cells. Figure 3.31 (b) shows the deviation from the target obtained in the case of an association between PD-NOMA and both MC-CDMA and SCM. The simulation parameters used here are the same as in subsection 3.3.3.2. The observed results are identical to those observed in the previous subsection except that the PD-NOMA scheme virtually doubled the number of subcarriers, considerably reducing the already low deviation obtained with the MC-CDMA association.

#### 3.3.3.4 In SDMA

Extending the user allocation problematic to SDMA present no interest as each element of the transmitter will essentially behave like an independent smaller cell, serving a smaller portion of the users.

### 3.4 Conclusions

The indoor multi-users VLC system studied in this work is the combination of the spectral efficiency optimizations for the multiband CAP modulation and the association with a multi-access scheme. The result is the design of a VLC attocell. The characteristics of such an arrangement are, as previously described, the total available throughput, the maximum number of users, the range and the cell size. The maximum data rate provided comes from the attributes of the modulation process. The range derivatives from the transceivers ability to still communicate at optimal conditions at a given distance. The maximum number of users depends on which multi-access scheme is used. Finally, the cell size relies on the capability to provide for the users within a certain area. This work focuses on the performances of a single attocell. Indeed, the focus of most research on multi-users access schemes is to decrease the amount of inter-user and inter-cell interferences. While this work focuses on single attocell performance analysis, there still is a complementarity between the two types as these demonstrations show the architecture of an attocell network while our production expands on the performance of individual access points.

The broadcast single user performances breakdown through numerical simulation of the indoor VLC system brought insight on the performance impact of each block described by the section 3.2.1:

- The LED is the most prominent hardware component in terms of impact on the performances. The low-pass effect of these emitters will considerably limit the usable signal bandwidth. This effect is mainly counteracted with the use of channel estimation and pre-equalization, as described in the performance's enhancements section. The optical characteristics of the LED also considerably impact the performances as they define the luminous flux and light wavelengths in a given room. The electrical characteristics also need to be considered when driving the LED with an electrical amplifier and a bias-tee to better use the linear range.
- The receiver hardware transforms the received optical signal into a voltage using a photodiode with a trans-impedance amplifier and, optionally, a lens and an optical filter. As shown, the lens has a sizable impact on the received power.
- The optical channel in general has been studied by simulating the impact of the SNR and the signal bandwidth on the BER for a CAP signal. Indeed, the SNR originates from the received power at the photodiode and thus is a result of all parameters of the optical channel.
- The modulation process has been separated into the  $M$ -QAM mapping and the pulse shaping filter parameters impact. The QAM mapper defines the sizes of the constellation used by the signal and thus the spectral efficiency. The filters have multiple parameters with the oversampling factor, the roll-off factor and

the filter span. The oversampling factor and the filter span are linked because they define the filter length. The higher the value, the better the performances but with a diminishing return and an increased computational efficiency. The roll-off factor defines the excess bandwidth and comes with a trade-off between the added signal bandwidth and the increased performances from the reduction in the magnitude of the filter response secondary lobes.

- The performances enhancements simulations give insight into which option should be applied in the case of an optimization process. The optical filter can offer an increase in the usable signal bandwidth however, the loss in SNR can be more damaging for a ph-LED. The channel estimation process helps by estimating the wireless optical channel at the receiver. Equalization is separated into pre-equalization which adapts the signal to the channel and is performed at the transmitter and post-equalization which corrects the received symbols at the receiver. Both can be combined for better performances and extension of the available bandwidth.

The multi-access schemes performances are defined and overviewed with numerical simulations. The definition of the VLC attocell and its performances are mainly linked to the single-user broadcast performance optimization. Indeed, with the SNR distribution in a room, the attocell size, the maximum attainable throughput and the range can be defined for a given indoor VLC system. The maximum number of users depends on the multi-access scheme used. Indeed, in the case of SCM, the limit of users is the number of subcarriers available in the scheme. Additionally, the deviation from the target data rate increases the more users are allocated. As such, if an acceptable deviation from target is defined for the schemes, it will generate a limit to the number of users. Breaking that limit will induce that each user will, on average, not reach its target data rate within the acceptable deviation. In the case of MC-CDMA, the number of users is limited by the number of orthogonal codes available. The deviation from the target is much lower than SCM since each user will use a complete set of an  $m$ -CAP signal and not just a fraction of it. However, the increase in the number of codes reduces orthogonality at the receivers. As a result, each subcarrier of the  $m$ -CAP signal need to have its modulation order optimized in a more significant way. PD-NOMA was shown to increase the maximum number of users as it virtually multiplies the number of available subcarriers. In turn, this boosts the number of available independent channels. But, it requires considerable computational resources with SIC. SDMA is the scheme with probably the most potential as it practically divides the attocell into smaller ones with less needs. But it is not studied here because of the way it works.

The prospects uncovered by this chapter open the discussion for the rest of this work on the experimental investigation of the indoor multi-users VLC system.

Chapter 4 will focus on the optimization of the spectral efficiency with experimental

measures. It will base itself on the conclusions drawn by part 3.2 on the single-user broadcast performances breakdown. The appendix A on the hardware component impact proved that the hardware choice is important. The LED, photodiode and trans-impedance amplifier references are indispensable as they define most of the characteristics which determine the SNR. The modulation process can be optimized for better spectral efficiency. The filter parameters were shown to have a sizable impact on the performances of the CAP and multiband CAP schemes. A perspective that was opened is the combined association of these parameters for each subcarrier in order to optimize a multiband CAP based on the state of the channel. Performances enhancements methods include equalization and channel estimation. Additionally, subcarrier spacing can be potentially combined with the other filter parameters and thus offer a very compelling perspective to increase the spectral efficiency without added computation costs.

Chapter 5 will focus on the attocell characteristics and the analysis of the user allocation process. It will be based on the conclusions drawn by part 3.3 on the multi-users access schemes. User allocation is a key problematic that need to be investigated in experimentation in order to better identify and quantify the differences between each multi-users access schemes in a realistic setup. SCM, MC-CDMA and PD-NOMA all show to resolve the user allocation problematic in different ways. And, as SDMA is a scheme that requires a physically very complex transmitter, it will not be studied experimentally. Finally, the definition and characterization of the generated attocells under different conditions can be used to conclude on each association advantages and disadvantages. The impact of each multi-access scheme on the attainable data rate need to be experimentally studied because of the potential impact that each multi-access scheme can have on it. Finally, the characterization of the range and attocell size can conclude the investigation of the system.

## Chapter 4

# Experimental Investigation of the VLC Indoor System and Proof of Concept

### Contents

---

<b>4.1</b>	<b>Proof-of-Concept Design</b>	<b>107</b>
4.1.1	Transmitter Design	108
4.1.2	Receiver Design	110
4.1.3	Experimental Setup	114
<b>4.2</b>	<b>System Characterization Methods</b>	<b>116</b>
4.2.1	Modulation Order in Quadrature Amplitude Modulation	117
4.2.2	Equalization	121
<b>4.3</b>	<b>Experimental Performance Enhancements</b>	<b>124</b>
4.3.1	Initial Performances of Multiband CAP	124
4.3.2	Individual Subcarrier Filter Optimization	128
4.3.3	Subcarrier Spacing	131
4.3.4	Flexibility and Performance Optimization	136
4.3.5	Single-User Broadcasting Characterization	138

---

## 4.1 Proof-of-Concept Design

The chapter 3 was concluded with an outlook onto the different paths for optimizing the performances of the experimental VLC indoor system. The main objective of this chapter is to enhance the performances and flexibility of multiband CAP in a single-user broadcast scenario. The goal is to prepare the scheme for the multi-users capability that will be added and investigated in chapter 5. Section 4.1.1 is a description of the transmitter used in the experimental setup with a characterization of the LED and its drivers and an explanation of the signal generation process with the waveform generator. Section 4.1.2 illustrates the complete receiver with a depiction of

the receiving circuit and an investigation of the signal identification method from the transmitter to the receiver. Section 4.1.3 concludes this part with a complete description of the experimental setup that will be used throughout the analysis performed in this chapter.

### 4.1.1 Transmitter Design

#### 4.1.1.1 LED Choice and Characterization

Our approach consists in optimizing the single-user broadcast performances before adding the multi-users component to the design in order to maximize the flexibility of the system. As such, the LED must be characterized in order to evaluate the potential performances. Indeed, all the LED main parameters impact the attainable throughput, as seen in chapter 3. The other aspect of our approach is to conceive as realistic experimental setup as possible. In consequence, a ph-based white LED has been favored. Indeed, they are both the most common type light-emitting diode in the market and are easier to drive than RGB-based white LEDs. Figure 4.1 shows a photo of the ph-based white LED used in the experimental setup. This LED is a 72W downlight that can be found in malls, offices or hospitals. It is used at a much lower power in this work. Presently, these types of LED are ubiquitous in these places because of the advantages brought by LED and because the implementation of RGBs LEDs demands more costly drivers [242].



FIGURE 4.1: Photo of the phosphor-based white LED down-light used in the experimental setup.

The characteristics of the transmitter define the potential performances attainable by the system. Figure 4.2 are the measured parameters of the LED. The first one is the forward current - bias voltage curve, or IV curve. This represents the current used by the LED in function of the forward voltage applied to it. The measurement process uses a multi-meter to measure the current going through the LED while changing the voltage applied to it. This measurement is associated with the measure of the illumination. The combination of the two curves is often called the LIV curve. They define the linear operating range of the LED, which needs to be used as optimally as possible in order to optimize the modulated signal range. The third measurement is the relative spectrum in function of the wavelength emitted. This characteristic needs to be used to choose the photodiode at the receiver. The fourth measurement is the frequency response and defines the -3dB modulation bandwidth. As seen in

the chapter 3, this parameter considerably impacts the potential attainable data rate. Also, it is an essential information in order to define the pre-equalization technique.

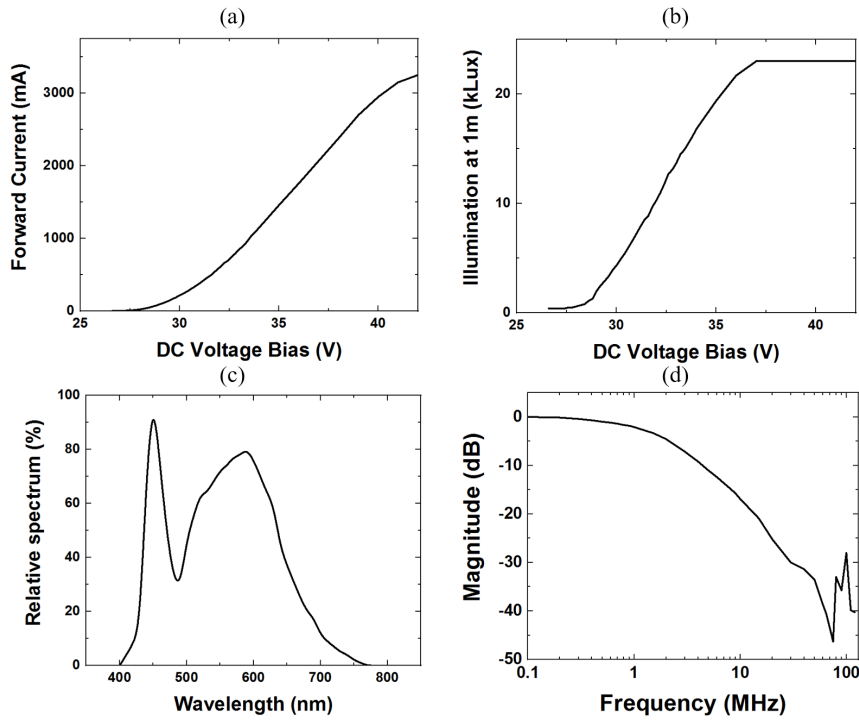


FIGURE 4.2: Experimental setup characteristics. (a) Measured white LED current response versus voltage. (b) Measured white LED illumination response versus voltage. (c) LED relative spectrum response versus wavelength characteristic. (d) Measured experimental system modulation frequency response.

Figures 4.2 (a) and (b) represents the LIV curve. The corresponding largest linear range in current comes with a bias voltage of 30 V to 38 V and in illumination comes with a voltage of 28 V to 37 V. Figure 4.2 (c) shows the relative spectrum versus the wavelength. It can be seen that the LED emits mainly in the blue and the yellow, like every ph-based white LED, and has a peak around 450 nm for the blue and around 590 nm for the yellow. Finally, figure 4.2 (d) shows the modulation frequency response of the LED. The measured -3 dB bandwidth is only 1.4 MHz and the magnitude reaches -40 dB at 70 MHz. This value reinforces the need for a pre-equalization scheme.

#### 4.1.1.2 LED Driving Circuit

As seen in the previous subsection, driving a LED implies:

- Adding a DC bias voltage to the modulated signal to pilot the LED in its operating range.
- The maximization of the linear range for the modulated signal.
- Impedance matching.

In consequence, the main components that are used to drive the LEDs are an electrical amplifier, a bias-tee and a driver. The schematic of the circuit used to drive the ph-based white LED of the experimental setup is shown figure 4.3.

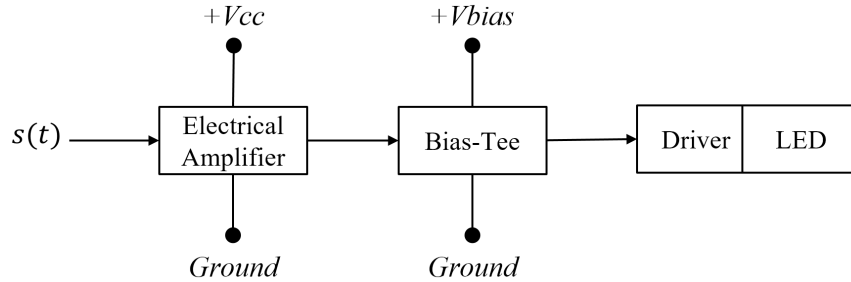


FIGURE 4.3: Schematic for the circuit that drives the LED in the experimental setup.

Each of the main components has characteristics that need to be taken into account. The LED parameters are already described in the previous subsection. The electrical amplifier used in the setup is a Minicircuit ZHL-6A+ and amplifies the signal outputted by the modulated signal generator. Its characteristics are resumed in part C.1 of appendix C. The bias-tee is a Minicircuit ZFBT-282 and adds the DC bias to the amplified modulated signal in order to operate in the operating range of the LED. Its characteristics are also resumed in part C.1 of appendix C. The ph-based white LED used in the setup includes its own driver.

#### 4.1.1.3 Signal Generation with the Arbitrary Waveform Generator

The arbitrary waveform generator (AWG) used in the experimental setup is in charge of outputting the modulated signal. The modulated signals are created with MATLAB. The process is illustrated figure 4.4 and an example of a waveform stored in the AWG is given figure 4.5. The AWG used is a Tektronix AFG3252C. A connection is first established through USB. Then, a modulated signal is created based on a random bit stream. An identification waveform is added to this signal and a time vector is created corresponding to the length of the signal. Before being stored in the AWG, the waveform needs to be adapted. This implies converting the double integer values of the signal into values between 0 and 16382. Then, the waveform is encoded into a binary stream in order to be transmitted through USB to the AWG. At the AWG, a signal sampling rate  $F_{s_{AWG}}$  is chosen for the stored waveform and the sampling rate for the signal is given by  $F_s = F_{s_{AWG}} L_{signal}$ . With  $L_{signal}$  being the number of samples in the stored modulated signal.

### 4.1.2 Receiver Design

#### 4.1.2.1 Receiving Circuit

The receiving circuit aims at transforming the optical signal into a voltage before post-processing. As described in chapter 3, this entails the use of a lens to focus the

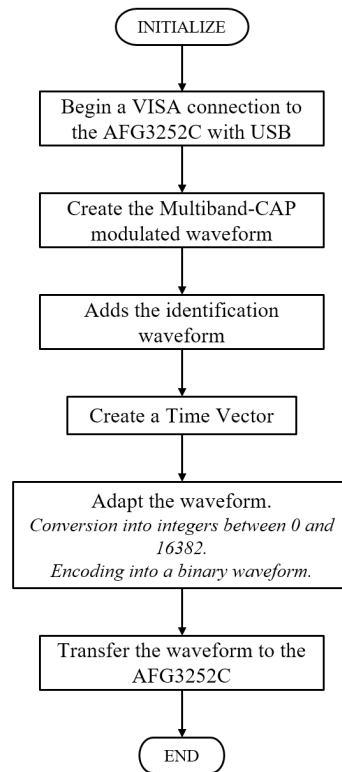


FIGURE 4.4: Illustration of the principle for the process of transfer and generation of the modulated signal with an AWG.

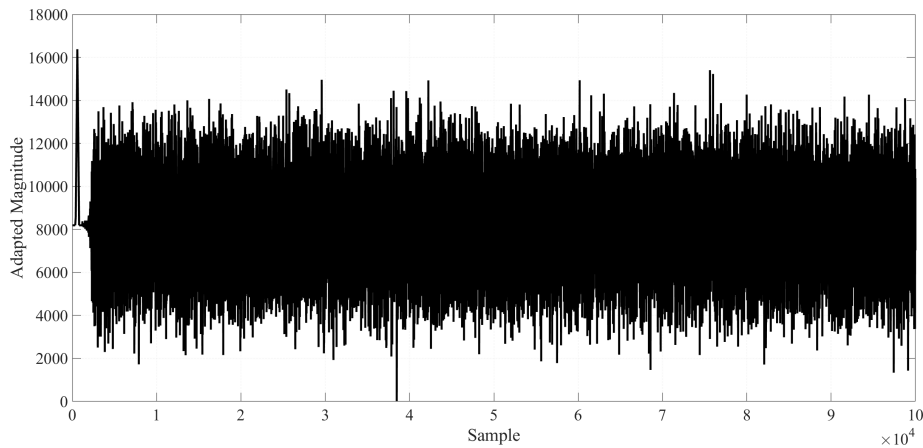


FIGURE 4.5: Example of a 100,000 points *m*-CAP modulated signal before transmission to the AWG.

received light to a photodiode (PD). The latter will convert the light to a current. A trans-impedance amplifier (TIA) is placed with the PD to amplify the current and convert it into a voltage. The lens can be preceded with an optical filter in the case of a ph-based white LED in order to remove the slower yellow response. However, it was concluded in chapter 3 that the loss in SNR associated was not compensated by the increase in the -3 dB modulation bandwidth. Figure 4.6 describes the schematic of the receiving circuit used in the experimental setup.

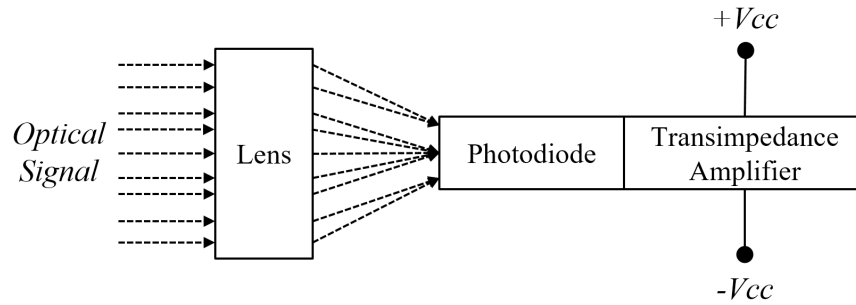


FIGURE 4.6: Schematic of the receiving circuit for the experimental setup.

The circuit has multiple characteristics that impact the performances and that were evaluated in the previous chapter:

- **Lens:** The refractive index of the lens can bring a gain for the received optical signal.
- **Photodiode:** The PD have a limited modulation bandwidth, usually larger than the LED's. The active area also directly correlates to the gain at the receiver. Its Field-of-View (FoV) as well. Its responsivity represents how much Ampere are created in function of the quantity of optical power received. The characteristics of the PD also impact the thermal and shot noise.
- **Trans-impedance amplifier:** The TIA has a limited modulation bandwidth, usually larger than the LED's in the same way as the PD. Its voltage gain represents the conversion between the photo-current and the output voltage. Its characteristics also impacts the thermal and amplifier noise.

In summary, the parameters of the receiving circuit mainly define the SNR. Part C.2 of appendix C lists the characteristics of the lens, PD and TIA.

#### 4.1.2.2 Oscilloscope for Offline Post-Processing

The oscilloscope role is to save the received signal that is outputted by the TIA. The reference used here is a Tektronix MDO3054. The experimental setup ease of use is increased with the use of an oscilloscope. Indeed, it can take on the role of a high-performance Analog-to-Digital Converter (ADC). The MDO3054 characteristics are:

- 500 MHz bandwidth, larger than the experimental VLC system.
- Can save a 10 Mpts signal.
- 2.5 GSps.

### 4.1.2.3 Signal Identification and Reconstruction

After the signal is received and saved by the oscilloscope, the post-process is operated off-line by a PC with MATLAB. At the transmitter, both an identification waveform and pilot data were added to the signal in order to perform this step, called synchronization.

It is a two-step method. The first step target is to identify the start of the data frame. A distinctive waveform is added at the beginning of the data frame and is identified at the receiver. The first sample from which the data frame begins needs to be precisely selected in order to allow the demodulation and decoding of the received modulated data frame. The second step is to correct the amplitude attenuation and phase offset induced by the communication channel. The data frame thus contains a known series of symbols placed at the beginning, called pilots, and the correction to be applied are deducted from the distortions on these received symbols.

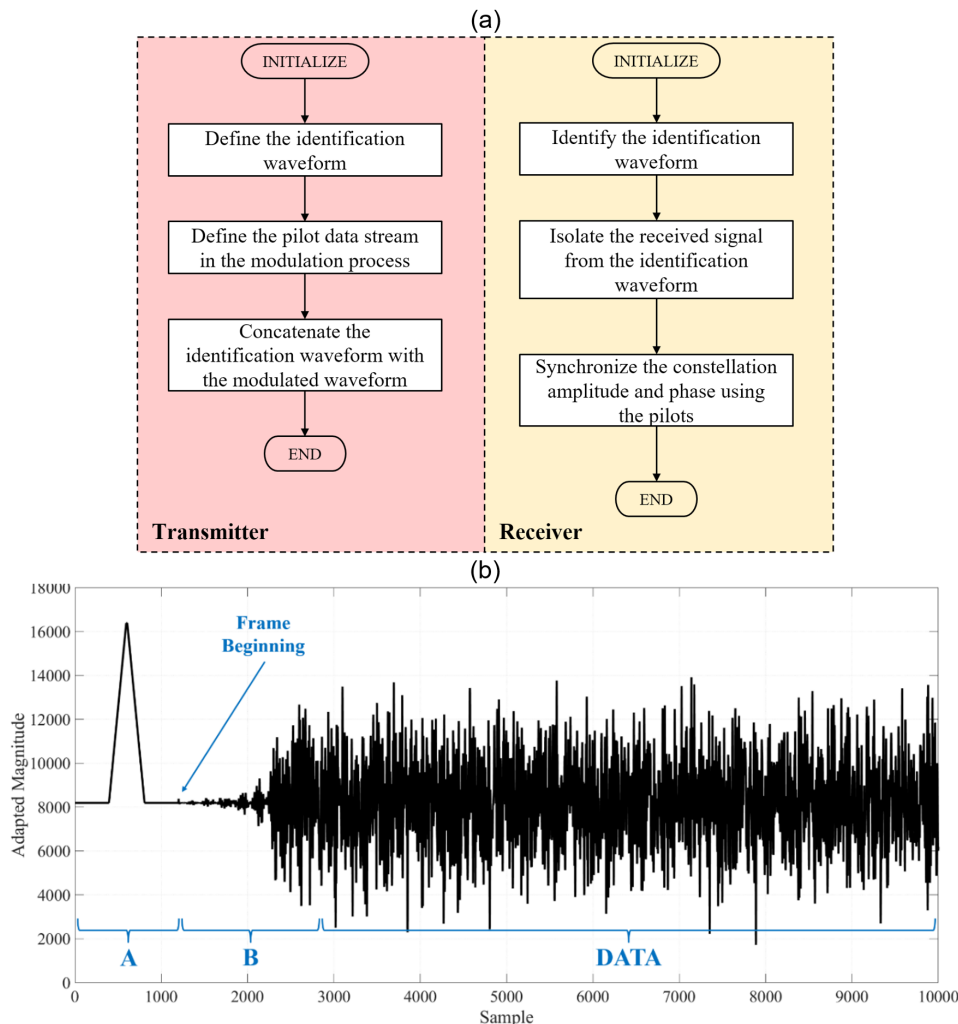


FIGURE 4.7: (a) Illustration of the principle of the signal identification and reconstruction process. (b) Total transmitted example waveform with a low spectrum impact pulse (A) and a series of known symbols (B) added to the CAP modulated data frame (DATA).

At a high signal bandwidth, the identification waveform needs to be easily identifiable in order to always find the first frame of data precisely. Without this information, the demodulation and decoding of data is impossible. As seen in figure 4.7 (b), a low spectrum impact pulse is added at the beginning of the data frame. It is defined as a slow pulse. At more than 30 times the LED -3 dB cutoff frequency, the waveform is detected with an accuracy of five samples. In order to alleviate this case, the pilots are tested to synchronize the post-processing to the beginning of the waveform. Figure 4.8 represents the process for the identification of this first frame.

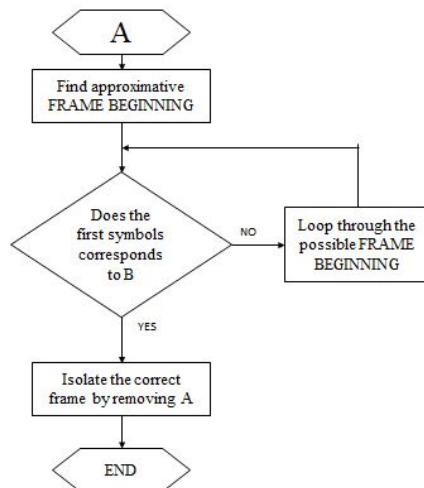


FIGURE 4.8: Simplified process schematic for the principle of identification of the first frame.

To synchronize the data and be able to demodulate and decode it correctly, the phase shift and the amplitude attenuation caused by the optical wireless communication channel and the LED must be correctly estimated and corrected. The pilots (B), as seen in figure 4.7 (b), are used as a reference to calculate the difference between the correct phase of the (B) symbols and their received phase. The same principle is used for the amplitude attenuation which is estimated and corrected after the phase shift correction. Figure 4.9 represents the process of synchronization with the pilots.

### 4.1.3 Experimental Setup

An AWG (AFG3252C) stores a total of  $m$  random data streams. Random bit streams are created on MATLAB, with each of these data streams assigned to a subcarrier for the  $m$ -CAP modulation process. For every one of them, an  $M$ -QAM mapper maps the corresponding data streams. Then, each symbol stream is separated into its real and imaginary component. The corresponding in-phase and quadrature raised cosine filters are applied to them. These FIR filters are configured at the center frequency defined by the subcarrier assignation. All the  $m$  resulting modulated data streams are added to produce the signal  $s(t)$ . Before the transmission, the signal is pre-equalized, as described in subsection 4.2.2.1, using a software implemented amplitude

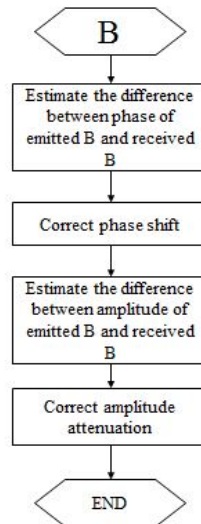


FIGURE 4.9: Simplified process schematic for the principle of amplitude and phase correction.

pre-emphasis pre-equalization filter to extend the available modulation bandwidth. In order to detect the transmitted frame at the receiver, a simple preamble is added at the beginning of the signal, before the transmission, as described in subsection 4.1.2.3. The signal is stored in the AWG.

After emission of the signal, a Minicircuit electrical amplifier (ZHL-6A+) is used to amplify the signal outputted by the AWG. A Minicircuit bias-tee (ZFBT-282) adds a DC bias to the signal before sending it to the LED. The white LED used throughout the experiments is a 72W down-light that can be found in malls, offices or hospitals. It operates at 19.2W of electrical power (32V, 0.6A), because of hardware limitations.

The receiving circuit is first composed of a Thorlabs 25 mm biconvex lens which concentrates the light into a photodiode. The latter is combined with a TIA with the Thorlabs PDA10A-EC to form the receiving circuit. The PD is a 1 mm diameter silicon receiver. The distance used, unless indicated otherwise, is set at 2.15 m between the transmitter and the receiver, with direct line-of-sight (LOS). This is the average distance between the ceiling and a desk in an office. The receiver output signal is saved using a digital oscilloscope (MDO3054). The resulting data is post-processed using MATLAB. After re-sampling the signal, the preamble is decoded to identify the start of the signal that was sent. The matched filters deployed for the demodulation depends on their definition at the receiver. The mapped symbols are corrected in gain and phase, then a decision feedback equalizer (DFE) performs a post-equalization, as will be seen in subsection 4.2.2.2. Lastly, they are de-mapped using the  $M$ -QAM demodulator. Thus, the original packet of data sent is obtained. Table 4.2 summarizes the experiment setup and parameters, in section 4.3.1.

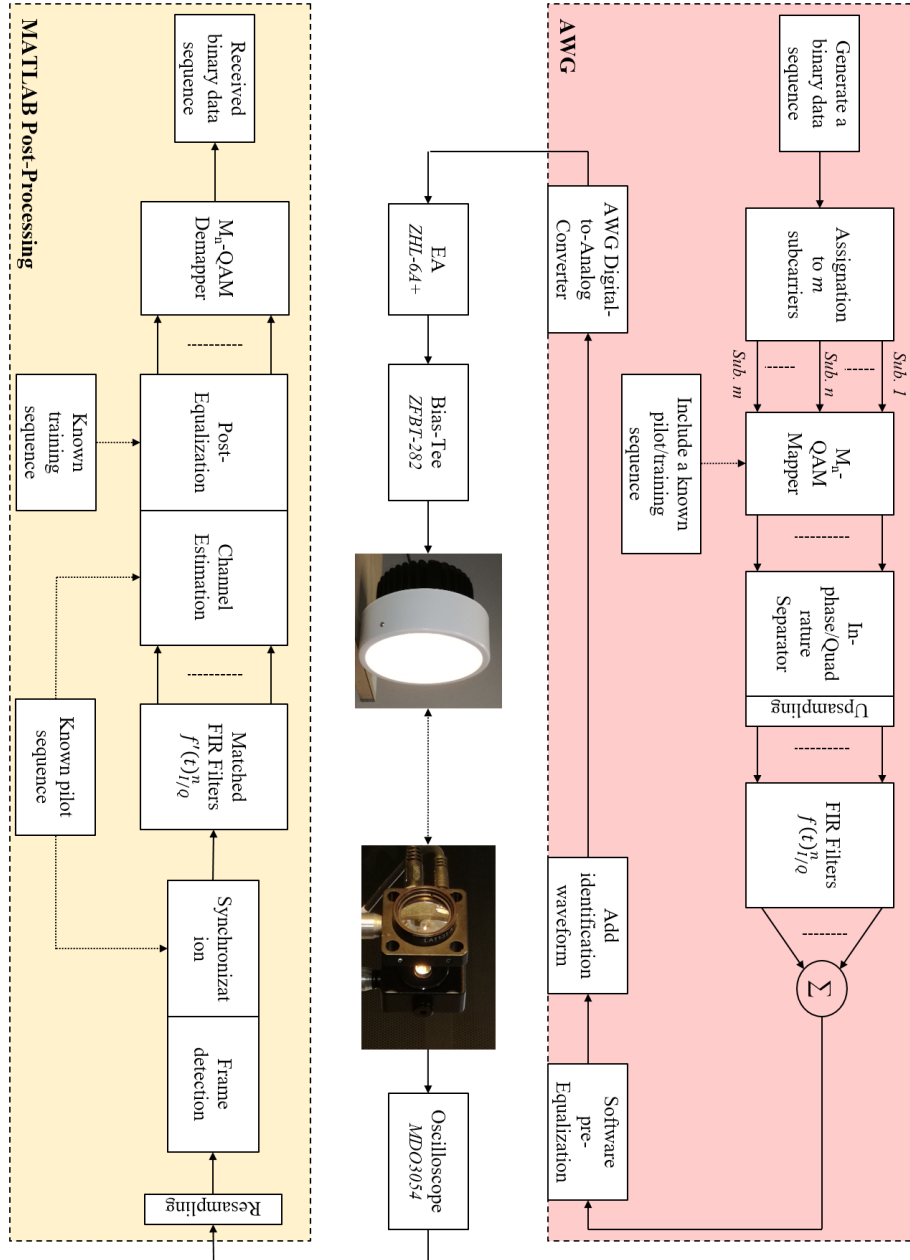


FIGURE 4.10: Schematic representing the experimental setup for the transmitted based on an AWG, an office down-light, and a receiver based on a photodiode and an offline post-process with MATLAB.

## 4.2 System Characterization Methods

After definition of the experimental setup, a crucial step is addressed in this part. This part aims at describing the techniques used in conjunction with the experimental setup. Section 4.2.1 is an investigation of the whole process of evaluating the modulation order at the quadrature amplitude modulation step in order to maximize the spectral efficiency at each subcarrier. Two different methods are presented and will be used throughout the measures presented in this chapter. Section 4.2.2 describes the equalization and channel estimation techniques applied to the system in order to

enhance the performances obtained throughout the measures.

### 4.2.1 Modulation Order in Quadrature Amplitude Modulation

Carrierless amplitude and phase (CAP) modulation and multiband-CAP ( $m$ -CAP) both uses rectangular quadrature amplitude modulation (QAM) as the mapping process. The mapper's job is to process groups of bits and transform them into complex reference positions in a constellation given by the modulation order of the QAM modulator. Essentially, a lookup table is used for each group of bits in order to map the value to a corresponding in-phase ( $I$ ) and quadrature ( $Q$ ) component, which are the axis of the QAM constellations.  $I$  and  $Q$  are the coordinates for the constellation and represent the real and imaginary value of the complex reference positions, respectively. In 16-QAM for example, with Gray coding, groups of 4 bits are mapped and 0000 will correspond to  $I = -3$  and  $Q = 3$ , 1111 will correspond to  $I = 1$  and  $Q = -1$ , etc. After the mapping process, the complex values are scaled, depending on the chosen constellation, called  $M$ -QAM. The 2-QAM (or BPSK), 4-QAM (or QPSK), 16-QAM, and 64-QAM output values are multiplied by the factors 1,  $1/\sqrt{2}$ ,  $1/\sqrt{10}$ , and  $1/\sqrt{42}$ , respectively. The reason is that all constellations will have the same root mean squared (RMS) value using these factors and thus, the same average output power.  $M$  is the number of symbols in the alphabet of the constellation. These two steps can be combined into a single step with mapping to an already scaled constellation.

The higher  $M$  is, the higher bits per symbol the modulation will use. Thus, the throughput increases with  $M$ . But, it also decreases the distance between each reference position. The constellation received at the receiver will need a higher signal to noise ratio (SNR) to decode the constellation without errors. In a visible light communication (VLC) system using multiband-CAP, it is important to use the appropriate  $M$  on each subcarrier in order to attain the performances required in throughput and bit error rate (BER), which is heavily emphasized in [243], [244], and [245]. Being a multi-subcarrier modulation scheme, its main advantage comes in the higher flexibility offered by the ability to select the modulation order for each subcarrier [246]. In addition to this, multiband-CAP reduces the innate sensibility to non-flat channel response that conventional CAP suffer from since every subcarrier occupies a smaller bandwidth than a conventional CAP band. Indeed, the optical wireless channel response is not flat [247] and a single carrier modulation scheme will suffer from this. It is why the following work focus on the evaluation of a subcarrier performance by focusing on the study of the QAM constellations.

#### 4.2.1.1 Subcarrier Evaluation

Binary data is regrouped as groups of  $k$  bits, with  $k = \log_2(M)$ . These groups of bits are then mapped using the  $M$ -QAM rectangular modulator. The constellation showed on the right of figure 4.11 is produced with a 16-QAM modulator. The optical wireless

channel, the transmitter hardware and the receiver hardware impact the transmitted signal and thus distortions are observed on the receiver [248]. It principally includes, and is not limited to, gain distortions, phase distortions, in-phase and quadrature imbalances and additional white Gaussian noise (AWGN).

QAM constellations need to be evaluated at the receiver in order to optimize the modulation order. The received signal at the photodiode is demodulated using the aforementioned pulse shaping filters in order to recover the in-phase and quadrature components that were transmitted. The additional post-processing methods are performed to synchronize and equalize the signal. A constellation is evaluated only after it has been corrected of its IQ imbalances as well as gain and phase distortions. Performance metrics usually include bit error rate (BER), signal to noise ratio (SNR) and error vector magnitude (EVM). The SNR can be measured before the demodulation and correction steps using the frequency response of the signal while the other two are obtainable after the constellation corrections.

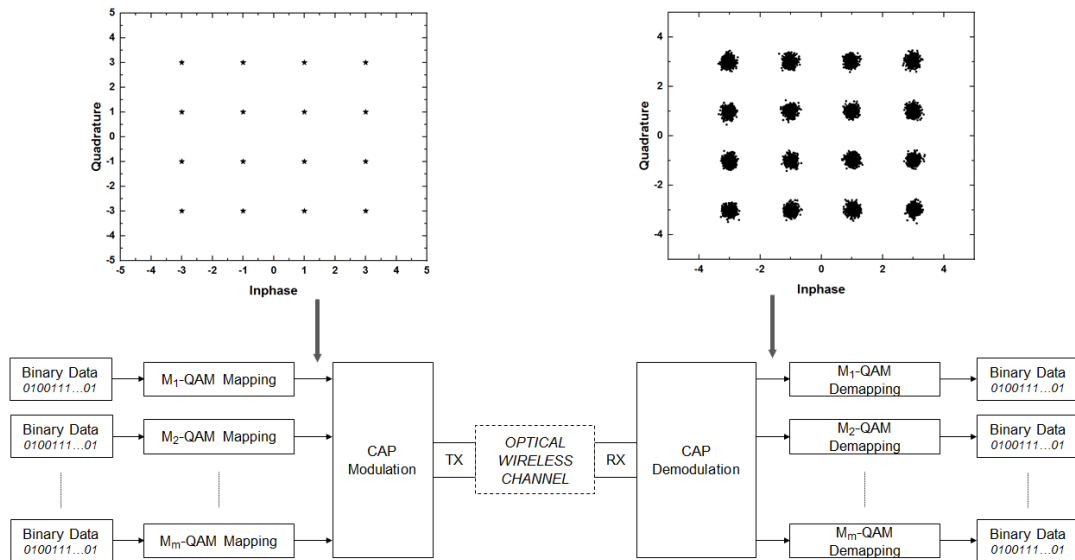


FIGURE 4.11: Schematic representing 16-QAM constellations at the transmitter and the receiver of a multiband CAP system for one of the subcarriers. The  $m$ -CAP principle diagram is simplified and  $m$  represents the number of subcarriers. TX block regroups the parts necessary for transmission of a VLC signal, including the LED. RX block regroups the parts needed for the reception, including a photodiode. In the constellation on the right, phase, gain and IQ distortions have been corrected in the CAP demodulation block.

**Bit Error Rate:** Bit error rate or bit error ratio (BER) is a performance metric used in the world of data transmission. QAM performance analysis commonly report BER as it indicates the number of error bits received out of the bits transmitted. Each received subcarrier of the multiband CAP signal arbors a different BER value. With its estimation, the appropriate modulation order  $M$  can be selected for the  $M$ -QAM process associated to the subcarrier. On a QAM constellation, BER is not directly shown but the symbol error rate (SER) is. Another way to demonstrate how the BER

impacts the performances of a system is the use of an eye diagram. The width of the eye provides information about tolerance to jitter and the height of the eye gives information about tolerance to additive noise. Eye closure is due to inter-symbol interferences (ISI), so the diagram gives an idea of the performances of an equalizer [249].

The BER is found after the post-processing corrections of the received signal:

$$BER = \frac{\text{number of error bits}}{\text{total number of bits}} \quad (4.1)$$

**Signal to Noise Ratio:** Signal to noise ratio (SNR) is a common performance metric for assessing the quality of communication. It is a direct measure of the background noise level relative to the signal. Noise can be considered the source of most errors in a communication system with a Gaussian noise channel model and thus the performances in reception can be predicted with SNR [250]. While exact results are measured with BER with the bit being erroneous or not, BER performance against SNR is a popular metric for reception quality.

Since each subcarrier uses a QAM constellation to transmit data, the SNR available on each of them can be estimated with after a measure of the error vector magnitude (EVM), which is described in the following subsection. When a BPSK (2-QAM) constellation is transmitted, the square of the root mean square EVM is used to obtain the SNR as shown [250]:

$$SNR = \frac{1}{EVM^2} \quad (4.2)$$

**Error Vector Magnitude:** The error vector magnitude (EVM) is another widely used performance metric for communication systems. It is essentially a measure of errors between the measured symbols on the received constellation and the expected symbols sent by the transmitter. It measures the performance of a modulator or demodulator in presence of impairments and is a vector difference between an ideal signal at the transmitter and the measured signal at the receiver.

The normalized average amplitude of the error vector is the EVM. It is defined in dB and is equal to the ratio of the amplitude of the error vector to the root mean square (RMS) amplitude of the reference:

$$EVM(dB) = 10 \log_{10} \left( \frac{P_{error}}{P_{ref}} \right) \quad (4.3)$$

#### 4.2.1.2 Selection of Constellation Size

**Method 1, From the SNR:**

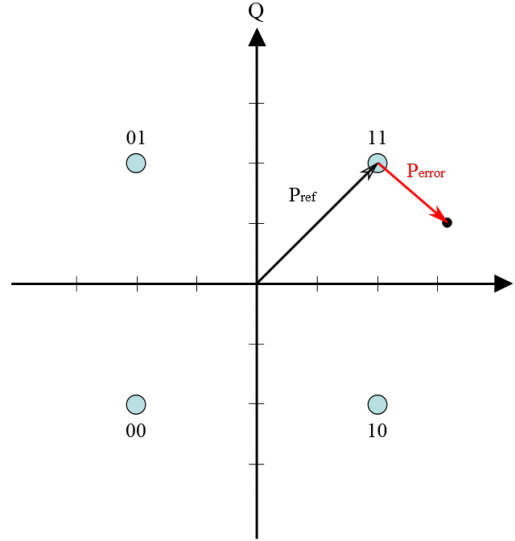


FIGURE 4.12: Constellation diagram with a representation of the EVM.  $P_{error}$  is the RMS amplitude of the error vector.  $P_{ref}$  is the amplitude of the highest power point in the reference signal constellation [251].

Every subcarrier can be associated with an available signal to noise ratio (SNR) in dB under the given conditions of the experiment used to measure the metric. The higher the SNR is, the higher the modulation order  $M$  of the QAM constellation can be for that subcarrier, while the BER stays under a target limit. The forward error correction (FEC) at 7% gives a BER limit of  $3.8 \times 10^{-3}$ . Essentially, theoretical thresholds for the SNR can be found in order to obtain the modulation order  $M$  usable for each subcarrier.

TABLE 4.1: Theoretically required SNR for the usable modulation order at each subcarrier in a multiband CAP signal.

M	Required SNR (dB)
4	6.7
8	9.5
16	10.5
32	13.5
64	14.7
128	18

If the measured SNR on a subcarrier is superior to a SNR threshold value, the associated modulation order can be used for that subcarrier. Theoretically the BER should end up below the FEC limit. The following method is thus used:

1. Measure the SNR of each subcarrier.
2. Select  $M$  for each subcarrier based on the theoretical SNR thresholds.

**Method 2, Iterative optimization:** The principle of this method is to go through each possible modulation order  $M$  for each subcarrier and measure the bit error rate

directly. If the BER is inferior to a given limit for a subcarrier using a certain  $M$ , then the modulation order can be increased. The BER threshold here is going to be the 7% FEC limit of  $3.8 * 10^{-3}$ . Thus, the following algorithm is used:

1. Measure the BER of each subcarrier at all modulation orders  $M$ .
2. Select appropriate  $M$  for the whole signal and measure the BER at each subcarrier
3. Optimize the modulation order of each subcarrier by increasing  $M$  as long as the BER is inferior to the FEC Limit. If it is, then reduce  $M$ .

The last step requires the use of an arbitrary margin for the FEC limit at each subcarrier. Here, if the BER is at most 100% below  $3.8 * 10^{-3}$ , we consider that  $M$  cannot be increased. This value is in relation with the fact that increasing  $M$  in a rectangular constellation doubles it. If the BER is above the FEC limit for a subcarrier, it is decreased.

## 4.2.2 Equalization

### 4.2.2.1 Pre-Equalization

The pre-equalization technique used throughout the experiments is based on an amplitude pre-emphasis method which attenuates the lower frequencies and amplifies the higher frequencies components of the signal, thus reducing the low-pass effect of the optical channel and LED. Figure 4.13 shows the simplified circuit of the implemented pre-equalizer. It is based on a bridged-T amplitude equalizer for a VLC system, demonstrated in [252]. The impedance of the equalizer must be considered in order to maintain the linearity of the VLC system over a wide frequency band. As, such the product of  $Z_{11}$  and  $Z_{22}$  must be a constant equal to  $R_0^2$ , where  $R_0$  is equal to the impedance of the VLC system, or 50 Ohm. A hardware equalizer following the schematic figure 4.13 is thus compared with a software implemented pre-emphasis scheme. The latter work simply by simulating what the hardware pre-equalizer realizes by applying a filter to the modulated waveform before transmission by the AWG.

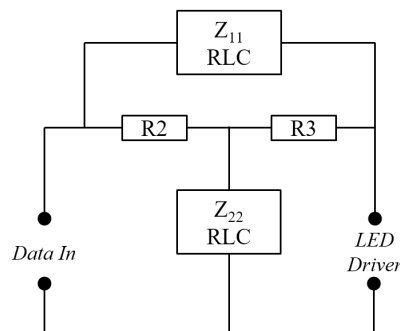


FIGURE 4.13: Schematic diagram of the bridged-T amplitude equalizer [252].

The hardware and software implementations are optimized for the characteristics of the experimental setup and are compared with the maximum attained spectral efficiency using a 10-CAP signal. The transmitter and receiver circuit are described by sections 4.1.1 and 4.1.2. The roll-off factor is set at 0.15 and the filter span at 12 with an oversampling factor of 10. The range of the system was set at 1 m. Figure 4.14 shows the results with the measured spectral efficiency against a variation of the signal bandwidth in such conditions.

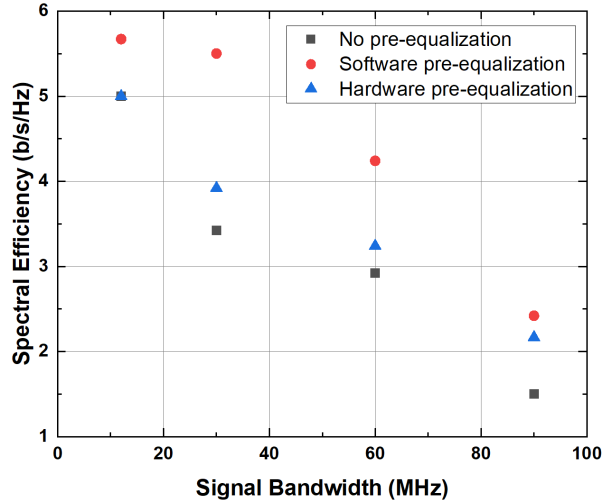


FIGURE 4.14: Measured spectral efficiency versus signal bandwidth for different pre-equalization implementations.

Using no pre-equalization, the spectral efficiency obtained is the lowest since the low-pass effect of the optical channel and LED has more influence than when using pre-equalization. Hardware pre-emphasis improved the spectral efficiency at a 30 MHz signal bandwidth from 3.42 b/s/Hz to 3.92 b/s/Hz or a 15% increase. At 60 MHz, an 11.3% increase is observed and at 90 MHz, a 44% increase in spectral efficiency is obtained. Since the hardware implementation uses passive components with specific values, the positive effect is higher around 100 MHz than at the lower signal bandwidth values due to the magnitude frequency response of the circuit. Software pre-equalization improved the spectral efficiency at 12 MHz by 13%, at 30 MHz by 45% and at 90 MHz by 60%. A software implementation instead of a hardware one considerably improves the flexibility of the pre-emphasis technique over a larger range of possible signal bandwidth. An optimal pre-equalization effect can be obtained throughout multiple sampling rate instead of just one with a single software implementation.

#### 4.2.2.2 Post-Equalization with Channel Estimation

The post-equalization and channel estimation techniques were studied in Chapter 3. The effects of these post-processing techniques have been studied in order to estimate the gains in spectral efficiency. The channel estimation method used here is

a pilot-based time domain MMSE technique using a smoothing matrix. The post-equalization method is based on an adaptive DFE using a linear RLS equalizer with 15 forward taps, 10 feedback taps, a 0.99 forgetting factor and a 500 training symbols sequence. These parameters were fixed after an iterative optimization of their performances. The rest of the experimental parameters are the same as in the previous subsection. The measured impact of a demodulation process on the spectral efficiency with no added technique is compared with the use of the channel estimation method, the decision feedback equalizer and the use of both.

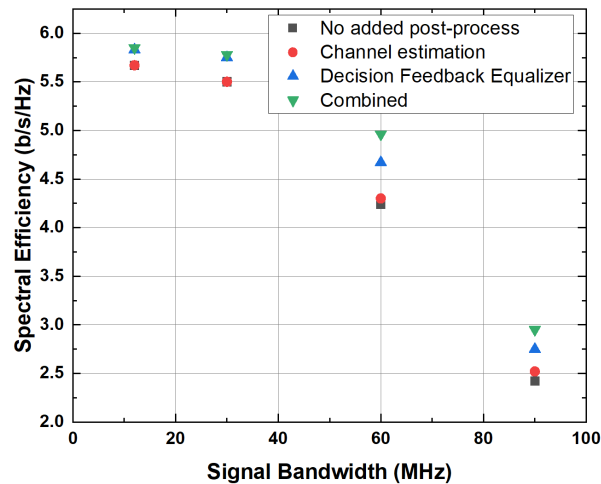


FIGURE 4.15: Measured spectral efficiency versus signal bandwidth for different post process methods.

The classic no-added post-process method is a one-tap equalizer. At the transmitter, a software pre-equalization scheme is also used. The channel estimation impact is lessened by the fact that the signal is divided into 10 subcarriers in *m*-CAP. The effect of the non-flat frequency response is attenuated, and the method overall impact is less than in 1-CAP. Gains of 1.41% and 3.96% in spectral efficiency are observed with signal bandwidths of 60 and 90 MHz. This small increase is mainly due to a positive effect on the first two to three subcarriers which are slightly impacted by clipping distortion due to non-linearity at very early frequencies. Since the overall impact of channel estimation is small, the MMSE technique has a noticeable impact only on these subbands because the method is more effective at higher SNR.

Decision Feedback Equalization used a 500 symbols sequence for training and is also combined with channel estimation for small supplementary gains in spectral efficiency. At 30 MHz for example, the gain is 4.35% for DFE only and 4.84% for DFE with channel estimation. At 60 MHz, the gain is 9.2% for DFE only and 14.51% for DFE with channel estimation. Although channel estimation alone does not bring significant performance increases, the combination of the two methods does provide the highest possible gains.

### 4.3 Experimental Performance Enhancements

The experimental investigation aims at optimizing the performances of the multiband CAP modulation to prepare the scheme for the addition of different multi-access techniques in multi-users scenario. Beyond the importance of raw throughput, the main guideline of this part is the improvement of the flexibility of the scheme. With multiple scenarios that can enhance the performances, the scheme will be able to better cope with the drastic changes in conditions in multi-users scenarios, presented in the following chapter. To start off the investigation, section 4.3.1 is an initial approach to the performances of the multiband CAP modulation in an indoor VLC system with baselines results to be compared after optimization of the efficiency. Then, section 4.3.2 describes the first optimization idea which is to optimize the filter parameters to the conditions of the channel in order to maximize the performances obtained. The roll-off factor impact is first analyzed, followed by the filter length. Section 4.3.3 is a parallel investigation on the promising performance enhancement technique showed in chapter 3: subcarrier spacing. The initial results from the technique are presented and its potential is described. After the presentation of these throughput and BER improvement methods, section 4.3.4 combines them in order to create a complete optimization procedure for the maximization of the performances on each subcarrier and on the whole waveform. The part is concluded in section 4.3.5 with a comparison between the final results measured after optimization and the baseline results described in the first section of this part.

#### 4.3.1 Initial Performances of Multiband CAP

The multiband CAP modulation scheme, or  $m$ -CAP, with  $m = 1$  corresponds to conventional CAP. With higher  $m$  values it becomes a multi-carrier modulation with  $m$  subcarriers in total. The more subcarrier there is, the smaller the frequency band occupied is. Thus, it leads to a reduction in the sensitivity to non-flat channel response, which, as seen in figure 4.2 (d), is the case in our realistic experimental setup. Since the frequency band occupied by each subband is smaller, the sampling rate of the pulse shaping filters is also reduced and approaches the Nyquist rate which reduces implementation complexity to some extent despite the augmentation in the number of filters ( $2m$ ). The potential for multi-users scenarios is in the maximization of the multi-access scheme flexibility. Indeed, at  $m = 10$  for example, it can be tricky to provide for more than 4 to 5 users with an equal quality of service. At  $m = 20$  though, more subcarriers can be dispatched to the users, allowing more possibilities to accommodate them in regard to inter-user interferences, channel quality, required data rate, etc ...

Using the experimental setup described in section 4.1.3 and the subcarrier evaluation methods characterized in section 4.2.1, the following measures aim at the evaluation of the initial performances of the multiband CAP in a realistic indoor VLC system. The parameters used in the measures are summarized in table 4.2. Figure 4.16 is an

illustration of the measured spectrum for both a 4-CAP and 10-CAP signal, as well as the measured received constellation for some subcarriers in the signals. Figure 4.17, on the other hand, is a measure of the impact of the number of subcarriers  $m$  on the measured overall BER of the signal. Using the parameters described table 4.2 for our realistic setup, a baseline characterization of the system can be performed, before the eventual optimization on the filter parameters.

TABLE 4.2: Experimental parameters used for the measurements on the impact of the number of subcarriers on  $m$ -CAP in figures 4.16 and 4.17.

Parameter	Value
Transmitter	72W Museum Downlight
Receiver	PDA10A-EC + 25 mm Biconvex Lens
Measured LED -3dB Bandwidth	1.4 MHz
Distance between the transmitter and the receiver	2.15 m
LED driving power	19.2 W (32V, 0.6A)
Illumination at the receiver	12 klux
Raised Cosine Filter parameters: Roll-off	0.15
Raised Cosine Filter parameters: Filter span	12
Raised Cosine Filter parameters: Oversampling factor	10
Pre-Equalization	Software amplitude pre-emphasis
Channel Estimation	Pilot-based Time Domain MMSE
Post Equalization	RLS/DFE Adaptive

Figure 4.16 illustrate a measured spectrum at the receiver for both a 4-CAP and 20-CAP modulated signals. The signal bandwidth for both the signal is the same since the same sampling rate was used in both cases. Different modulations orders were used throughout both signals and the constellation associated to some of the subcarriers were measured after the equalization process. One of the main advantages of multiband CAP is illustrated with the ability to use a different modulation order for each subband, called bit-loading. Also, the higher the number of subcarriers, the smaller the frequency band associated. Thus, in the 20-CAP signal, some could use a higher modulation order because they were less affected by the low-pass effect of the channel. In order to experimentally quantify this characteristic of the scheme to better optimize a subcarrier modulation order, a measure of the impact of the number of subcarriers on the performances of the experimental setup is performed.

Figure 4.17 (a) is the impact of the number of subcarriers on the BER. Using both a mapping constellation size of  $M = 16$  and  $M = 64$ , the bit error rate of the experimental setup in the conditions described by table 4.2 and section 4.1.3. The

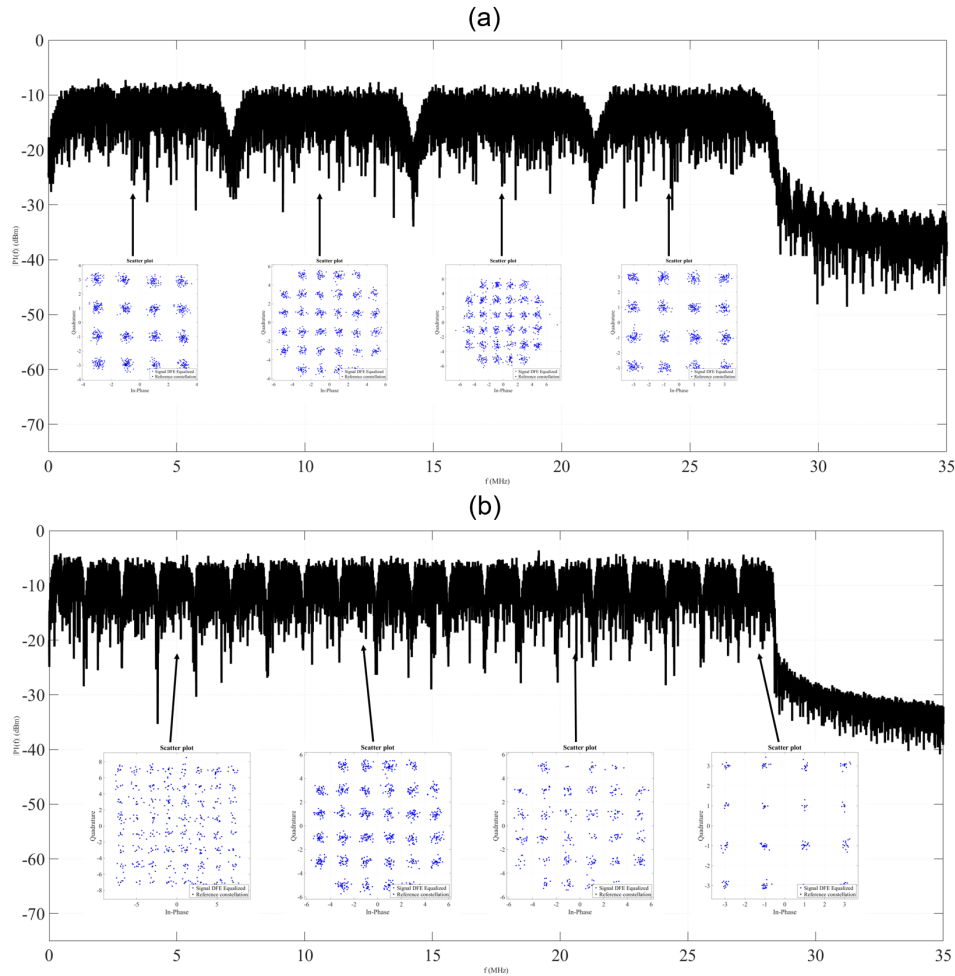


FIGURE 4.16: Measured electrical spectrum at the receiver of a (a) 4-CAP and (b) 10-CAP signal showing the constellations associated with some subcarriers. Different modulation orders are set for each subcarrier as a representation of the bit-loading method.

BER of the whole signal lowers with the increase of the number of subcarriers to a certain extent. Indeed, when increasing  $m$  from 4 to 14 with  $M = 16$ , the BER fell from  $9.8 \times 10^{-4}$  to  $1.25 \times 10^{-4}$ , or a decrease by a factor of almost 8. However, when increasing  $m$  from 15 to 25, the BER went down from  $1.1 \times 10^{-4}$  to  $0.7 \times 10^{-4}$ , or a decrease by a factor of only around 1.6. A similar observation can be made with the mapping constellation size of  $M = 64$ . This measurement indicates that increasing the number of subcarriers offers diminishing returns. Indeed, the non-flat effect of the channel has a limit to how much it needs to be attenuated by the amount of divided subbands. In our case, several subcarriers higher than 20 brings considerably lower boost in BER performances.

Figure 4.17 (b) is the impact of the number of subcarriers on the maximum available throughput. The latter characteristic is obtained by using the most optimally usable modulation order for each subband that still keep the BER of that specific subband under  $3.8 \times 10^{-3}$ . This corresponds to the Forward Error Correction (FEC)

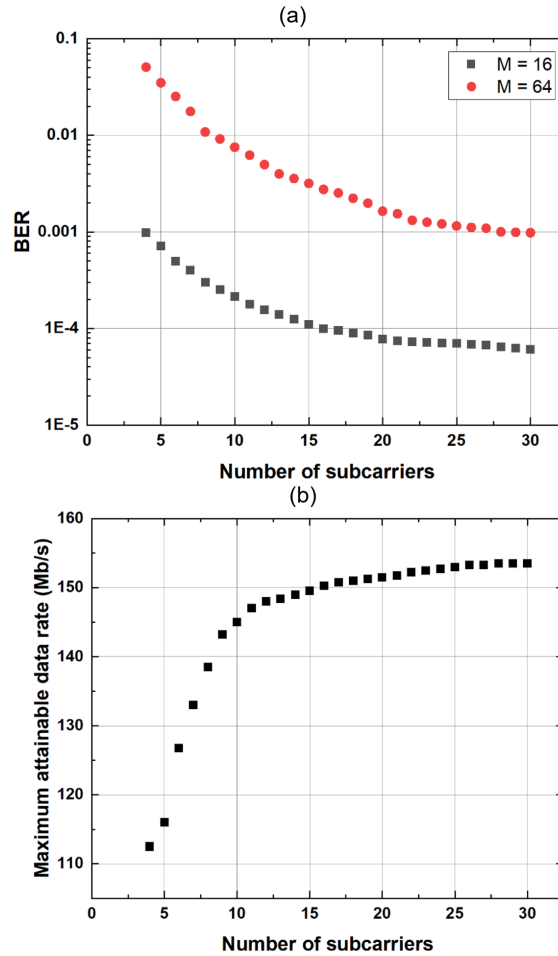


FIGURE 4.17: (a) Measured impact of the number of subcarriers on the BER for a modulation order of  $M = 16$  and  $M = 64$ . (b) Measured impact of the number of subcarriers on the obtained data rate.

7% overhead limit. The same observation as previously can be made. Indeed, when increasing the number of subcarriers from 4 to 14, the data rate goes from 112.5 Mb/s to 149 Mb/s, or a 32.44% increase of raw performances. However, when going from 15 to 25 subbands, the available throughput goes from 149.5 Mb/s to 153.2 Mb/s, or a 2.47% boost in raw data rate. This time, the diminishing return limit appears at around 12 subcarriers. Beyond this point, only a 3.7% gain in data rate can be obtained. A first observation is that this point appears sooner than in the case of the BER. This is because increasing the constellation size for the modulation order by only 1 bit/symbol raises the BER by a considerable margin. Thus, a decrease in BER, for example by 10%, does not directly translate to the same relative increase of raw data rate since the 7% FEC limit will not necessarily be crossed. In the case of a strict optimization of the data rate, the experimental setup used here do not need more than around 12 subcarriers for an already sizable boost in raw performances. However, the objective is to offer as much flexibility to the system for the associations with multi-access schemes in multi-users scenarios as possible. Thus, the 20 subcarriers limit found previously suits this scheme well since it offers an optimal decrease

in BER before the diminishing returns.

While optimizing the total number of subcarriers in the modulation scheme offers an increase in raw throughput and flexibility, the potential of the process for the latter has yet to be fully revealed. Indeed, during the measures performed and presented in this section, it could be noticed that the effect of the increment on the number of subbands was larger on some subcarriers than the others. In the case of the BER, the non-flat effect of the channel is higher on the higher frequencies. In consequence, the parameters of the modulation process can probably be optimized for each subcarrier depending on its position in the signal.

TABLE 4.3: Baseline characteristic for a 20-CAP signal in a single-user broadcast setup corresponding to Table 4.2.

Parameter	Value
Number of subcarriers	20
Signal bandwidth	28.5 MHz
AWG Sampling rate	250 MS/s
Distance	2.15 m
Total Throughput	151.25 Mb/s
Total BER on direct LOS	$1.84 * 10^{-3}$

### 4.3.2 Individual Subcarrier Filter Optimization

The base results described previously serve as a base result for comparison with the following performance optimization process. The premise is that each subcarrier could potentially have a slightly different transmit filter instead of the usual setups where only the center frequency changes. In the following subsection, the basic parameters of the filters for the modulation scheme are explored in the setup used by the base results. The idea is that each subcarrier has its own FIR filter defined on the transceivers. Since the aim of the work is to ultimately work in multi-users scenarios, receivers will be placed at different positions in regard to the transmitter. Each associated wireless optical channel is thus different. In order to accommodate to a user and keep a correct quality of service across receivers, the only choice is then either changing the constellation sizes of the allocated subcarriers or altering the subcarrier allocation. This relatively low flexibility on  $m$ -CAP means that increasing the quality of service for a user demanding a fixed data rate means the decrease in quality for other users since they'll have less allocated subcarriers. From this observation, the potential added flexibility in using a different set of filter parameters on each pair of FIR filters is explored.

#### 4.3.2.1 Roll-Off Factor

The roll-off factor, as seen in the chapter 3, defines the excess bandwidth. As such, the smaller the value is for a subcarrier, the higher the peak-to-average-power-ratio

(PAPR) for that subband is. This is especially important as all subcarriers are transmitted together. The premise for the optimization of the roll-off factor for each subcarrier is that in the realistic experimental setup for the indoor VLC system, different types of noise dominate the signal at different frequencies. Indeed, pre-equalization is used to extend the modulation bandwidth of the channel and thus virtually work ‘out-of-band’. As such, the received signal power is lower at higher frequencies due to the low-pass effect of the channel. Thus, the white Gaussian noise dominates at higher frequencies for the signal but less at lower frequencies where the clipping noise is lower. In consequence, the latter subcarriers will favor a lower roll-off factor for less excess bandwidth and the early subcarriers will prefer a higher value. Using the parameters of Table 4.2, except for the roll-off factor parameter, the impact of this value is measured, and shown figure 4.18, on the bit error rate for subcarriers (a) 1 to 5, (b) 6 to 10 (c) 11 to 15, and (d) 16 to 20 for a 20-CAP modulated signal. A constellation size of  $M = 64$  is used on all subcarriers.

Figure 4.18 shows the measured impact of the roll-off factor on the bit error rate at the reception of each subcarrier in a 20-CAP modulated waveform. The lowest BER for each subcarrier is indeed found at different values of this factor. For subcarriers 1 to 5, the average optimal roll-off factor is measured at 0.66. For subcarriers 6 to 10, it is measured at 0.46. For subcarriers 11 to 15, it is measured at 0.3. And, for subcarriers 16 to 20, it is measured at 0.26. This measure is supported by the observation noted previously. Indeed, the latter frequencies are placed at higher frequencies where the Gaussian noise dominates, in the case of the experimental setup described here. Thus, the latter subcarriers performances are optimized with a smaller excess bandwidth, or a smaller roll-off factor. The first subbands on the other hand benefit better from a reduction in the clipping noise. In consequence, their performances are optimized with a larger roll-off factor.

#### 4.3.2.2 Filter length

The oversampling factor and the filter span define the filter length together. The impact is simple to explain, as seen in chapter 3. Indeed, the SNR is increased across the signal bandwidth for the same sampling frequency. As such, a more positive impact should be seen in the latter subcarriers where the Gaussian noise dominates. A trade-off between the implementation cost needs to be noted. While the increase in the filter length provide better raw performances, a lengthier FIR filter will be more computationally taxing. In this work, this trade-off will not be analyzed as it does not make sense when using an AWG and MATLAB for offline pre- and post-processing. Figure 4.19 represents the measured impact of the filter length on the bit error rate for each subcarrier using the experimental setup with the parameters from Table 4.2. The same constellation size of  $M = 64$  was used throughout all subcarriers. Other constellation sizes gave the same trend while offering a lower BER if the modulation order was smaller.

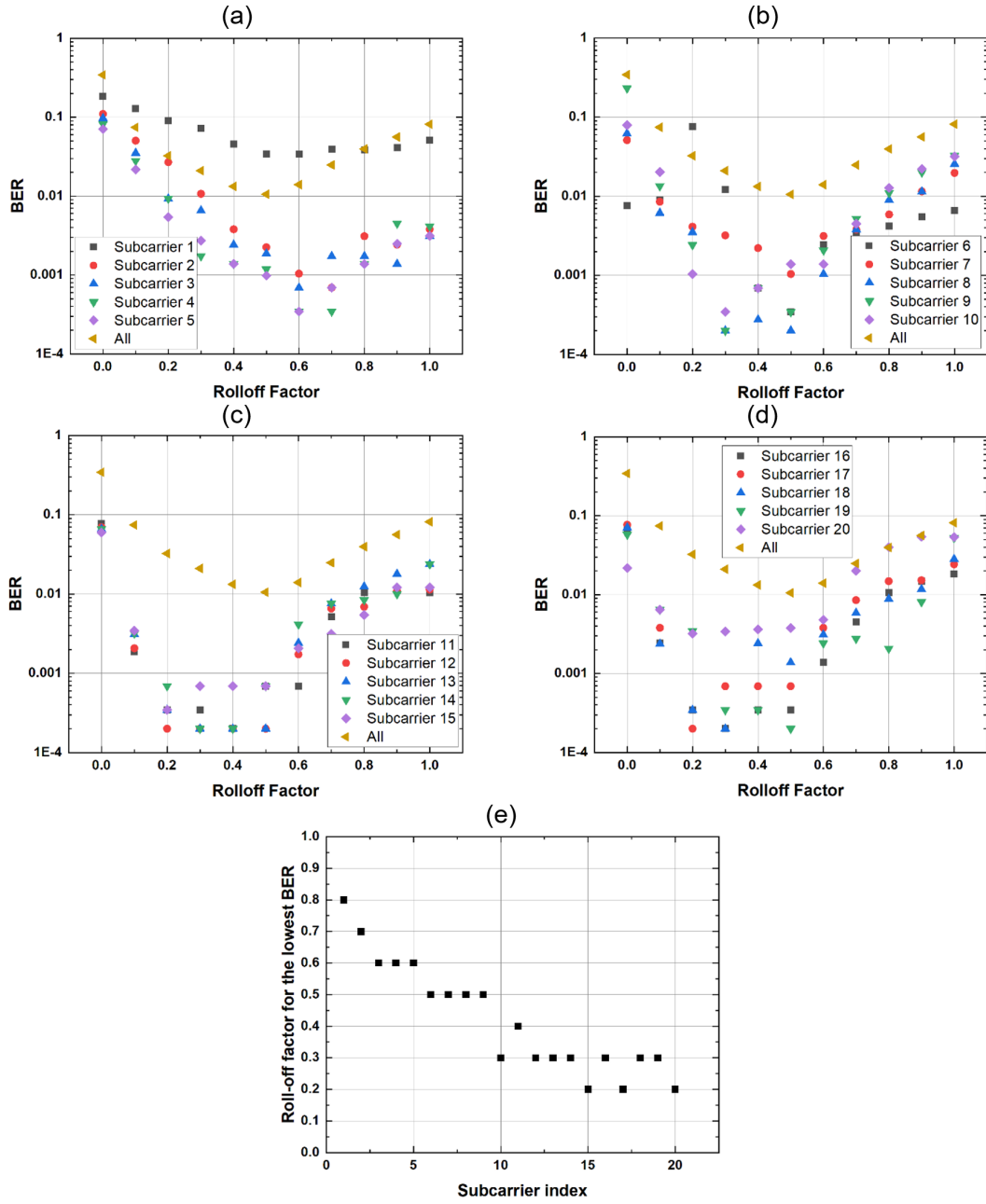


FIGURE 4.18: Measured impact of the roll-off factor on the BER of each subcarrier on a 20-CAP signal, for subcarriers (a) 1 to 5, (b) 6 to 10 (c) 11 to 15 and (d) 16 to 20 of a multiband CAP modulated waveform. (e) Measured roll-off factor associated to the lowest BER for each subcarrier.

Figure 4.19 shows the measured impact of the filter length on the bit error rate at the reception of each subcarrier in a 20-CAP modulated waveform. As explained previously, the lowest BER is attained with the highest filter length. At a filter length of 150, the BER attained is, for example,  $3.57 \times 10^{-3}$  at subcarrier 3 and  $8.15 \times 10^{-3}$  at subcarrier 20, the minimum in both cases. However, a lengthier FIR filter has a higher implementation cost when modulating and demodulating the CAP waveforms of each subcarrier. In terms of trade-off, the BER decreases between a filter length

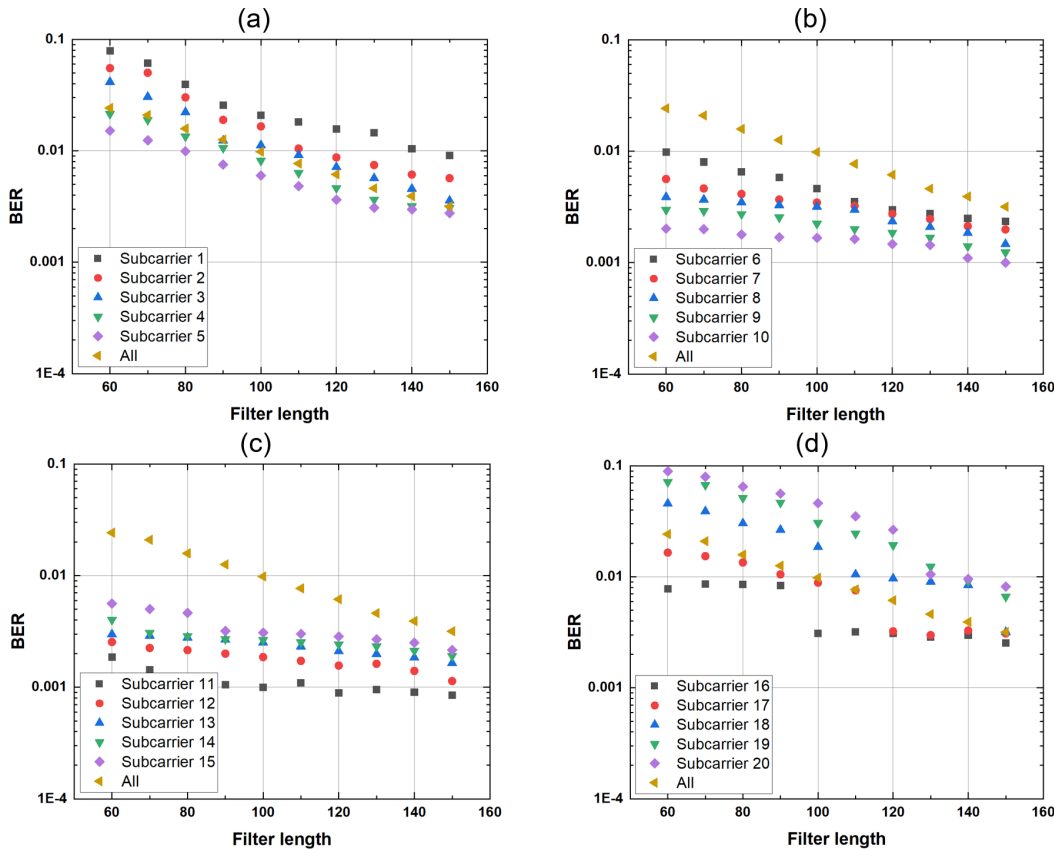


FIGURE 4.19: Measured impact of the filter length on the BER of each subcarrier on a 20-CAP signal, for subcarriers (a) 1 to 5, (b) 6 to 10 (c) 11 to 15 and (d) 16 to 20 of a multiband CAP modulated waveform.

of 120 and 150. This is a reduction of a factor of around 1.65 on average on all subcarriers. But, the latter option is 25% more computationally heavy. While such a decrease on the BER seems high, it has been noted in section 4.3.1 that with a 7% FEC limit, such a value is often not enough to be able to increase the modulation order of a specific subcarrier. However, it still provides a considerable increase in flexibility and the effect on the latter subcarriers is more pronounced with a BER decrease of a factor of around 3.065 for the last 3 subbands when increasing the filter length from 120 to 150. In consequence, the filter length optimization trade-off between performances and implementation cost is only worth it in our case for the latter subcarriers since we value the low-complexity of the system.

### 4.3.3 Subcarrier Spacing

#### 4.3.3.1 Subcarrier Spacing Impact on Individual Subcarriers

Multiband modulation schemes are prone to inter-channel interferences and multiband CAP is no exception since pulse shaping filters do not have a perfect rectangular response. These interferences caused by the secondary lobes in the filter's response reduce the quality of the signal at a given receiver, worsening the BER. Spacing the

subcarriers is a method used to mitigate these interferences. But it comes at the cost of an increased signal bandwidth. In a high-speed VLC system, it can be a disadvantage because of the low-pass model of the optical wireless channel and the need of high spectral efficiency modulations. The slightly modified filter definition equation showed in chapter 3 adds a factor to the description of the in-phase and quadrature square root raised cosine filters used for pulse shaping each subcarrier. The default value of  $p$  is 1 which corresponds to no subcarrier spacing. Adding 10% corresponds to  $p = 1.1$  and creates a spacing of 10% between the subcarriers center frequencies. The figures 4.20 and 4.21 show the measured impact of the subcarrier spacing on the BER of each subcarrier and on the performance in attainable throughput for the system described Table 4.2. An increase in subcarrier spacing translate directly to a decrease in inter-channel interferences. However, since it also results in an increase in total signal bandwidth, a reduction of BER is not obvious because of the low-pass effect of the channel.

Figure 4.20 represents the measured impact of subcarrier spacing on the bit error rate at the reception of each subcarrier in a 20-CAP modulated signal. All subcarriers were put at the same subcarrier spacing value. The observation noted in the previous paragraph holds true with the experimental measures. Indeed, subcarriers 1 to 5 obtain the lowest BER at an optimal subcarrier spacing value of around 25%. The corresponding decrease in BER for these subcarriers at their optimal spacing amount is measured at around 83.01%. Subcarriers 6 to 10 need an optimal spacing value of around 13%. The corresponding decrease in BER for these subcarriers at their optimal spacing amount is measured at around 81.59%. Subcarriers 11 to 15 need a spacing value of around 10%. The corresponding decrease in BER for these subcarriers at their optimal spacing amount is measured at around 63.68%. And, subbands 16 to 20 need a spacing value of around 3%. The corresponding decrease in BER for these subcarriers at their optimal spacing amount is measured at around 15.13%. Overall, it means that for each subcarrier, when the whole signal used the optimal spacing value indicated for that subband, a lower BER at that specific subcarrier was attained. Also, as explained previously, since the latter subcarriers are dominated by the Gaussian noise, a reduction in ICI by increasing the spacing will attenuate the signal at these subbands because of the low-pass effect of the channel. Thus, the larger the subcarrier center frequency is, the lower the optimal spacing value will be. And, the larger the subcarrier frequency is, the lower the decrease in BER will be at the optimal spacing value.

Figure 4.21 shows the measured performance variation in percentage depending on the subcarrier spacing value used by the signal. This variation is calculated with the maximum available throughput, obtained in the same way as explained in section 4.3.1. The same observation as in figure 4.20 is obtained here in less details. Indeed, in our situation with 250 MS/s as a sampling rate, the highest performance variation in raw data rate is measured at 4.23% for a spacing value of 10%. On the other

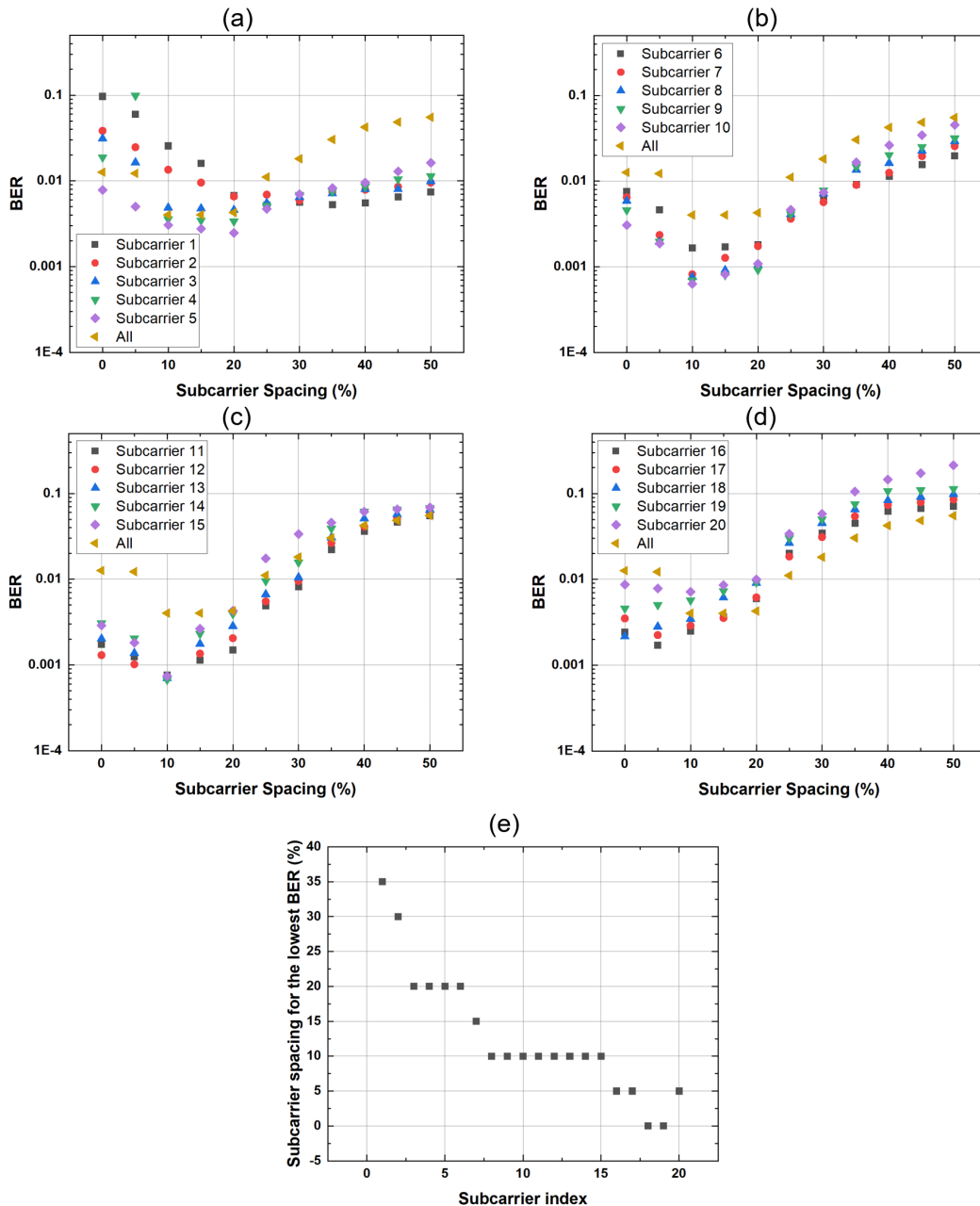


FIGURE 4.20: Measured impact of subcarrier spacing on the BER of each subcarrier on a 20-CAP signal, for subcarriers (a) 1 to 5, (b) 6 to 10 (c) 11 to 15 and (d) 16 to 20 of a multiband CAP modulated waveform. (e) Measured subcarrier spacing factor associated to the lowest BER for each subcarrier.

hand, a value of 50% provokes a decrease in raw throughput of 9.9% because the attenuation of the signal due to low-pass effect and signal bandwidth expansion more than compensate the reduction in ICI. Furthermore, at a sampling rate of 100 MS/s, the highest performance variation is measured at 1.29% for a spacing value of 20%. On the other hand, at a sampling rate of 500 MS/s, the optimal performance variation is measured at 4.49% at a spacing value of 5%. It means that the larger the signal bandwidth is, the lower the overall optimal spacing value for the signal will be. This

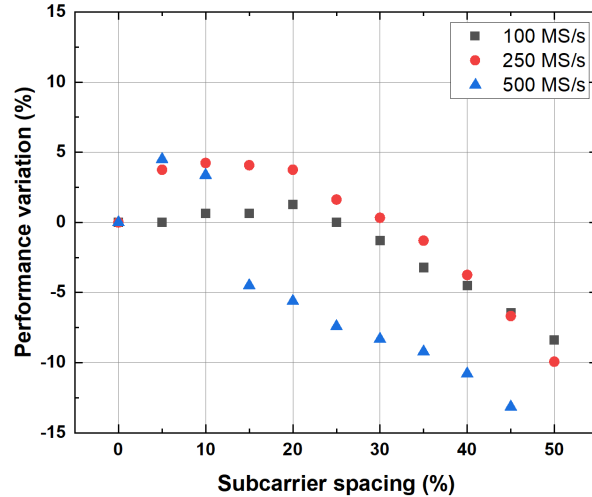


FIGURE 4.21: Measured performance variation for different values of subcarrier spacing for the whole signal at various sampling rates.

is due to the fact that with a larger signal bandwidth, the subcarriers are bigger and thus experience more of the LED's low-pass effect. Thus, the ICI reduction is not enough to compensate the losses due to the low-pass attenuation.

As uncovered in section 4.3.1, while these values do not represent a large boost in data rate, they do correspond to a sizable decrease in BER. Indeed, the main objective of this performance optimization process is to improve the flexibility of the modulation scheme with the objective of utilizing it in a multi-users scenario. And, we will see in Chapter 5 that the BER distribution offered by the scheme defines a number of the multi-users performances for the experimental system.

#### 4.3.3.2 Uniform and Optimized Subcarrier Spacing

The effect of different subcarrier spacing configuration on the spectral efficiency is investigated in the following measures. In order to measure it, the data rate is maximized in the condition of the experiment described section 4.1.3 and in Table 4.2. The first configuration uses no subcarrier spacing. The second configuration uses the same spacing value between each subcarrier and is called uniform subcarrier spacing. The spacing value chosen maximizes the data rate. Lastly, the last configuration uses the best subcarrier spacing between each subcarrier and is called optimized spacing. The data rate is, once again, maximized.

Figure 4.22 shows the measured impact of subcarrier spacing on the maximum attainable data rate. The first observation is similar to the one presented in the previous subsection. Indeed, an increase in the number of subcarriers results in an increase in performances. As already explained in section 4.3.3, the frequency response of the channel is not flat, thus with smaller subcarrier bandwidth, the associated response is more flat and thus the subband can use a higher modulation order. With the use of subcarrier spacing, the inter-channel interferences (ICI) have decreased but the

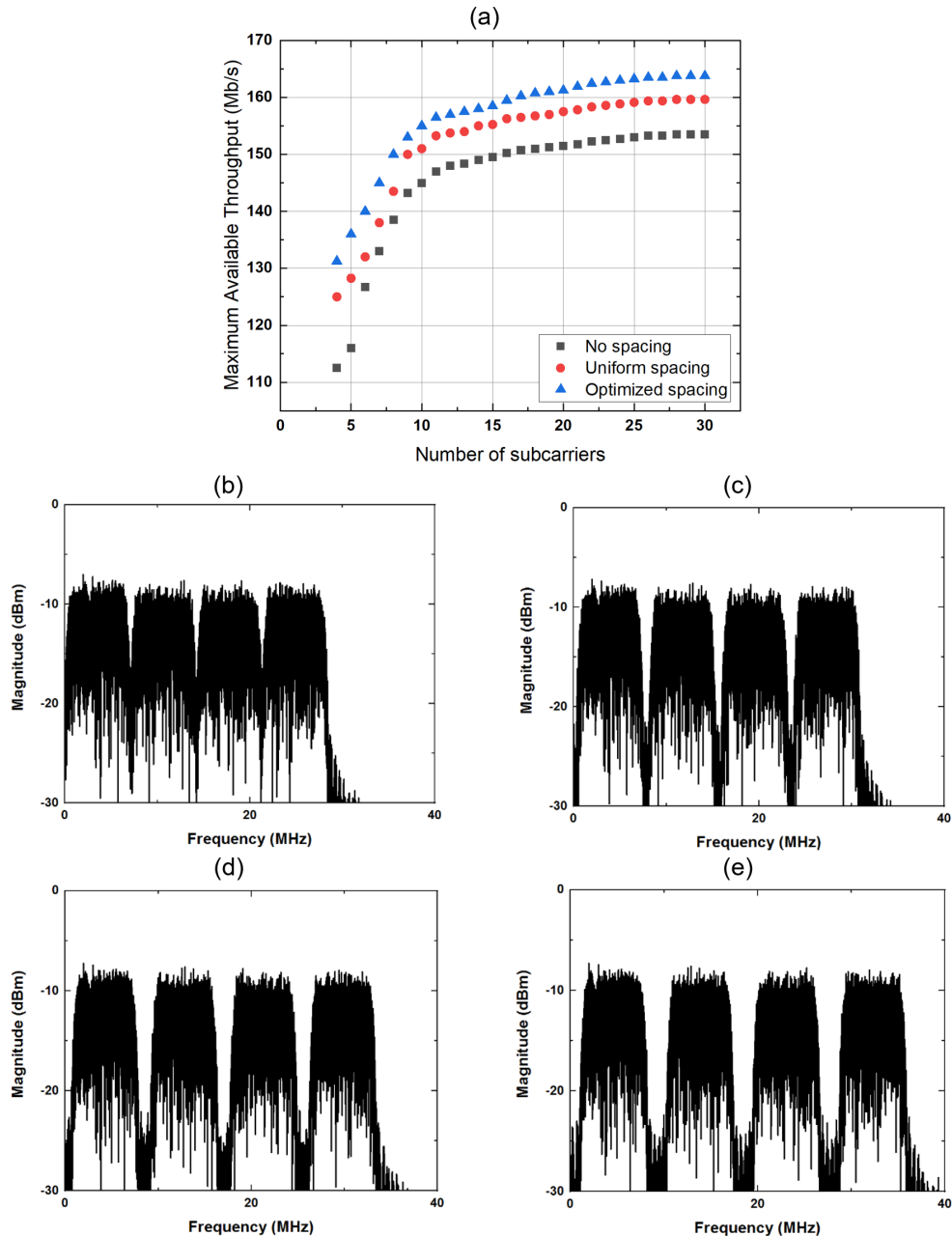


FIGURE 4.22: Measured impact of subcarrier spacing on the maximum attainable data rate (a). Obtained while maximizing the data rate against the number of subcarriers. The measurements are performed without spacing, with the same spacing value and with a spacing value optimized between each subband. Measured spectrum in a 4 subcarriers signal with no spacing (b), 5% spacing (c), 10% spacing (d), and 20% spacing (e).

bandwidth of signal increases. In turn, the SNR drops. With uniform spacing, the increase in performances for the first subcarriers compensate for the decrease in the last subcarriers. With optimized spacing, the first subcarriers have a larger spacing value than the last ones which use a smaller spacing or none. Essentially, the first subbands have a SNR high enough and the decrease in ICI is enough to allow the use

of a higher modulation order. But, in order to not increase the signal bandwidth too much, the last subcarriers use an average spacing of 2.5%. Thus, as shown in figure 4.22, an increase in data rate of 16.67% to 6.7% is obtained with 4 to 30 subcarriers using optimized spacing while the values are 11.11% to 4% using uniform spacing. With 20 subcarriers, the increase in data rate is measured at 6.43% for the optimized spacing method and 3.96% for the uniform spacing process. The difference is bigger when using a small number of subbands because the signal does not use an optimal number of subcarriers in order to compensate for the non-flatness of the channel. Indeed, a higher modulation order for a subband can be used when the frequency response associated is flatter. As such, the margin for an increase in performances using subcarrier spacing only decreases. Consequently, the optimization process is investigated further with the addition of the roll-off factor and filter length optimization. This more complete method aims at increasing the raw performances and the flexibility of the scheme even in addition to what subcarrier spacing adds.

#### 4.3.4 Flexibility and Performance Optimization

Multiband CAP is a very recent modulation scheme for VLC. The approach proposed here is to explore its capabilities further by improving the scheme in flexibility and data rate performances. The experimental setup used here is described section 4.1.3 and the parameters are summarized Table 4.2. The premises for the optimization of the performances were described in section 4.3.2 and 4.3.3 with the individual optimization of the filter parameters and the addition of subcarrier spacing.

More flexibility can be obtained with the optimization of the roll-off factor and the oversampling factor of the FIR filters, as seen in section 4.3.2. Indeed, the higher the roll-off factor is, the larger the bandwidth is and the lower the clipping noise. As such, when modifying all parameters at the same time, multiple scenarios with an increase in performances appear. That flexibility helps in a multi-users scenario where all receivers have very different SNRs.

In order to explore this flexibility, the impact of the roll-off factor on the data rate is compared with the results obtained in the previous section. With no spacing, and the same parameters, each subcarrier has a roll-off value optimized in order to maximize the total data rate. Then, subcarrier spacing is associated with roll-off factor in the optimization. The process to obtain the parameters for all subcarriers is described figure 4.23. As the subject of this work focuses on the results of the optimization and not the method itself, a conventional loop algorithm is used in two steps. The first one is a uniform optimization where the same global values for either of the parameters is set for all subbands. The objective is to obtain the value of subcarrier spacing and roll-off factor which minimize the BER,  $p_U$  and  $\alpha_U$  respectively. In regard to the filter length, a simple process where the latter subcarriers of the  $m$ -CAP signal use a slightly longer value was added. The second step of the algorithm is once again a conventional loop which finds the optimal value for  $p$  and  $\alpha$ . The results are compiled

in figure 4.24, adding intermediary results where only the roll-off factor or only the subcarrier spacing factor is optimized.

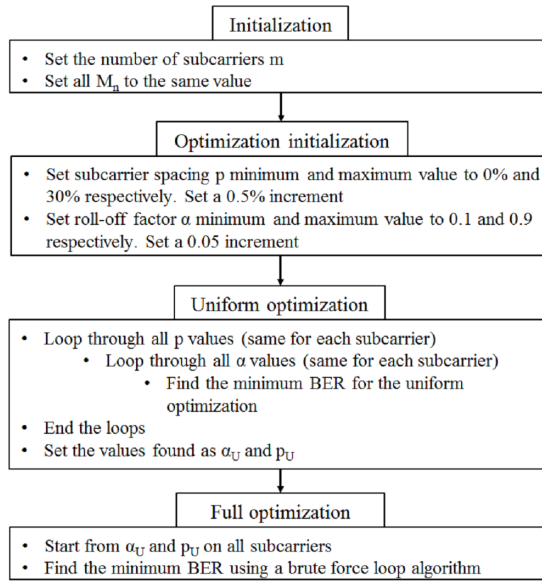


FIGURE 4.23: Optimization process pseudo-code for obtaining the optimized filter parameters in both the uniform optimization and the full optimization process.

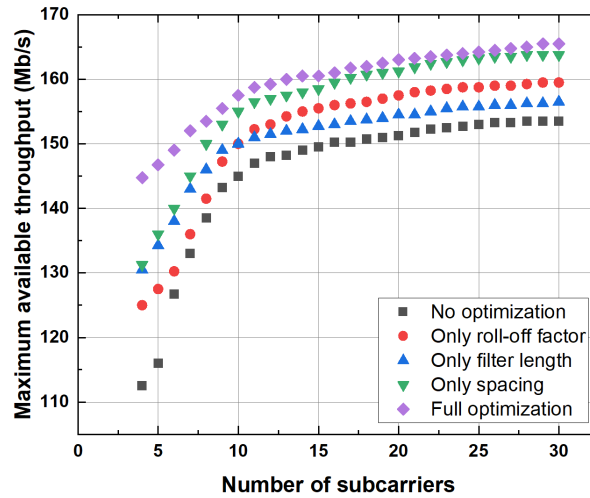


FIGURE 4.24: Measured change in data rate performances compared to no filter parameter optimization in the experimental setup. The process is applied on subcarrier spacing, the roll-off factor or both.

Figure 4.24 illustrates the impact of the number of subcarriers on the measured attained throughput for every optimization process. When optimizing only for the roll-off factor for each subcarrier, using a conventional loop as described in part of figure 4.23, the increase in raw performances reached 11.1% for a 4-CAP signal, 4% for a 20-CAP signal and 3.8% for a 30-CAP signal. When optimizing for the filter length, a global value of 120 was used throughout all subcarriers. Indeed, as seen in subsection 4.3.2.2, further increase in this value increases the implementation cost without a high enough reduction in BER. However, as explained in the previous

paragraph and shown in part of figure 4.23, the last 20% of the signal used filter length of 150 in the filter length optimization process. Thus, the 25% increase in implementation cost is attenuated. While this optimization process is less complete than for the other parameters, it fixes the increase in computation time to a known value. Hence, as measured, the increase in raw performances reached 16% for a 4-CAP signal, 2.15% for a 20-CAP signal and 1.95% for a 30-CAP signal. The optimization process with subcarrier spacing only was described in the previous section. With the full optimization process as described in figure 4.23, the increase in raw data rate attained 28.67% for a 4-CAP signal, 7.77% for a 20-CAP signal and 7.81% for a 30-CAP signal. At 20 subcarriers this is equivalent to an addition of 11.75 Mb/s. The full optimization process offers more degrees of liberty and thus more scenarios with an increase in data rate are observed. For example, a large roll-off factor increases the bandwidth of the subcarrier associated. In return, it augments the interferences between subbands. But, with subcarrier spacing, these interferences are reduced. As such, the full optimization process attains a larger increase in data rate than the others.

As observed throughout the experiments presented in figure 4.24, the enhancement in performance is higher at lower numbers of subcarriers. Indeed, a relative augmentation of 11.1% is observed for the roll-off factor only optimization, 16.67% for the subcarrier spacing only one and 28.67% for the full process in a 4 subbands scenario. When using a 20 subcarriers signal, these numbers go down to 4%, 6.43%, and 7.77% respectively. When subbands have a larger bandwidth, the effect of the low-pass distortion is stronger on them. However, adverse effects are prominent on the first few parts of the signal bandwidth for the clipping noise and the last parts for the Gaussian noise. With 4 subcarriers, a localized effect impacts a fourth of the total waveform while it only affects one twentieth when 20 subcarriers are used. Essentially, multiband CAP signals with higher total number of subbands have less headroom for data rate improvements. On the other hand, as exposed in sections 4.3.2 and 4.3.3, the BER can still be further reduced on all subcarriers even if not enough for an increase in throughput. The BER distribution in a room for the system can thus still be improved, thus expanding the attocell size as investigated in Chapter 5.

### 4.3.5 Single-User Broadcasting Characterization

Table 4.4 resumes the characteristics of the optimized 20-CAP signal in the case of the experimental setup described section 4.1.3 and the experimental parameters described Table 4.2, except when indicated otherwise.

The total increase in data rate compared to the baseline results was 11.75 Mb/s. Since subcarrier spacing was used, the signal bandwidth was impacted and went from 28.5 MHz to 31.45 MHz. In consequence, the spectral efficiency of the scheme was slightly reduced from 5.31 b/s/Hz to 5.18 b/s/Hz. In exchange, the total BER in

TABLE 4.4: Optimized characteristics for a 20-CAP signal in a single-user broadcast setup corresponding to Table 4.2.

Parameter	Value
Number of subcarriers	20
Subcarrier spacing	{30, 25, 20, 20, 20, 15, 15, 10, 10, 10, 10, 7.5, 5, 5, 2.5, 1, 0, 0, 0, 0}
Roll-off factor	{0.7, 0.6, 0.6, 0.6, 0.5, 0.5, 0.5, 0.4, 0.4, 0.4, 0.4, 0.3, 0.3, 0.2, 0.2, 0.2, 0.15, 0.15, 0.15, 0.15}
Filter length	{120, ... , 120, 150, 150, 150, 150}
Signal bandwidth	31.45 MHz
AWG Sampling rate	250 MS/s
Distance	2.15 m
Total Throughput	163 Mb/s
Total BER on direct LOS	$5.18 * 10^{-4}$

direct LOS was reduced significantly from  $1.84 * 10^{-3}$  to  $5.18 * 10^{-4}$ , or a decrease by a factor of 3.55, on top of the increase in data rate. As explained throughout the experimental investigation, this is due to the use of optimized filter parameter values for each subcarrier. While the decrease in BER is sometimes not enough to translate into an augmentation in modulation order for a specific subband, the bit error rate is oftentimes significantly reduced by relatively large factors. This corresponds, as previously said, to a boost in the flexibility of the scheme. It means that multiple scenarios exist where a higher data rate is attained, as explained in section 4.3.4. The BER distribution in a room will also be positively impacted by the optimization process. This characteristic is essential to the estimation of the multi-users capability of the experimental system. In consequence, Chapter 5 will be the subject of this investigation.



## Chapter 5

# Experimental Investigation of the Multi-Users Capabilities

### Contents

---

<b>5.1 Multi-Users Capabilities Evaluation Methods . . . . .</b>	<b>141</b>
5.1.1 Updated Experimental Setup . . . . .	142
5.1.2 Attocell Characterization Process . . . . .	144
5.1.3 User Serviceability . . . . .	145
<b>5.2 Characterization of the Multi-Users Systems . . . . .</b>	<b>149</b>
5.2.1 Utilization of the Multi-Access Schemes Associated with m-CAP . . . . .	151
5.2.2 Impact of the 3D Distributions . . . . .	154
5.2.3 User Allocations . . . . .	157
5.2.4 Impact of the Distance Between the Transmitter and the Receivers . . . . .	163
5.2.5 Total System Characterization . . . . .	163

---

## 5.1 Multi-Users Capabilities Evaluation Methods

The experimental investigation performed in Chapter 4 concluded with the optimization of the single-user broadcast performances of a multiband CAP signal in an indoor VLC system. Both an increase in raw throughput and an increase in flexibility through reductions in BER throughout all subcarriers was attained. These results are ready to be associated with the various multi-users access schemes that were considered and exposed in Chapter 3. The objective of the first part of Chapter 5 is the definition of the different processes and terms used throughout the measures that will be presented in the second part. Section 5.1.1 is a complete description of the experimental setup that will be used throughout the analysis performed in this chapter. Section 5.1.2 describes the process of attocell characterization with the presentation and explanation of the importance of the BER distribution, the impact of the range

of the system and a definition of the attocell size. Finally, section 5.1.3. exposes the problematic of user serviceability with the association's methodology described.

### 5.1.1 Updated Experimental Setup

Figure 5.1 shows the experimental setup that is used to obtain the measured results presented in this chapter. In the same way as chapter 4, an AWG (AFG3252C) is used as part of the transmission process. It stores a total of  $m$  random bits streams. With  $m$  corresponding to the number of subcarriers. The streams form packets of data for each user  $k$ . The modulation process depends on the multi-access method of choice:

- **SCM:** The number of bit streams assigned to each user depends on the given subcarriers' allocation  $c_k$  for each user. It means that a user  $k$  is allocated a packet of  $j$  (size of  $c_k$ ) bits streams. Each of these is assigned to a subcarrier. For every user, an  $M$ -QAM mapper maps each of the data streams forming its packet, resulting in multiple symbols streams. Following the modulation process, the  $m$  resulting modulated streams are added to produce the signal  $s(t)$ , as defined in chapter 4.
- **MC-CDMA:** A group of  $m$  bits streams is assigned to each user. Each of these streams is spread with an orthogonal code spreading process. A Walsh-Hadamard based technique is used here. The spread streams of data then follow a multiband CAP modulation process. The same number of subcarriers and FIR filter parameters are used for each spread stream of data. Finally, the signals for each user are added together to produce  $s(t)$ .
- **PD-NOMA:** A group of  $m$  bits streams is assigned to each group of users. In this experimental setup, two groups are considered, the close users' group and the far users' group. Additionally, PD-NOMA is associated with either SCM or MC-CDMA. In each case, the modulation process is similar to the one used for both these multi-access method in the case of each group of users. The signal for the close user group,  $s_{cu}(t)$  and the signal for the far user group,  $s_{fu}(t)$  are superposed using the power allocations  $p_{cu}$  and  $p_{fu}$ . If more power level were used, the SIC algorithm would have an increased complexity. While only two power levels are used, the particularities of PD-NOMA are still highlighted.

Before transmission by the AWG, the signal is pre-equalized using the same software implemented amplitude pre-emphasis filter as in Chapter 4. The preamble waveform described in detail in Chapter 4 is also reused. After emission by the AWG, the electrical driver components used previously are also utilized. The white LED functions at the same parameters described in Chapter 4, at 19.2 W (32V, 0.6A).

At the receiver, a 25 mm biconvex lens and a PD associated with a TIA (Thorlabs PDA10A) form the receiving circuit for a user  $k$ . The received output signal from the TIA is saved using a digital oscilloscope in order to post-process the measures.

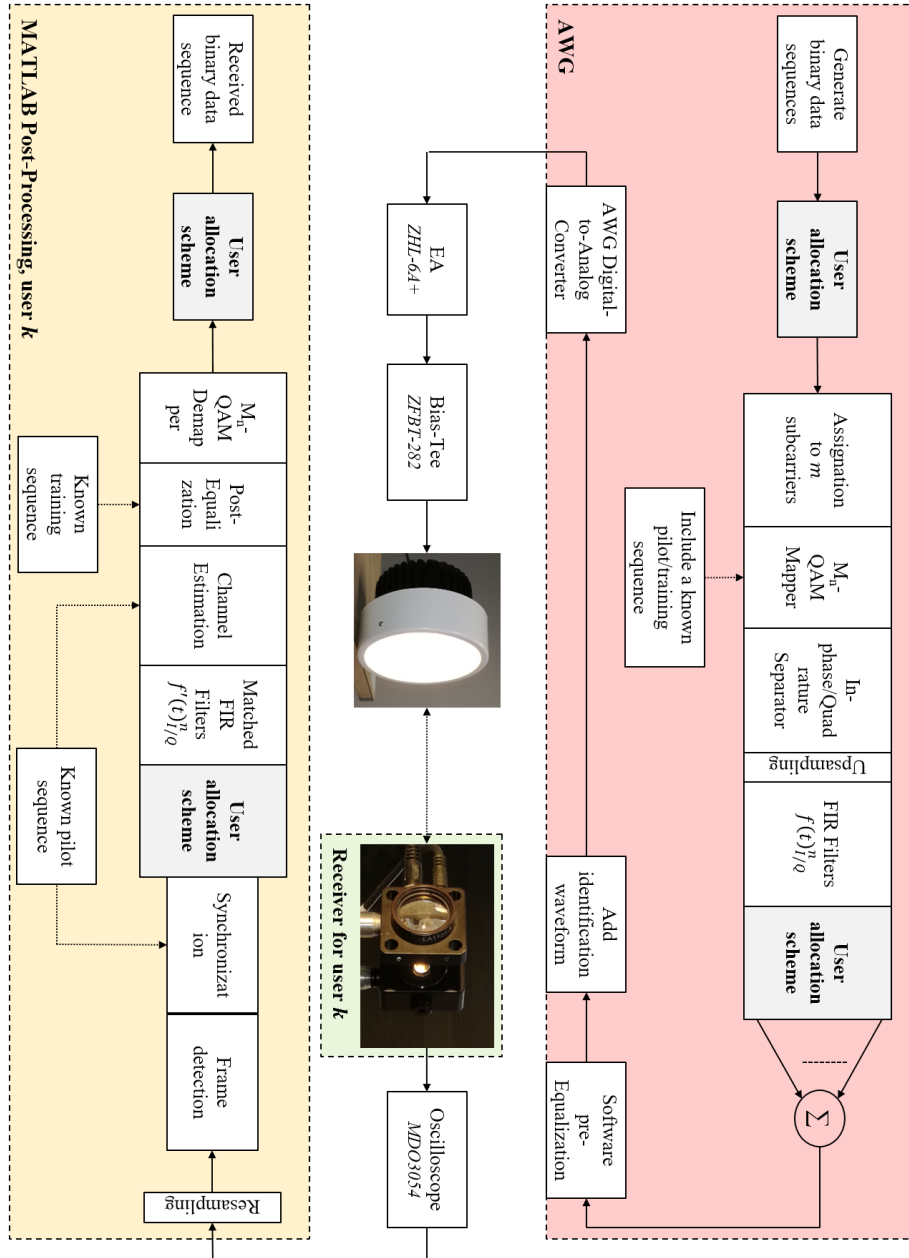


FIGURE 5.1: Schematic representing the experiment setup in a multi-users scenario for the transmitter based on an AWG, an office downlight, and a receiver for a user  $k$  based on a photodiode and an offline post-process with MATLAB.

After re-sampling the signal, the preamble waveform is identified. The rest of the demodulation process for user  $k$  depends on the multi-access method used by the experimental system:

- **SCM:** The matched filters deployed for demodulation depend on the allocation of subcarriers  $c_k$  for user  $k$ . The first subcarrier contains that information in the experimental process. Afterwards, the process is a standard  $m$ -CAP demodulation on the related subcarriers.
- **MC-CDMA:** Each user follows the demodulation process directly with matched

filters for each subcarrier. The process is a standard  $m$ -CAP demodulation. But, after de-mapping, the spreading code are used to de-spread the stream of data for user  $k$ . The receivers are considered to have the knowledge of the spreading code and the first subcarrier contains the information on which code the receiving user must consider.

- **PD-NOMA:** In the case of the far users' group, the demodulation process directly follows the one described for SCM or MC-CDMA depending on the original multi-access method association. In the case of the close users' group, a SIC process is first applied, where the far users group signal  $s_{fu}(t)$  is first estimated. Then, knowing the power allocations  $p_{cu}$  and  $p_{fu}$ , this estimated signal  $s'_{cu}(t)$  is removed from the received signal. Then, the demodulation process for the close users' group is applied.

## 5.1.2 Attocell Characterization Process

### 5.1.2.1 BER Distribution

The 3-Dimensional (3D) BER distribution indicates the bit error rate attained after the demodulation process by a receiver located at a certain point in the room. This location is on a receiving plane distanced from the transmitting plane at a defined distance using the LED emitter as the reference. A BER distribution graph represents the BER on the  $z$  axis, the length of the room on the  $x$  axis and the width of the room on the  $y$  axis. In consequence, the BER that a user experiences can be known. This is a direct representation of the performances of the system and numerous characteristics can thus be obtained:

- The maximum attainable throughput for any user located in the room which can be obtained with the BER and a known FEC limit.
- The size of the attocell and the range of the system which are represented by the area where the BER is low enough for a user to be able to fully experience the capabilities of the access point.
- A general indication on the flexibility of the multi-users system based on the BER distribution.

An example of a simulated BER distribution with the same conditions as the experiments here can be found in figure A.4 of part A.4 of appendix A.

### 5.1.2.2 Attocell Size

The size of the attocell is defined as the area in the receiving plane where a user can be fully served by the access point. In practice, for the experimental setup, it corresponds to the surface where the BER at the reception is below a certain value. A 7% FEC limit is chosen and this value is  $3.8 * 10^{-3}$ . Concretely, if the BER of all subcarriers of the multiband CAP signal is below this number, a user can fully

decode the waveform provided that 7% of the data is allocated to the forward error correction process.

An important note is that the attocell is also dependent on which multi-access method is used. Indeed, in the case of SCM, the multiband CAP waveform is unchanged compared to chapter 4 and thus, no matter the number of users allocated, the characteristics of the signal will not change. The attocell size in this case experiences no variance with different number of users. However, in the case of MC-CDMA, it was explained in chapter 3 that the more spreading codes are used, the more difficult it is to maintain orthogonality between users. In consequence, the multiband CAP waveform needs to be optimized to keep the orthogonality at a point where each user can still de-spread its data successfully. The attocell size thus risk to experience some variance with different amount of spreading codes. Also, the BER distribution varies in the room which means that the signal might not maintain the orthogonality for a certain amount of spreading codes throughout the entirety of the receiving plane. This problematic is further explored with the experimental setup in section 5.2.2.

An example of a simulated BER distribution on a plane with the same conditions as the experiments here can be found in figure A.5 of part A.4 of appendix A.

### 5.1.3 User Serviceability

Each combination of multiband CAP with either SCM, MC-CDMA or PD-NOMA uses a different resource to allocate its users. In order to measure the effectiveness of the user allocation method, we defined the deviation from the target throughput in chapter 3. The principle of each process is described in the following subsections for each association.

#### 5.1.3.1 With SCM

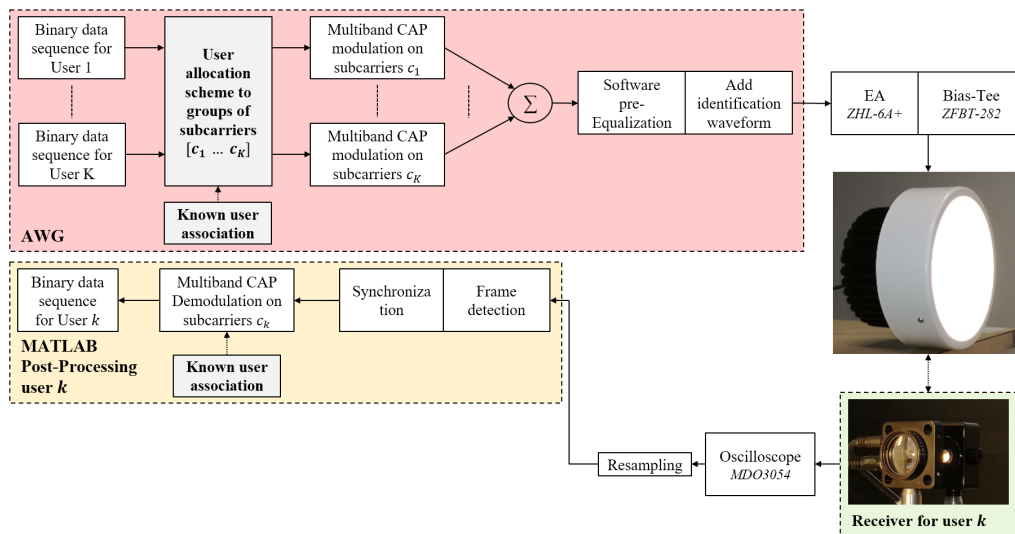


FIGURE 5.2: Simplified experimental setup diagram in the case of the multiband CAP association with SCM.

The first multi-users indoor VLC experimental system that is studied is the association of SCM with multiband CAP. The multiband CAP aspect of the experiments follows the optimization process in order to increase the flexibility of the scheme. The parameters of the FIR filters are optimized for each subcarrier and subcarrier spacing is added to maximize the data rate and the adaptability of the scheme. Table 4.4 in section 4.3.5 of chapter 4 summarizes the specification of the multiband CAP signal used in the conditions of the experimental setup. In regards to the multi-access aspect of the scheme, as shown in figure 5.2, the number of users to be served is defined at the transmitter. Then, each user is associated with a group of subcarriers following the user association algorithms described in subsection 3.3.3.1 of chapter 3. All subcarriers are part of a multiband CAP modulation scheme and their signals are added to produce the signal that is outputted by the AWG. The subcarrier-to-user associations are stored in the first subcarrier of the signal. At the receiver for any user, the first subcarrier is first decoded and then the subbands associated to that user are decoded in order to recover the data supposed to be transmitted to that receiver. Figure 5.3 is an example representing an SCM association in a 20-CAP signal using a frequency spectrum received by a PDA10A in a 4-users scenario.

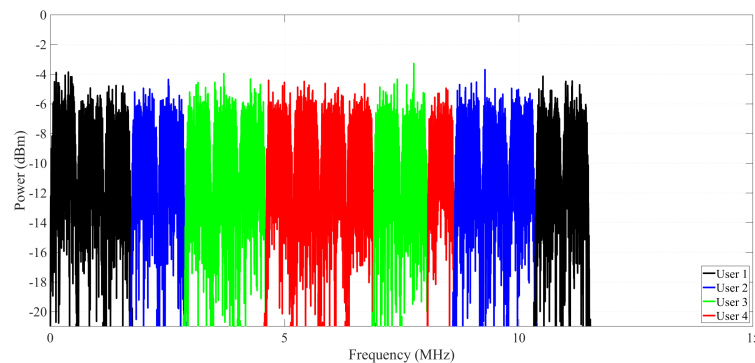


FIGURE 5.3: Illustration of an SCM association with a measured frequency spectrum of the signal received. User 1 is in black, user 2 in blue, user 3 in green and user 4 in red.

### 5.1.3.2 With MC-CDMA

The second multi-users indoor VLC experimental system that is studied is the association of MC-CDMA with multiband CAP. The multiband CAP aspects of the signal are optimized using the same process as described in section 4.3.4 of chapter 4 with a combination of ideal FIR filter parameter for each subcarrier and subband spacing. In regards to the multi-access aspect of the scheme, as shown figure 5.4, the number of users and codes is first defined at the transmitter. Then the Walsh-Hadamard matrix is generated based on the number of users and subcarriers. Each user corresponds to a binary data stream that follows an  $m$ -CAP modulation process after being spread using the previously generated codes. Thus, each spread data stream is summed after being modulated. At the receiver, the knowledge of each codes index being used for

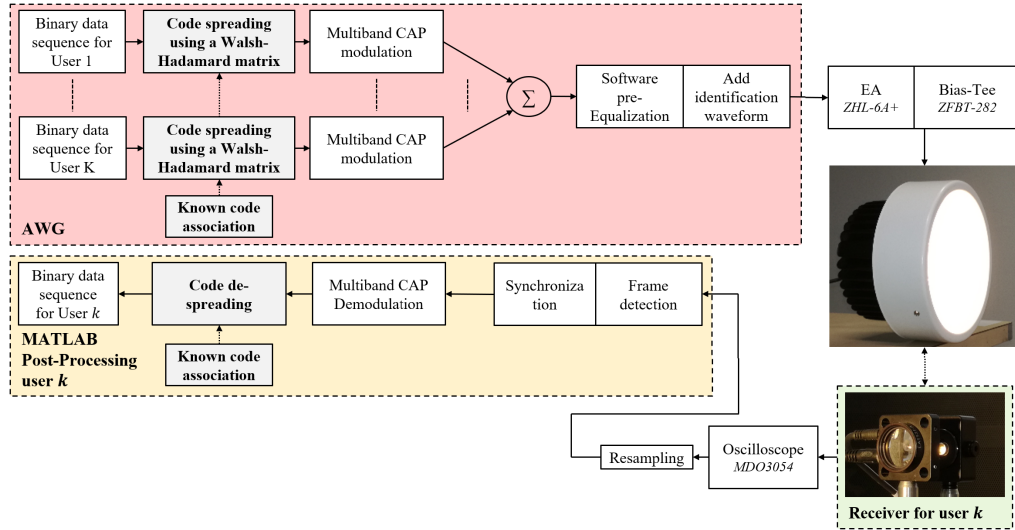


FIGURE 5.4: Simplified experimental setup diagram in the case of the multiband CAP association with MC-CDMA.

each user is supposed to be known. The  $m$ -CAP demodulation process is followed by a de-spreading of the resulting data stream using the user corresponding code in order to recover the data matching that receiver. Figure 5.5 is an example representing an MC-CDMA association in 20-CAP signals using their frequency spectrums spread on multiple code levels in a 4-users scenario.

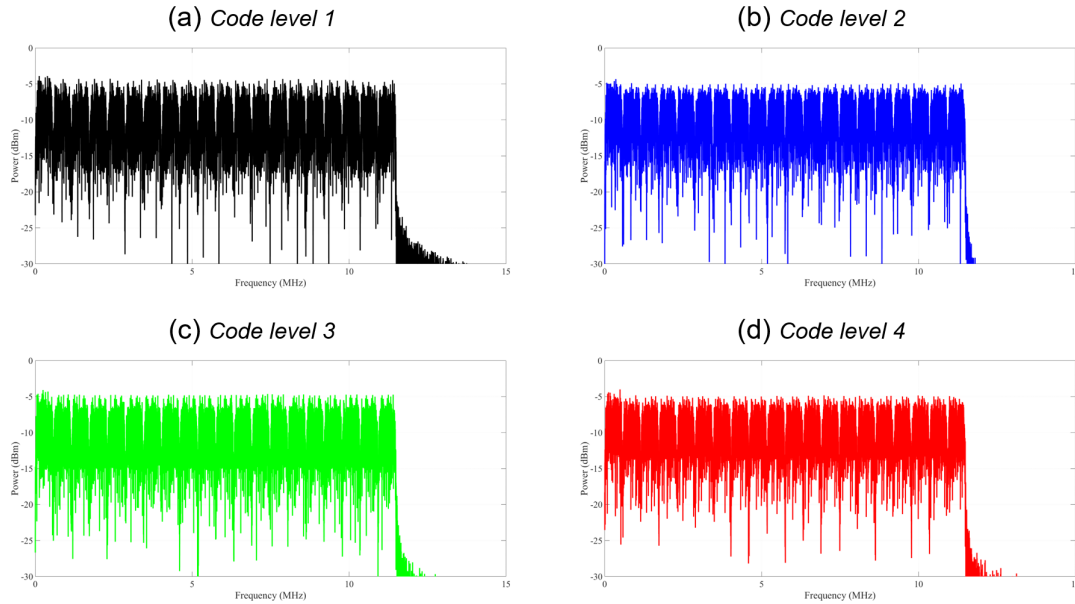


FIGURE 5.5: Illustration of an MC-CDMA association with a measured frequency spectrum of the signal received on a 4-code scenario. User 1 is in black, user 2 in blue, user 3 in green and user 4 in red.

### 5.1.3.3 With PD-NOMA

The third multi-users indoor VLC experimental system that is studied is the association of PD-NOMA with multiband CAP. As seen in chapter 3, PD-NOMA in this

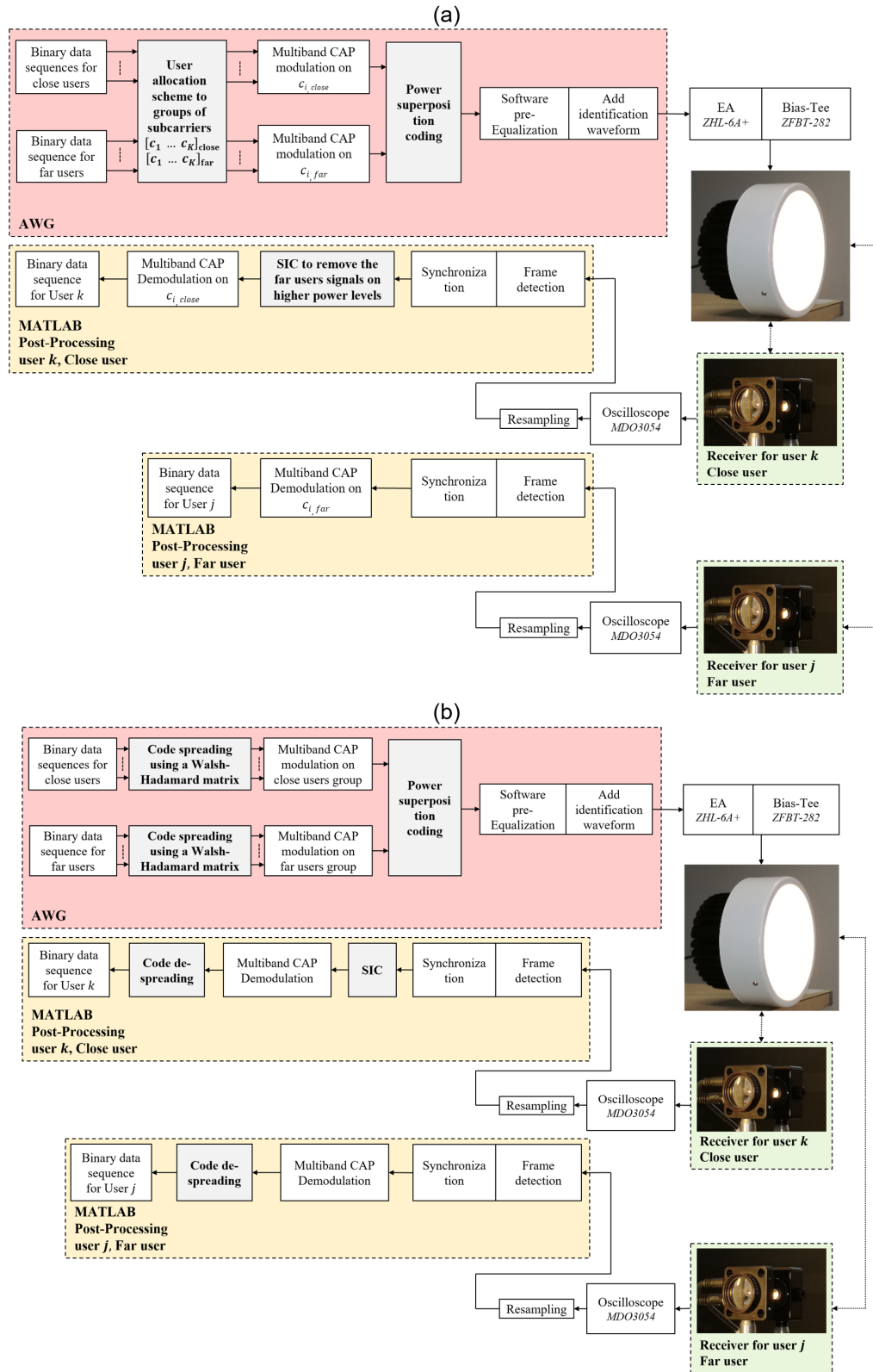


FIGURE 5.6: Simplified experimental setup in the case of the multi-band CAP association with (a) PD-NOMA combined with SCM and (b) PD-NOMA combined with MC-CDMA.

system uses two power levels and is combined with a secondary multi-access scheme

for each of them, namely SCM or MC-CDMA. The multiband CAP aspects of the signal are optimized using the same process as described in section 4.3.4 of chapter 4 with a combination of ideal FIR filter parameter for each subcarrier and subband spacing. In regard to the multi-access aspect of the scheme, the number of power levels is defined at the transmitter, as well as the number of users and the secondary multi-users access method used in combination with the PD-NOMA scheme. The two power levels define the close users' group and the far users' group. The knowledge of which user correspond to which group is known at the transmitter and the receivers. The definition of each group is such that half of the users are in the far user group and the other half in the close user group.

- If SCM is used as the secondary access scheme, both groups of users are allocated to a separate multiband CAP modulation process and different groups of subcarriers using the user association algorithms defined in subsection 3.3.3.1 of chapter 3. The first subcarrier of each waveform contains the associations that were defined. After each  $m$ -CAP modulation process, both the far users modulated signal and close users signal are added using superposition coding. At the receivers for the close users, SIC is used to remove the signal corresponding to the far users because they use a higher power level. Then, the appropriate subcarriers are decoded to recover the data for that user. At the receivers for the far users, the matching subbands are directly decoded. This is illustrated by figure 5.6 (a).
- If MC-CDMA is used as the secondary access scheme, both groups of users are allocated to separate spreading codes. At both power levels, the user data streams are spread and then follows a separate multiband CAP process. The modulation process output signals for each user group are added and then both resulting waveform use superposition coding. At the receivers for the close users, SIC is used to remove the signal corresponding to the close users because they use a higher power level. Then, the resulting signal is demodulated, and the corresponding stream of data is de-spread to obtain the originally transmit data for the matching user. At the receivers for the far users, the same process is followed without the use of SIC. This is illustrated by figure 5.6 (b).

Figure 5.7 represents two example both an association of PD-NOMA with SCM and PD-NOMA with MC-CDMA using the frequency response of 20-CAP signals at different power levels in a 4-users scenario.

## 5.2 Characterization of the Multi-Users Systems

The experimental characterization of the multi-users associations with multiband CAP aims at comparing the various multi-access techniques retained for this work in

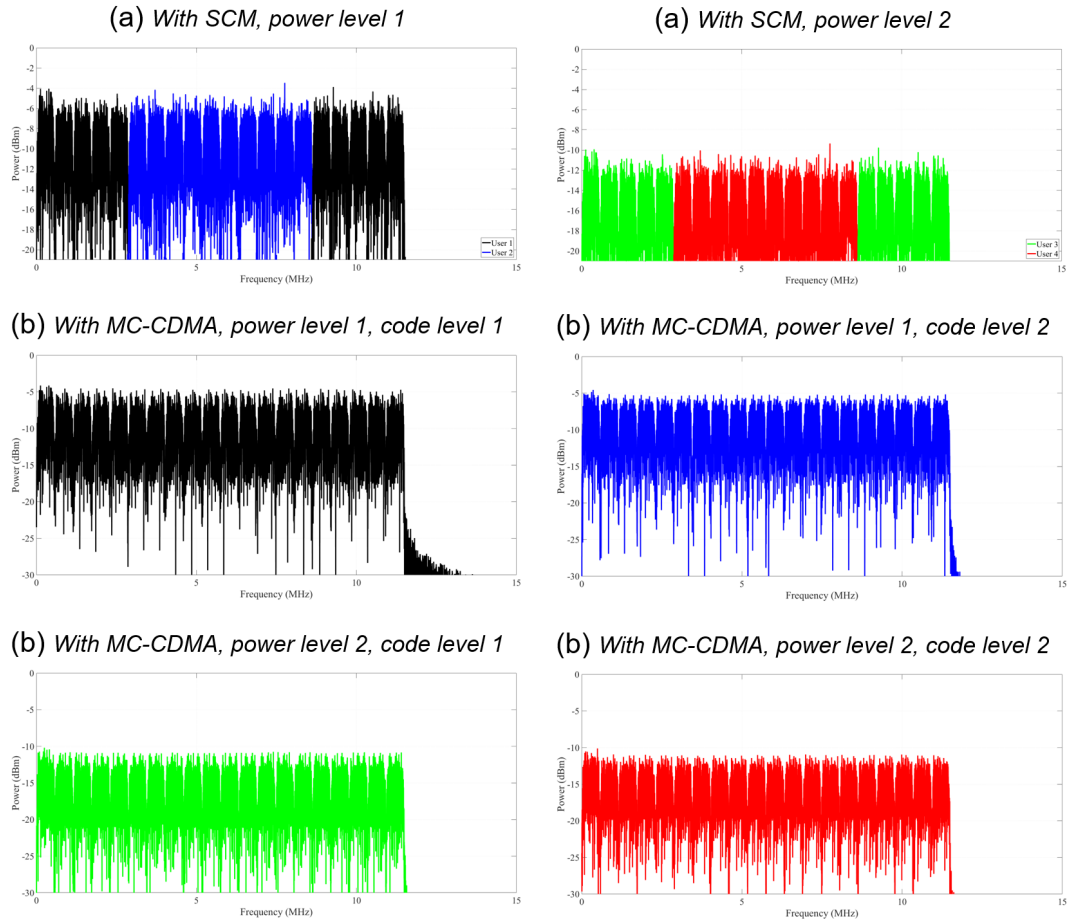


FIGURE 5.7: Illustration of a PD-NOMA association with (a) SCM and (b) MC-CDMA on a measured frequency spectrum of the signal at the receiver. User 1 is in black, user 2 in blue, user 3 in green and user 4 in red.

order to understand their impact on the parameters of a VLC attocell. The throughput attained by the system, the attocell size, the characteristics of the user serviceability and the impact of the distance are all parameters that need to be compared in order to compare the multi-access methods used in this work. To start the investigation, section 5.2.1 explains the initial impact of the addition of any of the multi-access schemes on the raw throughput performances of the optimized multiband CAP signal. Section 5.2.2 analyzes the impact of the use of the multi-users access techniques on the 3D BER distribution by experimentally evaluating the distribution of maximum number of users in 3D for the same conditions as with the BER. In consequence, attocell sizes linked to this metric can be obtained for each of the scheme. In order to further analyze the serviceability of every user, section 5.2.3 measures the deviation from each user target data rate for each of the multi-users multiband CAP associations. The conclusion of these measures is a relation between the tolerated deviation and the maximum number of users of the scheme. Section 5.2.4 quickly illustrates the impact of the distance between the LED and the receivers. 5.2.5 summarizes all

results. First is a link between chapter 4 and 5 through a measured 3D BER distribution before and after an optimization process in order to open up on the addition of flexibility for multi-users performances. A table compiles the characteristics of the obtained VLC attocell for each of the association studied in this work in order to compare them.

### 5.2.1 Utilization of the Multi-Access Schemes Associated with m-CAP

The utilization of a multi-access scheme on  $m$ -CAP has an effect on the performances of the scheme. A summary of the broadcast results is presented in table 5.1. In this section, the data rate per user for each association is compared to an ideal division of the data rate. Thus, the total throughput shown in table 5.1 is simply divided equally to the number of users without considering variations. This section will investigate how SCM, MC-CDMA and PD-NOMA impact the performances as compared to that ideal case.

TABLE 5.1: Optimized characteristics for a 20-CAP signal in a single-user broadcast setup. Summary of chapter 4 results.

Parameter	Value
Number of subcarriers	20
Signal bandwidth	31.45 MHz
Distance	2.15 m
Total Throughput	163 Mb/s
Total BER on direct LOS	$5.18 * 10^{-4}$

#### 5.2.1.1 SCM

The first measure presented in figure 5.8 has the objective of evaluating the impact of the use of the multi-access scheme on the data rate obtained with the multiband CAP modulation scheme described in chapter 4. In the case of SCM, no impact on the data rate should be noted. Indeed, the scheme only tell each user which subcarrier they need to decode. Thus, when measuring the average data rate per user in a limited number of user scenario, the result should be the total attainable throughput divided by the number of receivers.

The measured average data rate per user is shown in figure 5.8 for the addition of SCM against a perfect division of the data rate between all users. At all number of users scenarios, SCM attains the same throughput per user as an ideal division. In a 2-users scenario, 81.5 Mb/s is reached and in a 10-users scenario, 16.3 Mb/s per user is obtained. The difference shown in figure 5.8 is the variation of data rate between each user, which is represented here by the error bar. In the case of SCM, the variation is  $\pm 2.5$  Mb/s in a 2-users scenario and increases to  $\pm 12.5$  Mb/s in a 10-users scenario. When increasing the number of users, the number of subcarriers per receiver that can be allocated by SCM falls, which explains this increasing variation

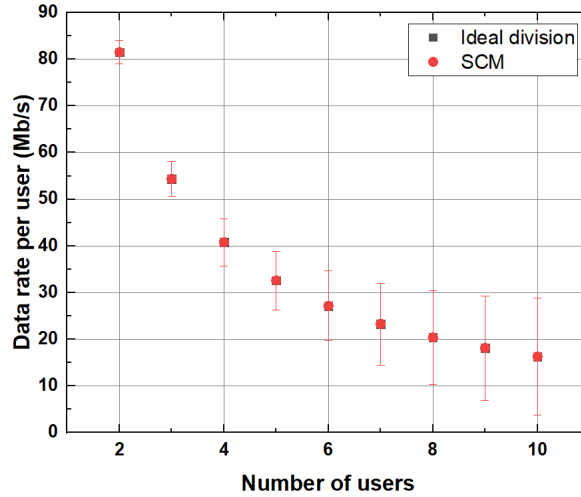


FIGURE 5.8: Graph representing the measured impact of the association with SCM on the single-user data rate against the total number of users.

of throughput between each user. This issue in the allocation of subcarriers to users in SCM is further highlighted in section 5.2.3.

### 5.2.1.2 MC-CDMA

The first measure presented in figure 5.9 has the objective of evaluating the impact of the use of the multi-access scheme on the data rate obtained with the multiband CAP modulation scheme described in chapter 4. In order to serve all users, the scheme need to maintain orthogonality. Each user will use the totality of a multiband CAP signal. However, each of these signal will not have the same throughput as the one described in section 4.3.5 of chapter 4. Indeed, maintaining orthogonality requires, as shown in the following figure, to divide the sampling rate of the  $m$ -CAP signals.

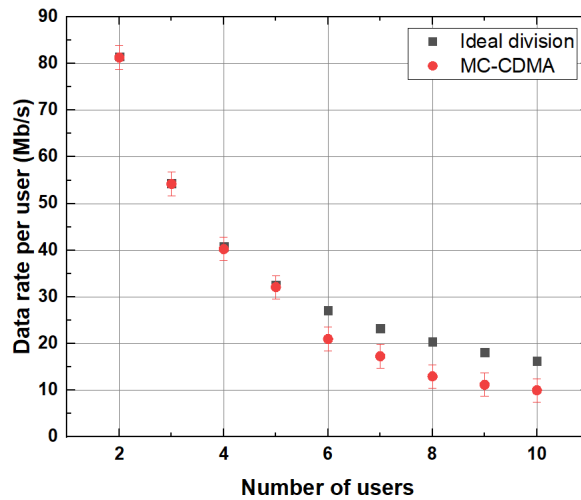


FIGURE 5.9: Graph representing the measured impact of the association with MC-CDMA on the single-user data rate against the total number of users.

The measured average data rate per user is shown in figure 5.9 for the addition of MC-CDMA against a perfect division of the data rate between all users. In a 2-users scenario, 81.3 Mb/s per user is reached. A number that decreases with the addition of more users, and thus more orthogonal codes. At 4-users, 40.25 Mb/s is reached and at 10-users 10 Mb/s per user is obtained. This small difference between the values obtained when using SCM comes from the fact that the signal needs to be re-optimized when the number of codes is augmented. This is necessary in order to serve more users because of the loss of orthogonality when more codes are used. With a fixed code length, the more users there are, the more MAI there is. Thus the SNR decreases, which impairs some of the orthogonality. The re-optimization of the data rate allows for an improved SNR which compensates for these losses. However, the main difference compared to SCM comes at this point because the variations between each user throughput is only down to  $\pm 2.5$  Mb/s as opposed to the deviation of  $\pm 2.5$  Mb/s to  $\pm 12.5$  Mb/s found with the first multi-access scheme. This small variation for MC-CDMA comes from the necessary changes applied to the signals in order to maintain orthogonality.

### 5.2.1.3 PD-NOMA

The first measure presented in figure 5.10 has the objective to evaluate the impact of the use of the multi-access scheme on the data rate obtained with the multiband CAP modulation scheme described in chapter 4. Both secondary multi-access schemes are considered. The observations shown in this figure are thus similar to what was observed in the two previous subsections. In addition, using two different power levels in the same outputted waveform increases the difficulty in decoding the signals but this is counteracted by the virtual increase in the number of available subcarriers for SCM and the decrease in the number of required codes per group of users for MC-CDMA.

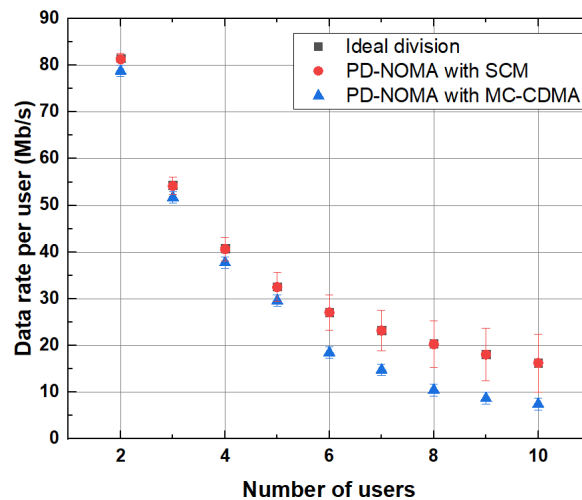


FIGURE 5.10: Graph representing the measured impact of the association of PD-NOMA with SCM and MC-CDMA on the single-user data rate against the total number of users.

The measured average data rate per user is shown in figure 5.10 for the addition of PD-NOMA to the scheme, along with SCM or MC-CDMA as secondary schemes, in comparison with a perfect division of the data rate between all users. The throughput per user attained in all number of users' scenarios is approximately the same for PD-NOMA with SCM and PD-NOMA with MC-CDMA as when using only both the respective secondary schemes. Indeed, in a 2-users scenario, 81.25 Mb/s per users is attained for PD-NOMA with SCM and 78.8 Mb/s is obtained for the second association. In a 10-users scenario, 16.25 Mb/s is reached by the first scheme and 7.5 Mb/s per user by the second. The small difference came from the further signal optimization in superposition coding in order to correctly exploit the difference in channel at the far users' group and the close users' group. The main advantage in data rate per user that PD-NOMA brings is the virtual doubling of the number of subcarriers. This impacts the measured variation in throughput between each user by halving it. Only  $\pm 1.25$  Mb/s to  $\pm 6.25$  Mb/s is obtained for PD-NOMA with SCM in 2 to 10-users' scenarios and  $\pm 1.25$  across all setups is reached for PD-NOMA with MC-CDMA. This result is the first measured confirmation of the considerably positive impact of the use of PD-NOMA on the maximum number of users. Further measures presenting the impact of the multi-access scheme on the characteristics of the indoor VLC attocell are described in the following sections.

### 5.2.2 Impact of the 3D Distributions

The measurement of the BER distribution in an indoor room for the experimental setup will, as explained in section 5.1.2 of this chapter, allows for a more complete characterization of the attocell created by all schemes. However, as hinted previously, each multi-users access scheme to multiband CAP association impact the cell capacity in different ways. The objective of the following figures is to investigate the impact of the use of each multi-users access scheme on the main characteristics deduced from the 3D distributions, namely the attocell size and the maximum number of users. The measurements performed involved the complete measure of the bit error rate distribution in a square surface measuring 9 m<sup>2</sup> in an indoor 5x5x3 m<sup>3</sup> room. Using the performances obtained by the application of the schemes, a visualization of the maximum number of users, and thus the attocell size, is shown in a 3D distribution.

Figure 5.11 first shows in (a) the 3D BER distribution in the indoor room obtained by the optimized 20-CAP signal described in section 4.3.5 of chapter 5. The receiving plane is situated 2.15 meters away from the transmitting plane and the BER was measured in locations of a 9 m<sup>2</sup> surface at the receiving plane. As expected, the obtained bit-error rate decreases the further the receiver is from the center of the reception plane. Indeed, it translates to an increased distance from the photodiode to the LED and, as expected, a reduction in the received optical power. When using the 7% FEC limit, it means that as long as a receiver is placed where the BER is

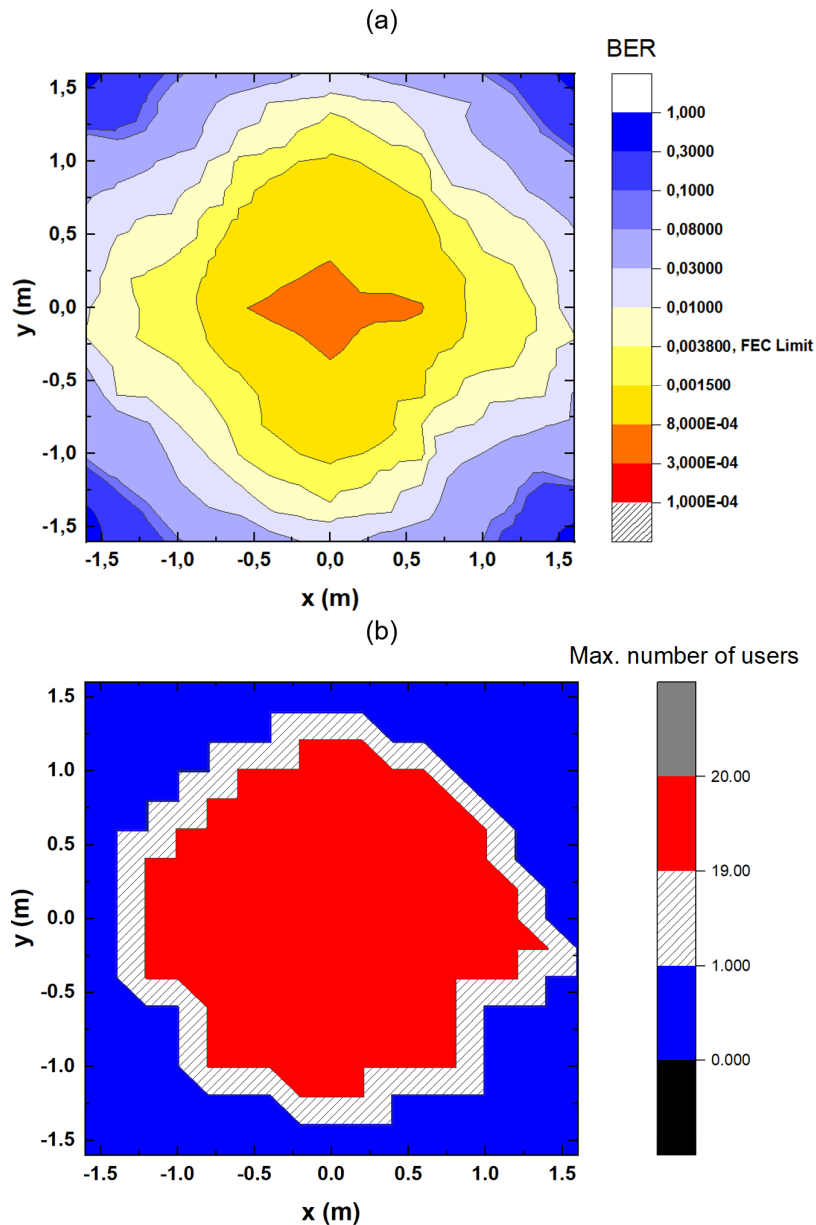


FIGURE 5.11: Measured transformation from (a) a BER 3D Distribution, to a 3D representation of the maximum number of users in the case of the multiband CAP association with (b) SCM.

below  $3.8 \times 10^{-3}$ , the waveform can be fully decoded, granted a 7% data overhead is added. It corresponds to a measured area of 4.56 square meters approximately.

In the case of SCM, it means that up to 20-users could be served in this 4.56 m<sup>2</sup> surface. Indeed, in this surface, indicated in red in figure 5.11 (b), all 20 subcarriers can be decoded and are thus available to any user. The cross hatched border is the zone where not all subcarriers can be decoded. Essentially, the attenuation at this distance from the transmitter makes some subcarriers impossible to decode without a much larger data overhead because of the dominant white Gaussian noise. As an example, a point in space situated at  $x = -1.4$  m and  $y = 0$  m corresponds to a

measured BER of  $4.73 \times 10^{-3}$ , as illustrated in figure 5.11 (a). Thus, in figure 5.11 (b) it translates to a cross hatched zone because the value is higher than  $3.8 \times 10^{-3}$  for some of the subcarriers in the signal. In conclusion, the attocell corresponding to SCM is measured at  $4.56 \text{ m}^2$  and up to 20-users can be served in that area.

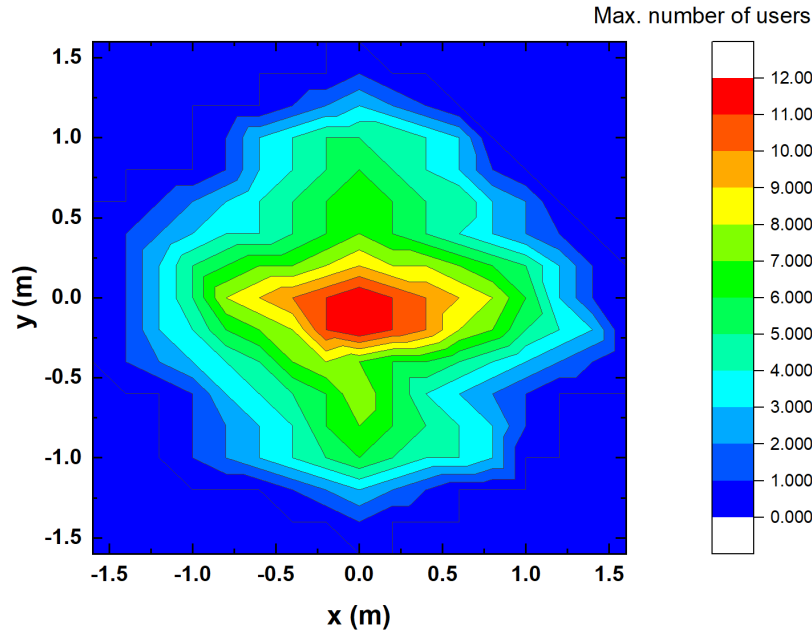


FIGURE 5.12: Measured transformation from a BER 3D Distribution, to a 3D representation of the maximum number of users in the case of the multiband CAP association with MC-CDMA.

In the case of MC-CDMA, the attenuation in the signal, imaged by the BER increase in figure 5.11 (a), reduces the orthogonality at the receiver. In consequence, the number of users that can be served falls with the distance from the transmitter, as shown by figure 5.12. It means that in the case of the use of this multi-access scheme, a different serviceable attocell size is obtained at each set limit of number of users. If a 12-users limit is considered, then the attocell area is measured at  $0.125 \text{ m}^2$  approximately. But, if a 4-users-limit is considered, then the measured attocell size is around  $2.81 \text{ m}^2$ . The caveat is that when considering small attocell areas below  $5 \text{ m}^2$  such as in the case of this experimental setup, more than 4-users is hardly realistic. In consequence, the attocell corresponding to MC-CDMA is considered to be measured at  $2.81 \text{ m}^2$  in an up to 4-users scenario.

In the case of PD-NOMA, the measured attocells were the same as when only the corresponding secondary multi-access scheme was used. In consequence, in the case of PD-NOMA and SCM, the corresponding attocell size is measured at  $4.56 \text{ m}^2$  approximately as well and up to 40-users can be served in that area, 20 per user group. In the case of PD-NOMA with MC-CDMA, the same results as with MC-CDMA only were attained in attocell size and serviceable number of users. The difference that PD-NOMA can bring, other than the increase in the maximum number of users

for SCM, is in the user allocation problematic, as further exposed in the following section.

### 5.2.3 User Allocations

#### 5.2.3.1 SCM

The association between SCM and  $m$ -CAP involves the association of each user to a group of subcarriers. Using the deviation from the user target, as defined in section 3.3.3 of chapter 3, the performances of the user allocation scheme is obtained experimentally and the results are shown in figure 5.13. As a reminder, this parameter is equal to 0 % when the target is attained or exceeded. And, when the target is not attained, the deviation from it is represented as a positive percentage. All the algorithms described in subsection 3.3.3.1 of chapter 3 are applied on the scheme in order to acquire the measurable. The first algorithm is a static allocation where the average center frequency of all the allocated subcarriers to a specific user is close to the center of the total signal bandwidth. The second algorithm is an SCM allocation scheme first found for OFDM in fiber-optic communication. The third algorithm is based on this previous method where the conditions are adapted to the large swings in SNR experienced in a VLC channel. The fourth algorithm is the same as the third except that the quality of service for each user is considered.

Figure 5.13 (a) shows the measured deviation from the user target data rate, abbreviated deviation in this section, against the number of subcarriers that the  $m$ -CAP signal uses in a 4-users scenario and for the four previously presented allocation algorithm. Figure 5.13 (b), on the other hand, shows the measured deviation attained by the 20-CAP optimized waveform for an increasing amount of users and using all four of the algorithms presented. The deviation against an increasing number of subcarriers first show the periodicity in figure 5.13 (a). Indeed, in the case of SCM this characteristic is observed on all four algorithms as a multiple of the number of users for the necessary amount of subbands. A 4-users scenario is considered and for example, if only 11 subcarriers are available for the 4 receivers, then, on average, 3 of them are allocated to 3 subbands while the last receiver only has 2 boosting its attained deviation. At 12 subcarriers, it is no longer the case. This effect is more important with lower amount of subbands. It explains why the fiber optic-based algorithm suffers more from this periodicity because it is designed for scenarios where the number of subcarriers to be allocated is much higher. The deviation attained by the first proposed algorithm goes from 18.86 % at 4 subcarriers to 0.91% at 30. The deviation attained by the second on goes from 16.61% to 1.01% in the same range of subbands. On the other hand, the static and fiber optic algorithms reached 5.79% and 3.55% respectively for 30 subcarriers. In a 4-users scenario, this figure shows the minimum number of subcarriers to be used for different tolerated deviation. With the first proposed algorithm, 20 subcarriers with a 4-users scenario corresponds to a deviation below 2%.

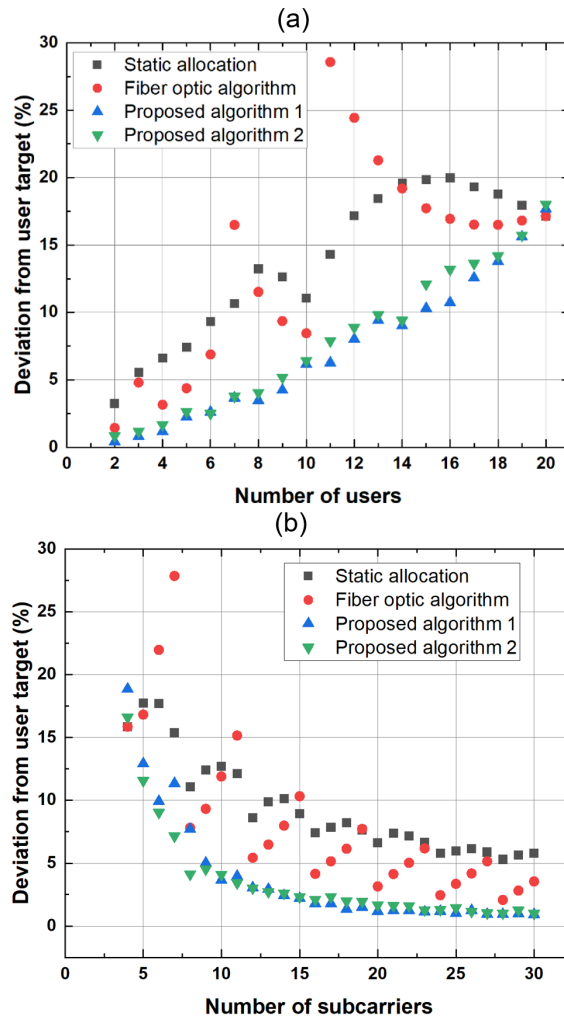


FIGURE 5.13: (a) Measured deviation from user target data rate in function of the number of users, (b) Measured deviation from user target in function of the number of subcarriers. The multiband CAP modulation is associated with SCM.

In figure 5.13 (b), corresponding to the  $m$ -CAP optimized signal used so far, the deviation periodicity is also observed but depends on the number of users this time, for the same reason as previously described. For a 4-users scenario, the deviation obtained was 6.61% for the static allocation, 3.15% for the fiber optic-based allocation, 1.17% for the first proposed allocation and 1.67% for the second proposed allocation. In an 8-users scenario, the deviation reached 13.23%, 11.52%, 3.47%, and 4.04% for the four algorithms respectively. The static allocation brought the worse results because of its static nature, then the proposed algorithms both optimized the results provided by the fiber optic algorithm by reducing the periodicity effect. The second proposed allocation has slightly worse results because it focuses on reducing the difference in QoS between each user.

### 5.2.3.2 MC-CDMA

In an association between MC-CDMA and multiband CAP, each user is assigned to an orthogonal code. The user allocation method used in this case is simply to assign a user to a code on the same index. Using the deviation from the user target, as defined in section 3.3.3 of chapter 3, the performances of the user allocation scheme is obtained experimentally and the results are shown in figure 5.14.

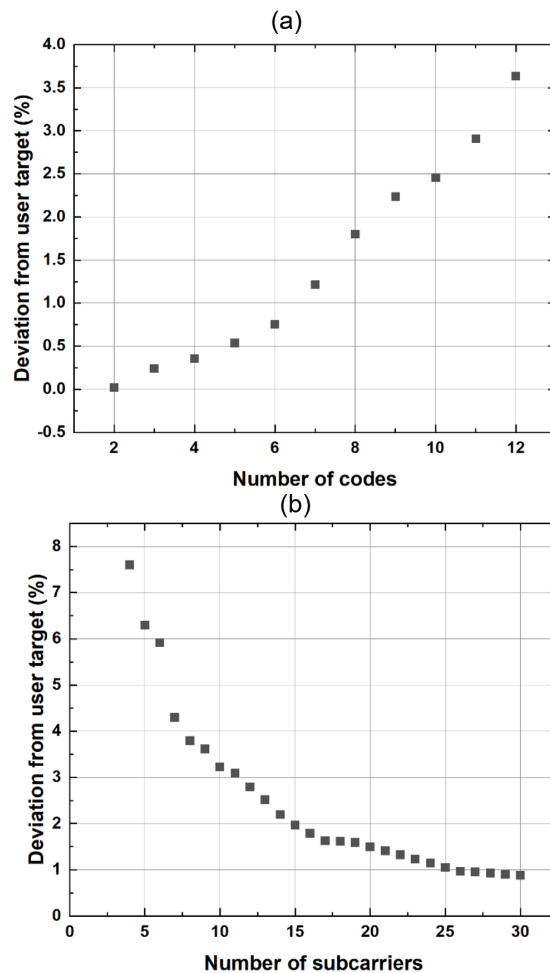


FIGURE 5.14: (a) Measured deviation from user target data rate in function of the number of codes, (b) Measured deviation from user target in function of the number of subcarriers. The multiband CAP modulation is associated with MC-CDMA.

Figure 5.14 (a) shows the measured deviation from the user target data rate, abbreviated deviation in this section, against the number of subcarriers that the  $m$ -CAP signal uses in a 4-users scenario. Figure 5.14 (b), on the other hand, shows the measured deviation attained by the 20-CAP optimized waveform for an increasing amount of users. The first characteristic for both figures is the absence of the periodicity effect because of the nature of MC-CDMA where the entire  $m$ -CAP signal is used for each user no matter the number of subcarriers or users. Deviations attained by the scheme were also very low for the same reason. Indeed, for a 4 subcarriers signal in figure

5.14 (a), the deviation was 7.6% and bottomed at 0.88% for 30 subcarriers. On the other hand, in figure 5.14 (b), with an increase in the number of codes from 2 to 20 in a 20 subcarrier signal, the deviation increased from 0.02% to 9.76% only.

### 5.2.3.3 PD-NOMA Combined with SCM

In an association between PD-NOMA combined with SCM and multiband CAP, each user is assigned to a power level depending on its known position and a group of subcarriers. The user allocation method used in this case is simply to re-use the third and fourth algorithms defined for SCM. Using the deviation from the user target, as defined in section 3.3.3 of chapter 3, the performances of the user allocation scheme is obtained experimentally and the results are shown in figure 5.15.

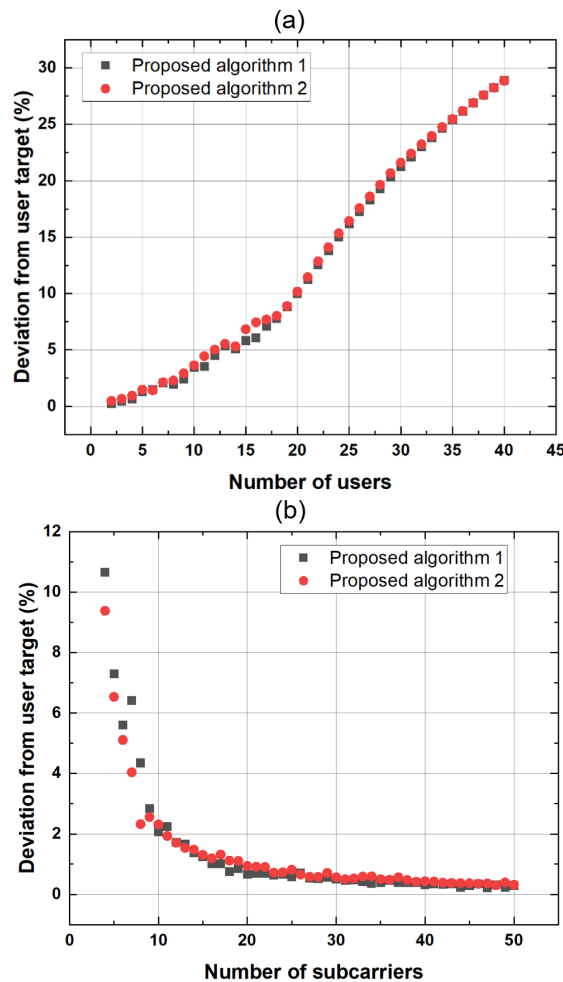


FIGURE 5.15: (a) Measured deviation from user target data rate in function of the number of users, (b) Measured deviation from user target in function of the number of subcarriers. The multiband CAP modulation is associated with PD-NOMA+SCM.

Figure 5.15 (a) shows the measured deviation from the user target data rate, abbreviated deviation in this section, against the number of subcarriers that the  $m$ -CAP signal uses in a 4-users scenario and for both the proposed algorithms in the SCM

case. Figure 5.15 (b), on the other hand, shows the measured deviation attained by the 20-CAP optimized waveform for an increasing amount of users and the two proposed user allocation algorithms. The periodicity characteristic is still present with the addition of PD-NOMA to the SCM scheme. Indeed, it only virtually adds more subcarriers and in practice each group of users, the close and far, experience the same number of subband as in SCM only. However, this characteristic of PD-NOMA almost halves the deviation obtained in measures. Indeed, for 4 subcarriers, the deviation reached 10.66% for the first proposed algorithm instead of 18.86% when using SCM only. When using the second proposed algorithm, 9.38% was attained. For 30 subcarriers, the deviation obtained was 0.51% and 0.57% for the first and second proposed algorithm respectively. When using the 20-CAP optimized signal, the deviation for 2 users is measured at 0.23% and 0.47% for the two allocation schemes. At 10-users, the results increased to 2.40% and 2.93%. This reduction in deviation as compared to the use of SCM only helps, as previously exposed, increasing the capacity of the scheme thanks to PD-NOMA.

#### 5.2.3.4 PD-NOMA Combined with MC-CDMA

In an association between PD-NOMA combined with MC-CDMA and multiband CAP, each user is assigned to a power level depending on its location and to an orthogonal code. The user allocation method used in this case is simply to assign a user to a code on the same index. Using the deviation from the user target, as defined in section 3.3.3 of chapter 3, the performances of the user allocation scheme is obtained experimentally and the results are shown in figure 5.16.

Figure 5.16 (a) shows the measured deviation from the user target data rate, abbreviated deviation in this section, against the number of subcarriers that the  $m$ -CAP signal uses in a 4-users scenario. Figure 5.16 (b), on the other hand, shows the measured deviation attained by the 20-CAP optimized waveform for an increasing amount of users. In the same way as in MC-CDMA only, the use of PD-NOMA and MC-CDMA observe no periodicity in deviation against the number of subcarriers or users. The virtual increase in subcarriers helps MC-CDMA in deviation by reducing the variations in throughput between each user. For a 4-subcarriers signal, the deviation reached 4.3% instead of 7.6% for just MC-CDMA. Similarly, at 30-subcarriers, the deviation measured was 0.5% instead of 0.88%. When using a 20-CAP optimized signal, the deviation was only 0.01% for 2 codes and reached 5.52% for 20 codes. The consequence can be observed in the attained maximum number of users.

#### 5.2.3.5 Number of Usable Independent Channels at a Defined Tolerated Deviation

Figure 5.17 concludes with the measured number of usable independent channels for a tolerated deviation. Each usable independent channel can be allocated to a user. In consequence, the value found for a set tolerated directly translates to the maximum

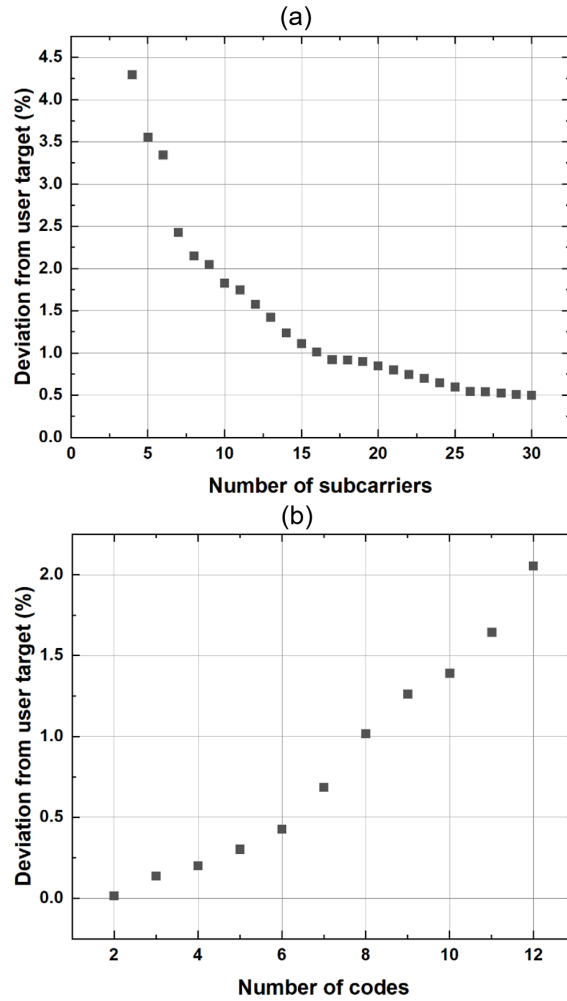


FIGURE 5.16: (a) Measured deviation from user target data rate in function of the number of codes, (b) Measured deviation from user target in function of the number of subcarriers. The multiband CAP modulation is associated with PD-NOMA+MC-CDMA.

number of users of the scheme. SCM with or without PD-NOMA is showed for both the proposed algorithms, since they offered the best performances in user allocation. For a 5% tolerated deviation, the number of usable independent channels with SCM is 9 for the first proposed algorithm and 8 for the second one. At 10% tolerated deviation, this number reaches 14 for both allocation schemes. Finally, the maximum attained is 20 because of the number of subcarriers, at tolerated deviations of 18% and beyond. When adding PD-NOMA, for a 5% tolerated deviation the number of channels is 12 as opposed to 9 in SCM only for the first proposed algorithm and 11 instead of 8 for the second one. At 10%, 20 and 19 are attained by the combination of PD-NOMA and SCM. As far as MC-CDMA is concerned, for a 5% tolerated deviation, the number of usable independent channels already reached the maximum of 12 that was found in section 5.2.2. In consequence, a tolerated deviation of only 4% is necessary in order to maximize user allocation for the scheme. When adding PD-NOMA, instead of a 4% tolerated deviation to maximize the 12-users maximum

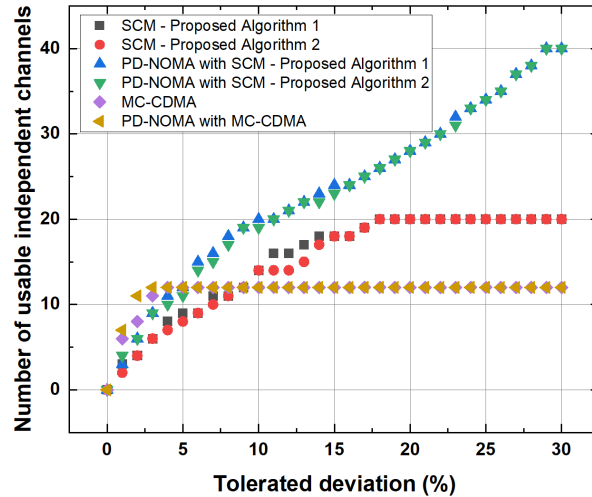


FIGURE 5.17: Measured number of usable independent channels for a set allowed deviation when using every association of multiband CAP with SCM, MC-CDMA and PD-NOMA.

of MC-CDMA, a value of only 3% is necessary in the case of PD-NOMA with MC-CDMA in order to reach the 12 channels.

#### 5.2.4 Impact of the Distance Between the Transmitter and the Receivers

Figure 5.18 concludes the analysis of the characteristics of the attocell by showing the measured influence of the distance between the transmitting and receiving planes on the maximum available throughput and the size of the cell when using SCM. As expected, data rate increases while the attocell size decreases when reducing the distance.

#### 5.2.5 Total System Characterization

Figure 5.19 shows the 3D BER distribution measured on a square surface measuring  $9 \text{ m}^2$  in an indoor  $5 \times 5 \times 3 \text{ m}^3$  room. The experimental setup is the same as described in section 4.1.3 of chapter 4 and the  $m$ -CAP signal used to obtain the bit-error rates at the different locations on the receiving plane is the non-optimized waveform for figure 5.19 (a) and the optimized waveform for figure 5.19 (b). The optimized signal is described in Table 4.4 in section 4.3.5 of chapter 4. In a multi-users scenario, each user will be spread randomly in the VLC attocell. Thus, there is a need to understand the impact of the performance optimizations explored throughout chapter 4 on the potential location of a user in the attocell.

The two graphs showed in figures 5.19 (a) and (b) allow the comparison of flexibility in BER obtained when the 20-CAP signal is optimized. Chapter 4 indeed concluded that multiband CAP signals with higher number of total subcarriers have less headroom for throughput improvements. However, the BER can still be reduced on all subcarriers even if not enough for an increase in data rate. The BER on the receiving plane can

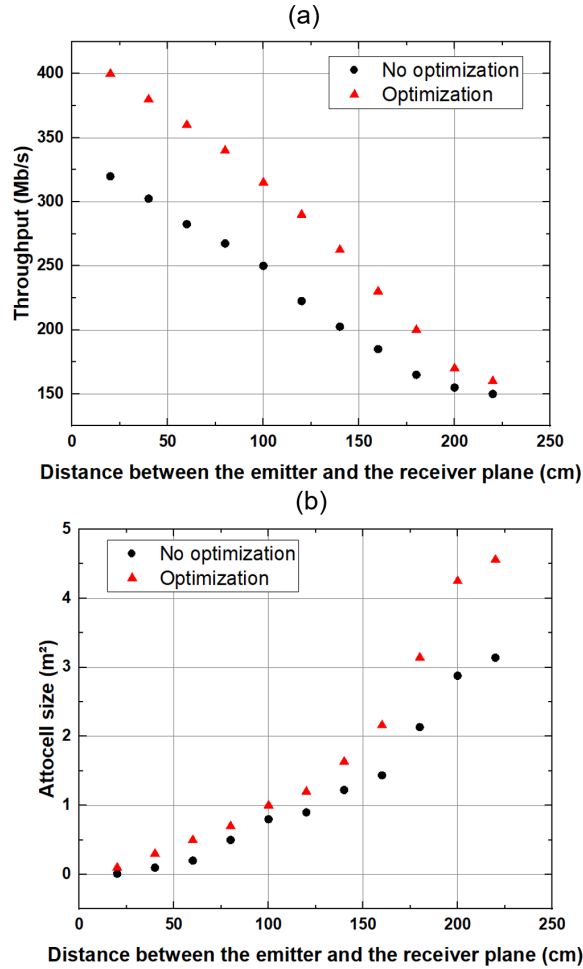


FIGURE 5.18: (a) Measured data rate versus range of the system with or without applying the optimization process. (b) Measured attocell size versus range of the system with or without applying the optimization process.

thus be improved and in consequence expands the size of the attocell. The results show that a cell size of approximately  $3.2 \text{ m}^2$  is obtained without the optimization and  $4.56 \text{ m}^2$  with it. The size is, as described previously, defined as the area where the BER for each subcarrier is below the 7% FEC limit. The decreases in certain subcarriers BER when the full optimization is applied is not enough for an increase in constellation size. This means that both attocells are essentially the same except that when applying the optimization process, the BER is overall decreased which means that a small part of the outer border now falls under the 7% FEC threshold.

The table 5.2 summarizes the performances of the indoor multi-users VLC system, for the measures described in both chapters 4 and 5. A 4-users scenario is chosen and a tolerated deviation of 5% is set.

Figure 5.20 shows the three dimensional BER measured under the conditions described in table 4.4 of section 4.3.5 of chapter 4 with an attocell size of  $4.56 \text{ m}^2$ . It

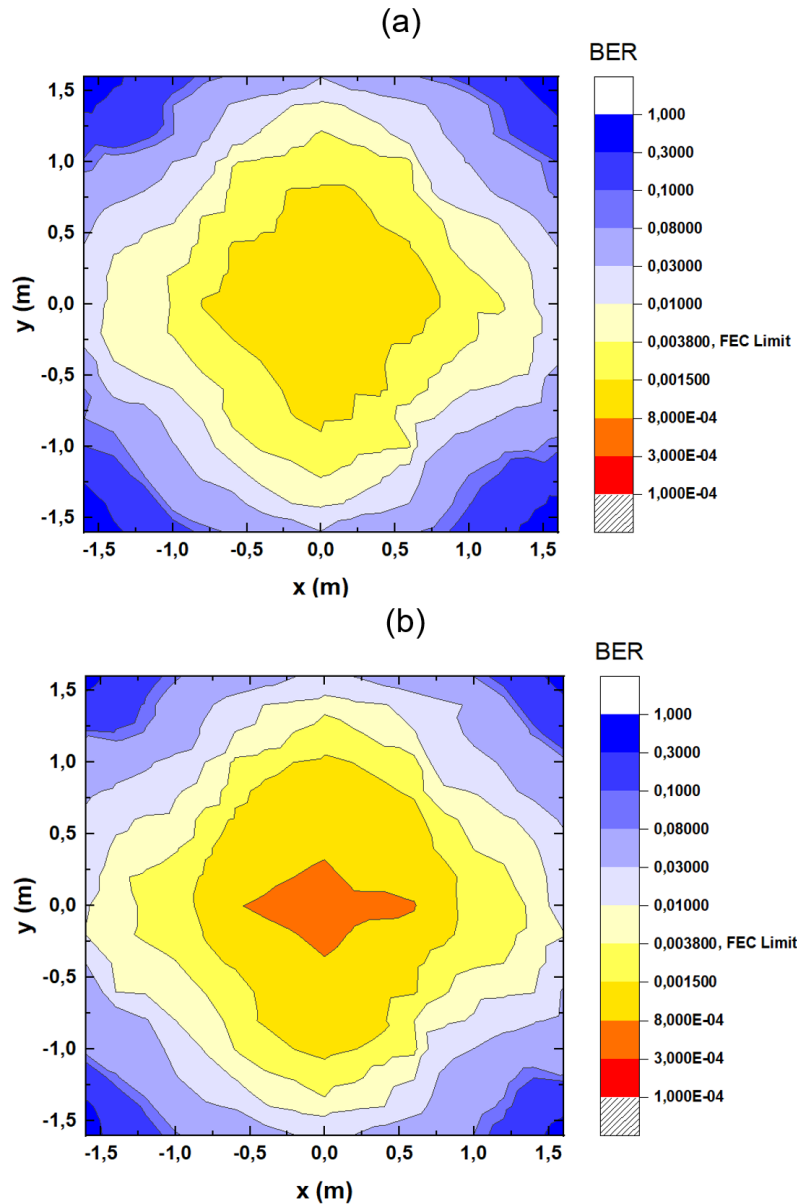


FIGURE 5.19: Graph representing the measured 3D BER surface on a plane a) without and b) with applying the broadcast performances optimization process.

represents the results obtained in the previous figure but does a better job showcasing the progression of the quality of service throughout the receiving plane. The cell total throughput capacity is 35.63 to 35.75 Mb/s/m<sup>2</sup> in the case of SCM or PD-NOMA with SCM and attains 54.09 to 57.29 Mb/s/m<sup>2</sup> in the case of MC-CDMA or PD-NOMA with MC-CDMA.

In conclusion, the associations can be compared as follows. All multi-access schemes to *m*-CAP associations offer similar data rate per user at around 40 Mb/s. However, the throughput variation between each receiver is an issue in the case of SCM because of the limited number of subcarriers. This is a limitation that is not present in MC-CDMA. Adding PD-NOMA to the schemes help reducing the variation by virtually

TABLE 5.2: Summary of the total indoor multi-users VLC experimental system.

Parameters	Value			
Number of subcarriers	20			
Performance optimization process	As per Chapter 4, section 4.3.4			
Distance between transmitting and receiving planes	2.15 m			
Total available throughput (without multi-access scheme)	163 Mb/s			
Total BER on direct LOS	$5.18 * 10^{-4}$			
Multiband CAP with	<b>SCM</b>	<b>MC-CDMA</b>	<b>PD-NOMA + SCM</b>	<b>PD-NOMA + MC-CDMA</b>
Average throughput per user (4-users scenario)	40.75 Mb/s	40.25 Mb/s	40.625 Mb/s	38 Mb/s
Variation of data rate between users	$\pm 5$ Mb/s	$\pm 2.5$ Mb/s	$\pm 2.5$ Mb/s	$\pm 1.25$ Mb/s
Maximum number of users	20	12	40	12
Maximum number of users at a 5% deviation	9	12	12	12
Attocell size	4.56 m <sup>2</sup>	2.81 m <sup>2</sup>	4.56 m <sup>2</sup>	2.81 m <sup>2</sup>
Data rate per unit of area	35.75 Mb/s/m <sup>2</sup>	58.36 Mb/s/m <sup>2</sup>	35.63 Mb/s/m <sup>2</sup>	55.5 Mb/s/m <sup>2</sup>

doubling the number of subcarriers, helping the SCM scheme. The main difference then lies in the fact that MC-CDMA loses orthogonality with attenuation. In that case, the larger the attocell is, the fewer amounts of users this scheme can serve. This disadvantage is not present with SCM. In conclusion, when considering a realistic amount of users, the PD-NOMA with SCM association attains only a  $\pm 2.5$  Mb/s of variation in a 4-users scenario and a 4.56 m<sup>2</sup> attocell at a sum data rate of nearly 163 Mb/s. PD-NOMA with MC-CDMA comes at an equal variation value but only a 2.81 m<sup>2</sup> attocell.

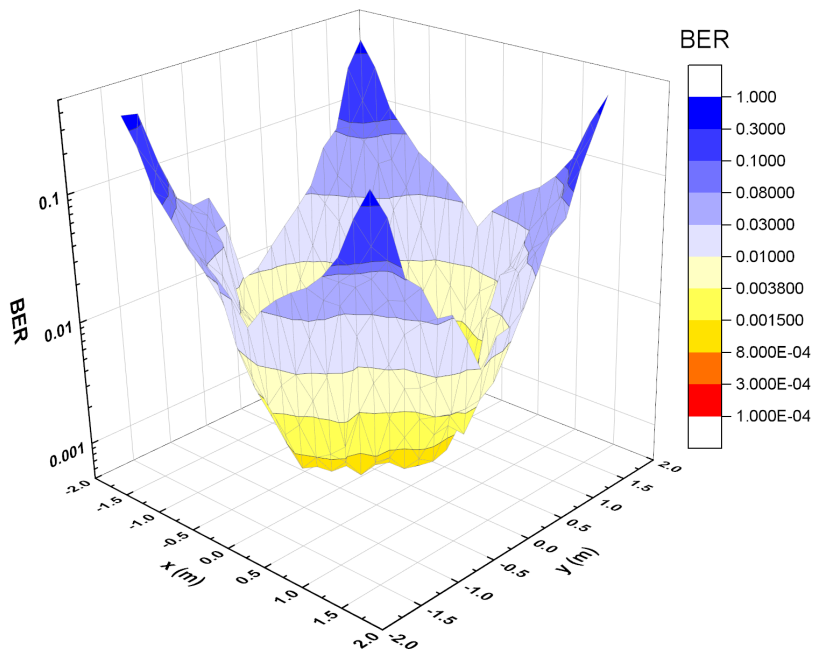


FIGURE 5.20: Measured 3D BER in a 5x5x3 m<sup>3</sup> indoor room for the experimental setup.



## Chapter 6

# Conclusions and Future Works

### Contents

---

<b>6.1 Contributions</b> . . . . .	<b>169</b>
6.1.1 Low-Cost Performance Optimization for Multiband CAP . . . . .	169
6.1.2 Experimental Comparison of the Performances of Multi-Users Access Schemes Associations with m-CAP in Indoor VLC . . . . .	171
<b>6.2 Future Challenges</b> . . . . .	<b>172</b>
6.2.1 Improving the Single-User Broadcast Performances . . . . .	173
6.2.2 Enhancing the Multi-Users Performances . . . . .	174
6.2.3 Bidirectional link . . . . .	174
<b>6.3 List of Publications from this work</b> . . . . .	<b>174</b>

---

## 6.1 Contributions

The growing demands of data everywhere in the world requires the use of new communication technologies. 5G is being introduced today but is still limited in indoor situations because of the low penetration of mmWaves. 6G aims at using all spectrum in combination for a covering of all scenarios with an optimal technique. Li-Fi, or VLC, can be one of the solutions for indoor wireless communication while offering illumination at the same time. However, the technology is still in a low-maturity stage and multiple approach can be taken, as demonstrated in Chapter 2. The goal of this thesis was thus to propose an experimental setup for a multi-users indoor VLC system that offer high performances with a realistic setup as well as more thorough study of multi-users access schemes. In this context, several contributions can be identified.

### 6.1.1 Low-Cost Performance Optimization for Multiband CAP

The first major contribution in performance optimization is the **optimization of the pulse shaping filters parameters defining each subcarrier** of the multiband CAP modulation scheme. The first aspect is that each subband roll-off factor and filter length can be optimized for better BER performances. The impact is different

for each subcarrier depending on its center frequency. Hence, there exist a set of parameters that can maximize the performances. As reported in Section 4.3.2, an **improvement in the BER** of a sizeable factor can thus be obtained **without an increase in computational cost**. The second aspect of this contribution is the subcarrier spacing which can reduce inter-channel interferences. This parameter can also be optimized in the same way as the pulse shaping filter characteristics. Decreases in BER of up to 80% can be attained when the optimal spacing values are used in between each subcarrier of the signal. The combination of these two aspects for an **increase in performances without a cost in complexity** has never been proposed before.

The first contribution is further studied in order to offer a new contribution in the form of **the optimization process**. Indeed, the maximization of the performances through the optimal choice of filter parameters and subcarrier spacing values can be attained with multiple routes. Two forms of spacing are analyzed: uniform, where all values for all subbands are the same, and optimized, where the values are ideally chosen in between each subcarrier. The performance increase is measured at up to 11.11% with the first form and 16.67% with the second. The former having the advantage of requiring a simpler optimization process while still offering a similar performance gain. **Multiple optimization processes** are thus studied, from a full optimization to an optimization on one parameter. **Performance boosts can range from 4% to 28.67%** depending on the process and the number of subcarriers. This is the first time that such processes are detailed and compared for the use of multiband CAP in VLC.

The final single-user broadcast performances are reported in Section 4.3.5 and a **total throughput of 163 Mb/s** is obtained with a **BER on direct line of sight of  $5.18 * 10^{-4}$** , at a realistic **range of 2.15 meter**. This is an increase of 11.75 Mb/s from the baseline results along with a decrease of BER by a factor of 3.55, augmenting the flexibility for the multi-users scenarios. The results are attained with a simple pre-emphasis pre-equalization scheme and a simple DFE post-equalization technique. An approach defined in Section 2.3.3 of Chapter 2 was showcased in figures 2.27 and 2.28. The system proposed has an estimated level of complexity of 6 with a spectral efficiency of 5.18 b/s/Hz, as shown in figure 6.1. Both the level-of-complexity to spectral efficiency and range to spectral efficiency approaches are followed, showing the overall contribution of this system to the existing literature. As far as the range of the system, 2.15 m was attained like our chapter 2's approach indicated, as shown in figure 6.2. But, this is mainly due to the high power of the LED used as compared to the works reaching a lower range.

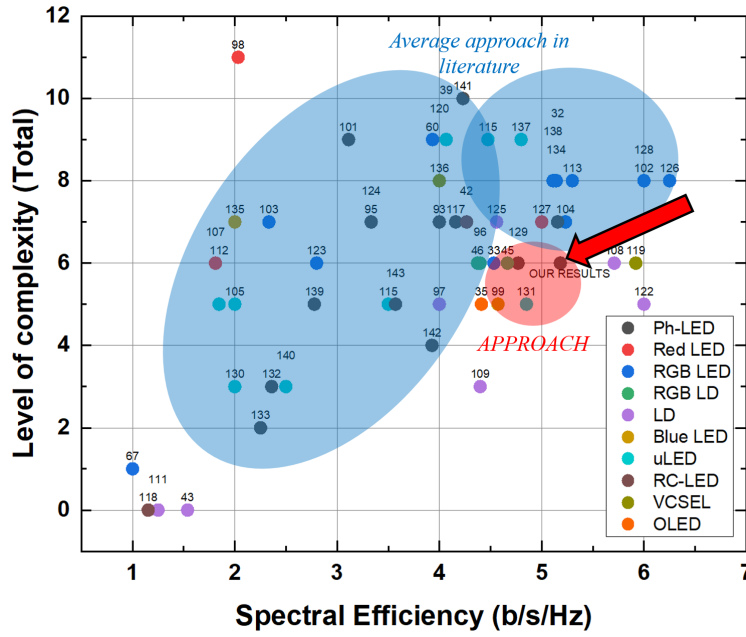


FIGURE 6.1: : Illustration of the approach taken by this work in terms of cost of implementation as per figure 2.27. The results obtained by this work are added as a comparison.

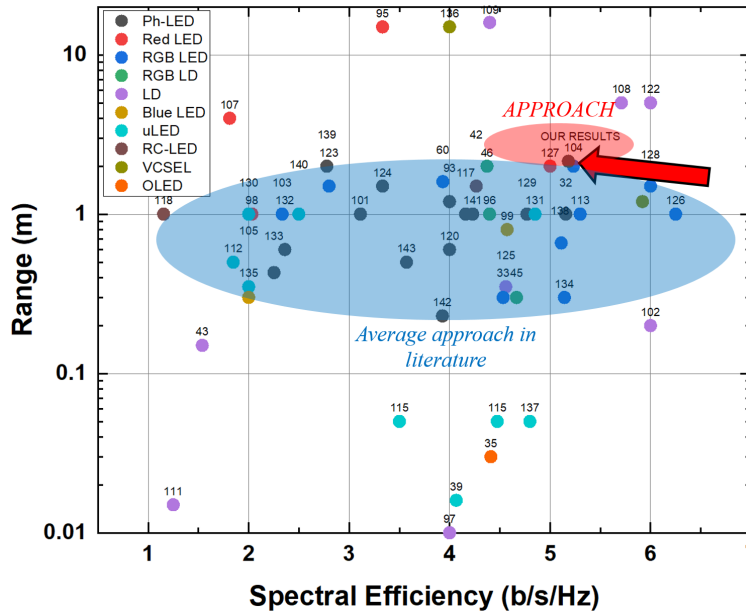


FIGURE 6.2: Illustration of the approach taken by this work in terms of system range as per figure 2.28. The results obtained by this work are added as a comparison.

### 6.1.2 Experimental Comparison of the Performances of Multi-Users Access Schemes Associations with m-CAP in Indoor VLC

The first major contribution in the experimental study of multiband CAP for VLC is the first-time direct comparison of the performances of SCM, MC-CDMA and PD-NOMA. It is also the first time PD-NOMA is combined with SCM and with

MC-CDMA in an experimental scenario. **SCM is shown to offer a natural multi-access method** with the association of users to groups of subcarriers. The single-user performances thus remain unchanged but the variation of data rate between users can reach upwards of  $\pm 5$  Mb/s. With **MC-CDMA**, this variation is halved but the difficulty in maintaining orthogonality for multiple users at certain range reduces the coverage area of the system. **PD-NOMA is shown to virtually augment the maximum number of users** when associated with the two former multi-access schemes.

The second major contribution is the analysis of two multi-users performances characteristics: **the deviation between each user target data rate and the attocell size**. The first one is defined as the difference between the throughput attained by the receiver after multi-access association and its target. In consequence, the maximum number of users can be redefined at different tolerated deviation. With a 5% value, SCM has 9 usable independent channels instead of the raw 20, 12 instead of 40 when PD-NOMA is associated. With MC-CDMA, the maximum number of users is 12 even with a 5% deviation. The second characteristic is the area on the receiver plane where the BER is below the 7% FEC limit. Using SCM, an attocell size of  $4.56 \text{ m}^2$  is obtained but with MC-CDMA an area of  $2.81 \text{ m}^2$ . These contributed experimental parameters allow **the comparison of the multi-access schemes to  $m$ -CAP associations**.

Using the PD-NOMA with SCM association with multiband CAP, a  **$\pm 2.5$  Mb/s variation** in a 4-users scenarios is attained with a  **$4.56 \text{ m}^2$  attocell** at a sum data rate of nearly 163 Mb/s. Or  **$40.625$  Mb/s per user in that 4-receivers scenario**. The maximum number of users is 40 along with a **12 usable channels at a tolerated deviation of 5%**. An approach was defined in Section 2.3.3 of Chapter 2, with figure 2.29. The system proposed exceeds the initial estimation made as a guideline for our work, as shown in figure 6.3. While such a high user count is unrealistic for such a small cell size, it still showcases the flexibility of the scheme used.

## 6.2 Future Challenges

The VLC system studied in this work offers optimized performances at a realistic distance and for an off-the-shelf white LED. However, the raw performances are restricted because of the hardware limitations of the setup. The growing demands of data in the future, as explained in Chapter 1, can only be met with the use of high-performances systems. Li-Fi can be one complementary solution but the system analyzed here is still challenged. In consequence, there are still key performances issues that the studied setup of this work needs to answer before being considered.



### 6.2.2 Enhancing the Multi-Users Performances

Four multi-users access scheme associations with multiband CAP were studied but the number of MUA techniques available in the literature is larger. One scheme that was mentioned throughout this work but not studied is **SDMA**. The method has considerable potential for the **enhancement of the performances of multi-users VLC**. The transmitter needs to be able to form optical beams towards the known position of a receiver. Narrow beams of light can offer **higher broadcast performances** because the optical power is concentrated. While the emitter is very complex, it offers **considerable flexibility** with the ability to be combined with other MUA schemes, similarly to PD-NOMA. It has yet to be experimentally demonstrated in VLC, which would be a major contribution to the literature.

### 6.2.3 Bidirectional link

A bidirectional link would add the ability to configure the distribution of subbands in a multi-carriers system. The up-link aspect can be achieved by multiple methods, including visible or infrared light, radio-frequency techniques, near-ultraviolet or even retro-reflective transceivers. VLC requires an amount of power to generate light that cannot be attained by mobile devices and in this case, a VLC-based up-link would therefore not be preferred. Also, interferences are created by the reflect light between the two channels. A first alternative is RF as it is easy to use but requires the transceivers to work in two domains and cannot be used when electromagnetic interferences need to be minimized. As a second alternative, retro-reflective transceivers reflect light to transmit data. So far, the technology is only promising as the modulation speed is still low despite ongoing efforts to improve it. Finally, a near-UV or near IR up-link seems to be the most viable solution as it shares the same characteristics as a VLC down-link.

## 6.3 List of Publications from this work

Some of the works detailed in this manuscript have been presented previously in several research papers.

### Journal Papers

- RICL1. M. M. Merah, H. Guan and L. Chassagne, "Experimental Multi-Users Visible Light Communication Attocell Using Multiband Carrierless Amplitude and Phase Modulation," *IEEE Access*, vol. 7, pp. 12742-12754, 2019.

### Conference Papers

- CICL1. M. M. Merah, H. Guan and L. Chassagne, "Performance optimization in Multi-Users multiband carrierless amplitude and phase modulation for visible light communication," *2018 Global LIFI Congress (GLC)*, Paris, 2018,

pp. 1-4.

- CICL2. M. M. Merah, L. Chassagne and H. Guan, "Experimental Demonstration of User Allocation in a Subcarrier Multiplexing-Based Multiuser LiFi System," *2018 IEEE Photonics Conference (IPC)*, Reston, VA, 2018, pp. 1-2.
- CICL3. M. M. Merah, H. Guan and L. Chassagne, "Experimental Comparison of Multi-Users Access Schemes with Multiband CAP," accepted to the *2019 Global LIFI Congress (GLC)*, Paris, 2019.



# Bibliography

- [1] M. Minges and P. Simkhada, *The evolution to 3g mobile*, <https://www.itu.int/itunews/issue/2003/06/> Jul. 2003.
- [2] 3GPP, *About 3gpp home*, <http://www.3gpp.org/about-3gpp/about-3gpp>.
- [3] M. H. K. S. A. ur Rahman, “Multi-carrier hspa evolution and its performance evaluation with emphasis on the downlink”, Master’s thesis, Blekinge Institute of Technology, Jan. 2013.
- [4] Cisco, *Cisco visual networking index: Global mobile data traffic forecast update, 2013–2018*, <https://ytd2525.wordpress.com/2014/02/06/cisco-visual-networking-index-global-mobile-data-traffic-forecast-update-2013-2018/>, 2014.
- [5] TP-Link, *What is wifi 5? (802.11ax)*, <https://www.tp-link.com/us/wifi6/>, 2019.
- [6] M. Giordani, M. Polese, M. Mezzavilla, S. Rangan, and M. Zorzi, “Towards 6g networks: Use cases and technologies”, *CoRR*, vol. abs/1903.12216, 2019.
- [7] Z. Ghassemlooy, W. Popoola, and S. Rajbhandari, *Optical Wireless Communications: System and Channel Modelling with MATLAB*. Aug. 2012, ISBN: 978-4398-5188-3. DOI: [10.1201/b12687](https://doi.org/10.1201/b12687).
- [8] VICS, *How vics works*, <http://www.vics.or.jp/en/vics/>.
- [9] F. R. Gfeller and U. Bapst, “Wireless in-house data communication via diffuse infrared radiation”, *Proceedings of the IEEE*, vol. 67, no. 11, pp. 1474–1486, Nov. 1979, ISSN: 0018-9219. DOI: [10.1109/PROC.1979.11508](https://doi.org/10.1109/PROC.1979.11508).
- [10] VLCC, *Visible light communications consotium (vlcc)*, <http://www.vlcc.net/>.
- [11] I. Nakagawa Laboratories, *Nakagawa laboratories creates the next generation ubiquitous society using visible light communication*, <http://www.naka-lab.jp>.
- [12] M. Nakagawa, *Illuminative light communication device*, pat. US7583901B2, <http://www.google.com/patents/US7583901>, Oct. 2003.
- [13] VLCA, *Visible light communications association*, <http://vlca.net/>.
- [14] I. S. Association, *Ieee 802.15 documents*, <https://mentor.ieee.org/802.15/documents>.
- [15] “Ieee standard for local and metropolitan area networks–part 15.7: Short-range wireless optical communication using visible light”, *IEEE Std 802.15.7-2011*, pp. 1–309, Sep. 2011. DOI: [10.1109/IEEESTD.2011.6016195](https://doi.org/10.1109/IEEESTD.2011.6016195).
- [16] Osram, *Solericq s 15, gw kagmb5.em - datasheet*, <https://www.osram.com/>.
- [17] O. O. Semiconductors, *Osram bpx 61 photodiode - datasheet*, <https://www.osram.com/>.
- [18] J. M. Kahn and J. R. Barry, “Wireless infrared communications”, *Proceedings of the IEEE*, vol. 85, no. 2, pp. 265–298, Feb. 1997, ISSN: 0018-9219. DOI: [10.1109/5.554222](https://doi.org/10.1109/5.554222).

- [19] Cisco, *Cisco visual networking index: Global mobile data traffic forecast update 2014–2022 white paper*, <https://www.cisco.com/c/en/us/solutions/collateral/service-provider/visual-networking-index-vni/white-paper-c11-738429.html>, Tech. Rep. 2015.
- [20] C. Han, T. Harrold, S. Armour, I. Krikidis, S. Videv, P. M. Grant, H. Haas, J. S. Thompson, I. Ku, C. Wang, T. A. Le, M. R. Nakhai, J. Zhang, and L. Hanzo, “Green radio: Radio techniques to enable energy-efficient wireless networks”, *IEEE Communications Magazine*, vol. 49, no. 6, pp. 46–54, Apr. 2011, ISSN: 0163-6804. DOI: [10.1109/MCOM.2011.5783984](https://doi.org/10.1109/MCOM.2011.5783984).
- [21] A. Wilkins, J. Veitch, and B. Lehman, “Led lighting flicker and potential health concerns: Ieee standard par1789 update”, Oct. 2010, pp. 171–178. DOI: [10.1109/ECCE.2010.5618050](https://doi.org/10.1109/ECCE.2010.5618050).
- [22] C. Le Bas, S. Sahuguede, A. Julien-Vergonjanne, A. Behloul, P. Combeau, and L. Aveneau, “Impact of receiver orientation and position on visible light communication link performance”, in *2015 4th International Workshop on Optical Wireless Communications (IWOW)*, Sep. 2015, pp. 1–5. DOI: [10.1109/IWOW.2015.7342254](https://doi.org/10.1109/IWOW.2015.7342254).
- [23] A. Beata Cece, *Li-fi on board*, <https://www.airbus.com/newsroom/news/en/2017/03/Li-Fi.html>, 2017.
- [24] S. Joumessi-Demeffo, P. Combeau, S. Sahuguede, D. Sauveron, B. Mercier, L. Aveneau, H. Boeglen, and A. Julien-Vergonjanne, “A Link Reliability Study of Optical Wireless Headset inside Aircraft Cockpit”, in *Global Lifi Congress*, Paris, France, Jun. 2019. [Online]. Available: <https://hal.archives-ouvertes.fr/hal-02152390>.
- [25] I. Moreno and C.-C. Sun, “Modeling the radiation pattern of leds”, *Opt. Express*, vol. 16, no. 3, pp. 1808–1819, Feb. 2008. DOI: [10.1364/OE.16.001808](https://doi.org/10.1364/OE.16.001808).
- [26] P. Luo, Z. Ghassemlooy, H. L. Minh, E. Bentley, A. Burton, and X. Tang, “Performance analysis of a car-to-car visible light communication system”, *Appl. Opt.*, vol. 54, no. 7, pp. 1696–1706, Mar. 2015. DOI: [10.1364/AO.54.001696](https://doi.org/10.1364/AO.54.001696).
- [27] S. J. Lee, J. K. Kwon, S. Y. Jung, and Y. H. Kwon, “Simulation modeling of visible light communication channel for automotive applications”, in *2012 15th International IEEE Conference on Intelligent Transportation Systems*, Sep. 2012, pp. 463–468. DOI: [10.1109/ITSC.2012.6338610](https://doi.org/10.1109/ITSC.2012.6338610).
- [28] M. Breslin, *Global led market expected to reach \$42.7 billion by 2020*, <https://www.ecmag.com/sectors/business/global-led-market-expected-reach-427-billion-2020>, 2014.
- [29] D. Karunatilaka, F. Zafar, V. Kalavally, and R. Parthiban, “Led based indoor visible light communications: State of the art”, *IEEE Communications Surveys Tutorials*, vol. 17, no. 3, pp. 1649–1678, Aug. 2015, ISSN: 1553-877X. DOI: [10.1109/COMST.2015.2417576](https://doi.org/10.1109/COMST.2015.2417576).
- [30] J. Foote and B. Gohn, “Energy efficient lighting for commercial markets- led lighting adoption and global outlook for led, fluorescent, halogen, and hid

- lamps and luminaires in commercial buildings: Market analysis and forecasts”, *Navigant Research*, 2013.
- [31] D. A. Steigerwald, J. C. Bhat, D. Collins, R. M. Fletcher, M. O. Holcomb, M. J. Ludowise, P. S. Martin, and S. L. Rudaz, “Illumination with solid state lighting technology”, *IEEE Journal of Selected Topics in Quantum Electronics*, vol. 8, no. 2, pp. 310–320, Mar. 2002, ISSN: 1077-260X. DOI: [10.1109/2944.999186](https://doi.org/10.1109/2944.999186).
- [32] Y. Zhou, J. Zhao, M. Zhang, J. Shi, and N. Chi, “2.32 gbit/s phosphorescent white led visible light communication aided by two-staged linear software equalizer”, in *2016 10th International Symposium on Communication Systems, Networks and Digital Signal Processing (CSNDSP)*, Jul. 2016, pp. 1–4. DOI: [10.1109/CSNDSP.2016.7573913](https://doi.org/10.1109/CSNDSP.2016.7573913).
- [33] G. Cossu, A. M. Khalid, P. Choudhury, R. Corsini, and E. Ciaramella, “3.4 gbit/s visible optical wireless transmission based on rgb led”, *Opt. Express*, vol. 20, no. 26, B501–B506, Dec. 2012. DOI: [10.1364/OE.20.00B501](https://doi.org/10.1364/OE.20.00B501).
- [34] P. Chvojka, P. Dvorak, P. Pesek, S. Zvanovec, P. A. Haigh, and Z. Ghassemlooy, “Characterization of the organic led based visible light communications”, in *2016 10th International Symposium on Communication Systems, Networks and Digital Signal Processing (CSNDSP)*, Jul. 2016, pp. 1–4.
- [35] P. A. Haigh, Z. Ghassemlooy, H. Le Minh, S. Rajbhandari, F. Arca, S. F. Tedde, O. Hayden, and I. Papakonstantinou, “Exploiting equalization techniques for improving data rates in organic optoelectronic devices for visible light communications”, *Journal of Lightwave Technology*, vol. 30, no. 19, pp. 3081–3088, Oct. 2012, ISSN: 0733-8724.
- [36] H. Chen, Z. Xu, Q. Gao, and S. Li, “A 51.6 mb/s experimental vlc system using a monochromic organic led”, *IEEE Photonics Journal*, vol. 10, no. 2, pp. 1–12, Apr. 2018, ISSN: 1943-0655.
- [37] P. A. Haigh, F. Bausi, H. Le Minh, I. Papakonstantinou, W. O. Popoola, A. Burton, and F. Cacialli, “Wavelength-multiplexed polymer leds: Towards 55 mb/s organic visible light communications”, *IEEE Journal on Selected Areas in Communications*, vol. 33, no. 9, pp. 1819–1828, Sep. 2015, ISSN: 0733-8716.
- [38] A. E. Kelly, J. J. D. McKendry, S. Zhang, D. Massoubre, B. R. Rae, R. P. Green, R. K. Henderson, and M. D. Dawson, “High-speed gan micro-led arrays for data communications”, in *2012 14th International Conference on Transparent Optical Networks (ICTON)*, Jul. 2012, pp. 1–5. DOI: [10.1109/ICTON.2012.6253883](https://doi.org/10.1109/ICTON.2012.6253883).
- [39] M. S. Islim, R. X. Ferreira, X. He, E. Xie, S. Videv, S. Viola, S. Watson, N. Bamiedakis, R. V. Penty, I. H. White, A. E. Kelly, E. Gu, H. Haas, and M. D. Dawson, “Towards 10&#x2009;&#x2009;gb/s orthogonal frequency division multiplexing-based visible light communication using a gan violet micro-led”, *Photon. Res.*, vol. 5, no. 2, A35–A43, Apr. 2017. DOI: [10.1364/PRJ.5.000A35](https://doi.org/10.1364/PRJ.5.000A35).

- [40] E. F. Schubert, Y. Wang, A. Y. Cho, L. Tu, and G. J. Zydzik, “Resonant cavity light-emitting diode”, *Applied Physics Letters*, vol. 60, no. 8, pp. 921–923, 1992. DOI: [10.1063/1.106489](https://doi.org/10.1063/1.106489).
- [41] T. Komine, J. H. Lee, S. Haruyama, and M. Nakagawa, “Adaptive equalization system for visible light wireless communication utilizing multiple white led lighting equipment”, *IEEE Transactions on Wireless Communications*, vol. 8, no. 6, pp. 2892–2900, Apr. 2009, ISSN: 1536-1276. DOI: [10.1109/TWC.2009.060258](https://doi.org/10.1109/TWC.2009.060258).
- [42] H. Chun, S. Rajbhandari, G. Faulkner, D. Tsonev, E. Xie, J. J. D. McKendry, E. Gu, M. D. Dawson, D. C. O’Brien, and H. Haas, “Led based wavelength division multiplexed 10 gb/s visible light communications”, *Journal of Light-wave Technology*, vol. 34, no. 13, pp. 3047–3052, Jul. 2016, ISSN: 0733-8724. DOI: [10.1109/JLT.2016.2554145](https://doi.org/10.1109/JLT.2016.2554145).
- [43] C. Lee, C. Zhang, M. Cantore, R. M. Farrell, S. H. Oh, T. Margalith, J. S. Speck, S. Nakamura, J. E. Bowers, and S. P. DenBaars, “4 gbps direct modulation of 450 nm gan laser for high-speed visible light communication”, *Opt. Express*, vol. 23, no. 12, pp. 16 232–16 237, Jun. 2015. DOI: [10.1364/OE.23.016232](https://doi.org/10.1364/OE.23.016232).
- [44] J. Piprek, “Efficiency droop in nitride-based light-emitting diodes”, *physica status solidi (a)*, vol. 207, no. 10, pp. 2217–2225, 2010. DOI: [10.1002/pssa.201026149](https://doi.org/10.1002/pssa.201026149).
- [45] D. Tsonev, S. Videv, and H. Haas, “Towards a 100 gb/s visible light wireless access network”, *Opt. Express*, vol. 23, no. 2, pp. 1627–1637, Jan. 2015. DOI: [10.1364/OE.23.001627](https://doi.org/10.1364/OE.23.001627).
- [46] L. Wei, C. Hsu, C. Chow, and C. Yeh, “40-gbit/s visible light communication using polarization-multiplexed r/g/b laser diodes with 2-m free-space transmission”, in *2019 Optical Fiber Communications Conference and Exhibition (OFC)*, Mar. 2019, pp. 1–3.
- [47] M. Sönmez, “Frequency response comparison of photo-detectors for visible light communication systems”, in *Applied Electromagnetic Engineering for Advanced Materials from Macro-to Nanoscale under Static-to Shock Loading*, ser. Materials Science Forum, vol. 915, Trans Tech Publications Ltd, Apr. 2018, pp. 220–223. DOI: [10.4028/www.scientific.net/MSF.915.220](https://doi.org/10.4028/www.scientific.net/MSF.915.220).
- [48] N. Chi, *LED-based Visible Light Communications*, ser. Signals and communication technology. Springer, 2018, ISBN: 9783662566596. [Online]. Available: [https://books.google.fr/books?id=\\\_HpuwAEACAAJ](https://books.google.fr/books?id=\_HpuwAEACAAJ).
- [49] J. Vucic, C. Kottke, S. Nerreter, K. Habel, A. Buttner, K. Langer, and J. W. Walewski, “125 mbit/s over 5 m wireless distance by use of oom-modulated phosphorescent white leds”, in *2009 35th European Conference on Optical Communication*, Sep. 2009, pp. 1–2.

- [50] J. Armstrong, R. J. Green, and M. D. Higgins, "Comparison of three receiver designs for optical wireless communications using white leds", *IEEE Communications Letters*, vol. 16, no. 5, pp. 748–751, May 2012, ISSN: 1089-7798. DOI: [10.1109/LCOMM.2012.031912.112206](https://doi.org/10.1109/LCOMM.2012.031912.112206).
- [51] E. Monteiro and S. Hranilovic, "Design and implementation of color-shift keying for visible light communications", *Journal of Lightwave Technology*, vol. 32, May 2014. DOI: [10.1109/JLT.2014.2314358](https://doi.org/10.1109/JLT.2014.2314358).
- [52] Y. Tanaka, T. Komine, S. Haruyama, and M. Nakagawa, "Indoor visible light data transmission system utilizing white led lights", English, *IEICE Transactions on Communications*, vol. E86-B, no. 8, pp. 2440–2454, Aug. 2003, ISSN: 0916-8516.
- [53] J. Vučić, C. Kottke, K. Habel, and K. Langer, "803 mbit/s visible light wdm link based on dmt modulation of a single rgb led luminary", in *2011 Optical Fiber Communication Conference and Exposition and the National Fiber Optic Engineers Conference*, Mar. 2011, pp. 1–3.
- [54] N. Saha, R. K. Mondal, and Yeong Min Jang, "Receiver performance improvement utilizing diversity in mimo vlc", in *2013 International Conference on ICT Convergence (ICTC)*, Oct. 2013, pp. 546–549. DOI: [10.1109/ICTC.2013.6675417](https://doi.org/10.1109/ICTC.2013.6675417).
- [55] C. Chen, W.-D. Zhong, D. Wu, and Z. Ghassemlooy, "Wide-fov and high-gain imaging angle diversity receiver for indoor sdm-vlc systems", *IEEE Photonics Technology Letters*, vol. 28, Jun. 2016. DOI: [10.1109/LPT.2016.2584185](https://doi.org/10.1109/LPT.2016.2584185).
- [56] A. H. Azhar, T. Tran, and D. O'Brien, "Demonstration of high-speed data transmission using mimo-ofdm visible light communications", in *2010 IEEE Globecom Workshops*, Dec. 2010, pp. 1052–1056. DOI: [10.1109/GLOCOMW.2010.5700095](https://doi.org/10.1109/GLOCOMW.2010.5700095).
- [57] S. Moghe and R. Upadhyay, "Comparison of siso and mimo techniques in 802.11n wireless local area network", in *2009 International Conference on Emerging Trends in Electronic and Photonic Devices Systems*, Dec. 2009, pp. 245–246. DOI: [10.1109/ELECTRO.2009.5441127](https://doi.org/10.1109/ELECTRO.2009.5441127).
- [58] Fang-Ming Wu, Chun-Ting Lin, Chia-Chien Wei, Cheng-Wei Chen, Zhen-Yu Chen, and Hou-Tzu Huang, "3.22-gb/s wdm visible light communication of a single rgb led employing carrier-less amplitude and phase modulation", in *2013 Optical Fiber Communication Conference and Exposition and the National Fiber Optic Engineers Conference (OFC/NFOEC)*, Mar. 2013, pp. 1–3.
- [59] L. Zeng, D. C. O'Brien, H. L. Minh, G. E. Faulkner, K. Lee, D. Jung, Y. Oh, and E. T. Won, "High data rate multiple input multiple output (mimo) optical wireless communications using white led lighting", *IEEE Journal on Selected Areas in Communications*, vol. 27, no. 9, pp. 1654–1662, Dec. 2009, ISSN: 0733-8716. DOI: [10.1109/JSAC.2009.091215](https://doi.org/10.1109/JSAC.2009.091215).

- [60] R. Bian, I. Tavakkolnia, and H. Haas, “15.73 gb/s visible light communication with off-the-shelf leds”, *Journal of Lightwave Technology*, vol. 37, no. 10, pp. 2418–2424, May 2019, ISSN: 0733-8724. DOI: [10.1109/JLT.2019.2906464](https://doi.org/10.1109/JLT.2019.2906464).
- [61] S. Wilson, S. Wilson, and E. Biglieri, *Academic Press Library in Mobile and Wireless Communications: Transmission Techniques for Digital Communications*. Jul. 2016, pp. 1–727.
- [62] S. Dimitrov and H. Haas, *Principles of LED Light Communications: Towards Networked Li-Fi*. Mar. 2015, ISBN: 978-1107049420. DOI: [10.1017/CB09781107278929](https://doi.org/10.1017/CB09781107278929).
- [63] J. K. Kwon, “Inverse source coding for dimming in visible light communications using nrz-ook on reliable links”, *IEEE Photonics Technology Letters*, vol. 22, no. 19, pp. 1455–1457, Oct. 2010, ISSN: 1041-1135. DOI: [10.1109/LPT.2010.2062498](https://doi.org/10.1109/LPT.2010.2062498).
- [64] E. Cho, J. Choi, C. Park, M. Kang, S. Shin, Z. Ghassemlooy, and C. G. Lee, “Nrz-ook signaling with led dimming for visible light communication link”, in *2011 16th European Conference on Networks and Optical Communications*, Jul. 2011, pp. 32–35.
- [65] K. Kim, K. Lee, and K. Lee, “Appropriate rll coding scheme for effective dimming control in vlc”, *Electronics Letters*, vol. 52, no. 19, pp. 1622–1624, 2016, ISSN: 0013-5194. DOI: [10.1049/e1.2016.1695](https://doi.org/10.1049/e1.2016.1695).
- [66] T. Elganimi, “Performance comparison between ook, ppm and pam modulation schemes for free space optical (fso) communication systems: Analytical study”, *International Journal of Computer Applications - Foundation of Computer Science - New York, NY 10001, USA*, vol. Vol.79, pp. 22–27, Oct. 2013. DOI: [10.5120/13786-1838](https://doi.org/10.5120/13786-1838).
- [67] K. Choi, Y. Jang, Jingyoung Noh, MinChul Ju, and Y. Park, “Visible light communications with color and dimming control by employing vppm coding”, in *2012 Fourth International Conference on Ubiquitous and Future Networks (ICUFN)*, Jul. 2012, pp. 10–12. DOI: [10.1109/ICUFN.2012.6261654](https://doi.org/10.1109/ICUFN.2012.6261654).
- [68] Bo Bai, Zhengyuan Xu, and Yangyu Fan, “Joint led dimming and high capacity visible light communication by overlapping ppm”, in *The 19th Annual Wireless and Optical Communications Conference (WOCC 2010)*, May 2010, pp. 1–5. DOI: [10.1109/WOCC.2010.5510410](https://doi.org/10.1109/WOCC.2010.5510410).
- [69] X. You, J. Chen, H. Zheng, and C. Yu, “Efficient data transmission using mppm dimming control in indoor visible light communication”, *IEEE Photonics Journal*, vol. 7, no. 4, pp. 1–12, Aug. 2015, ISSN: 1943-0655. DOI: [10.1109/JPHOT.2015.2451619](https://doi.org/10.1109/JPHOT.2015.2451619).
- [70] Jupeng Ding, Zhitong Huang, and Yuefeng Ji, “Indoor white light wireless data transmission based on new generation environment-friendly solid state lighting”, in *2010 IEEE International Conference on Wireless Communications, Networking and Information Security*, Apr. 2010, pp. 87–91. DOI: [10.1109/WCINS.2010.5541760](https://doi.org/10.1109/WCINS.2010.5541760).

- [71] Da-Shan Shiu and J. M. Kahn, “Differential pulse-position modulation for power-efficient optical communication”, *IEEE Transactions on Communications*, vol. 47, no. 8, pp. 1201–1210, Aug. 1999, ISSN: 0090-6778. DOI: [10.1109/26.780456](https://doi.org/10.1109/26.780456).
- [72] M. Noshad and M. Brandt-Pearce, “Application of expurgated ppm to indoor visible light communications—part i: Single-user systems”, *Journal of Lightwave Technology*, vol. 32, no. 5, pp. 875–882, Mar. 2014, ISSN: 0733-8724. DOI: [10.1109/JLT.2013.2293341](https://doi.org/10.1109/JLT.2013.2293341).
- [73] R. Mesleh and A. Younis, *Space Modulation Techniques*. Jun. 2018, ISBN: 978-1-119-37569-2.
- [74] B. Béchadergue, L. Chassagne, and H. Guan, “Experimental comparison of pulse-amplitude and spatial modulations for vehicle-to-vehicle visible light communication in platoon configurations”, *Opt. Express*, vol. 25, no. 20, pp. 24 790–24 802, Oct. 2017. DOI: [10.1364/OE.25.024790](https://doi.org/10.1364/OE.25.024790).
- [75] M. A. Kashani and M. Kavehrad, “On the performance of single- and multi-carrier modulation schemes for indoor visible light communication systems”, in *2014 IEEE Global Communications Conference*, Dec. 2014, pp. 2084–2089. DOI: [10.1109/GLOCOM.2014.7037115](https://doi.org/10.1109/GLOCOM.2014.7037115).
- [76] R. v. Nee and R. Prasad, *OFDM for Wireless Multimedia Communications*, 1st. Norwood, MA, USA: Artech House, Inc., 2000, ISBN: 0890065306.
- [77] J. Campello, “Practical bit loading for dmt”, in *1999 IEEE International Conference on Communications (Cat. No. 99CH36311)*, vol. 2, Apr. 1999, 801–805 vol.2. DOI: [10.1109/ICC.1999.765384](https://doi.org/10.1109/ICC.1999.765384).
- [78] H. E. Levin, “A complete and optimal data allocation method for practical discrete multitone systems”, vol. 1, Feb. 2001, 369 –374 vol.1, ISBN: 0-7803-7206-9. DOI: [10.1109/GLOCOM.2001.965141](https://doi.org/10.1109/GLOCOM.2001.965141).
- [79] J. Armstrong and B. J. C. Schmidt, “Comparison of asymmetrically clipped optical ofdm and dc-biased optical ofdm in awgn”, *IEEE Communications Letters*, vol. 12, no. 5, pp. 343–345, May 2008, ISSN: 1089-7798. DOI: [10.1109/LCOMM.2008.080193](https://doi.org/10.1109/LCOMM.2008.080193).
- [80] R. Mesleh, H. Elgala, and H. Haas, “On the performance of different ofdm based optical wireless communication systems”, *IEEE/OSA Journal of Optical Communications and Networking*, vol. 3, no. 8, pp. 620–628, Aug. 2011, ISSN: 1943-0620. DOI: [10.1364/JOCN.3.000620](https://doi.org/10.1364/JOCN.3.000620).
- [81] S. D. Dissanayake and J. Armstrong, “Comparison of aco-ofdm, dco-ofdm and ado-ofdm in im/dd systems”, *Journal of Lightwave Technology*, vol. 31, no. 7, pp. 1063–1072, Apr. 2013, ISSN: 0733-8724. DOI: [10.1109/JLT.2013.2241731](https://doi.org/10.1109/JLT.2013.2241731).
- [82] H. Elgala and T. D. C. Little, “Reverse polarity optical-ofdm (rpo-ofdm): Dimming compatible ofdm for gigabit vlc links”, *Opt. Express*, vol. 21, no. 20, pp. 24 288–24 299, Oct. 2013. DOI: [10.1364/OE.21.024288](https://doi.org/10.1364/OE.21.024288).

- [83] D. Tsonev, S. Sinanovic, and H. Haas, “Novel unipolar orthogonal frequency division multiplexing (u-ofdm) for optical wireless”, in *2012 IEEE 75th Vehicular Technology Conference (VTC Spring)*, May 2012, pp. 1–5. DOI: [10.1109/VETECS.2012.6240060](https://doi.org/10.1109/VETECS.2012.6240060).
- [84] N. Fernando, Y. Hong, and E. Viterbo, “Flip-ofdm for optical wireless communications”, in *2011 IEEE Information Theory Workshop*, Oct. 2011, pp. 5–9. DOI: [10.1109/ITW.2011.6089566](https://doi.org/10.1109/ITW.2011.6089566).
- [85] D. Tsonev and H. Haas, “Avoiding spectral efficiency loss in unipolar ofdm for optical wireless communication”, in *2014 IEEE International Conference on Communications (ICC)*, Apr. 2014, pp. 3336–3341. DOI: [10.1109/ICC.2014.6883836](https://doi.org/10.1109/ICC.2014.6883836).
- [86] M. I. Olmedo, T. Zuo, J. B. Jensen, Q. Zhong, X. Xu, S. Popov, and I. T. Monroy, “Multiband carrierless amplitude phase modulation for high capacity optical data links”, *Journal of Lightwave Technology*, vol. 32, no. 4, pp. 798–804, Feb. 2014, ISSN: 0733-8724. DOI: [10.1109/JLT.2013.2284926](https://doi.org/10.1109/JLT.2013.2284926).
- [87] P. A. Haigh, S. T. Le, S. Zvanovec, Z. Ghassemlooy, P. Luo, T. Xu, P. Chvojka, T. Kanesan, E. Giacomidis, P. Canyelles-Pericas, H. L. Minh, W. Popoola, S. Rajbhandari, I. Papakonstantinou, and I. Darwazeh, “Multi-band carrier-less amplitude and phase modulation for bandlimited visible light communications systems”, *IEEE Wireless Communications*, vol. 22, no. 2, pp. 46–53, Apr. 2015, ISSN: 1536-1284. DOI: [10.1109/MWC.2015.7096284](https://doi.org/10.1109/MWC.2015.7096284).
- [88] S. C. J. Lee, S. Randel, F. Breyer, and A. M. J. Koonen, “Pam-dmt for intensity-modulated and direct-detection optical communication systems”, *IEEE Photonics Technology Letters*, vol. 21, no. 23, pp. 1749–1751, Dec. 2009, ISSN: 1041-1135. DOI: [10.1109/LPT.2009.2032663](https://doi.org/10.1109/LPT.2009.2032663).
- [89] K. Ahn and J. K. Kwon, “Color intensity modulation for multicolored visible light communications”, *IEEE Photonics Technology Letters*, vol. 24, no. 24, pp. 2254–2257, Dec. 2012, ISSN: 1041-1135. DOI: [10.1109/LPT.2012.2226570](https://doi.org/10.1109/LPT.2012.2226570).
- [90] P. M. Butala, J. C. Chau, and T. D. C. Little, “Metameric modulation for diffuse visible light communications with constant ambient lighting”, in *2012 International Workshop on Optical Wireless Communications (IWOW)*, Oct. 2012, pp. 1–3. DOI: [10.1109/IWOW.2012.6349697](https://doi.org/10.1109/IWOW.2012.6349697).
- [91] C. Yeh, C. Chow, and L. Wei, “1250 mbit/s oofdm wireless white-light vlc transmission based on phosphor laser diode”, *IEEE Photonics Journal*, vol. 11, no. 3, pp. 1–5, Apr. 2019, ISSN: 1943-0655. DOI: [10.1109/JPHOT.2019.2911411](https://doi.org/10.1109/JPHOT.2019.2911411).
- [92] J. Ma, J. He, J. Shi, J. He, Z. Zhou, and R. Deng, “Nonlinear compensation based on k-means clustering algorithm for nyquist pam-4 vlc system”, *IEEE Photonics Technology Letters*, vol. 31, no. 12, pp. 935–938, Apr. 2019, ISSN: 1041-1135. DOI: [10.1109/LPT.2019.2913662](https://doi.org/10.1109/LPT.2019.2913662).
- [93] F. Hu, P. Zou, G. Li, W. Yu, and N. Chi, “Enhanced performance of cap modulated visible light communication system utilizing geometric shaping and

- rotation coding”, *IEEE Photonics Journal*, pp. 1–1, 2019, ISSN: 1943-0655. DOI: [10.1109/JPHOT.2019.2919070](https://doi.org/10.1109/JPHOT.2019.2919070).
- [94] Y. Hong, L.-K. Chen, and J. Zhao, “Performance-enhanced gigabit/s mimo-ofdm visible light communications using csi-free/dependent precoding techniques”, *Opt. Express*, vol. 27, no. 9, pp. 12 806–12 816, Apr. 2019. DOI: [10.1364/OE.27.012806](https://doi.org/10.1364/OE.27.012806).
- [95] Y. Mao, X. Jin, W. Pan, W. Liu, M. Jin, C. Gong, and Z. Xu, “Real-time investigation of cap transceivers with hybrid digital equalization for visible light communication”, *Opt. Express*, vol. 27, no. 7, pp. 9382–9393, Apr. 2019. DOI: [10.1364/OE.27.009382](https://doi.org/10.1364/OE.27.009382).
- [96] L.-Y. Wei, C.-W. Hsu, C.-W. Chow, and C.-H. Yeh, “20.231 gbit/s tricolor red/green/blue laser diode based bidirectional signal remodulation visible-light communication system”, *Photon. Res.*, vol. 6, no. 5, pp. 422–426, May 2018. DOI: [10.1364/PRJ.6.000422](https://doi.org/10.1364/PRJ.6.000422).
- [97] K.-T. Ho, R. Chen, G. Liu, C. Shen, J. Holguin-Lerma, A. A. Al-Saggaf, T. K. Ng, M.-S. Alouini, J.-H. He, and B. S. Ooi, “3.2 gigabit-per-second visible light communication link with ingan/gan mqw micro-photodetector”, *Opt. Express*, vol. 26, no. 3, pp. 3037–3045, Feb. 2018. DOI: [10.1364/OE.26.003037](https://doi.org/10.1364/OE.26.003037).
- [98] S. Liang, L. Qiao, X. Lu, and N. Chi, “Enhanced performance of a multiband super-nyquist cap16 vlc system employing a joint mimo equalizer”, *Opt. Express*, vol. 26, no. 12, pp. 15 718–15 725, Jun. 2018. DOI: [10.1364/OE.26.015718](https://doi.org/10.1364/OE.26.015718).
- [99] K. Wu, J. He, J. Ma, and Y. Wei, “A bipcm scheme based on oct precoding for a 256-qam ofdm-vlc system”, *IEEE Photonics Technology Letters*, vol. 30, no. 21, pp. 1866–1869, Nov. 2018, ISSN: 1041-1135. DOI: [10.1109/LPT.2018.2870114](https://doi.org/10.1109/LPT.2018.2870114).
- [100] W. Xu, M. Zhang, D. Han, Z. Ghassemlooy, P. Luo, and Y. Zhang, “Real-time 262-mb/s visible light communication with digital predistortion waveform shaping”, *IEEE Photonics Journal*, vol. 10, no. 3, pp. 1–10, Apr. 2018, ISSN: 1943-0655. DOI: [10.1109/JPHOT.2018.2829905](https://doi.org/10.1109/JPHOT.2018.2829905).
- [101] K. Werfli, P. Chvojka, Z. Ghassemlooy, N. B. Hassan, S. Zvanovec, A. Burton, P. A. Haigh, and M. R. Bhatnagar, “Experimental demonstration of high-speed 4 x 4 imaging multi-cap mimo visible light communications”, *Journal of Lightwave Technology*, vol. 36, no. 10, pp. 1944–1951, May 2018, ISSN: 0733-8724. DOI: [10.1109/JLT.2018.2796503](https://doi.org/10.1109/JLT.2018.2796503).
- [102] R. Chen, K. Park, C. Shen, T. K. Ng, B. S. Ooi, and M. Alouini, “Visible light communication using dc-biased optical filter bank multi-carrier modulation”, in *2018 Global LIFI Congress (GLC)*, Feb. 2018, pp. 1–6. DOI: [10.23919/GLC.2018.8319094](https://doi.org/10.23919/GLC.2018.8319094).
- [103] N. Chi, Y. Zhou, S. Liang, F. Wang, J. Li, and Y. Wang, “Enabling technologies for high-speed visible light communication employing cap modulation”, *Journal of Lightwave Technology*, vol. 36, no. 2, pp. 510–518, Jan. 2018, ISSN: 0733-8724.

- [104] J. Zhang, X. Hong, J. Liu, and C. Guo, "Experimental demonstration of an ofdm based visible light communication system using inter-block precoding and superimposed pilots", *Optics Communications*, vol. 412, pp. 219–225, 2018, ISSN: 0030-4018. DOI: <https://doi.org/10.1016/j.optcom.2017.12.020>.
- [105] R. Bian, S. Videv, A. D. Griffiths, J. J. D. McKendry, E. Xie, E. Gu, M. D. Dawson, and H. Haas, "Experimental demonstration of generalised space shift keying for visible light communication", in *2017 IEEE International Black Sea Conference on Communications and Networking (BlackSeaCom)*, Apr. 2017, pp. 1–5. DOI: [10.1109/BlackSeaCom.2017.8277716](https://doi.org/10.1109/BlackSeaCom.2017.8277716).
- [106] Y. Hong, L. Chen, and J. Zhao, "Experimental demonstration of performance-enhanced mimo-ofdm visible light communications", in *2017 Optical Fiber Communications Conference and Exhibition (OFC)*, Mar. 2017, pp. 1–3.
- [107] A. F. Hussein, H. Elgala, B. Fahs, and M. M. Hella, "Experimental investigation of dco-ofdm adaptive loading using si pn-based receiver", in *2017 26th Wireless and Optical Communication Conference (WOCC)*, Apr. 2017, pp. 1–5. DOI: [10.1109/WOCC.2017.7928982](https://doi.org/10.1109/WOCC.2017.7928982).
- [108] Q. Chen, J. He, R. Deng, M. Chen, F. Zhang, M. Dai, F. Long, and L. Chen, "Experimental research on adaptive 128/64qam dft-spread ifft/fft size efficient ofdm with a high se in vllc system", *IEEE Photonics Journal*, vol. 9, no. 1, pp. 1–8, Feb. 2017, ISSN: 1943-0655. DOI: [10.1109/JPHOT.2016.2639786](https://doi.org/10.1109/JPHOT.2016.2639786).
- [109] Y. Huang, C. Tsai, H. Kao, Y. Chi, H. Wang, T. Shih, and G. Lin, "17.6-gbps universal filtered multi-carrier encoding of gan blue led for visible light communication", in *2017 Conference on Lasers and Electro-Optics (CLEO)*, May 2017, pp. 1–2.
- [110] S. H. Younus and J. M. H. Elmirghani, "Wdm for high-speed indoor visible light communication system", in *2017 19th International Conference on Transparent Optical Networks (ICTON)*, Jul. 2017, pp. 1–6.
- [111] C. Lee, C. Shen, C. Cozzan, R. M. Farrell, J. S. Speck, S. Nakamura, B. S. Ooi, and S. P. DenBaars, "Gigabit-per-second white light-based visible light communication using near-ultraviolet laser diode and red-, green-, and blue-emitting phosphors", *Opt. Express*, vol. 25, no. 15, pp. 17 480–17 487, Jul. 2017. DOI: [10.1364/OE.25.017480](https://doi.org/10.1364/OE.25.017480).
- [112] S. Rajbhandari, A. V. N. Jalajakumari, H. Chun, G. Faulkner, K. Cameron, R. Henderson, D. Tsonev, H. Haas, E. Xie, J. J. D. McKendry, J. Herrnsdorf, R. Ferreira, E. Gu, M. D. Dawson, and D. O'Brien, "A multigigabit per second integrated multiple-input multiple-output vlc demonstrator", *Journal of Light-wave Technology*, vol. 35, no. 20, pp. 4358–4365, Oct. 2017, ISSN: 0733-8724. DOI: [10.1109/JLT.2017.2694486](https://doi.org/10.1109/JLT.2017.2694486).
- [113] I. Lu, C. Lai, C. Yeh, and J. Chen, "6.36 gbit/s rgb led-based wdm mimo visible light communication system employing ofdm modulation", in *2017 Optical Fiber Communications Conference and Exhibition (OFC)*, Mar. 2017, pp. 1–3.

- [114] B. Fahs, M. J. Senneca, J. Chellis, B. Mazzara, S. Ray, J. Ghasemi, Y. Miao, P. Zarkesh-Ha, V. J. Koomson, and M. M. Hella, "A meter-scale 600-mb/s 2x2 imaging mimo vlc link using commercial leds and si p-n photodiode array", in *2017 26th Wireless and Optical Communication Conference (WOCC)*, Apr. 2017, pp. 1–6. DOI: [10.1109/WOCC.2017.7928983](https://doi.org/10.1109/WOCC.2017.7928983).
- [115] R. X. G. Ferreira, E. Xie, J. J. D. McKendry, S. Rajbhandari, H. Chun, G. Faulkner, S. Watson, A. E. Kelly, E. Gu, R. V. Penty, I. H. White, D. C. O'Brien, and M. D. Dawson, "High bandwidth gan-based micro-leds for multi-gb/s visible light communications", *IEEE Photonics Technology Letters*, vol. 28, no. 19, pp. 2023–2026, Oct. 2016, ISSN: 1041-1135. DOI: [10.1109/LPT.2016.2581318](https://doi.org/10.1109/LPT.2016.2581318).
- [116] X. Li, N. Bamiedakis, X. Guo, J. J. D. McKendry, E. Xie, R. Ferreira, E. Gu, M. D. Dawson, R. V. Penty, and I. H. White, "Wireless visible light communications employing feed-forward pre-equalization and pam-4 modulation", *Journal of Lightwave Technology*, vol. 34, no. 8, pp. 2049–2055, Apr. 2016, ISSN: 0733-8724. DOI: [10.1109/JLT.2016.2520503](https://doi.org/10.1109/JLT.2016.2520503).
- [117] Yingjun Zhou, Shangyu Liang, Siyuan Chen, X. Huang, and N. Chi, "2.08gb/s visible light communication utilizing power exponential pre-equalization", in *2016 25th Wireless and Optical Communication Conference (WOCC)*, May 2016, pp. 1–3. DOI: [10.1109/WOCC.2016.7506539](https://doi.org/10.1109/WOCC.2016.7506539).
- [118] C. Tsai, Y. Lu, and S. Ko, "Resonant-cavity light-emitting diodes (rcleds) made from a simple dielectric coating of transistor outline (to)-can packaged ingan leds for visible light communications", *IEEE Transactions on Electron Devices*, vol. 63, no. 7, pp. 2802–2806, Jul. 2016, ISSN: 0018-9383. DOI: [10.1109/TED.2016.2561621](https://doi.org/10.1109/TED.2016.2561621).
- [119] I. Lu, C. Yeh, D. Hsu, and C. Chow, "Utilization of 1-ghz vcsel for 11.1-gbps ofdm vlc wireless communication", *IEEE Photonics Journal*, vol. 8, no. 3, pp. 1–6, Apr. 2016, ISSN: 1943-0655. DOI: [10.1109/JPHOT.2016.2553839](https://doi.org/10.1109/JPHOT.2016.2553839).
- [120] I.-C. Lu, Y.-L. Liu, and C.-H. Lai, "High-speed 2x2 mimo-ofdm visible light communication employing phosphorescent led", in *2016 Eighth International Conference on Ubiquitous and Future Networks (ICUFN)*, Jul. 2016, pp. 222–224. DOI: [10.1109/ICUFN.2016.7537021](https://doi.org/10.1109/ICUFN.2016.7537021).
- [121] J. Li, Y. Xu, J. Shi, Y. Wang, X. Ji, H. Ou, and N. Chi, "A 2x2 imaging mimo system based on led visible light communications employing space balanced coding and integrated pin array reception", *Optics Communications*, vol. 367, pp. 214–218, 2016, ISSN: 0030-4018. DOI: <https://doi.org/10.1016/j.optcom.2016.01.041>.
- [122] Y.-C. Chi, D.-H. Hsieh, C.-T. Tsai, H.-Y. Chen, H.-C. Kuo, and G.-R. Lin, "450-nm gan laser diode enables high-speed visible light communication with 9-gbps qam-ofdm", *Opt. Express*, vol. 23, no. 10, pp. 13 051–13 059, May 2015. DOI: [10.1364/OE.23.013051](https://doi.org/10.1364/OE.23.013051).

- [123] G. Cossu, W. Ali, R. Corsini, and E. Ciaramella, “Gigabit-class optical wireless communication system at indoor distances (1.5 – 4 m)”, *Opt. Express*, vol. 23, no. 12, pp. 15 700–15 705, Jun. 2015. DOI: [10.1364/OE.23.015700](https://doi.org/10.1364/OE.23.015700).
- [124] X. Huang, S. Chen, Z. Wang, J. Shi, Y. Wang, J. Xiao, and N. Chi, “2.0-gb/s visible light link based on adaptive bit allocation ofdm of a single phosphorescent white led”, *IEEE Photonics Journal*, vol. 7, no. 5, pp. 1–8, Oct. 2015, ISSN: 1943-0655. DOI: [10.1109/JPHOT.2015.2480541](https://doi.org/10.1109/JPHOT.2015.2480541).
- [125] H. Chun, S. Rajbhandari, D. Tsonev, G. Faulkner, H. Haas, and D. O’Brien, “Visible light communication using laser diode based remote phosphor technique”, in *2015 IEEE International Conference on Communication Workshop (ICCW)*, Apr. 2015, pp. 1392–1397.
- [126] Y. Wang, L. Tao, X. Huang, J. Shi, and N. Chi, “8-gb/s rgb led-based wdm vlc system employing high-order cap modulation and hybrid post equalizer”, *IEEE Photonics Journal*, vol. 7, no. 6, pp. 1–7, Dec. 2015, ISSN: 1943-0655. DOI: [10.1109/JPHOT.2015.2489927](https://doi.org/10.1109/JPHOT.2015.2489927).
- [127] Xingxing Huang, Jianyang Shi, Jiehui Li, Yiguang Wang, Yuanquan Wang, and Nan Chi, “750mbit/s visible light communications employing 64qam-ofdm based on amplitude equalization circuit”, in *2015 Optical Fiber Communications Conference and Exhibition (OFC)*, Mar. 2015, pp. 1–3.
- [128] Y. Wang, X. Huang, L. Tao, J. Shi, and N. Chi, “4.5-gb/s rgb-led based wdm visible light communication system employing cap modulation and rls based adaptive equalization”, *Opt. Express*, vol. 23, no. 10, pp. 13 626–13 633, May 2015. DOI: [10.1364/OE.23.013626](https://doi.org/10.1364/OE.23.013626).
- [129] H. Li, Y. Zhang, X. Chen, C. Wu, J. Guo, Z. Gao, W. Pei, and H. Chen, “682mbit/s phosphorescent white led visible light communications utilizing analog equalized 16qam-ofdm modulation without blue filter”, *Optics Communications*, vol. 354, pp. 107 –111, 2015, ISSN: 0030-4018. DOI: <https://doi.org/10.1016/j.optcom.2015.05.033>.
- [130] S. Rajbhandari, H. Chun, G. Faulkner, K. Cameron, A. V. N. Jalajakumari, R. Henderson, D. Tsonev, M. Ijaz, Z. Chen, H. Haas, E. Xie, J. J. D. McKendry, J. Herrnsdorf, E. Gu, M. D. Dawson, and D. O’Brien, “High-speed integrated visible light communication system: Device constraints and design considerations”, *IEEE Journal on Selected Areas in Communications*, vol. 33, no. 9, pp. 1750–1757, Sep. 2015, ISSN: 0733-8716. DOI: [10.1109/JSAC.2015.2432551](https://doi.org/10.1109/JSAC.2015.2432551).
- [131] P. A. Haigh, A. Burton, K. Werfli, H. L. Minh, E. Bentley, P. Chvojka, W. O. Popoola, I. Papakonstantinou, and S. Zvanovec, “A multi-cap visible-light communications system with 4.85-b/s/hz spectral efficiency”, *IEEE Journal on Selected Areas in Communications*, vol. 33, no. 9, pp. 1771–1779, Sep. 2015, ISSN: 0733-8716. DOI: [10.1109/JSAC.2015.2433053](https://doi.org/10.1109/JSAC.2015.2433053).

- [132] H. Li, X. Chen, J. Guo, and H. Chen, "A 550 mbit/s real-time visible light communication system based on phosphorescent white light led for practical high-speed low-complexity application", *Opt. Express*, vol. 22, no. 22, pp. 27 203–27 213, Nov. 2014. DOI: [10.1364/OE.22.027203](https://doi.org/10.1364/OE.22.027203).
- [133] H. Li, X. Chen, B. Huang, D. Tang, and H. Chen, "High bandwidth visible light communications based on a post-equalization circuit", *IEEE Photonics Technology Letters*, vol. 26, no. 2, pp. 119–122, Jan. 2014, ISSN: 1041-1135. DOI: [10.1109/LPT.2013.2290026](https://doi.org/10.1109/LPT.2013.2290026).
- [134] Y. Wang, L. Tao, Y. Wang, and N. Chi, "High speed wdm vlc system based on multi-band cap64 with weighted pre-equalization and modified cmma based post-equalization", *IEEE Communications Letters*, vol. 18, no. 10, pp. 1719–1722, Oct. 2014, ISSN: 1089-7798. DOI: [10.1109/LCOMM.2014.2349990](https://doi.org/10.1109/LCOMM.2014.2349990).
- [135] Y. Wang and N. Chi, "Demonstration of high-speed 2 x 2 non-imaging mimo nyquist single carrier visible light communication with frequency domain equalization", *Journal of Lightwave Technology*, vol. 32, no. 11, pp. 2087–2093, Apr. 2014, ISSN: 0733-8724. DOI: [10.1109/JLT.2014.2320306](https://doi.org/10.1109/JLT.2014.2320306).
- [136] H.-H. Lu, Y.-P. Lin, P.-Y. Wu, C.-Y. Chen, M.-C. Chen, and T.-W. Jhang, "A multiple-input-multiple-output visible light communication system based on vcsels and spatial light modulators", *Opt. Express*, vol. 22, no. 3, pp. 3468–3474, Feb. 2014. DOI: [10.1364/OE.22.003468](https://doi.org/10.1364/OE.22.003468).
- [137] D. Tsonev, H. Chun, S. Rajbhandari, J. McKendry, S. Videv, E. Gu, M. Haji, S. Watson, A. Kelly, G. Faulkner, M. Dawson, H. Haas, and D. O'Brien, "A 3-gb/s single-led ofdm-based wireless vlc link using a gallium nitride u-led", *IEEE Photonics Technology Letters*, vol. PP, p. 1, Jan. 2014. DOI: [10.1109/LPT.2013.2297621](https://doi.org/10.1109/LPT.2013.2297621).
- [138] Y. Wang, Y. Wang, N. Chi, J. Yu, and H. Shang, "Demonstration of 575-mb/s downlink and 225-mb/s uplink bi-directional scm-wdm visible light communication using rgb led and phosphor-based led", *Opt. Express*, vol. 21, no. 1, pp. 1203–1208, Jan. 2013. DOI: [10.1364/OE.21.001203](https://doi.org/10.1364/OE.21.001203).
- [139] L. Grobe, A. Paraskevopoulos, J. Hilt, D. Schulz, F. Lassak, F. Hartlieb, C. Kottke, V. Jungnickel, and K. Langer, "High-speed visible light communication systems", *IEEE Communications Magazine*, vol. 51, no. 12, pp. 60–66, Dec. 2013, ISSN: 0163-6804. DOI: [10.1109/MCOM.2013.6685758](https://doi.org/10.1109/MCOM.2013.6685758).
- [140] S. Zhang, S. Watson, J. J. D. McKendry, D. Massoubre, A. Cogman, E. Gu, R. K. Henderson, A. E. Kelly, and M. D. Dawson, "1.5 gbit/s multi-channel visible light communications using cmos-controlled gan-based leds", *Journal of Lightwave Technology*, vol. 31, no. 8, pp. 1211–1216, Apr. 2013, ISSN: 0733-8724. DOI: [10.1109/JLT.2013.2246138](https://doi.org/10.1109/JLT.2013.2246138).
- [141] A. H. Azhar, T. Tran, and D. O'Brien, "A gigabit/s indoor wireless transmission using mimo-ofdm visible-light communications", *IEEE Photonics Technology Letters*, vol. 25, no. 2, pp. 171–174, Jan. 2013, ISSN: 1041-1135. DOI: [10.1109/LPT.2012.2231857](https://doi.org/10.1109/LPT.2012.2231857).

- [142] F. Wu, C. Lin, C. Wei, C. Chen, H. Huang, and C. Ho, "1.1-gb/s white-led-based visible light communication employing carrier-less amplitude and phase modulation", *IEEE Photonics Technology Letters*, vol. 24, no. 19, pp. 1730–1732, Oct. 2012, ISSN: 1041-1135. DOI: [10.1109/LPT.2012.2210540](https://doi.org/10.1109/LPT.2012.2210540).
- [143] A. M. Khalid, G. Cossu, R. Corsini, P. Choudhury, and E. Ciaramella, "1-gb/s transmission over a phosphorescent white led by using rate-adaptive discrete multitone modulation", *IEEE Photonics Journal*, vol. 4, no. 5, pp. 1465–1473, Oct. 2012, ISSN: 1943-0655. DOI: [10.1109/JPHOT.2012.2210397](https://doi.org/10.1109/JPHOT.2012.2210397).
- [144] C. Xi, A. Mirvakili, and V. J. Koomson, "A visible light communication system demonstration based on 16-level pulse amplitude modulation of an led array", in *2012 Symposium on Photonics and Optoelectronics*, May 2012, pp. 1–4. DOI: [10.1109/SOP0.2012.6271071](https://doi.org/10.1109/SOP0.2012.6271071).
- [145] F. M. Wu, C. T. Lin, C.-C. Wei, C. W. Chen, Z. Y. Chen, H.-T. Huang, and S. V. X. Chi, "Performance comparison of ofdm signal and cap signal over high capacity rgb-led-based wdm visible light communication", *IEEE Photonics Journal*, vol. 5, pp. 7901 507–7901 507, 2013.
- [146] Y. Park and J. Choi, "Radio access techniques", in *Enhanced Radio Access Technologies for Next Generation Mobile Communication*, Y. Park and F. Adachi, Eds. Dordrecht: Springer Netherlands, 2007, pp. 39–79. DOI: [10.1007/1-4020-5532-3\\_2](https://doi.org/10.1007/1-4020-5532-3_2). [Online]. Available: [https://doi.org/10.1007/1-4020-5532-3\\_2](https://doi.org/10.1007/1-4020-5532-3_2).
- [147] "Multiple access techniques: Fdma, tdma, and cdma", in *RF Measurements for Cellular Phones and Wireless Data Systems*. John Wiley and Sons, Ltd, 2008, ch. 30, pp. 413–429, ISBN: 9780470378014. DOI: [10.1002/9780470378014.ch30](https://doi.org/10.1002/9780470378014.ch30). eprint: <https://onlinelibrary.wiley.com/doi/pdf/10.1002/9780470378014.ch30>.
- [148] Y. Hou, S. Xiao, H. Zheng, and W. Hu, "Multiple access scheme based on block encoding time division multiplexing in an indoor positioning system using visible light", *IEEE/OSA Journal of Optical Communications and Networking*, vol. 7, no. 5, pp. 489–495, May 2015, ISSN: 1943-0620. DOI: [10.1364/JOCN.7.000489](https://doi.org/10.1364/JOCN.7.000489).
- [149] N. Karafolas and D. Uttamchandani, "Optical fiber code division multiple access networks: A review", *Optical Fiber Technology*, vol. 2, no. 2, pp. 149–168, 1996, ISSN: 1068-5200. DOI: <https://doi.org/10.1006/ofte.1996.0017>.
- [150] M. F. Guerra-Medina, O. Gonzalez, B. Rojas-Guillama, J. A. Martin-Gonzalez, F. Delgado, and J. Rabadan, "Ethernet-ocdma system for multi-user visible light communications", *Electronics Letters*, vol. 48, no. 4, pp. 227–228, Feb. 2012, ISSN: 0013-5194. DOI: [10.1049/el.2011.4035](https://doi.org/10.1049/el.2011.4035).
- [151] Y. Qiu, S. Chen, H. Chen, and W. Meng, "Visible light communications based on cdma technology", *IEEE Wireless Communications*, vol. 25, no. 2, pp. 178–185, Apr. 2018, ISSN: 1536-1284. DOI: [10.1109/MWC.2017.1700051](https://doi.org/10.1109/MWC.2017.1700051).

- [152] J. Dang and Z. Zhang, "Comparison of optical ofdm-idma and optical ofdma for uplink visible light communications", in *2012 International Conference on Wireless Communications and Signal Processing (WCSP)*, Oct. 2012, pp. 1–6. DOI: [10.1109/WCSP.2012.6542858](https://doi.org/10.1109/WCSP.2012.6542858).
- [153] M. Ergen, "Principles of ofdma", in *Mobile Broadband: Including WiMAX and LTE*. Boston, MA: Springer US, 2009, pp. 177–220, ISBN: 9780387681924. DOI: [10.1007/978-0-387-68192-4\\_5](https://doi.org/10.1007/978-0-387-68192-4_5). [Online]. Available: [https://doi.org/10.1007/978-0-387-68192-4\\_5](https://doi.org/10.1007/978-0-387-68192-4_5).
- [154] V. Arokiamary, *Cellular and Mobile Communications*. Technical Publications, 2009, ISBN: 9788184315851. [Online]. Available: <https://books.google.fr/books?id=0nDgbzMRcbwC>.
- [155] S.-M. Kim and H.-J. Lee, "Visible light communication based on space-division multiple access optical beamforming", *Chin. Opt. Lett.*, vol. 12, no. 12, pp. 120 601–120 601, Dec. 2014.
- [156] J. B. Carruther and J. M. Kahn, "Angle diversity for nondirected wireless infrared communication", *IEEE Transactions on Communications*, vol. 48, no. 6, pp. 960–969, Apr. 2000, ISSN: 0090-6778. DOI: [10.1109/26.848557](https://doi.org/10.1109/26.848557).
- [157] H. Elgala, R. Mesleh, and H. Haas, "Indoor optical wireless communication: Potential and state-of-the-art", *IEEE Communications Magazine*, vol. 49, no. 9, pp. 56–62, Sep. 2011, ISSN: 0163-6804. DOI: [10.1109/MCOM.2011.6011734](https://doi.org/10.1109/MCOM.2011.6011734).
- [158] S. M. R. Islam, M. Zeng, and O. A. Dobre, "Noma in 5g systems: Exciting possibilities for enhancing spectral efficiency", *CoRR*, vol. abs/1706.08215, 2017. arXiv: [1706.08215](https://arxiv.org/abs/1706.08215). [Online]. Available: <http://arxiv.org/abs/1706.08215>.
- [159] L. Dai, B. Wang, Y. Yuan, S. Han, C. I, and Z. Wang, "Non-orthogonal multiple access for 5g: Solutions, challenges, opportunities, and future research trends", *IEEE Communications Magazine*, vol. 53, no. 9, pp. 74–81, Sep. 2015, ISSN: 0163-6804. DOI: [10.1109/MCOM.2015.7263349](https://doi.org/10.1109/MCOM.2015.7263349).
- [160] S. M. R. Islam, N. Avazov, O. A. Dobre, and K. Kwak, "Power-domain non-orthogonal multiple access (noma) in 5g systems: Potentials and challenges", *IEEE Communications Surveys Tutorials*, vol. 19, no. 2, pp. 721–742, Apr. 2017, ISSN: 1553-877X. DOI: [10.1109/COMST.2016.2621116](https://doi.org/10.1109/COMST.2016.2621116).
- [161] J. Choi, "Noma: Principles and recent results", in *2017 International Symposium on Wireless Communication Systems (ISWCS)*, Aug. 2017, pp. 349–354. DOI: [10.1109/ISWCS.2017.8108138](https://doi.org/10.1109/ISWCS.2017.8108138).
- [162] Z. Ding, P. Fan, and H. V. Poor, "Impact of user pairing on 5g nonorthogonal multiple-access downlink transmissions", *IEEE Transactions on Vehicular Technology*, vol. 65, no. 8, pp. 6010–6023, Aug. 2016, ISSN: 0018-9545. DOI: [10.1109/TVT.2015.2480766](https://doi.org/10.1109/TVT.2015.2480766).
- [163] Y. Cai, Z. Qin, F. Cui, G. Y. Li, and J. A. McCann, "Modulation and multiple access for 5g networks", *IEEE Communications Surveys Tutorials*, vol. 20, no. 1, pp. 629–646, Jan. 2018, ISSN: 1553-877X. DOI: [10.1109/COMST.2017.2766698](https://doi.org/10.1109/COMST.2017.2766698).

- [164] R. Hoshyar, F. P. Wathan, and R. Tafazolli, “Novel low-density signature for synchronous cdma systems over awgn channel”, *IEEE Transactions on Signal Processing*, vol. 56, no. 4, pp. 1616–1626, Apr. 2008, ISSN: 1053-587X. DOI: [10.1109/TSP.2007.909320](https://doi.org/10.1109/TSP.2007.909320).
- [165] M. Al-Imari, P. Xiao, M. A. Imran, and R. Tafazolli, “Uplink non-orthogonal multiple access for 5g wireless networks”, in *2014 11th International Symposium on Wireless Communications Systems (ISWCS)*, Aug. 2014, pp. 781–785. DOI: [10.1109/ISWCS.2014.6933459](https://doi.org/10.1109/ISWCS.2014.6933459).
- [166] H. Nikopour and H. Baligh, “Sparse code multiple access”, in *2013 IEEE 24th Annual International Symposium on Personal, Indoor, and Mobile Radio Communications (PIMRC)*, Sep. 2013, pp. 332–336. DOI: [10.1109/PIMRC.2013.6666156](https://doi.org/10.1109/PIMRC.2013.6666156).
- [167] Z. Yuan, G. Yu, W. Li, Y. Yuan, X. Wang, and J. Xu, “Multi-user shared access for internet of things”, in *2016 IEEE 83rd Vehicular Technology Conference (VTC Spring)*, May 2016, pp. 1–5. DOI: [10.1109/VTCSpring.2016.7504361](https://doi.org/10.1109/VTCSpring.2016.7504361).
- [168] X. Dai, S. Chen, S. Sun, S. Kang, Y. Wang, Z. Shen, and J. Xu, “Successive interference cancelation amenable multiple access (sama) for future wireless communications”, in *2014 IEEE International Conference on Communication Systems*, Nov. 2014, pp. 222–226. DOI: [10.1109/ICCS.2014.7024798](https://doi.org/10.1109/ICCS.2014.7024798).
- [169] S. Chen, B. Ren, Q. Gao, S. Kang, S. Sun, and K. Niu, “Pattern division multiple access—a novel nonorthogonal multiple access for fifth-generation radio networks”, *IEEE Transactions on Vehicular Technology*, vol. 66, no. 4, pp. 3185–3196, Apr. 2017, ISSN: 0018-9545. DOI: [10.1109/TVT.2016.2596438](https://doi.org/10.1109/TVT.2016.2596438).
- [170] X. Chen, C. Liu, L. Nian, M. Cheng, S. Fu, M. Tang, D. Liu, and L. Deng, “Boma and ofdm/oqam modulation for a radio-over-fiber system with enhanced spectral efficiency”, *Opt. Lett.*, vol. 43, no. 20, pp. 4859–4862, Oct. 2018. DOI: [10.1364/OL.43.004859](https://doi.org/10.1364/OL.43.004859).
- [171] D. Fang, Y. Huang, Z. Ding, G. Geraci, S. Shieh, and H. Claussen, “Lattice partition multiple access: A new method of downlink non-orthogonal multiuser transmissions”, in *2016 IEEE Global Communications Conference (GLOBECOM)*, Dec. 2016, pp. 1–6. DOI: [10.1109/GLOCOM.2016.7841947](https://doi.org/10.1109/GLOCOM.2016.7841947).
- [172] A. Technologies and M. Rumney, *LTE and the Evolution to 4G Wireless: Design and Measurement Challenges*, 2nd. Wiley Publishing, 2013, ISBN: 1119962579, 9781119962571.
- [173] Q. H. Spencer, A. L. Swindlehurst, and M. Haardt, “Zero-forcing methods for downlink spatial multiplexing in multiuser mimo channels”, *IEEE Transactions on Signal Processing*, vol. 52, no. 2, pp. 461–471, Feb. 2004, ISSN: 1053-587X. DOI: [10.1109/TSP.2003.821107](https://doi.org/10.1109/TSP.2003.821107).
- [174] R. Zhang, “Cooperative multi-cell block diagonalization with per-base-station power constraints”, in *2010 IEEE Wireless Communication and Networking Conference*, Apr. 2010, pp. 1–6. DOI: [10.1109/WCNC.2010.5506527](https://doi.org/10.1109/WCNC.2010.5506527).

- [175] V. Nguyen, L. Tran, T. Q. Duong, O. Shin, and R. Farrell, “An efficient precoder design for multiuser mimo cognitive radio networks with interference constraints”, *IEEE Transactions on Vehicular Technology*, vol. 66, no. 5, pp. 3991–4004, May 2017, ISSN: 0018-9545. DOI: [10.1109/TVT.2016.2602844](https://doi.org/10.1109/TVT.2016.2602844).
- [176] H. Li, Z. Huang, Y. Xiao, S. Zhan, and Y. Ji, “A power and spectrum efficient noma scheme for vlc network based on hierarchical pre-distorted laco-ofdm”, *IEEE Access*, vol. 7, pp. 48 565–48 571, 2019, ISSN: 2169-3536. DOI: [10.1109/ACCESS.2019.2908524](https://doi.org/10.1109/ACCESS.2019.2908524).
- [177] D. Chen, J. Wang, H. Lu, L. Feng, and J. Jin, “Experimental demonstration of quasi-synchronous cdma-vlc systems employing a new ozcz code construction”, *Opt. Express*, vol. 27, no. 9, pp. 12 945–12 956, Apr. 2019. DOI: [10.1364/OE.27.012945](https://doi.org/10.1364/OE.27.012945).
- [178] B. Lin, X. Tang, and Z. Ghassemlooy, “Optical power domain noma for visible light communications”, *IEEE Wireless Communications Letters*, pp. 1–1, 2019, ISSN: 2162-2337. DOI: [10.1109/LWC.2019.2913830](https://doi.org/10.1109/LWC.2019.2913830).
- [179] C. Chen, W. Zhong, H. Yang, P. Du, and Y. Yang, “Flexible-rate sic-free noma for downlink vlc based on constellation partitioning coding”, *IEEE Wireless Communications Letters*, vol. 8, no. 2, pp. 568–571, Apr. 2019, ISSN: 2162-2337. DOI: [10.1109/LWC.2018.2879924](https://doi.org/10.1109/LWC.2018.2879924).
- [180] Y. Xiao, Z. Huang, and Y. Ji, “Multiple access with polarity division sparse code for visible light communication”, *IEEE Photonics Journal*, vol. 11, no. 1, pp. 1–10, Feb. 2019, ISSN: 1943-0655. DOI: [10.1109/JPHOT.2018.2889432](https://doi.org/10.1109/JPHOT.2018.2889432).
- [181] J. Shi, Y. Hong, J. He, R. Deng, and L. Chen, “Experimental demonstration of oqam-ofdm based mimo-noma over visible light communications”, in *2018 Optical Fiber Communications Conference and Exposition (OFC)*, Mar. 2018, pp. 1–3.
- [182] B. Lin, W. Ye, X. Tang, and Z. Ghassemlooy, “Experimental demonstration of bidirectional noma-ofdma visible light communications”, *Opt. Express*, vol. 25, no. 4, pp. 4348–4355, Feb. 2017. DOI: [10.1364/OE.25.004348](https://doi.org/10.1364/OE.25.004348).
- [183] X. Lu, K. Wang, L. Qiao, W. Zhou, Y. Wang, and N. Chi, “Nonlinear compensation of multi-cap vlc system employing clustering algorithm based perception decision”, *IEEE Photonics Journal*, vol. 9, no. 5, pp. 1–9, Oct. 2017, ISSN: 1943-0655. DOI: [10.1109/JPHOT.2017.2748153](https://doi.org/10.1109/JPHOT.2017.2748153).
- [184] J.-Y. Sung, C.-H. Yeh, C.-W. Chow, W.-F. Lin, and Y. Liu, “Orthogonal frequency-division multiplexing access (ofdma) based wireless visible light communication (vlc) system”, *Optics Communications*, vol. 355, pp. 261 –268, 2015, ISSN: 0030-4018. DOI: <https://doi.org/10.1016/j.optcom.2015.06.070>.
- [185] C. Yang, Y. Wang, Y. Wang, X. Huang, and N. Chi, “Demonstration of high-speed multi-user multi-carrier cdma visible light communication”, *Optics Communications*, vol. 336, pp. 269 –272, 2015, ISSN: 0030-4018. DOI: <https://doi.org/10.1016/j.optcom.2014.09.072>.

- [186] O. González, M. F. Guerra-Medina, I. R. Martín, F. Delgado, and R. Pérez-Jiménez, “Adaptive whts-assisted sdma-ofdm scheme for fair resource allocation in multi-user visible light communications”, *IEEE/OSA Journal of Optical Communications and Networking*, vol. 8, no. 6, pp. 427–440, Jun. 2016, ISSN: 1943-0620. DOI: [10.1364/JOCN.8.000427](https://doi.org/10.1364/JOCN.8.000427).
- [187] J. Lian and M. Brandt-Pearce, “Multiuser mimo indoor visible light communication system using spatial multiplexing”, *Journal of Lightwave Technology*, vol. 35, no. 23, pp. 5024–5033, Dec. 2017, ISSN: 0733-8724. DOI: [10.1109/JLT.2017.2765462](https://doi.org/10.1109/JLT.2017.2765462).
- [188] C. Chen, W. Zhong, H. Yang, and P. Du, “On the performance of mimonoma-based visible light communication systems”, *IEEE Photonics Technology Letters*, vol. 30, no. 4, pp. 307–310, Feb. 2018, ISSN: 1041-1135. DOI: [10.1109/LPT.2017.2785964](https://doi.org/10.1109/LPT.2017.2785964).
- [189] D. C. O’Brien, L. Zeng, H. Le-Minh, G. Faulkner, J. W. Walewski, and S. Randel, “Visible light communications: Challenges and possibilities”, in *2008 IEEE 19th International Symposium on Personal, Indoor and Mobile Radio Communications*, Sep. 2008, pp. 1–5. DOI: [10.1109/PIMRC.2008.4699964](https://doi.org/10.1109/PIMRC.2008.4699964).
- [190] Hoa Le Minh, D. O’Brien, G. Faulkner, L. Zeng, Kyungwoo Lee, Daekwang Jung, and YunJe Oh, “80 mbit/s visible light communications using pre-equalized white led”, in *2008 34th European Conference on Optical Communication*, Sep. 2008, pp. 1–2. DOI: [10.1109/ECOC.2008.4729532](https://doi.org/10.1109/ECOC.2008.4729532).
- [191] J. Grubor, S. Randel, K. Langer, and J. W. Walewski, “Bandwidth-efficient indoor optical wireless communications with white light-emitting diodes”, in *2008 6th International Symposium on Communication Systems, Networks and Digital Signal Processing*, Jul. 2008, pp. 165–169. DOI: [10.1109/CSNDSP.2008.4610769](https://doi.org/10.1109/CSNDSP.2008.4610769).
- [192] C. Kottke, J. Hilt, K. Habel, J. Vučić, and K. Langer, “1.25 gbit/s visible light wdm link based on dmt modulation of a single rgb led luminary”, in *2012 38th European Conference and Exhibition on Optical Communications*, Sep. 2012, pp. 1–3. DOI: [10.1364/ECEOC.2012.We.3.B.4](https://doi.org/10.1364/ECEOC.2012.We.3.B.4).
- [193] O. O. Oyerinde and S. H. Mneney, “Review of channel estimation for wireless communication systems”, *IETE Technical Review*, vol. 29, no. 4, pp. 282–298, 2012. DOI: [10.4103/0256-4602.101308](https://doi.org/10.4103/0256-4602.101308).
- [194] X. Chen and M. Jiang, “Adaptive statistical bayesian mmse channel estimation for visible light communication”, *IEEE Transactions on Signal Processing*, vol. 65, no. 5, pp. 1287–1299, Mar. 2017, ISSN: 1053-587X. DOI: [10.1109/TSP.2016.2630036](https://doi.org/10.1109/TSP.2016.2630036).
- [195] X. Huang, J. Shi, J. Li, Y. Wang, and N. Chi, “A gb/s vlc transmission using hardware preequalization circuit”, *IEEE Photonics Technology Letters*, vol. 27, no. 18, pp. 1915–1918, Sep. 2015, ISSN: 1041-1135. DOI: [10.1109/LPT.2015.2445781](https://doi.org/10.1109/LPT.2015.2445781).

- [196] I. Stefan, H. Elgala, R. Mesleh, D. O'Brien, and H. Haas, "Optical wireless ofdm system on fpga: Study of led nonlinearity effects", in *2011 IEEE 73rd Vehicular Technology Conference (VTC Spring)*, May 2011, pp. 1–5. DOI: [10.1109/VETECS.2011.5956691](https://doi.org/10.1109/VETECS.2011.5956691).
- [197] I. Neokosmidis, T. Kamalakis, J. W. Walewski, B. Inan, and T. Sphicopoulos, "Impact of nonlinear led transfer function on discrete multitone modulation: Analytical approach", *Journal of Lightwave Technology*, vol. 27, no. 22, pp. 4970–4978, Nov. 2009, ISSN: 0733-8724. DOI: [10.1109/JLT.2009.2028903](https://doi.org/10.1109/JLT.2009.2028903).
- [198] H. Elgala, R. Mesleh, and H. Haas, "An led model for intensity-modulated optical communication systems", *IEEE Photonics Technology Letters*, vol. 22, no. 11, pp. 835–837, Apr. 2010, ISSN: 1041-1135. DOI: [10.1109/LPT.2010.2046157](https://doi.org/10.1109/LPT.2010.2046157).
- [199] A. A. Sharifi, "Papr reduction of optical ofdm signals in visible light communications", *ICT Express*, 2019, ISSN: 2405-9595. DOI: <https://doi.org/10.1016/j.icte.2019.01.001>.
- [200] H. Elgala, R. Mesleh, and H. Haas, "Predistortion in optical wireless transmission using ofdm", in *2009 Ninth International Conference on Hybrid Intelligent Systems*, vol. 2, Aug. 2009, pp. 184–189. DOI: [10.1109/HIS.2009.321](https://doi.org/10.1109/HIS.2009.321).
- [201] H. Qian, S. J. Yao, S. Z. Cai, and T. Zhou, "Adaptive postdistortion for nonlinear leds in visible light communications", *IEEE Photonics Journal*, vol. 6, no. 4, pp. 1–8, Aug. 2014, ISSN: 1943-0655. DOI: [10.1109/JPHOT.2014.2331242](https://doi.org/10.1109/JPHOT.2014.2331242).
- [202] M. Khalighi, S. Long, S. Bourennane, and Z. Ghassemlooy, "Pam- and cap-based transmission schemes for visible-light communications", *IEEE Access*, vol. 5, pp. 27 002–27 013, 2017, ISSN: 2169-3536. DOI: [10.1109/ACCESS.2017.2765181](https://doi.org/10.1109/ACCESS.2017.2765181).
- [203] M. Noshad and M. Brandt-Pearce, "Hadamard-coded modulation for visible light communications", *IEEE Transactions on Communications*, vol. 64, no. 3, pp. 1167–1175, Mar. 2016, ISSN: 0090-6778. DOI: [10.1109/TCOMM.2016.2520471](https://doi.org/10.1109/TCOMM.2016.2520471).
- [204] J. G. Proakis, *Digital Communications*, 3rd. McGraw-Hill, 1995.
- [205] A. H. Abdolhamid and D. A. Johns, "A comparison of cap/qam architectures", in *ISCAS '98. Proceedings of the 1998 IEEE International Symposium on Circuits and Systems (Cat. No.98CH36187)*, vol. 4, May 1998, 316–316/3 vol.4. DOI: [10.1109/ISCAS.1998.698823](https://doi.org/10.1109/ISCAS.1998.698823).
- [206] F. Sjöberg, "A vdsl tutorial", Lulea tekniska universitet, Tech. Rep. 2000:02, 2000, Godkänd; 2000; 20070912 (margjo), p. 62.
- [207] I. W. Selesnick, "The design of approximate hilbert transform pairs of wavelet bases", *IEEE Transactions on Signal Processing*, vol. 50, no. 5, pp. 1144–1152, May 2002, ISSN: 1053-587X. DOI: [10.1109/78.995070](https://doi.org/10.1109/78.995070).
- [208] U. Mengali, *Synchronization Techniques for Digital Receivers*, ser. Applications of Communications Theory. Springer US, 1997, ISBN: 9780306457258. [Online]. Available: <https://books.google.fr/books?id=89Gscsw7PvoC>.

- [209] P. Chvojka, P. A. Haigh, S. Zvanovec, P. Pesek, and Z. Ghassemlooy, "Evaluation of multi-band carrier-less amplitude and phase modulation performance for vlc under various pulse shaping filter parameters", in *Proceedings of the 13th International Joint Conference on e-Business and Telecommunications*, ser. ICETE 2016, Lisbon, Portugal: SCITEPRESS - Science and Technology Publications, Lda, 2016, pp. 25–31, ISBN: 978-989-758-196-0. DOI: [10.5220/0005956900250031](https://doi.org/10.5220/0005956900250031).
- [210] S. Long, M. A. Khalighi, M. Wolf, S. Bourennane, and Z. Ghassemlooy, "Investigating channel frequency selectivity in indoor visible-light communication systems", *IET Optoelectronics*, vol. 10, no. 3, pp. 80–88, 2016, ISSN: 1751-8768. DOI: [10.1049/iet-opt.2015.0015](https://doi.org/10.1049/iet-opt.2015.0015).
- [211] "Low-timing-sensitivity waveform design for carrierless amplitude and phase modulation in visible light communications", English, *IET Optoelectronics*, vol. 9, 317–324(7), 6 Dec. 2015, ISSN: 1751-8768.
- [212] K. O. Akande and W. O. Popoola, "Impact of timing jitter on the performance of carrier amplitude and phase modulation", in *2016 International Conference for Students on Applied Engineering (ICSAE)*, Oct. 2016, pp. 259–263. DOI: [10.1109/ICSAE.2016.7810199](https://doi.org/10.1109/ICSAE.2016.7810199).
- [213] G. Keiser, "Optical fiber communications", in *Wiley Encyclopedia of Telecommunications*. American Cancer Society, 2003, ISBN: 9780471219286. DOI: [10.1002/0471219282.eot158](https://doi.org/10.1002/0471219282.eot158).
- [214] R. Hui, B. Zhu, R. Huang, C. T. Allen, K. R. Demarest, and D. Richards, "Subcarrier multiplexing for high-speed optical transmission", *J. Lightwave Technol.*, vol. 20, no. 3, p. 417, Mar. 2002.
- [215] *Analogue Optical Fibre Communications*, ser. Telecommunications. Institution of Engineering and Technology, 1995.
- [216] K. Fazel and S Kaiser, "Multi-carrier and spread spectrum systems", in. Jan. 2003, pp. 1–298, ISBN: 0-470-84899-5. DOI: [10.1002/0470871385](https://doi.org/10.1002/0470871385).
- [217] J F Weng, G Q Xue, T. Le-Ngoc, and S. Tahar, "Frequency hopping cdma: A review", Apr. 2019.
- [218] Y. Saito, Y. Kishiyama, A. Benjebbour, T. Nakamura, A. Li, and K. Higuchi, "Non-orthogonal multiple access (noma) for cellular future radio access", in *2013 IEEE 77th Vehicular Technology Conference (VTC Spring)*, Apr. 2013, pp. 1–5. DOI: [10.1109/VTCSpring.2013.6692652](https://doi.org/10.1109/VTCSpring.2013.6692652).
- [219] S. Vanka, S. Srinivasa, Z. Gong, P. Vizi, K. Stamatiou, and M. Haenggi, "Superposition coding strategies: Design and experimental evaluation", *IEEE Transactions on Wireless Communications*, vol. 11, no. 7, pp. 2628–2639, Jul. 2012, ISSN: 1536-1276.
- [220] Z. Chen and H. Haas, "Space division multiple access in visible light communications", in *2015 IEEE International Conference on Communications (ICC)*, IEEE, Jun. 2015. DOI: [10.1109/icc.2015.7249135](https://doi.org/10.1109/icc.2015.7249135).

- [221] F. M. Wu, C. T. Lin, C. C. Wei, C. W. Chen, Z. Y. Chen, H. T. Huang, and S. Chi, "Performance comparison of ofdm signal and cap signal over high capacity rgb-led-based wdm visible light communication", *IEEE Photonics Journal*, vol. 5, no. 4, pp. 7 901 507–7 901 507, Aug. 2013, ISSN: 1943-0655. DOI: [10.1109/JPHOT.2013.2271637](https://doi.org/10.1109/JPHOT.2013.2271637).
- [222] T. Komine, S. Haruyama, and M. Nakagawa, "Bi-directional visible-light communication using corner cube modulator", English, in *Proceedings of the IASTED International Conference on Wireless and Optical Communications*, L. Hesselink, Ed., vol. 3, 2003, pp. 598–603, ISBN: 0889863741.
- [223] X. Jin, B. A. Hristovski, C. M. Collier, S. Geoffroy-Gagnon, B. Born, and J. F. Holzman, "Spherical transceivers for ultrafast optical wireless communications", vol. 9744, 2016. DOI: [10.1117/12.2208343](https://doi.org/10.1117/12.2208343).
- [224] M. Vladescu and D. T. Vuza, "Redundant uplink optical channel for visible light communication systems", vol. 9258, 2015. DOI: [10.1117/12.2070632](https://doi.org/10.1117/12.2070632).
- [225] K. Cui, G. Chen, Q. He, and Z. Xu, "Indoor optical wireless communication by ultraviolet and visible light", vol. 7464, 2009. DOI: [10.1117/12.826312](https://doi.org/10.1117/12.826312).
- [226] V. Mathuranathan and M. Viswanathan, *Digital Modulations Using Matlab: Build Simulation Models from Scratch*. Amazon Digital Services LLC - Kdp Print Us, 2017, ISBN: 9781521493885. [Online]. Available: <https://books.google.fr/books?id=gCTjtAEACAAJ>.
- [227] F. Gray, *Pulse code communications*, U.S. Patent 2 632 058, Mar. 1953.
- [228] Y. Wang, L. Tao, Y. Wang, and N. Chi, "High speed wdm vlc system based on multi-band cap64 with weighted pre-equalization and modified cmma based post-equalization", *IEEE Communications Letters*, vol. 18, no. 10, pp. 1719–1722, Oct. 2014, ISSN: 1089-7798. DOI: [10.1109/LCOMM.2014.2349990](https://doi.org/10.1109/LCOMM.2014.2349990).
- [229] K. Okokpujie and O. Obinna, "Comparative analysis of channel estimation techniques in siso, miso and mimo systems", *International Journal of Electronics and Telecommunications*, vol. 63, pp. 299–304, Aug. 2017. DOI: [10.1515/elete1-2017-0040](https://doi.org/10.1515/elete1-2017-0040).
- [230] I. Guvenc, S. Gezici, Z. Sahinoglu, and U. C. Kozat, *Reliable Communications for Short-Range Wireless Systems*, 1st. New York, NY, USA: Cambridge University Press, 2011, ISBN: 0521763177, 9780521763172.
- [231] Y. S. Hussein, M. Y. Alias, and A. A. Abdulkafi, "On performance analysis of ls and mmse for channel estimation in vlc systems", in *2016 IEEE 12th International Colloquium on Signal Processing Its Applications (CSPA)*, Mar. 2016, pp. 204–209. DOI: [10.1109/CSPA.2016.7515832](https://doi.org/10.1109/CSPA.2016.7515832).
- [232] J. G. Proakis, M. Salehi, N. Zhou, and X. Li, *Communication systems engineering vol. 1*, Prentice-hall Englewood Cliffs, 1994.
- [233] S. Sun, K. Adachi, P. H. Tan, Y. Zhou, J. Joung, and C. K. Ho, "Heterogeneous network: An evolutionary path to 5g", in *2015 21st Asia-Pacific Conference on Communications (APCC)*, Oct. 2015, pp. 174–178. DOI: [10.1109/APCC.2015.7412506](https://doi.org/10.1109/APCC.2015.7412506).

- [234] R. Ghosh and K. Lerman, "Structure of heterogeneous networks", in *2009 International Conference on Computational Science and Engineering*, vol. 4, Aug. 2009, pp. 98–105. DOI: [10.1109/CSE.2009.142](https://doi.org/10.1109/CSE.2009.142).
- [235] V. Chandrasekhar, J. G. Andrews, and A. Gatherer, "Femtocell networks: A survey", *IEEE Communications Magazine*, vol. 46, no. 9, pp. 59–67, Sep. 2008, ISSN: 0163-6804. DOI: [10.1109/MCOM.2008.4623708](https://doi.org/10.1109/MCOM.2008.4623708).
- [236] H. Haas, "High-speed wireless networking using visible light", *SPIE Newsroom*, Apr. 2013. DOI: [10.1117/2.1201304.004773](https://doi.org/10.1117/2.1201304.004773).
- [237] Thorlabs, *Pda10a-ec si fixed gain detector*, <https://www.thorlabs.com/thorproduct.cfm?partnum=EC>.
- [238] C. Li and Q. Yang, "Optical ofdm/oqam for the future fiber-optics communications", *Procedia Engineering*, vol. 140, pp. 99–106, 2016, International Conference on Materials for Advanced Technologies (ICMAT2015) – 4th Photonics Global Conference 2015, ISSN: 1877-7058. DOI: <https://doi.org/10.1016/j.proeng.2015.09.238>.
- [239] A.-R., "Analytical study of signal-to-noise ratio for visible light communication by using single source", *Journal of Computer Science*, vol. 8, pp. 141–144, Jan. 2012. DOI: [10.3844/jcssp.2012.141.144](https://doi.org/10.3844/jcssp.2012.141.144).
- [240] Y. Otani, S. Ohno, K. a. Donny Teo, and T. Hinamoto, "Subcarrier allocation for multi-user ofdm system", in *2005 Asia-Pacific Conference on Communications*, Oct. 2005, pp. 1073–1077. DOI: [10.1109/APCC.2005.1554229](https://doi.org/10.1109/APCC.2005.1554229).
- [241] Y. Saito, Y. Kishiyama, A. Benjebbour, T. Nakamura, A. Li, and K. Higuchi, "Non-orthogonal multiple access (noma) for cellular future radio access", in *2013 IEEE 77th Vehicular Technology Conference (VTC Spring)*, Apr. 2013, pp. 1–5. DOI: [10.1109/VTCSpring.2013.6692652](https://doi.org/10.1109/VTCSpring.2013.6692652).
- [242] P. H. Pathak, X. Feng, P. Hu, and P. Mohapatra, "Visible light communication, networking, and sensing: A survey, potential and challenges", *IEEE Communications Surveys Tutorials*, vol. 17, no. 4, pp. 2047–2077, Oct. 2015, ISSN: 1553-877X. DOI: [10.1109/COMST.2015.2476474](https://doi.org/10.1109/COMST.2015.2476474).
- [243] Y. Wang, L. Tao, Y. Wang, and N. Chi, "High speed wdm vlc system based on multi-band cap64 with weighted pre-equalization and modified cmma based post-equalization", *IEEE Communications Letters*, vol. 18, no. 10, pp. 1719–1722, Oct. 2014, ISSN: 1089-7798.
- [244] P. A. Haigh, S. T. Le, S. Zvanovec, Z. Ghassemlooy, P. Luo, T. Xu, P. Chvojka, T. Kanesan, E. Giacomidis, P. Canyelles-Pericas, H. L. Minh, W. Popoola, S. Rajbhandari, I. Papakonstantinou, and I. Darwazeh, "Multi-band carrier-less amplitude and phase modulation for bandlimited visible light communications systems", *IEEE Wireless Communications*, vol. 22, no. 2, pp. 46–53, Apr. 2015, ISSN: 1536-1284. DOI: [10.1109/MWC.2015.7096284](https://doi.org/10.1109/MWC.2015.7096284).
- [245] P. A. Haigh, A. Burton, K. Werfli, H. L. Minh, E. Bentley, P. Chvojka, W. O. Popoola, I. Papakonstantinou, and S. Zvanovec, "A multi-cap visible-light communications system with 4.85-b/s/hz spectral efficiency", *IEEE Journal*

- on Selected Areas in Communications*, vol. 33, no. 9, pp. 1771–1779, Sep. 2015, ISSN: 0733-8716.
- [246] M. I. Olmedo, T. Zuo, J. B. Jensen, Q. Zhong, X. Xu, S. Popov, and I. T. Monroy, “Multiband carrierless amplitude phase modulation for high capacity optical data links”, *Journal of Lightwave Technology*, vol. 32, no. 4, pp. 798–804, Feb. 2014, ISSN: 0733-8724. DOI: [10.1109/JLT.2013.2284926](https://doi.org/10.1109/JLT.2013.2284926).
- [247] Z. Ghassemlooy, W. Popoola, and S. Rajbhandari, *Optical Wireless Communications: System and Channel Modelling with MATLAB*, 1st. Boca Raton, FL, USA: CRC Press, Inc., 2012, ISBN: 1439851883, 9781439851883.
- [248] S. Arnon, *Visible Light Communication*, 1st. New York, NY, USA: Cambridge University Press, 2015, ISBN: 1107061555, 9781107061552.
- [249] S. V. S. Srivastava D. Behera and S. Tiwari, *Eye diagram basics: Reading and applying eye diagrams*, 2011.
- [250] R. A. Shafik, M. S. Rahman, and A. R. Islam, “On the extended relationships among evm, ber and snr as performance metrics”, in *2006 International Conference on Electrical and Computer Engineering*, Dec. 2006, pp. 408–411. DOI: [10.1109/ICECE.2006.355657](https://doi.org/10.1109/ICECE.2006.355657).
- [251] M. D Mckinley, K. A Remley, M. Myslinski, J Stevenson Kenney, D. Schreurs, and B. Nauwelaers, “Evm calculation for broadband modulated signals”, Jan. 2004.
- [252] Xingxing Huang, Jianyang Shi, Jiehui Li, Yiguang Wang, Yuanquan Wang, and Nan Chi, “750mbit/s visible light communications employing 64qam-ofdm based on amplitude equalization circuit”, in *2015 Optical Fiber Communications Conference and Exhibition (OFC)*, Mar. 2015, pp. 1–3.
- [253] J. Grubor, S. Randel, K. Langer, and J. W. Walewski, “Broadband information broadcasting using led-based interior lighting”, *Journal of Lightwave Technology*, vol. 26, no. 24, pp. 3883–3892, Dec. 2008, ISSN: 0733-8724. DOI: [10.1109/JLT.2008.928525](https://doi.org/10.1109/JLT.2008.928525).
- [254] T. Komine and M. Nakagawa, “Fundamental analysis for visible-light communication system using led lights”, *IEEE Transactions on Consumer Electronics*, vol. 50, no. 1, pp. 100–107, Feb. 2004, ISSN: 0098-3063. DOI: [10.1109/TCE.2004.1277847](https://doi.org/10.1109/TCE.2004.1277847).
- [255] F. R. Gfeller and U. Bapst, “Wireless in-house data communication via diffuse infrared radiation”, *Proceedings of the IEEE*, vol. 67, no. 11, pp. 1474–1486, Nov. 1979, ISSN: 0018-9219. DOI: [10.1109/PROC.1979.11508](https://doi.org/10.1109/PROC.1979.11508).
- [256] O. Bouchet, *Wireless Optical Communications*, ser. ISTE. Wiley, 2013, ISBN: 9781118563274. [Online]. Available: <https://books.google.fr/books?id=HBFSt4064VgC>.
- [257] R. Dudeja, *Pearson Guide To Objective Physics For Iit-Jee*. Dorling Kindersley (india) Pvt Limited, 2007, ISBN: 9788131700259. [Online]. Available: <https://books.google.fr/books?id=5Bq19o21yv0C>.

- 
- [258] A. Al-Kinani, C. Wang, H. Haas, and Y. Yang, “Characterization and modeling of visible light communication channels”, in *2016 IEEE 83rd Vehicular Technology Conference (VTC Spring)*, May 2016, pp. 1–5. DOI: [10.1109/VTCSpring.2016.7504160](https://doi.org/10.1109/VTCSpring.2016.7504160).
- [259] Z. Ghassemlooy, W. Popoola, and S. Rajbhandari, *Optical Wireless Communications: System and Channel Modelling with MATLAB*. Aug. 2012, ISBN: 978-4398-5188-3. DOI: [10.1201/b12687](https://doi.org/10.1201/b12687).

## Appendix A

# Components Impacts Breakdown

### A.1 Transmitter Hardware and Optics

The transmitter hardware is composed of the LED emitter and the components used to adapt it to the modulated output coming from the digital to analog converter. Usually, they are composed of an electrical amplifier and a bias-tee to pilot the LED. In general, these components do not impact the performances when chosen correctly, they just allow the LED to be used optimally. However, the later has a considerable impact on the final characteristics of a VLC system [253]. The half-intensity radiation angle is a parameter of practical importance. It determines the area in a room that will be illuminated by the LED and thus, with a large angle, less LEDs are necessary to illuminate a room, lowering a VLC system complexity. With a lower angle and the same optical power, the SNR will be higher as the beam of light will be more concentrated. This is a scenario found in SDMA where the transmitter is composed of multiple narrow FOV LEDs. The luminous intensity and optical power are key components which will determine the received power at the receiver side and thus determine the performances of the system since it impacts the SNR tremendously. Finally, a LED has a limited bandwidth and adds a low-pass effect to the channel. Thus, it impacts the modulation speed that can be used and the throughput that can be attained [254].

The function of the LED, as an optical transmitter, is to convert the modulated electrical signal into a modulated optical signal. A LED lamp in a VLC system usually follows a generalized Lambertian radiation pattern, given by [255]:

$$R(\alpha^T) = \frac{m+1}{2\pi} \cos^m(\alpha^T), \quad \alpha^T \in \left[-\frac{\pi}{2} : \frac{\pi}{2}\right] \quad (\text{A.1})$$

With  $\alpha^T$  the angle of irradiance,  $m$  the mode number of the radiation lobe which describes the directionality of the source and is calculated via:

$$m = -\frac{0.693}{\ln(\cos(HP))} \quad (\text{A.2})$$

Where  $HP$  is the half power emission angle of the LED. Most LEDs have a HP equal to  $60^\circ$  and  $m$  equal to 1 [256]. Luminous intensity of an optical source is defined as the luminous flux per unit of solid angle in a given direction. LEDs present a generalized Lambertian radiation pattern and thus the luminous intensity is given as [257]

$$I(\alpha^T) = I(0)R(\alpha^T) \quad (\text{A.3})$$

Where  $I(0)$  is the center luminous intensity of a LED which is provided by manufacturers.  $I(\alpha^T)$  is the luminous intensity, in unit of candela (cd).

The phosphorus white LED model is described hereafter. The electrical driving signal  $i_{LED}(t)$  passes through the blue chip and generates blue light. The generation of which is described by an impulse response  $h_b(t)$  (or frequency response  $H_b(f)$ ). Then, some part of this light is emitted directly, and some is captured by the phosphorescent layer and converted to longer wavelength. The response of phosphorous layer is denoted as  $h_y(t)$  (or  $H_y(f)$ ). The whole process can be described [258]:

$$i_{PD} \propto i_{LED} \otimes [G_b h_b + G_y h_y] \quad (\text{A.4})$$

With  $G_b$  the equivalent gain of the blue component,  $G_y$  the equivalent gain of the yellow component,  $i_{LED}$  the modulating current of the LED and  $i_{PD}$  the received PD current. The impulse response of the blue LED can be described by a decaying exponential function:

$$h_b(t) = u(t) \exp\left(-\frac{t}{\tau_b}\right) \quad (\text{A.5})$$

With  $u(t)$  a unit step and  $\tau_b$  a time constant. The same equation can be used for  $h_y$  by replacing  $\tau_b$  with  $\tau_y$ . The model has 4 independent parameters depending on LED manufacturer and type ( $\tau_{b/y}$  and  $G_{b/y}$ ).  $G_{b/y}$  can be calculated by taking into account the LED emission spectrum and the responsivity of the photodiode. The LED emission spectrum is the sum of 2 components (blue and yellow):  $S(\lambda) = S_b(\lambda) + S_y(\lambda)$ .

Thus, a low-pass model is used to define a ph-based white LED. The cut-off frequency is defined with  $\tau_b$  and  $\tau_y$ , which can be measured experimentally if a specific LED needs to be modeled. The frequency is usually measured around a few MHz for a phosphor-based LED.

Figure A.1 (a) has been obtained with the following simulation characteristics:

A low-pass model is used to define a ph-based white LED. The cut-off frequency is defined with  $\tau_b$  and  $\tau_y$ , which are measured experimentally on the LED referenced by

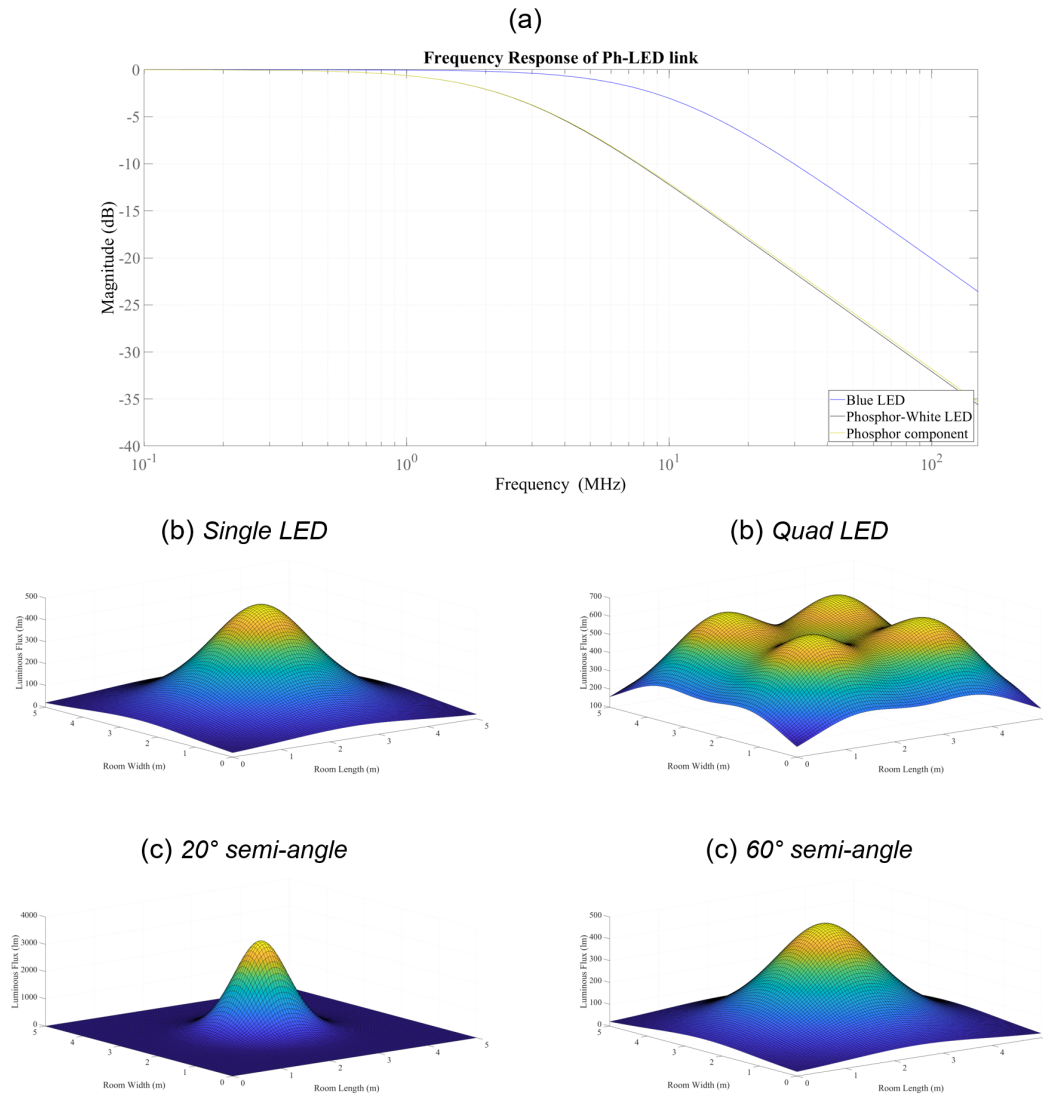


FIGURE A.1: (a) Simulated bode diagram for a white and blue LED model, (b) Simulated optical power received for different transmitter configuration. (c) Simulated luminous flux emitted in three-dimension in a  $5 \times 5 \times 3 \text{ m}^3$  room for a transmitter with a 20-degree semi-angle at half power (left) and 60-degree semi-angle (right).

TABLE A.1: Simulation parameters for figure A.1 (a). The values were obtained with measures on a commercially available white LED.

Parameter	Value
LED reference	OSRAM LE UW Q9WP
$\tau_{blue}$	16 ns
$\tau_{yellow}$	62 ns
Power coefficient of the blue component	0.25
Power coefficient of the yellow component	0.75

table A.1. As shown by figure A.1 (a), the transmitter total -3dB cutoff frequency is, in this case, 2.54 MHz which is approximately the same as for the phosphor component. As expected, the blue component is faster, with a cutoff frequency at 9.95 MHz, almost four times faster. This characteristic of the ph-based white LED is a good support for the potential of a blue light filter at the receiver, in order to remove this component and only retain the faster component for a potential in performance enhancement.

Other than its frequency response, one of the LED most important parameter is its illumination traits. Indeed, the optical power generated, and the pattern of illumination are important attributes that need to be evaluated for a performance estimation. Figure A.1 (b) describes the luminous flux emitted by a LED setup in an indoor room and has been obtained with the following simulation characteristics:

TABLE A.2: Simulation parameters for figure A.1 (b) and (c).

Parameter	Value
Room size	5x5x3 m <sup>3</sup>
Location (1 LED)	(2.5, 2.5, 3)
Location (4 LEDs)	(1.25, 3.75, 3), (3.75, 1.25, 3), (3.75, 3.75, 3), (1.25, 1.25, 3)
LED semi-angle at half power	65°
Transmitted power	1.83 W
Receiver plane above the floor	0.85 m

As seen in the figure and described by table A.2, two transmitter setups are used, one with 4 LEDs on the ceiling and another one with a single LED. The luminous flux is the measure of the perceived power of light and is adjusted to reflect the varying sensitivity of the human eye. Here, the coverage of the room by a 4 LED setup is obviously larger and attain a maximum of 637 lm under each of the LED while the single LED setup attain a maximum of 497 lm at the center of the room. This is due to the neighboring effect of the other LEDs. The result in illumination through the room depends on how the LED is driven, at what current and voltage, as well as the wavelength characteristics of it. Finally, another parameter inherent to the transmitter impacts the performances as well, the semi-angle at half power.

Figure A.1 (c) illustrate two beams obtained at different semi-angle and their luminous flux. The same characteristics as described in Table A.2 are used here as well. The tighter beam uses a value of 20° and the larger one 60°. As expected, the tighter beam concentrates its luminous flux a lot more with a maximum of 3343.7 lm directly under the LED but 0 lm is attained in the majority of the room. On the other hand, the 60° beam obtains a luminous flux of only 550.7 lm under the LED but illuminate the whole room with at least 19.4 lm. With the main characteristics of the LED covered, the next hardware element analyzed is the receiver.

## A.2 Receiver Hardware and Optics

A.2 Receiver hardware and optics The receiver hardware block is usually composed of a lens, a photodiode (PD) and a transimpedance amplifier (TIA). The first one concentrates the light received into the photodiode and thus directly increases the received optical power at the photodiode and enhances the FOV. The PD and TIA work in pair to transform the optical signal into a voltage. The responsivity of the PD determines how the incident light power is transformed into a photocurrent and the TIA gain determines the transformation of this current into a voltage. The system also has a bandwidth but is almost always higher than that of the LED. The sensitivity of the PD also impacts the results as it will be more or less sensitive depending on the optical signal wavelength.

The modulated light signal that contains the information is collected and converted into an electrical current.

At the receiving side, the PD is modelled as active area  $A_R$  collecting the radiation incident at angle  $\alpha^R$  smaller than the PD Field-of-View (FoV). Only rays that incident within receiver FoV will be captured. The wireless optical channel gain at the receiving side is proportional to the square of the distance between the optical source and the PD (the inverse square law), and to the effective collection area of the PD  $A_{R_{eff}}$ , which is given as:

$$A_{R_{eff}} = A_R \cos(\alpha^R) \text{ when } 0 \leq \alpha^R \leq FoV \quad A_{R_{eff}} = 0 \text{ when } \alpha^R > FoV \quad (\text{A.6})$$

The receiver model for a phosphorus white LED model is described hereafter. The photodiode responsivity for blue and yellow component is:

$$R_{b/y}(t) = \frac{1}{P_\omega} \int_0^\infty S_{b/y}(\lambda) R(\lambda) d\lambda \quad (\text{A.7})$$

With  $S_{b/y}(\lambda)$  the spectrum of either one of the blue or yellow component,  $R(\lambda)$  the wavelength-dependent responsivity of the PD and  $P_\omega$  the power calculated from the emission spectrum, given by:

$$P_\omega = \int_{380nm}^{720nm} S(\lambda) d\lambda \quad (\text{A.8})$$

The responsivity of the photodiode is separated into the blue component and the yellow component.

$$R_{eff} = R_b + R_y \quad (\text{A.9})$$

The power gain coefficients are:

$$G_{b/y} = P \frac{R_{b/y}}{R_{eff}} \quad (\text{A.10})$$

With  $P$  the power of optical signal incident on the photodiode. Performance of VLC system can be defined as a function of illuminance. For power budget calculations, it is more useful to know the optical power incident on the photodiode.  $V(\lambda)$  is the sensitivity function of the human eye, the luminous flux is:

$$\Phi = 683 \frac{\text{lm}}{\text{W}} \int_{380\text{nm}}^{720\text{nm}} S(\lambda) V(\lambda) d\lambda \quad (\text{A.11})$$

The total power of the white spectrum is  $P_\omega$ . The conversion factor can be calculated as  $P_\omega/\Phi$ . Power of the optical signal incident on the photodetector then is:

$$P = \frac{P_\omega}{\Phi} E_v A \quad (\text{A.12})$$

With  $E_v$  the illuminance in lux (lx) and  $A$  the photodetector area.

Thus, the photodiode and the lens are modeled by constants representing a gain. The value depends on the manufacturer's data and the wavelength of the LED used as the emitter.

At the receiver, the optical power received by the combination of the optical filter, the lens and the photodiode is a representation of the potential performances of a setup. Figure A.2 is an example of the received power in dBm when an optical concentrator, or lens, is used (a) or not (b). The simulation parameters used to obtain these figures is described as follows:

TABLE A.3: Simulation parameter used to obtain the received optical power in figure A.2.

Parameter	Value
Room size	5x5x2.55 m <sup>3</sup>
LED Location	(2.5, 2.5, 2.55)
LED semi-angle at half power	60°
Transmitted power	72 W
Distance between the transmitter and the receiver plane	1 m
Photodiode active area	1 cm <sup>2</sup>
Receiver half-angle FOV	60°
Refractive index of the lens at the receiver	1.5
Transmission coefficient of the optical filter	1

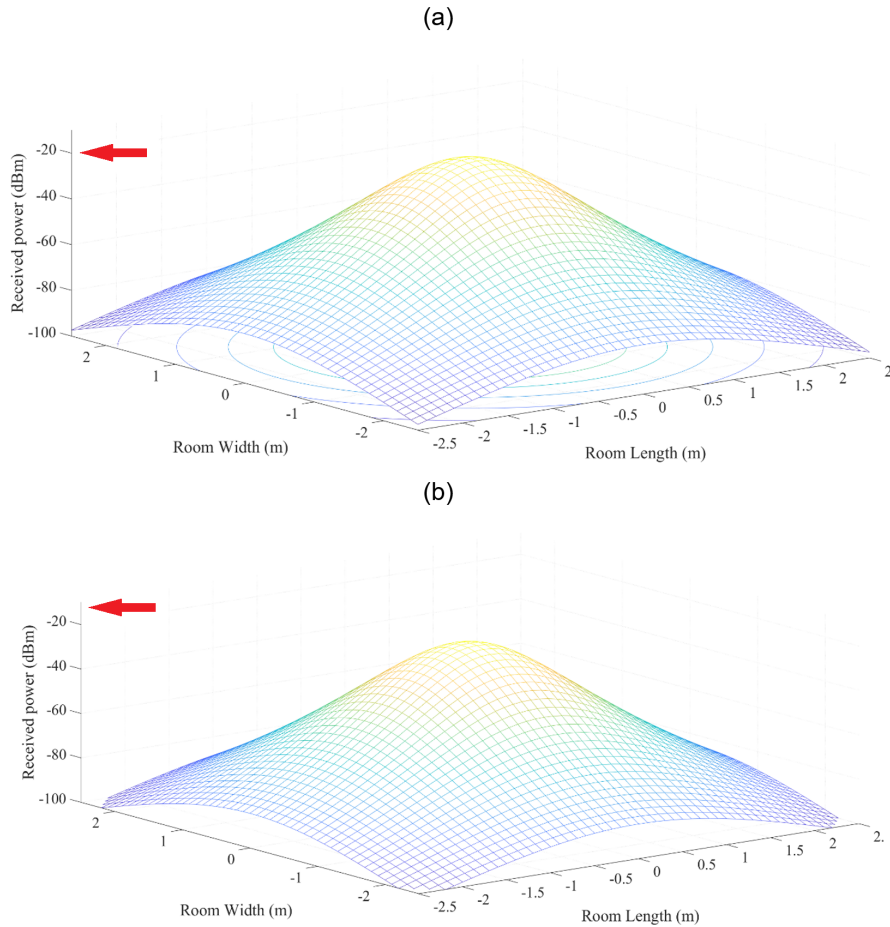


FIGURE A.2: (a) Simulated optical power received for a receiver comprised of a lens and a photodiode and a (b) receiver composed of a photodiode without the optical concentrator.

Since the same LED is used in both cases, the pattern of the optical power received throughout the room is the same as the luminous flux received does not change in both cases. However, when a lens is used, the maximum optical power is  $-17.48$  dBm while  $-19.98$  dBm is attained when no optical concentrator is present. This difference of  $2.5$  dBm will be present at the SNR and as such the performances of a modulation scheme could suffer because of it. In order to estimate the impact of such a possibility, the following section will examine the impact of the SNR on the CAP performances.

### A.3 Channel, Range, Noise, and Incidence angle

Free-space propagation is an important step of the process as the optical signal must travel through the indoor free space optical channel (FSO), described in section 2.2.1 of chapter 2. The signal is impacted by perturbations, degradations induced by the atmospheric conditions, the surrounding light sources and the electronics used for light collection and conversion. These degradations are divided into two categories, the signal attenuation and the receiver noise. Attenuations are due to the distance between the transmitter and the receiver, the PD responsivity, the system bandwidth,

the incidence angle, the orientation of the source or the lack of lens. They impact the optical power received at the PD and thus directly affect the performances. The noise also impacts the SNR and has multiple sources. Shot noise increases with the number of photons collected and thus with the incident luminous flux. Also, the thermal noise is reflected by the movement of the charge carriers at a certain temperature. And, the background noise which is introduced by the amplifiers and other electrical components. They will determine the noise side of the SNR and thus directly impact the performances [259].

A LED has a Lambertian radiant intensity pattern that can be modeled with:

$$R_0 = \frac{m+1}{2\pi} \cos^m(\varphi) \quad (\text{A.13})$$

With  $m$  the order of the Lambertian emission equal to  $-\ln(2)/\ln(\cos(\varphi_{1/2}))$ ,  $\varphi$  the irradiance angle and  $\psi$  the incidence angle. As a reminder, the transmitted power is:

$$P_{tx} = P_{LED} R_0(\varphi) \quad (\text{A.14})$$

With  $P_{LED}$  being the power emitted by the LED. For the LOS Channel part of the channel, the DC gain can be estimated accurately by considering the LOS propagation path:

$$H_{LOS}(0) = \frac{A_{rx}}{d^2} R_0(\varphi) \cos(\psi) \text{ when } 0 \leq \psi \leq \psi_C \quad H_{LOS}(0) = 0 \text{ when } \psi > \psi_C \quad (\text{A.15})$$

With  $A_{rx}$  the detector area,  $d$  the distance between the transmitter and the receiver,  $R_0(\varphi)$  the transmitter radiant intensity given by equation (44),  $\psi$  the angle of incidence and  $\psi_C$  the FoV of the photodiode. Thus, the total power of  $i$  LEDs in the directed path is:

$$P_{rx,LOS} = \sum_{i=1}^{LEDs} P_{tx} H_{LOS}^i(0) \quad (\text{A.16})$$

With  $H_{LOS}^i(0)$  being the  $i^{th}$  LED channel DC gain. For the diffuse channel part of the optical channel, the first diffuse reflection of a wide-beam optical source emits an intensity  $I_1$  over the whole room surface  $A_{room}$  and is given by:

$$I_1 = \rho_1 \frac{P_{total}}{A_{room}} \quad (\text{A.17})$$

With  $\rho_1$  being the reflectivity of the surface,  $P_{total}$  the total power of all LEDs. The average reflectivity is given by:

$$\langle \rho \rangle = \frac{1}{A_{room}} \sum_i A_i \rho_i \quad (A.18)$$

With  $A_i$  being the areas of walls, windows and objects and  $\rho_i$  being reflectivity of these walls, windows and objects. Thus, the total intensity is given by summing up a geometric series:

$$I = I_1 \sum_{j=1}^{\infty} \langle \rho \rangle^{j-1} = \frac{I_1}{1 - \langle \rho \rangle} \quad (A.19)$$

Where  $j$  is the index of the number of reflections. The receiver is a small part of the surface:

$$P_{diff} = A_{rx} I \quad (A.20)$$

In consequence, the diffuse channel loss is given by:

$$\eta_{diff} = \frac{P_{diff}}{P_{total}} = \frac{A_{rx}}{A_{room}} \frac{\rho_1}{1 - \langle \rho \rangle} \quad (A.21)$$

For the receiving power budget, at the receiver the light passes through an optical filter sometimes and a concentrator (lens), as shown in the following equation:

$$P_{rx} = (P_{LOS} + P_{diff}) T_f(\psi) g(\psi) \quad (A.22)$$

Where  $T_f(\psi)$  is the transmission coefficient of the optical filter and  $g(\psi)$  is the concentrator gain. The photodiode transformed the received optical power into electrical current:

$$i = P_{rx} R \quad (A.23)$$

With  $R$  being the photodiode responsivity in Ampere per Watt. The Signal to Noise Ratio (SNR) is thus given by:

$$SNR = \frac{(R \cdot P_{rx})^2}{\sigma_{total}^2} \quad (A.24)$$

With the total noise variance  $\sigma_{total}^2$ :

$$\sigma_{total}^2 = \sigma_{shot}^2 + \sigma_{amplifier}^2 \quad (A.25)$$

The shot noise variance:

$$\sigma_{shot}^2 = 2qR(P_{rx} + P_n)B_n \quad (\text{A.26})$$

Where:  $B_n$  is the noise-bandwidth,  $P_n$  is the noise power of the ambient light,  $R_b$  is the data rate and  $I_2$  is the noise bandwidth factor. The amplifier noise variance, on the other hand, is given by:

$$\sigma_{amplifier}^2 = i_{amplifier}^2 B_a \quad (\text{A.27})$$

With  $B_a$  the amplifier bandwidth. The BER is calculated with:

$$BER = Q(\sqrt{SNR}) \quad (\text{A.28})$$

With:

$$Q(x) = \frac{1}{\sqrt{2\pi}} \int_x^\infty \exp\left(-\frac{y^2}{2}\right) dy \quad (\text{A.29})$$

Thus, when multiple LEDs are transmitting the same data, a larger amount of power is received and the SNR increases, lowering the BER. In total, the real time overall channel response is given by:

$$h(t) = h_{LOS}(t) + h_{diff}(t - \delta t) \quad (\text{A.30})$$

With  $h_{LOS}$  and  $h_{diff}$  the real-time LOS and diffuse channel responses respectively and  $\delta t$  the delay between the arrival of the LOS and diffuse rays. However, the diffused component is generally not considered when the receiver and transmitter are under line of sight as it is significantly lower.

The characteristics of the channel will impact the signal by attenuating it. As such the SNR is a good estimate to evaluate the performances of the CAP modulation in a variety of scenario by making the signal-to-noise ratio vary. Figure A.3 (a) and (b) show the impact of the SNR and signal bandwidth, which can represent the data rate, on the BER with the CAP modulation. The following simulation parameters were used:

Figure A.3 (b) is the impact on the BER of the SNR, with a signal bandwidth of 1 MHz. As expected, the higher it is, the lower the BER is. A more complete overview can be given by also making the signal bandwidth vary, as shown in figure A.3 (a) where the signal bandwidth goes from 1 MHz to 40 MHz. The higher it is, the stronger the low-pass effect and thus the attenuation from the whole wireless optical channel. As such, the BER increases with the signal bandwidth. These figures also give a preview of the impact of the modulation order. With a larger  $M$ , the constellation

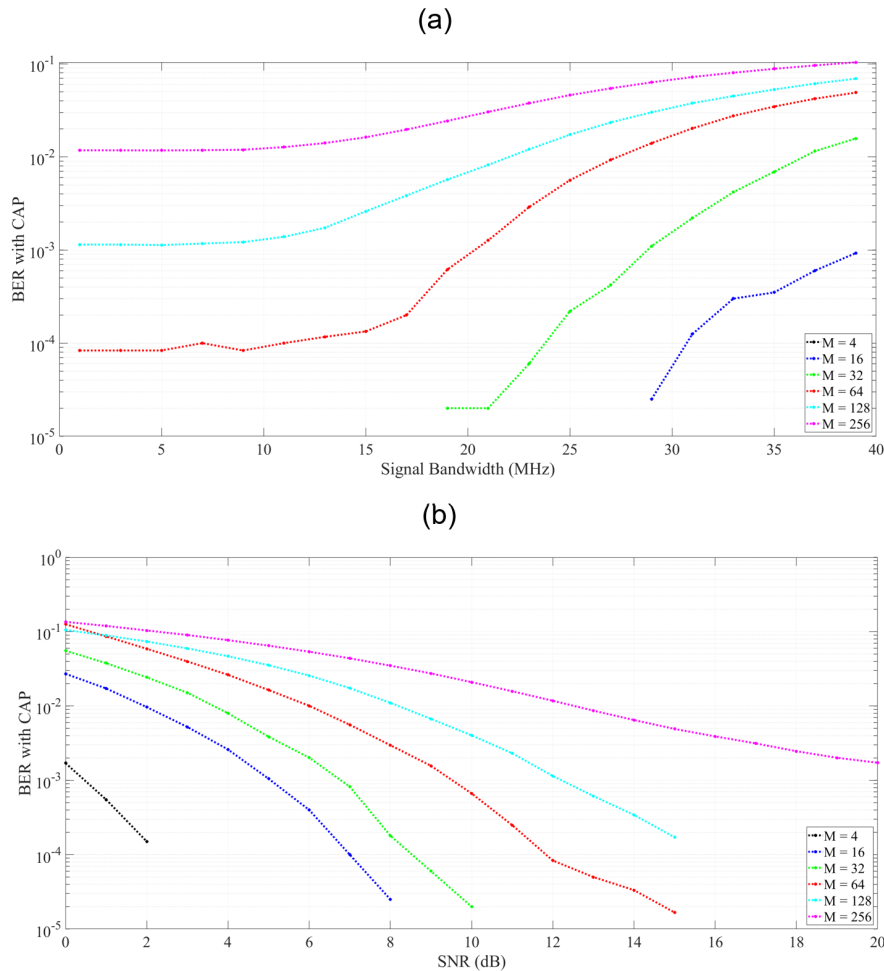


FIGURE A.3: (a) Simulated BER in 1-CAP for different signal bandwidth values at a range of 1 meter and direct line of sight, for a fixed SNR of 12 dB and multiple constellation sizes. (b) Simulated BER in 1-CAP for different values of SNR, a fixed signal bandwidth of 1 MHz, the same 1-meter range and multiple constellation sizes.

size increases and as such the distance between each point becomes smaller, as the same power is used throughout the simulation. In consequence, the higher  $M$  is, the higher the impact of the SNR and the signal bandwidth. The continuation of this study on  $M$ -QAM mapping is given in subsection 3.2.2.1 of chapter 3.

## A.4 Simulation of a BER Distribution

Figure A.4 is an example for a BER distribution obtained in numerical simulations. As represented by the 3D chart, a BER value corresponds to each location in the room. The further a user is from the center of the room, the higher the BER experienced will be. Indeed, this directly translates to an augmentation of the distance between the receiver and the emitter, located in the center of the ceiling. The parameters of the simulation were the same as in the experimental setup for chapter 5 except that only 1 user is considered and conventional CAP is used as the modulation process. In

TABLE A.4: Simulation parameters used to obtain the BER in different conditions in figure A.3.

Parameter	Value
LED cutoff frequency	5 MHz
LED semi-angle at half power	70°
Transmitted power	72 W
Distance between the transmitter and the receiver plane	50 cm
Photodiode active area	1 cm <sup>2</sup>
Receiver half-angle FOV	60°
Reflective index of lens at the receiver	1.5
Transmission coefficient of the optical filter	1
Upsampling factor	10
Roll-off factor	0.15
Filter span	12

this simulated example, the data rate considered for the CAP signal is approximately 50 Mb/s. The following parameters were used to obtain these simulated results:

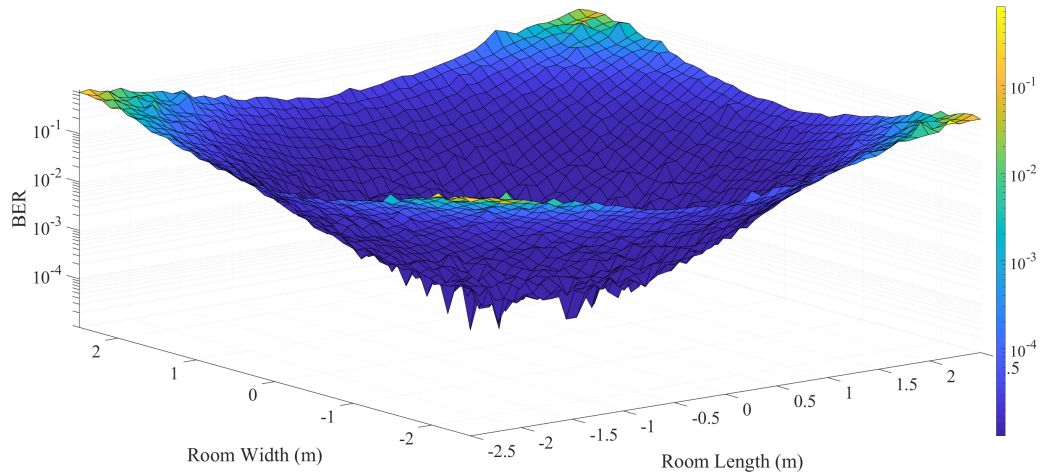


FIGURE A.4: Simulated 3D bit error rate distribution in a 5x5x3 m indoor room. Characteristics of the simulation are included in Table A.5.

Figure A.5 illustrates the attocell in a clearer way. In the case of a 7% FEC limit, the attocell size associated would be approximately 8.04 m<sup>2</sup>. It corresponds to the area where the received BER is smaller than  $3.8 \times 10^{-3}$  and thus decodable by a receiver using a 7% overhead.

TABLE A.5: Simulation parameters used to obtain the 3D BER distribution in figure A.4.

Parameter	Value
Room size	5x5x3 m <sup>3</sup>
Reflection coefficient	0.8
LED Location	(2.5, 2.5, 3)
LED semi-angle at half-power	30°
Transmitted power	72 W
Distance between the transmitter and the receiver plane	1.5 m or 2.15 m
Photodiode active area	1 cm <sup>2</sup>
Receiver half-angle FOV	70°
Refractive index of the lens at the receiver	1.5
Transmission coefficient of the optical filter	1
Photodiode responsivity	0.4 A/W
Amplifier bandwidth	150 MHz
Data rate	50 Mb/s
Dark current	2 uA
Open-loop voltage gain	5000 V/A
Absolute temperature	298 K
Fixed capacitance of the photodiode per unit area	112 pF
FET trans conductance	0.03 S
Noise-bandwidth factor $I_2$	0.562
Noise-bandwidth factor $I_3$	0.0868
Number of symbols	10000
Modulation order M	16
Upsampling factor	10
Roll-off factor	0.15
Filter span	12
Linear equalizer type	Recursive Least-Squares (RLS)
Training length	100 symbols
RLS parameter (forget factor)	0.99
Number of feedforward weights	15
Number of feedback weights	10

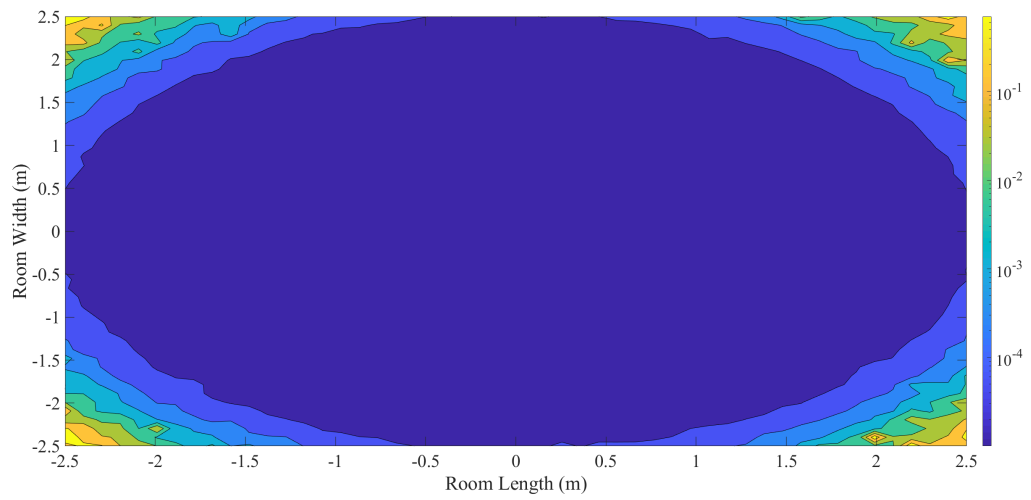


FIGURE A.5: Simulated 3D bit error rate distribution on plane using a color map. The simulation is the same as described figure A.4.

## Appendix B

# Experimental Setup Hardware Components Specifications

### B.1 Basis of Implementation of CAP for the Numerical Simulations

Figure B.2 is a diagram in blocks which presents the implementation process step by step for a CAP modulation process. The first step is the generation of a binary bit sequence which is usually a Pseudo random binary sequence (PRBS). The resulting data stream is converted into a packet of symbols in order to be mapped into an  $M$ -QAM constellation. As explained in the previous subsection, a symbol is constituted of  $k = \log_2(M)$  bits. The constellation points are arranged in a square grid, with the number of points being a power of 2. Which means that  $M$  is usually equal to 2, 4, 8 ... Additionally, since QAM is usually square, the most common forms found are 16-QAM, 64-QAM and 256-QAM. The higher the order of the constellation, the higher the bits per symbols are, as described by  $k$ . However, as the mean energy of the constellation should remain the same, the constellation points are going to come closer together as  $M$  increases, thus increasing the sensitivity to noise and artifacts.

Following the mapping, each component is represented in the mapping by a real and imaginary component which are separated to be filtered by the Hilbert pair described by equations (2) and (3). The implementation of the raised cosine filters is described in figure B.1. Finally, the summed orthogonal components form the signal which is going to be transmitted by the emitter. Before being applied to the LED, the waveform is usually amplified by the use of an electrical amplifier (EA) and a direct current bias must be applied using a bias-tee (BT). Indeed, the LED has certain linear range, obtained by the measure of the IV response curve, and can only emit a real positive signal, hence the need for both these components.

Figure B.3 is the diagram in blocks which presents the implementation process step by step for a CAP demodulation process. The receiving circuit serves to generate the signal  $r(t)$  which corresponds to  $S(t)$  after crossing the optical channel. It is usually composed of a lens to concentrate the received light from the LED emitter into a

photo-diode (PD). The current created by the PD is then transformed into a voltage and amplified by a transimpedance amplifier (TIA). Finally, an ADC puts the signal into digital form for post-processing. After separation of the received signal into two identical signals, the matched filters are used to recreate the real and imaginary components corresponding to what was originally transmitted. The matched filters are recreated in the same way as in the transmitter, as described figure B.1. The de-mapping and decoding process follow in order to recover the original PRBS. The performances of the modulation and the whole system can be measured with the bit-error rate which is the number of bit errors divided by the total number of bits transmitted during a specific time interval.

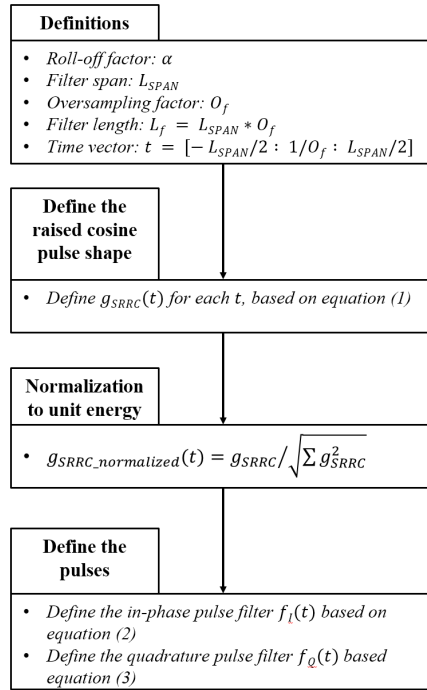


FIGURE B.1: Schematic describing the basis of implementation for the raised cosine filter generation in a conventional CAP modulation process.

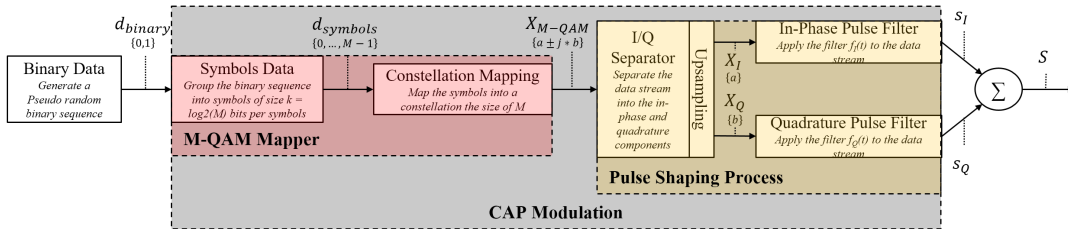


FIGURE B.2: Schematic presenting the principle of implementation for the CAP modulation process.

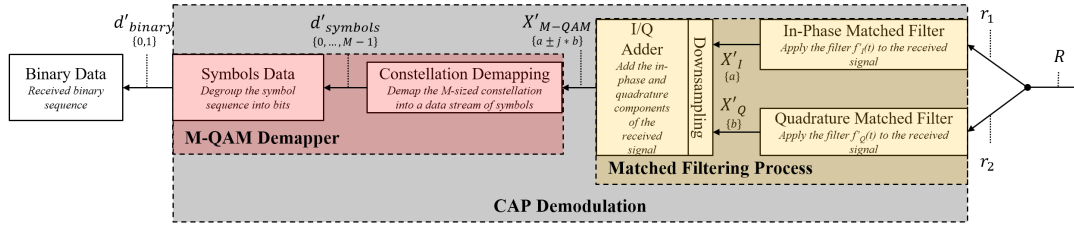


FIGURE B.3: Schematic presenting the principle of implementation for the CAP demodulation process.

## B.2 Basis of Implementation of m-CAP for the Numerical Simulations

As shown in figure B.5, the implementation process is the same as with conventional CAP except that the process is performed for each of the subcarriers. The PRBS is separated into  $m$  data streams of equal length before the  $M^n$ -QAM mapping. Each  $M^n$  can be different, giving the modulation scheme ability to use a bit-loading algorithm. Each Hilbert pair can be defined as described by equation (11) and (12). The SRRC pulse shaping generation for multiband CAP is described in figure B.4. After the generation of the output signal, defined by equation (16), the DAC and other electrical components before the LED signal emission are the same as explained in part B.1 of this appendix.

In the same way, figure B.6 represents the demodulation process in multiband CAP and is similar to conventional CAP. The receiving circuit does not change from the one described in part B.1 of this appendix. After digitalization of the signal, the  $2m$  matched filters, which are defined as described by figure B.4, are applied to recover the real and imaginary components originally transmitted. The final steps of the demodulation are exactly the same as in conventional CAP to recover the multiple bit sequence and reform the original PRBS.

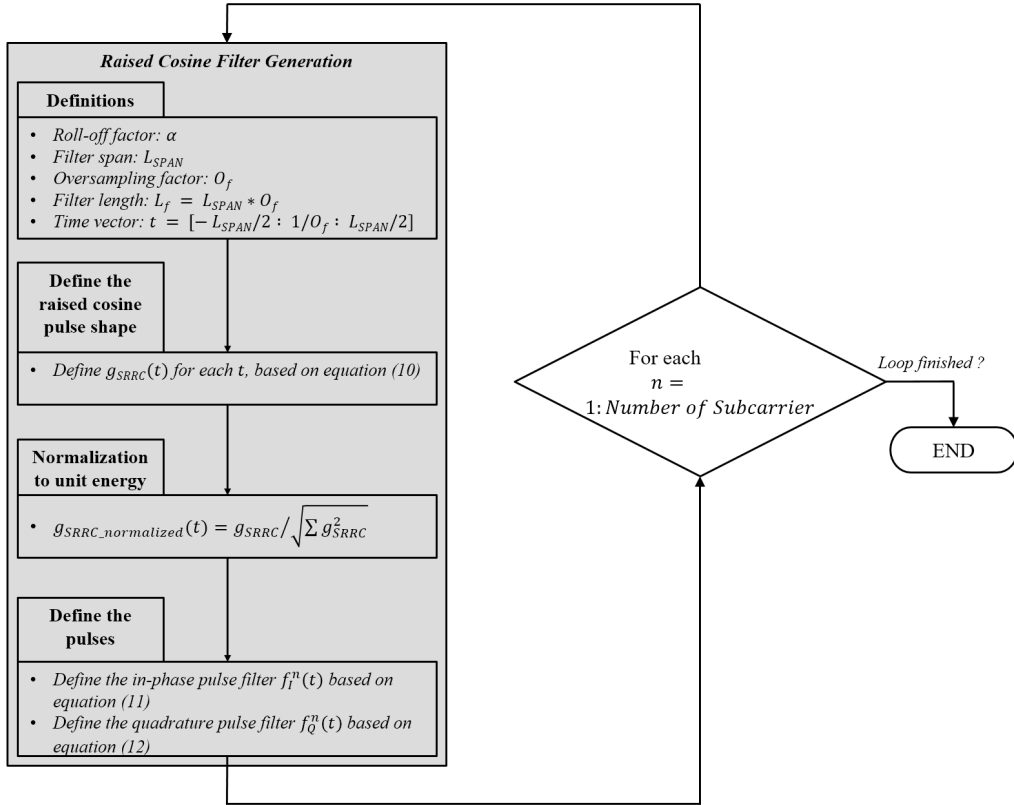


FIGURE B.4: Schematic describing the basis of implementation for the raised cosine filter generation in a multiband CAP modulation process.

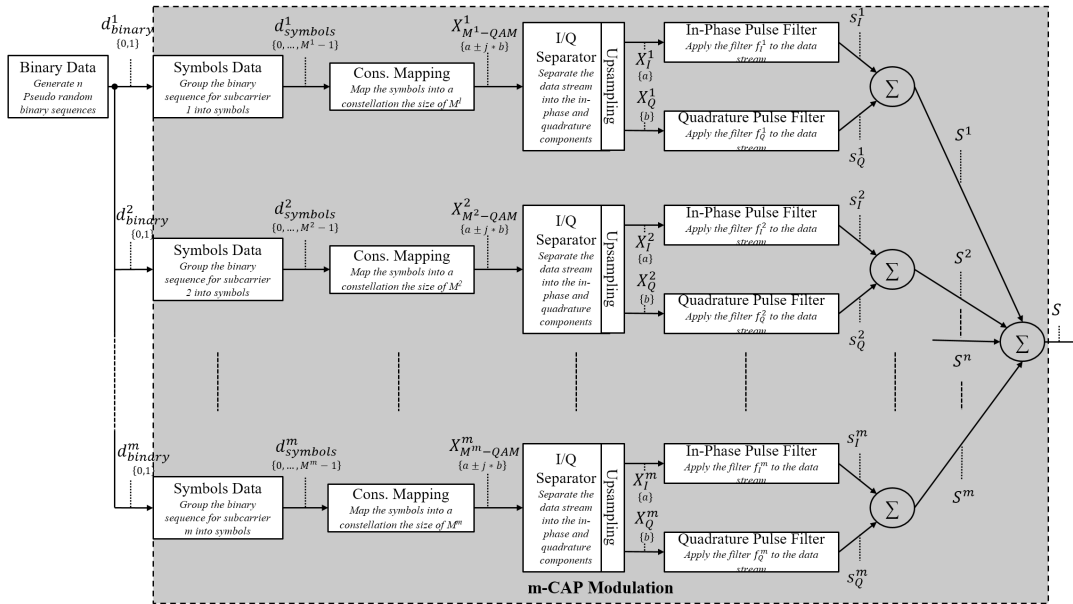


FIGURE B.5: Schematic presenting the principle of implementation for the CAP modulation process.

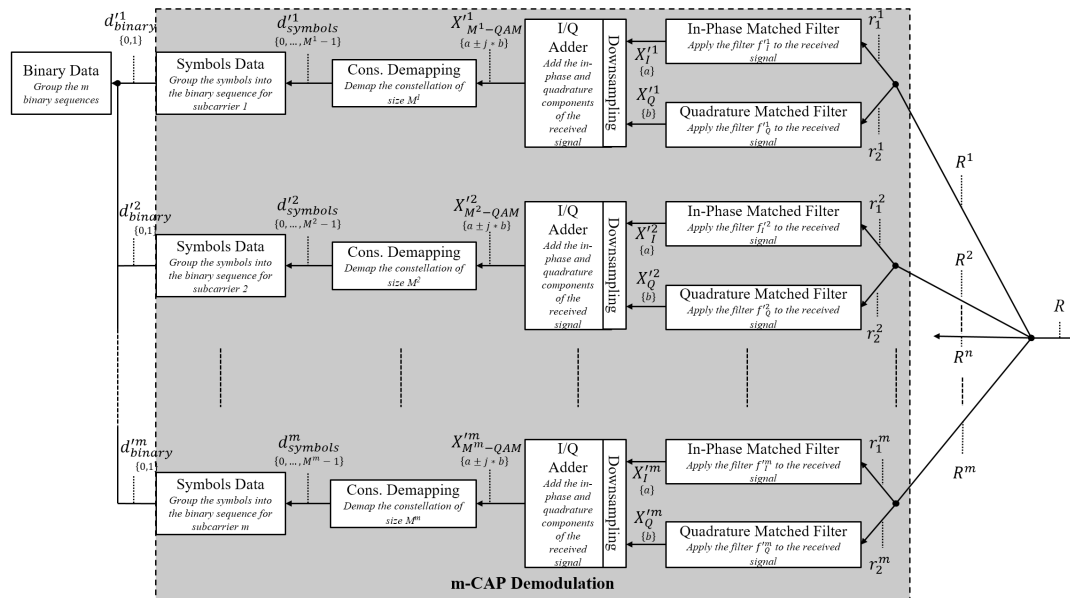


FIGURE B.6: Schematic presenting the principle of implementation for the CAP demodulation process.



## Appendix C

# Experimental Setup Hardware Components Specifications

### C.1 Specifications for LED Driver Minicircuit ZHL-6A+ and Bias-Tee Minicircuit ZFBT-282

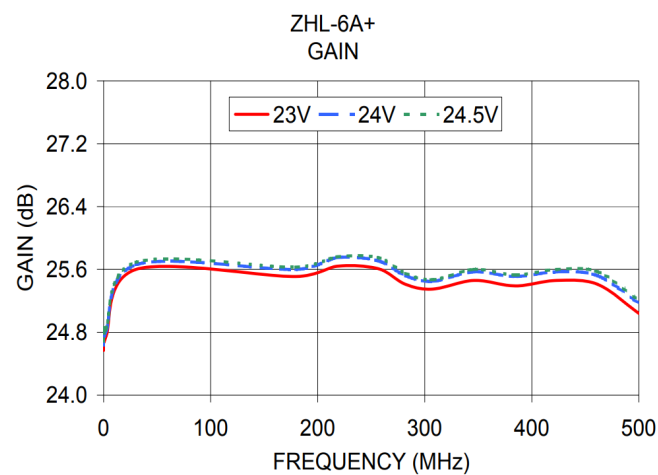


FIGURE C.1: Graph of the gain versus frequency the electrical amplifier ZHL-6A+ from Minicircuit.

### C.2 Specifications for Thorlabs Lens LA1027 and Thorlabs PIN Photodiode and Transimpedance Amplifier PDA10A-EC

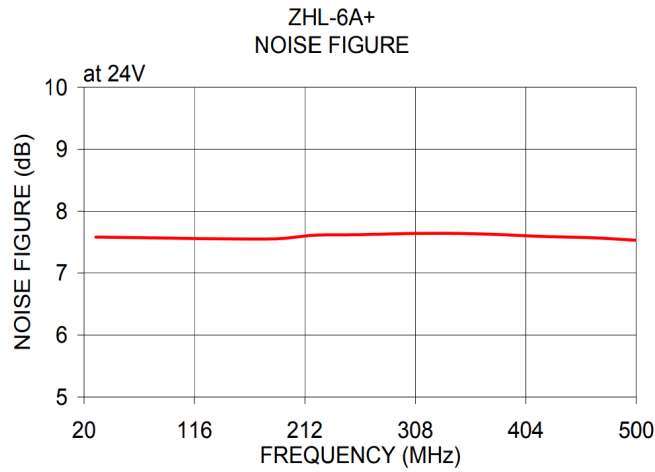


FIGURE C.2: Graph of the noise figure versus frequency the electrical amplifier ZHL-6A+ from Minicircuit.

Specification	Rating		
Model	ZHL-6A+		
Frequency range (MHz)	$f_L$ Lower range	$f_U$ Upper range	
	0.0025	500	
Gain (dB)	Typ.	Min.	Flatness Max.
	25	21	$\pm 2.2$
Maximum power output (dBm)	(1 dB Compr.) Min.	Input (no damage)	
	+22	+10	
Dynamic range	NF (dB) Typ.	IP3 (dBm) Typ.	
	9.5	+34	
VSWR (:1) Typ.	In	Out	
	1.8	2.0	
DC Power	Volt (V) Nom.	Current (A) Max.	
	24	0.350	

FIGURE C.3: Summary of the characteristics for the electrical amplifier ZHL-6A+ from Minicircuit.

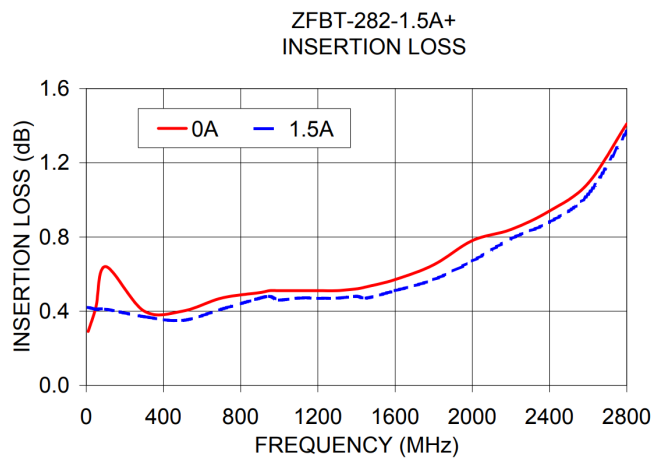


FIGURE C.4: Graph of the insertion loss versus frequency for the bias-tee ZFBT-282 from Minicircuit.

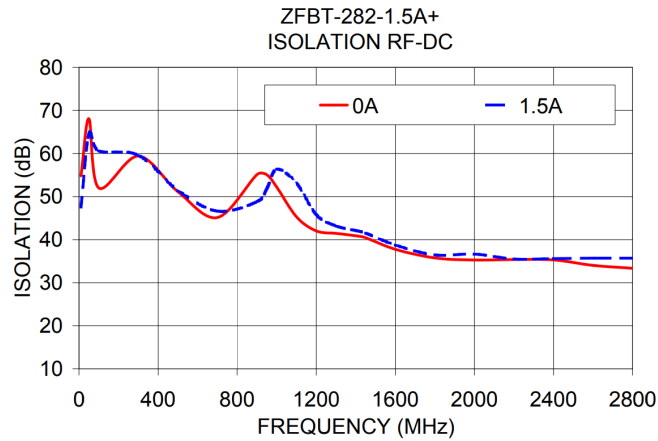


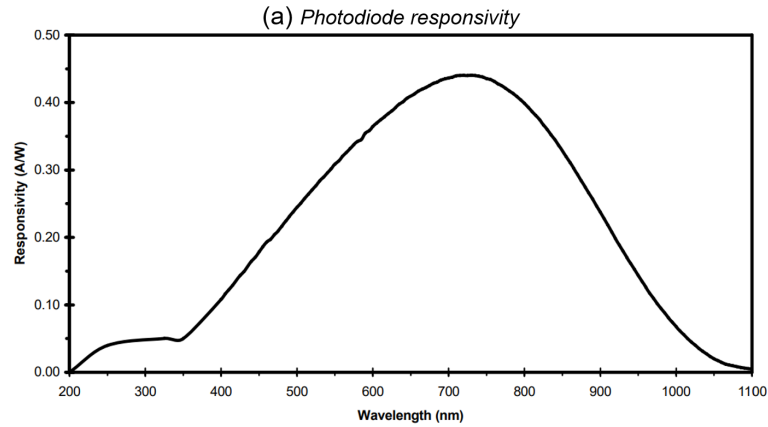
FIGURE C.5: Graph of the isolation versus frequency for the bias-tee ZFBT-282 from Minicircuit.

Specification	Rating					
Model	ZFBT-282-1.5A+					
Frequency range (MHz)	$f_L$ Lower range			$f_U$ Upper range		
	2800					
Insertion Loss (dB)	L		M		U	
	Typ.	Max.	Typ.	Max.	Typ.	Max.
	0.5	1.0	0.6	1.0	0.8	1.6
Isolation(dB)	L		M		U	
	Typ.	Min.	Typ.	Min.	Typ.	Min.
	50	30	45	30	30	20
VSWR (:1)	L		M		U	
	Typ.	Max.	Typ.	Max.	Typ.	Max.
	1.16	1.35	1.10	1.20	1.08	1.35

FIGURE C.6: Summary of the characteristics for the bias-tee ZFBT-282 from Minicircuit.

Specification	Rating
Model	LA1027
Focal length (mm)	35
Diameter (mm)	25.4
Glass Type	N-BK7

FIGURE C.7: Characteristics of the Thorlabs LA1027 lens.



(b) Photodiode + Transimpedance amplifier, summary of characteristics

Specification	Rating			
Model	PDA10A-EC (Includes the PD and TIA)			
Detector Type	Silicon			
Active Area (mm <sup>2</sup> )	0.8			
Response range (nm)	Min.	Max.		
	200	1100		
Peak Response (A/W)	0.45 at 750 nm			
Small Signal Bandwidth (MHz)	150			
NEP (W/√Hz, 960 nm)	5.5*10 <sup>-11</sup>			
Noise (mV, RMS)	2.0			
Dark Offset (mV)	20			
Output Voltage range (V)	50 Ω		Hi-Z	
	Min.	Max.	Min.	Max.
	0	5	0	10
Transimpedance Gain (V/A)	50 Ω		Hi-Z	
	5*10 <sup>3</sup>		1*10 <sup>4</sup>	

FIGURE C.8: Characteristics of the silicon photodiode and transimpedance amplifier. Both the PD and TIA are contained in Thorlabs PDA10A-EC in this experimental setup.

## Appendix D

# Résumé Détaillé en Français

De nos jours, le nombre d'appareils connectés nécessitant un accès aux données mobiles est en augmentation constante. L'arrivée d'encore plus d'objets multimédias connectés et la demande croissante d'informations par appareil ont mis en évidence les limites de la quatrième génération de réseaux cellulaires (4G). Cela a poussé au développement de nouvelles méthodes, dont la 5G. L'objectif est d'être en mesure de prendre en charge la croissance des systèmes portables, des capteurs ou des systèmes associés à l'internet des objets (IoT). La vision derrière la 5G est de permettre une société entièrement mobile et connectée avec une expérience consistante.

Les petites cellules sont la base des normes de communication avancées telles que 4G et maintenant 5G. Ils résultent de l'utilisation de bandes de fréquences plus élevées pour l'accès radiofréquences (RF) afin de supporter de nouvelles normes et exigences croissantes en bande passante. La 5G utilise des ondes millimétriques et nécessite un déploiement dans un environnement urbain intérieur et urbain dense, ce qui peut s'avérer être un défi. C'est là que la 5G devra inclure des solutions de réseau hybrides et pouvoir coexister avec d'autres technologies d'accès sans fil. La communication par lumière visible (VLC) s'inscrit dans ce moule puisque la lumière visible correspond à la bande comprise entre 400 et 800 THz. Le spectre disponible est des milliers de fois plus large que le spectre RF et il n'interfère pas avec celui-ci. Le principe se base sur la combinaison de l'éclairage avec un lien de communication pouvant atteindre des dizaines de gigabits par seconde. Le potentiel est d'offrir un complément à la 5G dans un réseau hybride, offrant une vitesse élevée, aucune interférence et une sécurité accrue au prix d'une couverture limitée et d'une faible maturité technologique.

L'objectif de cette thèse est donc de proposer et d'évaluer une implémentation expérimentale d'un système VLC en intérieur et multi-utilisateurs afin de répondre aux objectifs de la configuration light-fidelity (Li-Fi) dans le contexte d'une petite cellule. Premièrement, la portée est définie comme la distance moyenne entre un plafond et un bureau, soit 2,15 mètres. Deuxièmement, le haut débit doit être atteint pour permettre les applications tels que la vidéo 4K en streaming, soit plus de 100 Mb/s comme définit en France. Troisièmement, un accès multi-utilisateurs doit être possible. La cellule doit en effet être capable de servir indépendamment plusieurs receveurs

lors d'applications tels que les IoTs. Vu la taille des cellules Li-Fi en intérieur, au moins 4 utilisateurs doivent pouvoir être servis par le transmetteur. Quatrièmement, la facilité d'implémentation est soulignée lors du travail exposé pour exploiter le fait qu'un système VLC peut réutiliser l'infrastructure de lumière à LED.

La première étape de cette étude est un état de l'art détaillé sur le principe de VLC dans la communication sans fil en intérieur et de l'accès multi-utilisateur. Cela permet de mieux expliquer le concept de notre design et de comparer notre approche aux travaux existants. VLC est une technique de communication optique sans fil où la lumière produite par une LED dans le spectre visible est utilisée pour transmettre des données avec une modulation à intensité (IM). À l'émission, un signal modulé contrôle la LED pour être converti en un signal optique. Le canal optique comprend les distorsions que le signal optique expérimente. Le receveur convertit la lumière reçue en un signal électrique. Cette technique est nommée détection directe (DD) dans un système VLC car le signal optique est converti en signal électrique proportionnel. Les photodiodes (PD) sont le plus utilisées pour le Li-Fi mais d'autres types de détecteurs existent. Les principes de bases des systèmes VLC leur permettent d'avoir des avantages soulignant leur complémentarité aux systèmes RF. Premièrement, le spectre de la lumière visible a une grande bande passante d'environ 300 THz qui est gratuite et sans régulation. Deuxièmement, une LED peut être modulée à de très grandes vitesses ce qui veut dire qu'un grand débit peut être atteint avec une grande efficacité spectrale. Troisièmement, la bande passante de la lumière visible n'interfère pas avec celle des systèmes RF et ne peut pas passer à travers les murs. Cela signifie que ceux-ci peuvent être utilisés ensemble et que les systèmes VLC peuvent aussi apporter une sécurité supplémentaire. Enfin, une LED a une grande durée de vie, une consommation électrique basse et un prix bas. Pour ces raisons, les LED remplacent les sources de lumière traditionnelles. En conséquence, il y a un réseau potentiel de transmetteurs VLC installés partout.

Le choix de la LED pour ces travaux se porte sur les LED blanches à base de phosphore (ph-LED). La bande passante de celles-ci est limitée comparées aux LEDs colorés RGB, aux micros-LEDs ou encore aux LED à cavité résonante (RC-LED). Cela est dû au temps lent de relaxation du phosphore. Cependant, les ph-LED puissantes sont plus communes et moins chères, ce qui permet d'atteindre la portée de 2,15 mètres plus facilement. Aussi, ce sont les LEDs installées quasiment partout et elles sont les moins complexes à piloter. Le choix de la photodiode importe peu dans notre cas car les options sont très proches et avec une bande passante beaucoup plus grande que la LED choisie, les performances ne sont pas impactées par ce choix.

La modulation utilisée pour un système VLC est un critère important pour optimiser l'efficacité spectrale du système. Cette métrique est la plus importante car elle indique quel débit sera atteint en fonction de la bande passante modulable. Les autres caractéristiques importantes sont l'efficacité en puissance, le coût d'implémentation

et la présence ou non d'un support de dimming naturel à la modulation. En conclusion les modulations à haute efficacité spectrale ont d'abord été retenues dû fait que les ph-LEDs ont de faibles bandes passantes. Dans ce contexte la modulation CAP/ $m$ -CAP est l'option préférée pour une efficacité spectrale et en puissance haute. La modulation OFDM est très explorée en littérature alors que  $m$ -CAP est nouvelle et n'a donc pas été étudiée dans ces travaux. Le schéma d'accès utilisateurs permet d'allouer des ressources aux utilisateurs pour leur permettre d'accéder en même temps au système de transmission. Pour effectuer le choix de la technique pour le système VLC décrit dans ces travaux, plusieurs métriques sont utilisées. La première est l'efficacité spectrale par utilisateur, qui indiquera quel débit un utilisateur peut atteindre en fonction de la bande passante pour n'importe quel schéma d'accès multi-utilisateur. La seconde métrique est la flexibilité qui correspond à la capacité du schéma à compenser les états variantes du canal de transmission. C'est une caractéristique importante en VLC car les receveurs font l'objet de larges variations dans l'atténuation du canal en fonction de leur position et de l'angle d'incidence par rapport au point d'accès. La complexité est la troisième métrique essentielle car elle définit le coût d'implémentation de chaque technique d'accès multi-utilisateurs. Enfin, le nombre maximum d'utilisateurs supporté par le schéma est la quatrième métrique. Les techniques les plus utilisés en VLC ont été comparés, sauf TDMA et quelques formes rares de NOMA. Contrairement au choix de modulation, il n'y a pas de schémas clairement évident à préférer. SCM offre une manière naturelle d'ajouter un aspect multi-utilisateur à  $m$ -CAP, CDMA est équilibré, SDMA ou PD-NOMA sont très complexe à implémenter mais très performantes. En conséquence, l'étude prend en compte et comparera les schémas d'accès utilisables avec une seule LED blanche parmi ceux comparés, soit SCM, CDMA et PD-NOMA.

Les résultats de l'étude de l'état de l'art permettent de préciser le design utilisé dans ces travaux. La structure de l'émetteur est composée d'un bloc de traitement de signal numérique permettant de générer le signal modulé, d'un pilote de LED et de la LED elle-même. L'implémentation en temps réel n'est pas étudiée dans ce travail alors le choix de la LED a le plus d'impact sur les performances. L'objectif principal de la conception est le réalisme de l'expérience et est lié à l'objectif final qui est de concevoir un système VLC expérimental multi-utilisateurs d'intérieur. La plupart des travaux existants ont une portée inférieure à 1,5 m dans un scénario intérieur alors que la distance moyenne entre le plafond et le bureau est de 2,15 m dans la réalité. La deuxième limite est liée aux méthodes très lourdes et restrictives de post-égalisation et d'amélioration des performances utilisées dans tous les résultats d'efficacité spectrale élevée. Dans un scénario multi-utilisateurs, les conditions dans une cellule VLC changent radicalement. Un élément important est donc la flexibilité du schéma. En effet, plus la technique est flexible, plus il sera facile de réagir à un changement soudain des conditions. Par conséquent, ce travail vise à réduire la complexité en n'utilisant pas de post-traitement lourd et une plus grande flexibilité en proposant des techniques d'amélioration avec une flexibilité et un faible coût de mise

en œuvre. Une ph-LED standard est utilisée comme émetteur. Elle ajoute au réalisme et à l'aspect à faible coût d'implémentation. Cependant, une limitation principale qui a été discutée est la bande passante utilisable inférieure. Afin d'atteindre des débits rapides ( $> 100$  Mb/s) avec ce type de LED plus lentes, deux chemins sont explorés simultanément. Le premier est l'extension de la bande passante à 3 dB avec égalisation. La seconde est l'optimisation de l'utilisation de la bande passante avec l'exploration d'un schéma de modulation d'efficacité spectrale élevée. En fin de compte, le débit brut ne sera pas comparable à certains travaux présentés de la littérature, mais l'efficacité spectrale le sera. La structure de récepteur est composée d'un récepteur à base de photodiode et d'un bloc de traitement de signal numérique pour décoder le signal reçu. L'implémentation en temps réel n'étant pas étudiée dans ce travail, cette dernière partie est traitée hors ligne avec un PC. Le choix dans la structure du récepteur vient à la photodiode. Les APD offrent un niveau de sensibilité supérieur à celui des PDP en raison de l'effet avalanche. D'autre part, il produit un niveau de bruit plus élevé car ce même effet est non linéaire. Même s'il s'agit d'autres différences, elles n'affectent pas autant les performances que cette caractéristique. En fin de compte, nous avons fini par utiliser un PD pour NIP, car ce n'est pas un élément essentiel des enquêtes menées tout au long de ce travail.

La deuxième étape consiste en une analyse des principes et des hypothèses pour le système VLC multi-utilisateurs en intérieur portant à la fois sur la technique de modulation et sur les schémas d'accès multi-utilisateurs. Les conclusions tirées des analyses théoriques et numériques servent de base pour la suite du travail. Le principe de  $m$ -CAP consiste à diviser un signal CAP classique en  $m$  sous-bandes indépendantes occupant différentes bandes de fréquences. En conséquence, un signal  $m$ -CAP peut être décrit comme la somme de plusieurs signaux CAP, chacun utilisant une fréquence porteuse différente. Cette capacité permet au schéma d'utiliser un ordre de modulation et une puissance optique différents pour chaque signal CAP, ou sous-porteuses. Le CAP conventionnel, ou 1-CAP, est un schéma très sensible à la réponse en fréquence d'un canal non plat et les canaux VLC ne présentent pas de réponses en bande plate. Cet inconvénient peut être atténué en divisant le signal en plusieurs sous-porteuses, car cela réduira la longueur de fréquence de chaque sous-bande pour la même largeur de bande totale du signal. La réponse du canal pour chaque bande apparaîtra donc «plus plate» que la réponse entière. Il en résulte que  $m$ -CAP est moins sujet à la distorsion induite par l'atténuation du canal que la CAP classique. Cette caractéristique est associée à la flexibilité inhérente à un schéma de modulation multi-sous-porteuse. Chaque sous-bande peut être adaptée à la réponse du canal avec un ordre de modulation spécifique via un mappage  $M$ -QAM et une puissance optique spécifique.

Le multiplexage de sous-porteuse (SCM) ou l'accès multiple de sous-porteuse (SCMA) est utilisé pour combiner différents signaux de communication de manière similaire au multiplexage par répartition en longueur d'onde (WDM). Chaque signal occupe

une partie différente du spectre optique entourant la fréquence centrale de l'ensemble du signal optique. Les signaux sont ainsi multiplexés dans le domaine fréquentiel et transmis par une seule longueur d'onde. Le SCM représente une association naturelle avec le  $m$ -CAP en VLC. En effet, le schéma de modulation sépare ses données en plusieurs sous-porteuses autour d'une fréquence centrale avec un signal transmis par un composant optique à une longueur d'onde spécifique. Les deux systèmes partagent le fait que leur principal coût de mise en œuvre est leur principal critère. En pratique, avec l'association de  $m$ -CAP avec la SCM dans plusieurs utilisateurs, les flux de données de sous-porteuses multiples correspondent à plusieurs utilisateurs. Chaque donnée utilisateur est contenue dans une ou plusieurs sous-bandes. Par exemple, si deux utilisateurs sont attribués avec 4-CAP, deux sous-porteuses par utilisateur ou trois pour l'utilisateur 1 et un pour l'utilisateur 2 peuvent être attribués. Cette capacité à attribuer un nombre varié de sous-bandes à chaque utilisateur dépend des besoins et de l'état du canal, offrant un degré de liberté multiple de MU- $m$ -CAP pour une flexibilité accrue du schéma à accès multiples. Un utilisateur peut également se voir allouer dynamiquement plus de sous-porteuses que les autres s'il doit augmenter son débit de données ou si la qualité de son signal diminue, avec une puissance de calcul minimale. De plus, si  $m$  augmente, cette flexibilité augmente avec le nombre de sous-porteuses disponibles pour chaque utilisateur.

CDMA (accès multiple par répartition de code) est une méthode à canaux d'accès multiples. Plusieurs utilisateurs peuvent envoyer des informations sur un seul canal de communication, permettant ainsi le partage d'une même largeur de bande de signal. Le principe consiste à utiliser une technologie à spectre étalé et un schéma de codage spécial pour réaliser la communication sans interférences entre utilisateurs. Chaque utilisateur se voit attribuer un code lors de la transmission. Le récepteur utilise le même code pour extraire les données originales transmises. Le code ne contient aucune information. CDMA multi-porteuse (MC-CDMA) est adapté pour être utilisé avec  $m$ -CAP dans ces travaux. Il est utilisé dans OFDM pour prendre en charge plusieurs utilisateurs sur la même bande de fréquence. Chaque symbole d'utilisateur est acheminé sur plusieurs sous-porteuses parallèles mais est déphasé en fonction de la valeur du code. Le récepteur sépare les signaux des différents utilisateurs car ils ont des valeurs de code orthogonales.

Le concept de base de derrière NOMA consiste à desservir plus d'un utilisateur dans le même bloc de ressources, par exemple un code, un espace ou une sous-porteuse. Il promet une connectivité massive, une latence réduite et une équité utilisateur et une efficacité spectrale améliorées par rapport aux techniques d'accès orthogonales multiples (OMA). Il existe plusieurs types de schémas d'accès multiple non orthogonaux (NOMA). Le domaine de code (CD-NOMA) et le domaine de puissance (PD-NOMA) sont les deux catégories principales. Cependant, l'accent est mis ici sur PD-NOMA, qui multiplexe les données sur le domaine de la puissance. Le principe consiste à superposer plusieurs utilisateurs à différents niveaux de puissance et à exploiter la

différence de gain de canal entre utilisateurs multiplexés. Au niveau de l'émetteur, un codeur de superposition est utilisé pour superposer les signaux de divers utilisateurs. Au niveau du récepteur, des algorithmes de détection multi-utilisateurs (MUD), tels que l'annulation d'interférence successive (SIC), sont utilisés pour détecter les signaux désirés.

L'approche choisie pour notre système VLC multi-utilisateurs intérieur consiste donc à combiner un schéma de modulation hautement efficace du point de vue spectral avec une technique multiaccès afin d'offrir un moyen peu complexe d'atteindre des débits de données élevés avec une capacité multi-utilisateurs élevée.  $m$ -CAP représente le schéma de modulation qui convient le mieux à l'approche. Le traitement utilise un principe de multi-sous-porteuses pour réduire la sensibilité à une réponse de canal non plate. De plus, une flexibilité accrue s'accompagne de la possibilité de sélectionner un ordre de modulation pour chaque sous-bande. Son potentiel est trop peu exploré dans VLC et  $m$ -CAP est donc un schéma de modulation idéal pour notre approche. L'une des métriques les plus importantes d'une performance brute de modulation est le débit, car il montre la capacité d'atteindre une efficacité spectrale élevée. En effet, la principale limitation des LED est leur bande passante. En tant que tel, la capacité à optimiser le débit pour une largeur de bande limitée est une caractéristique essentielle à optimiser. Dans la  $m$ -CAP, le principal degré de liberté se situe dans les paramètres des filtres définissant chaque sous-porteuse. Le facteur roll-off et la longueur du filtre sont des paramètres qui peuvent être modifiés pour optimiser les performances. Pour améliorer encore les résultats, il est également possible d'ajouter un facteur constant ajustant la fréquence centrale de chaque sous-porteuse et d'obtenir ainsi un autre paramètre: l'espacement entre les sous-porteuses. Outre les techniques de post-traitement telles que l'estimation et l'égalisation de canaux, l'optimisation des facteurs de filtrage et l'espacement des sous-porteuses permet à  $m$ -CAP de maximiser son efficacité spectrale de différentes manières. La  $m$ -CAP n'ayant pas encore été complètement explorée pour les systèmes VLC en intérieur, sa combinaison avec des systèmes à accès multiples est l'un des domaines qui nécessitent davantage de prospection. Le multiplexage de sous-porteuses représente le moyen le plus naturel d'ajouter un composant multi-utilisateurs au schéma de modulation. CDMA multi-porteuse peut être adapté à  $m$ -CAP. Nous avons décidé de nous concentrer sur les schémas de modulation les plus prometteurs pour la 5G avec PD-NOMA. Les associations de  $m$ -CAP avec SCM, MC-CDMA, PD-NOMA sont donc explorées dans ces travaux. Le système VLC multi-utilisateurs d'intérieur étudié dans ce travail associe l'optimisation de l'efficacité spectrale pour la modulation CAP multi-bande et son association à un schéma multiaccès. Le résultat est la conception d'une attocell VLC. Les caractéristiques d'un tel agencement sont le débit total disponible, la capacité de l'utilisateur, la plage et la taille de la cellule. Le débit de données maximal fourni provient des attributs du processus de modulation. La plage dérive de la capacité des émetteurs-récepteurs à toujours communiquer dans des conditions optimales à une distance donnée. La capacité de l'utilisateur dépend

du schéma multi-accès utilisé. Enfin, la taille de la cellule repose sur la capacité de fournir aux utilisateurs dans une zone donnée. Ce travail se concentre sur les performances d'un seul attocell. En effet, la plupart des recherches sur les schémas d'accès multi-utilisateurs ont pour objectif de réduire le nombre d'interférences entre utilisateurs et entre cellules.

La répartition des performances d'un utilisateur à la diffusion par la simulation numérique du système VLC intérieur a permis de mieux cerner l'impact de chaque bloc décrit sur la performance globale:

- La LED est le composant matériel le plus important en termes d'impact sur les performances. L'effet passe-bas de ces émetteurs limitera considérablement la largeur de bande utilisable du signal. Cet effet est principalement neutralisé par l'utilisation de l'estimation de canal et de la pré-égalisation, comme décrit dans la section Améliorations de la performance. Les caractéristiques optiques de la LED ont également un impact considérable sur les performances car elles définissent le flux lumineux et les longueurs d'onde de la lumière dans une pièce donnée. Les caractéristiques électriques doivent également être prises en compte lors du pilotage de la LED avec un amplificateur électrique et un bias-tee afin de mieux utiliser la plage linéaire.
- Le récepteur transforme le signal optique reçu en une tension utilisant une photodiode avec un amplificateur à transimpédance et, éventuellement, une lentille et un filtre optique. Comme indiqué, la lentille a un impact considérable sur la puissance reçue.
- Le canal optique en général a été étudié en simulant l'impact du SNR et de la largeur de bande du signal sur le BER pour un signal CAP. En effet, le SNR provient de la puissance reçue au niveau de la photodiode et résulte donc de tous les paramètres du canal optique.
- Le processus de modulation a été séparé en mappage  $M$ -QAM et les paramètres de filtre de mise en forme d'impulsions. Le mappeur QAM définit les tailles de la constellation utilisée par le signal et donc l'efficacité spectrale. Les filtres ont plusieurs paramètres avec le facteur de sur-échantillonnage, le facteur de roll-off et la longueur du filtre. Le facteur de sur-échantillonnage et l'étendue du filtre sont liés car ils définissent la longueur du filtre. Plus la valeur est élevée, meilleures sont les performances, mais avec un rendement décroissant et une efficacité de calcul accrue. Le facteur de roll-off définit la bande passante excédentaire et vient avec un compromis entre la largeur de bande du signal ajoutée et les performances accrues résultant de la réduction de l'amplitude des lobes secondaires à réponse de filtre.
- Les simulations d'amélioration des performances donnent un aperçu de l'option à appliquer dans le cas d'un processus d'optimisation. Le filtre optique peut offrir une augmentation de la bande passante du signal utilisable, mais la

perte de SNR peut être plus dommageable pour une ph-LED. Le processus d'estimation de canal aide en estimant le canal optique sans fil au niveau du récepteur. L'égalisation est séparée en pré-égalisation qui adapte le signal au canal et est effectuée au niveau de l'émetteur et en post-égalisation qui corrige les symboles reçus au niveau du récepteur. Les deux peuvent être combinés pour de meilleures performances et permettre l'extension de la bande passante disponible.

Les performances des schémas multi-accès sont définies et synthétisées à l'aide de simulations numériques. La définition de l'attocell VLC et de ses performances est principalement liée à l'optimisation des performances de diffusion pour un utilisateur unique. En effet, avec la distribution SNR dans une pièce, la taille de l'attocell, le débit maximum pouvant être atteint et la plage peuvent être définis pour un système VLC intérieur donné. La capacité de l'utilisateur dépend du schéma multi-accès utilisé. En effet, dans le cas de SCM, la limite d'utilisateurs est le nombre de sous-porteuses disponibles dans le schéma. De plus, l'écart par rapport au débit de données cible augmente à mesure que plus d'utilisateurs sont alloués. En tant que tel, si un écart acceptable par rapport à la cible est défini pour les schémas, il en résultera une limite du nombre d'utilisateurs. Si cette limite est dépassée, chaque utilisateur n'atteindra en moyenne pas son débit de données cible dans les limites de l'écart acceptable. Dans le cas de MC-CDMA, le nombre d'utilisateurs est limité par le nombre de codes orthogonaux disponibles. L'écart par rapport à la cible est bien inférieur à celui du SCM, car chaque utilisateur utilisera un ensemble complet d'un signal  $m$ -CAP et non une fraction de celui-ci. Cependant, l'augmentation du nombre de codes réduit l'orthogonalité au niveau des récepteurs. Par conséquent, l'ordre de modulation de chaque sous-porteuse du signal  $m$ -CAP doit être optimisé de manière plus significative. Il a été démontré que PD-NOMA augmentait la capacité des utilisateurs en multipliant pratiquement le nombre de sous-porteuses disponibles. Mais, cela nécessite des ressources de calcul considérables avec SIC.

La troisième étape consiste en plusieurs analyses expérimentales sur l'optimisation des performances de diffusion pour un utilisateur unique, puis sur les performances multi-utilisateurs du système à l'aide de divers schémas d'accès.

Le montage expérimental est utilisé pour toutes les mesures présentés dans ces travaux. Il est composé d'un AWG (AFG3252C) stocke un total de  $m$  flux de données aléatoires. Des flux de bits aléatoires sont créés sur MATLAB, chacun de ces flux de données étant affecté à une sous-porteuse pour le processus de modulation  $m$ -CAP. Pour chacun d'entre eux, un mappeur  $M$ -QAM mappe les flux de données correspondants. Ensuite, chaque flux de symboles est séparé en son composant réel et son composant imaginaire. Les filtres cosinus en relief et en quadrature correspondants leur sont appliqués. Ces filtres FIR sont configurés à la fréquence centrale définie par l'attribution de sous-porteuse. Tous les flux de données modulés résultants  $m$  sont ajoutés pour produire le signal à émettre. Avant la transmission, le signal est

pré-égalisé à l'aide d'un filtre de pré-égalisation de pré-accentuation d'amplitude implémenté par logiciel pour étendre la bande passante de modulation disponible. Afin de détecter la trame transmise au récepteur, un simple préambule est ajouté au début du signal, avant la transmission. Le signal est stocké dans l'AWG. Après l'émission du signal, un amplificateur électrique (ZHL-6A +) est utilisé pour amplifier le signal émis par l'AWG. Un bias-tee (ZFBT-282) ajoute une polarisation continue au signal avant de l'envoyer à la LED. La LED blanche utilisée au cours des expériences est un downlight de 72W que l'on peut trouver dans les centres commerciaux, les bureaux ou les hôpitaux. Il fonctionne à 19,2 W de puissance électrique (32V, 0.6A). Le circuit de réception est d'abord composé d'une lentille biconvexe Thorlabs de 25 mm qui concentre la lumière dans une photodiode. Ce dernier est combiné avec un TIA avec le Thorlabs PDA10A-EC pour former le circuit de réception. Le PD est un récepteur au silicium de 1 mm de diamètre. La distance utilisée, sauf indication contraire, est fixée à 2,15 m entre l'émetteur et le récepteur, avec une ligne de visée directe. Le signal de sortie du récepteur est enregistré à l'aide d'un oscilloscope numérique (MDO3054). Les données obtenues sont post-traitées à l'aide de MATLAB. Après ré-échantillonnage du signal, le préambule est décodé pour identifier le début du signal envoyé. Les filtres adaptés déployés pour la démodulation dépendent de leur définition au niveau du récepteur. Les symboles mappés sont corrigés en gain et en phase, puis un égaliseur à décision (DFE) effectue une post-égalisation. Enfin, ils sont démappés à l'aide du démodulateur  $M$ -QAM. Ainsi, le paquet de données original envoyé est obtenu.

Le processus d'optimisation des performances permet d'optimiser le débit total. Le principe est que chaque sous-porteuse pourrait potentiellement avoir un filtre de transmission légèrement différent au lieu des configurations habituelles où seule la fréquence centrale change. L'idée est que chaque sous-porteuse a son propre filtre FIR défini sur les émetteurs-récepteurs. Afin de satisfaire un utilisateur et de conserver une qualité de service correcte pour tous les récepteurs, le seul choix en  $m$ -CAP est de modifier la taille de la constellation des sous-porteuses attribuées ou de modifier l'attribution de sous-porteuses. Cette flexibilité relativement faible sur  $m$ -CAP signifie que l'amélioration de la qualité de service pour un utilisateur exigeant un débit de données fixe signifie une baisse de qualité pour les autres utilisateurs car ils auront moins de sous-porteuses allouées. À partir de cette observation, nous explorons la possibilité supplémentaire d'utiliser un jeu de paramètres de filtre différent sur chaque paire de filtres FIR.

Le facteur de roll-off définit la bande passante excédentaire. Ainsi, plus la valeur est petite pour une sous-porteuse, plus le rapport de puissance crête sur moyenne (PAPR) est élevé pour cette sous-bande. Le principe d'optimisation du facteur pour chaque sous-porteuse est que, dans la configuration expérimentale réaliste du système VLC intérieur, différents types de bruit dominant le signal à différentes fréquences.

En effet, la pré-égalisation est utilisée pour étendre la largeur de bande de modulation du canal et fonctionne donc virtuellement «hors bande». En tant que tel, la puissance du signal reçu est plus faible aux fréquences les plus élevées en raison de l'effet passe-bas du canal. Ainsi, le bruit blanc gaussien domine à haute fréquence pour le signal mais moins à basse fréquence où le bruit de clipping est plus faible. En conséquence, les dernières sous-porteuses privilégieront un facteur de réduction plus faible pour une largeur de bande moins excessive et les premières sous-porteuses préféreront une valeur plus élevée. Le BER le plus bas pour chaque sous-porteuse se trouve à différentes valeurs de ce facteur roll-off. Dans un signal 20-CAP, pour les sous-porteuses 1 à 5, le facteur d'abattement optimal moyen est mesuré à 0,66. Pour les sous-porteuses 6 à 10, il est mesuré à 0,46. Pour les sous-porteuses 11 à 15, il est mesuré à 0,3. Et, pour les sous-porteuses 16 à 20, il est mesuré à 0,26.

Le facteur de suréchantillonnage et l'étendue du filtre définissent ensemble la longueur du filtre. Le rapport signal sur bruit augmente dans la largeur de bande du signal pour la même fréquence d'échantillonnage. De ce fait, un impact plus positif devrait être constaté sur les dernières sous-porteuses où le bruit gaussien est dominant. Un compromis entre les coûts de mise en œuvre doit être noté. Alors que l'augmentation de la longueur du filtre offre de meilleures performances brutes, un filtre FIR plus long sera plus éprouvant pour les calculs. Dans ce travail, ce compromis ne sera pas analysé. Pour une longueur de filtre de 150, le BER atteint est, par exemple, de  $3,57 * 10^{-3}$  à la sous-porteuse 3 et de  $8,15 * 10^{-3}$  à la sous-porteuse 20, le minimum dans les deux cas. Cependant, un filtre FIR plus long a un coût de mise en œuvre plus élevé lors de la modulation et de la démodulation des formes d'onde CAP de chaque sous-porteuse. En termes de compromis, le BER diminue entre une longueur de filtre de 120 et 150. Il s'agit d'une réduction d'un facteur d'environ 1,65 en moyenne pour toutes les sous-porteuses. Mais, cette dernière option est 25% plus lourde en calcul. Bien qu'une telle diminution du BER semble élevée une telle valeur n'est souvent pas suffisante pour pouvoir augmenter l'ordre de modulation d'un signal spécifique. Cependant, il offre toujours une augmentation considérable de la flexibilité et l'effet sur ces dernières sous-porteuses est plus prononcé avec une diminution du BER d'environ 3,065 pour les 3 dernières sous-bandes lors de l'augmentation de la longueur du filtre de 120 à 150. Le compromis d'optimisation de la longueur entre les performances et le coût de mise en œuvre ne vaut que dans notre cas pour ces dernières sous-porteuses.

Les schémas de modulation multi-bande sont sujets aux interférences inter-canaux et le CAP multi-bande ne déroge pas à la règle puisque les filtres de mise en forme d'impulsions n'ont pas une réponse rectangulaire parfaite. Ces interférences causées par les lobes secondaires dans la réponse du filtre réduisent la qualité du signal sur un récepteur donné, ce qui aggrave le BER. L'espacement des sous-porteuses est une méthode utilisée pour atténuer ces interférences. Mais cela se fait au prix d'une bande passante accrue. Dans un système VLC à haut débit, cela peut être un inconvénient en

raison du modèle passe-bas du canal optique sans fil et de la nécessité de modulations à efficacité spectrale élevée. L'équation de définition de filtre légèrement modifiée dans ces travaux ajoute un facteur à la description des filtres cosinus en relief et en racine carrée en phase et en quadrature utilisés pour la mise en forme des impulsions de chaque sous-porteuse. La valeur par défaut de ce facteur  $p$  est 1, ce qui correspond à l'absence d'espacement entre les sous-porteuses. Ajouter 10 % correspond à  $p = 1.1$  et crée un espacement de 10 % entre les fréquences centrales des sous-porteuses. Une augmentation de l'espacement des sous-porteuses se traduit directement par une diminution des interférences entre canaux. Cependant, étant donné que cela entraîne également une augmentation de la largeur de bande totale du signal, une réduction du BER n'est pas évidente en raison de l'effet de passe-bas du canal. Avec le montage expérimental et une modulation 20-CAP, les sous-porteuses 1 à 5 obtiennent le BER le plus faible avec une valeur optimale d'espacement des sous-porteuses d'environ 25%. Les sous-porteuses 6 à 10 nécessitent un espacement optimal d'environ 13 %. Les sous-porteuses 11 à 15 nécessitent un espacement d'environ 10%. Les sous-bandes 16 à 20 nécessitent un espacement d'environ 3%. L'effet de différentes configurations d'espacement de sous-porteuses sur l'efficacité spectrale est étudié. La première configuration n'utilise pas d'espacement entre sous-porteuses. La deuxième configuration utilise la même valeur d'espacement entre chaque sous-porteuse et s'appelle un espacement uniforme des sous-porteuses. La valeur d'espacement choisie maximise le débit de données. Enfin, la dernière configuration utilise le meilleur espacement de sous-porteuse entre chaque sous-porteuse et est appelée espacement optimisé. Avec l'utilisation de l'espacement entre sous-porteuses, les interférences entre canaux (ICI) ont diminué mais la largeur de bande du signal augmente. À son tour, le SNR diminue. Avec un espacement uniforme, l'augmentation des performances des premières sous-porteuses compense la diminution des dernières sous-porteuses. Avec un espacement optimisé, les premières sous-porteuses ont une valeur d'espacement plus grande que les dernières qui utilisent un espacement plus petit ou nul. Essentiellement, les premières sous-bandes ont un SNR suffisamment élevé et la diminution de ICI est suffisante pour permettre l'utilisation d'un ordre de modulation plus élevé. Toutefois, afin de ne pas trop augmenter la bande passante du signal, les dernières sous-porteuses utilisent un espacement moyen de 2,5 %. Ainsi, une augmentation du débit de données de 16,67 % à 6,7 % est obtenue avec 4 à 30 sous-porteuses utilisant un espacement optimisé, les valeurs comprises entre 11,11 % à 4 % utilisant des valeurs uniformes. Avec 20 sous-porteuses, l'augmentation du débit de données est mesurée à 6,43 % pour la méthode d'espacement optimisé et à 3,96 % pour le processus d'espacement uniforme.

Vous pouvez obtenir plus de flexibilité en optimisant le facteur de roll-off et le facteur de suréchantillonnage des filtres FIR. Lors de la modification simultanée de tous les paramètres, plusieurs scénarios avec une augmentation des performances apparaissent. Cette flexibilité est utile dans un scénario multi-utilisateurs où tous les récepteurs ont des RSB très différents. Afin d'explorer cette flexibilité, l'impact du

facteur de roll-off sur le débit de données est comparé aux résultats obtenus avec l'espacement des sous-porteuses. Sans espacement et avec les mêmes paramètres, chaque sous-porteuse a une valeur de roll-off optimisée afin de maximiser le débit de données total. Ensuite, l'espacement des sous-porteuses est associé à un facteur de roll-off dans l'optimisation. Lors de l'optimisation uniquement pour le facteur de roll-off de chaque sous-porteuse, en utilisant une boucle d'optimisation conventionnelle, l'augmentation des performances brutes a atteint 11,1 % pour un signal 4-CAP, 4 % pour un signal 20-CAP et 3,8 % pour un signal 30-CAP. Lors de l'optimisation de la longueur du filtre, une valeur globale de 120 a été utilisée pour toutes les sous-porteuses. Ainsi, comme mesuré, l'augmentation des performances brutes a atteint 16 % pour un signal 4-CAP, 2,15% pour un signal 20-CAP et 1,95% pour un signal 30-CAP. Avec le processus d'optimisation complet sur tous les paramètres, l'augmentation du débit de données brutes a atteint 28,67% pour un signal 4-CAP, 7,77 % pour un signal 20-CAP et 7,81 % pour un signal 30%. Avec 20 sous-porteuses, cela équivaut à un ajout de 11,75 Mb/s. Le processus d'optimisation complète offre plus de degrés de liberté, ce qui permet d'observer davantage de scénarios avec une augmentation du débit de données. Par exemple, un facteur de roll-off important augmente la bande passante de la sous-porteuse associée. En retour, il augmente les interférences entre les sous-bandes. Mais, avec l'espacement des sous-porteuses, ces interférences sont réduites. Le processus d'optimisation complète permet une augmentation du débit de données supérieure à celle des autres.

L'augmentation totale du débit de données par rapport aux résultats de base était de 11,75 Mb/s. Etant donné que l'espacement des sous-porteuses a été utilisé, la largeur de bande du signal a été modifiée et est passée de 28,5 MHz à 31,45 MHz. En conséquence, l'efficacité spectrale du schéma a été légèrement réduite de 5,31 b/s/Hz à 5,18 b/s/Hz. En contrepartie, le BER total en ligne directe de service a été réduit de manière significative, passant de  $1,84 * 10^{-3}$  à  $5,18 * 10^{-4}$ , soit une diminution d'un facteur de 3,55, en plus de l'augmentation du débit de données. Cela est dû à l'utilisation de valeurs de paramètres de filtre optimisées pour chaque sous-porteuse. Bien que la diminution du BER ne soit parfois pas suffisante pour se traduire par une augmentation de l'ordre de modulation pour une sous-bande spécifique, le taux d'erreur sur les bits est souvent considérablement réduit par des facteurs relativement importants. Cela correspond à une augmentation de la flexibilité du système. Cela signifie qu'il existe plusieurs scénarios permettant d'atteindre un débit de données plus élevé. Le processus d'optimisation aura également un impact positif sur la répartition du BER dans une salle. Cette caractéristique est essentielle à l'estimation de la capacité multi-utilisateurs du système expérimental.

Le montage expérimental est légèrement modifié pour accommoder l'utilisation des associations de  $m$ -CAP avec SCM, MC-CDMA et PD-NOMA. PD-NOMA est associé avec SCM ou MC-CDMA pour pouvoir servir plus que 2 utilisateurs car le schéma est limité à deux niveaux de puissance pour faciliter l'implémentation.

La distribution BER tridimensionnelle (3D) indique le taux d'erreur sur les bits atteint après le processus de démodulation par un récepteur situé à un certain point de la pièce. Cet emplacement se trouve sur un plan de réception éloigné du plan de transmission à une distance définie en utilisant l'émetteur LED comme référence. En conséquence, le BER qu'un utilisateur expérimente peut être connu. Ceci est une représentation directe des performances du système et de nombreuses caractéristiques peuvent ainsi être obtenues:

- Le débit maximum pouvant être obtenu pour tout utilisateur situé dans la salle avec le BER et une limite FEC connue.
- La taille de l'attocell et la portée du système qui sont représentées par la zone où le BER est suffisamment bas pour qu'un utilisateur puisse pleinement profiter des capacités du point d'accès.
- Une indication générale sur la flexibilité du système multi-utilisateurs basé sur la distribution BER.

La taille de l'attocell est définie comme la zone dans le plan de réception où un utilisateur peut être entièrement desservi par le point d'accès. En pratique, pour le montage expérimental, cela correspond à la surface où le BER à la réception est inférieur à une certaine valeur. Une limite de 7 % FEC est choisie et cette valeur est  $3,8 \cdot 10^{-3}$ . Concrètement, si le BER de toutes les sous-porteuses du signal CAP multi-bande est inférieur à ce nombre, un utilisateur peut entièrement décoder la forme d'onde à condition que 7 % des données soient allouées au processus de correction d'erreur en aval. Une remarque importante est que l'attocell dépend également de la méthode multi-accès utilisée. En effet, dans le cas du SCM, la forme d'onde du CAP multi-bande est inchangée et, quel que soit le nombre d'utilisateurs attribués, les caractéristiques du signal ne changeront pas. Dans ce cas, la taille d'attocell ne varie pas avec le nombre d'utilisateurs. Cependant, dans le cas de MC-CDMA, plus on utilise de codes d'étalement, plus il est difficile de maintenir l'orthogonalité entre les utilisateurs. En conséquence, la forme d'onde du CAP multi-bande doit être optimisée pour maintenir l'orthogonalité à un point où chaque utilisateur peut toujours disséminer ses données avec succès. La taille des attocell risque donc de subir une certaine variance avec différentes quantités de codes d'étalement. De plus, la répartition du BER varie dans la pièce, ce qui signifie que le signal peut ne pas conserver l'orthogonalité pour un certain nombre de codes d'étalement sur l'ensemble du plan récepteur.

Chaque combinaison de CAP multi-bande avec SCM, MC-CDMA ou PD-NOMA utilise une ressource différente pour allouer ses utilisateurs. Afin de mesurer l'efficacité de la méthode d'allocation utilisateur, nous avons défini l'écart par rapport au débit cible. Cette métrique permet d'évaluer la capacité d'un schéma à servir un utilisateur par rapport au débit qu'il requiert.

L'utilisation d'un schéma à accès multiples sur  $m$ -CAP a un effet sur les performances du schéma. Le débit de données par utilisateur pour chaque association est comparé à une division idéale du débit de données. Ainsi, le débit total est simplement divisé également en nombre d'utilisateurs sans prendre en compte les variations. Cette section examinera comment SCM, MC-CDMA et PD-NOMA affectent les performances par rapport à ce cas idéal. Quel que soit le nombre d'utilisateurs, SCM atteint le même débit par utilisateur qu'une division idéale. Dans un scénario à 2 utilisateurs, 81,5 Mb/s est atteint et dans un scénario à 10 utilisateurs, 16,3 Mb/s par utilisateur. La variation est de 2,5 Mb/s dans un scénario à 2 utilisateurs et passe à 12,5 Mb/s dans un scénario à 10 utilisateurs. Lorsque vous augmentez le nombre d'utilisateurs, le nombre de sous-porteuses par récepteur pouvant être alloué par SCM diminue, ce qui explique cette variation croissante du débit entre chaque utilisateur. Pour MC-CDMA, dans un scénario à 2 utilisateurs, 81,3 Mb/s par utilisateur est atteint. Un nombre qui diminue avec l'ajout de plus d'utilisateurs, et donc de codes plus orthogonaux. À 4 utilisateurs, 40,25 Mb/s est atteint et à 10 utilisateurs, 10 Mb/s par utilisateur. Cette petite différence entre les valeurs obtenues lors de l'utilisation de SCM provient du fait que le signal doit être ré-optimisé lorsque le nombre de codes est augmenté. Cela est nécessaire pour servir plus d'utilisateurs en raison de la perte d'orthogonalité lorsque plus de codes sont utilisés. Cependant, la principale différence par rapport à la SCM se situe à ce stade, car les écarts entre le débit de chaque utilisateur ne sont que de 2,5 Mb/s, alors que l'écart de 2,5 Mb/s à 12,5 Mb/s trouvé avec le premier schéma multi-accès. Le débit par utilisateur atteint dans tous les scénarios utilisateurs est approximativement le même pour PD-NOMA avec SCM et PD-NOMA avec MC-CDMA que lorsque vous utilisez uniquement les deux schémas secondaires respectifs. En effet, dans un scénario à 2 utilisateurs, 81,25 Mb/s par utilisateur est atteint pour PD-NOMA avec SCM et 78,8 Mb/s pour la deuxième association. Dans un scénario à 10 utilisateurs, 16,25 Mb/s est atteint par le premier schéma et 7,5 Mb/s par utilisateur par seconde. La petite différence vient de l'optimisation supplémentaire du signal dans le codage par superposition afin d'exploiter correctement la différence de canal entre les groupes d'utilisateurs éloignés et proches. PD-NOMA présente le principal avantage en termes de débit de données par utilisateur: le doublement virtuel du nombre de sous-porteuses. Cela influe sur la variation de débit mesurée entre chaque utilisateur en la réduisant de moitié. Seulement 1,25 Mb/s à 6,25 Mb/s est obtenu pour PD-NOMA avec SCM dans des scénarios de 2 à 10 utilisateurs et 1,25 Mb/s pour toutes les configurations est atteint pour PD-NOMA avec MC-CDMA.

La mesure de la distribution du BER dans une salle intérieure pour la configuration expérimentale permettra une caractérisation plus complète de l'attocell créée par tous les schémas. Toutefois, comme indiqué précédemment, chaque schéma d'accès multi-utilisateurs à une association CAP multi-bande affecte la capacité de l'utilisateur de différentes manières. En mesure, le taux d'erreur sur les bits obtenu diminue d'autant plus que le récepteur est éloigné du centre du plan de réception. En effet, cela se

traduit par une augmentation de la distance de la photodiode à la LED et, comme prévu, par une réduction de la puissance optique reçue. Lorsque vous utilisez la limite de 7 % FEC, cela signifie que tant que le récepteur est placé, le BER étant inférieur à  $3,8 * 10^{-3}$ , le signal peut être entièrement décodé, moyennant un surcoût de 7%. Cela correspond à une superficie mesurée d'environ 4,56 mètres carrés. Dans le cas de SCM, cela signifie que jusqu'à 20 utilisateurs pourraient être desservis sur cette surface de 4,56 m<sup>2</sup>. En effet, sur cette surface, les 20 sous-porteuses peuvent être décodées et sont donc disponibles pour tout utilisateur. Dans le cas de MC-CDMA, l'atténuation dans le signal réduit l'orthogonalité au niveau du récepteur. En conséquence, le nombre d'utilisateurs pouvant être desservis diminue avec la distance qui le sépare de l'émetteur. Cela signifie que dans le cas de l'utilisation de ce schéma à accès multiples, une taille d'attocell différente est obtenue à chaque limite de capacité utilisateur. Si une limite de 12 utilisateurs est prise en compte, la surface d'attocell est mesurée à environ 0,125 m<sup>2</sup>. Mais, si on considère une limite de 4 utilisateurs, la taille d'attocell mesurée est d'environ 2,81 m<sup>2</sup>. Dans le cas de PD-NOMA, les attocell mesurées étaient les mêmes que lorsque seul le schéma à accès multiple secondaire correspondant était utilisé. Par conséquent, dans le cas de PD-NOMA et de SCM, la taille de l'attocell correspondante est également mesurée à 4,56 m<sup>2</sup> et jusqu'à 40 utilisateurs peuvent être desservis dans cette zone, soit 20 par groupe d'utilisateurs. Dans le cas de PD-NOMA avec MC-CDMA, les mêmes résultats que pour MC-CDMA ont été atteints uniquement pour la taille d'attocell et le nombre d'utilisateurs utilisables. La différence que PD-NOMA peut apporter, outre l'augmentation de la capacité utilisateur pour la gestion de la chaîne logistique, réside dans la problématique de l'affectation des utilisateurs.

La capacité utilisateur atteinte mesurée par rapport à la déviation au débit cible tolérée permet d'estimer la capacité à atteindre les besoins de plusieurs utilisateurs. Pour un écart toléré de 5 %, la capacité de l'utilisateur avec SCM est de 9. À un écart toléré de 10%, la capacité atteint 14 et enfin, la capacité maximale est de 20 en raison du nombre de sous-porteuses, à des écarts tolérés de 18% et plus. Lors de l'ajout de PD-NOMA, pour un écart toléré de 5 %, la capacité de l'utilisateur est de 12, contre 9 en mode SCM uniquement. À 10%, les capacités de 20 et 19 sont atteintes par la combinaison de PD-NOMA et de SCM. En ce qui concerne MC-CDMA, pour un écart toléré de 5 %, la capacité utilisateur a déjà atteint la capacité maximale de 12. En conséquence, un écart toléré de seulement 4 % est nécessaire afin de maximiser la répartition des utilisateurs pour le schéma. Lors de l'ajout de PD-NOMA, au lieu d'un écart toléré de 4 % afin de maximiser la capacité de MC-CDMA pour 12 utilisateurs, une valeur de seulement 3 % est nécessaire dans le cas de PD-NOMA avec MC-CDMA afin d'atteindre la capacité de 12 utilisateurs

En conclusion, le débit total avec une LED blanche commerciale atteint 163 Mb/s avec un taux d'erreur réduit d'un facteur de 3,55 grâce au processus d'optimisation des performances. Cette technique a l'avantage d'augmenter la flexibilité pour un scénario

avec plusieurs utilisateurs sans augmenter la complexité car seuls les paramètres des filtres de modulation sont altérés. La taille de la cellule obtenue est de  $4.56 \text{ m}^2$  à une distance de 2,15 mètres du transmetteur. La capacité peut atteindre jusqu'à 40 utilisateurs, ou 40.62 Mb/s dans un scénario à 4 utilisateurs. Il est donc démontré que le système proposé pourrait fonctionner comme une cellule à une distance réaliste, avec un débit de données élevé et la capacité de répondre aux besoins d'un grand nombre d'utilisateurs tout en limitant les coûts de mise en œuvre.